Université de Montréal

Elementary Steps in Aqueous Proton Transfer Reactions : A First Principles Molecular Dynamics Study

par

Vibin Thomas

Département de chimie

Faculté des Arts et des Sciences

Thèse présentée à la Faculté des Études Supérieures

en vue de l'obtention du grade de Philosophiæ Doctor (Ph. D.)

en chimie

Novembre, 2012

Résumé

La nature des acides dans un environnement aqueux est primordiale dans de nombreux aspects de la chimie et de la biologie. La caractéristique principale d'un acide est sa capacité à transférer un proton vers une molécule d'eau ou vers n'importe quelle base, mais ce procédé n'est pas aussi simple qu'il y paraît. Il peut au contraire être extrêmement complexe et dépendre de manière cruciale de la solvatation des différents intermédiaires de réaction impliqués. Cette thèse décrit les études computationnelles basées sur des simulations de dynamique moléculaire ab initio qui ont pour but d'obtenir une description à l'échelle moléculaire des divers procédés de transferts de proton entre acide et bases dans un milieu aqueux.
Pour cela, nous avons étudié une serie de système, dont l'acide hydrofluorique aqueux, l'acide trifluoroacétique aqueux, et un système modèle constitué d'un phénol et d'une entité carboxylate reliés entre eux par une molécule d'eau en solution aqueuse.
Deux états intermédiaires ont été identifiés pour le transfert d'un proton depuis un acide. Ces intermédiaires apparaissent stabilisés par un motif local de solvatation via des ponts H. Leurs signatures spectroscopiques ont été caractérisées au moyen de la spectroscopie infrarouge, en utilisant le formalisme de la dynamique moléculaire ab initio, qui inclut l'effet quantique nucléaire de manière explicite.
Cette étude a aussi identifié trois chemins de réaction élémentaire, qui sont responsable pour le transfert d'un proton d'un acide à une base, ainsi que leurs échelles de temps caractéristiques.
Les conclusions tirées de ces études sont discutées dans les détails, au niveau moléculaire, avec une emphase sur les comparaisons entre les résultats théoriques et les mesures expérimentales obtenues dans a littérature ou via des collaborateurs.

Mots-clés : Dynamique moléculaire ab initio, Dynamique moléculaire centroide ab initio, Transfert de protons, Intermédiaires de réaction dans un transfert de protons, Réactions acide-base, Dissociation d'acides, Intermédiaires de réaction dans une dissociation d'acide, Transformée par wavelettes, Spectroscopie infrarouge.

Abstract

The nature of acids in an aqueous environment is fundamental to many aspects of chemistry and biology. The defining feature of an acid is its ability to transfer a proton to water or to any accepting base, but this seemingly simple process can be complex and highly dependent on the solvation involving different reaction intermediate species. This thesis describes computational studies based on first principles molecular dynamics simulations aimed at obtaining molecular-level descriptions of diverse proton transfer process involving acids and bases in liquid water.

For that, we have investigated a variety of systems including aqueous hydrofluoric acid, aqueous trifluoroacetic acid and a model system comprising of a phenol and a carboxyate molecule bridged by a water molecule in aqueous solution.

Two different intermediate stages of proton transfer from an acid were identified which are found to be stabilized by distinct local H-bond solvation pattern. Their spectroscopic signatures were characterized using infrared spectroscopy computed from first principles molecular dynamics simulations which incorporate nuclear quantum effects explicitly. This study also identified three elementary reaction pathways that are responsible for proton translocation from acid to the base and their characteristic time scales. Conclusions drawn from this study are discussed in molecular detail, highlighting experimental comparisons.

Keywords : Ab initio Molecular Dynamics, Ab initio Centroid Molecular Dynamics, Proton Transfer, Proton Transfer Intermediates, Acid-Base Reaction, Acid Dissociation, Acid dissociation Intermediates, Wavelet Trasform, Infrared Spectroscopy.

Table des matières

1. Introduction

1.1 Water, Hydrogen Bonding and Time Scales 1

1.2 Hydrogen Bonding as Incipient Proton Transfer Reaction 2

1.3 Acid-Base Reactions in Water 3

1.4 Proton Diffusion In Water 4

1.4.1 Grotthuss Mechanism of Proton Transfer 5

1.4.2 Other Proton Transport Mechanism 7

1.5 What drives bond-breaking and bond-forming in aqueous proton transfer 8

1.5.1 Bell's Picture (Traditional View) 8

1.5.2 Hynes Picture (Non Traditional View) 9

1.6 Investigation of Ultrafast Proton Transfer Dynamics inside Encounter Pair Complex 11

1.6.1 Ultrafast Time-Resolved Studies 12

1.6.2 Ultrafast-Time Resolved Infrared Spectroscopic Studies 13

1.6.3 Mechanism of Proton Transfer inside Encounter Pairs 14

1.7 Motivation and Objective of this thesis 15

1.8 Strategy of Investigation and Outline of the Thesis 17

1.9 References 18

2. Computational Methods 23

2.1 Choice of Method 23

2.2 Fundamentals of Molecular Dynamics Simulation 24

2.2.1 Periodic Boundary Condition and Minimum Image convention 25

2.2.2 Long Range Interactions Using PBC:

Ewald's Summation 27
2.2.3 A general framework for Newton's laws: Lagrangian Formalism 29
2.2.4 Integrating Equations of Motion 30
2.3 Classical Molecular Dynamics Simulation 31
2.3.1 Advantages and Limitation of Classical Molecular Dynamics Simulations 32
2.4 Quantum Treatment of Electrons in Molecular Dynamics Simulations: AIMD 33
2.4.1 Density Functional Theory 33
2.4.2 Local Density Approximation 34
2.4.3 Generalized gradient approximation (GGA) 35
2.5 Born-Oppenheimer Molecular Dynamics 36
2.6 Car-Parinello Molecular Dynamics 37
2.6.1 Car-parinello Vs Born-Oppenheimer Molecular Dynamics 38
2.6.2 Plane waves and Pseudopotentials 38
2.7 Quantum Treatment of Nuclei in Ab Initio Molecular Dynamics 39
2.7.1 Feynman Path Integrals 40
2.7.2 Ab initio Path Integral Molecular Dynamics:Statics 43
2.7.3 Ab Initio Path Centroids: Dynamics 44
2.8 Computing Observables from MD Simulation 47
2.8.1 Radial Distribution Function 48
2.8.2 Diffusion Coefficient 48
2.8.3 Infrared Spectra and Vibrational Mode Analysis From Molecular Dynamics Simulation 49
2.9 References 53

3. Spectral Signatures and Molecular Origin of Acid Dissociation

Intermediates **61**

3.1 Introduction 61

3.2 Results and Discussion 65

3.2.1 Cryogenic mixtures of HF and H_2O show very broad absorptions that differ from those of fully dissociated acids. 65

3.2.2 The continuum of absorption is generated by heterogeneous broadening of the shared-proton asymmetric stretching frequency. 68

3.2.3 A mechanism for acid ionization and the microscopic solvent reaction coordinate for proton transfer by a weak acid 70

3.2.4 Assignment of the experimental spectral features 73

3.3 Conclusions and Outlook 74

3.4 Experimental and computational methods 75

3.4.1 Experimental approach. 75

3.4.2 Computational methods and their accuracy 77

3.5 Acknowledgments 81

3.6 Reference 82

4. Towards Understanding the Dissociation of Weak Acids in Water: 1. Using IR Spectroscopy to Identify proton-Shared Hydrogen Bonded Ion-Pair Intermediates **85**

4.1 Introduction 86

4.2 Computational Methods and Their Reliability 89

4.2.1 Linear response theory and the centroid approximation. 90

4.2.2 The influence of the fictitious electron mass and of the plane wave cutoff in Car-Parrinello molecular dynamics calculations of IR spectra 92

4.2.3 The reliability of the present simulation protocol in predicting IR spectra for pure H_2O and pure HF 94

4.3 Results and Discussion 99

4.3.1 Cryogenic spectra calculation strategy 99
4.3.2 The relevant experimental data 100
4.3.3 Mixtures containing a large excess of HF can be used to investigate the spectral properties of FHF^- and of H_3O^+ in the amorphous phase 103
4.3.4 The chemical species responsible for the broad and Intense absorption centered at 1800 cm^{-1} are proton-shared ion pairs. 105
4.3.5 Nuclear quantum effects 110
4.4 Conclusions and Outlook 113
4.5 Acknowledgements 116
4.6 References 116
5. On the Formation of Proton-Shared and Contact-Ion Pair forms During the Dissociation of Moderately Strong Acids: An Ab Initio Molecular Dynamics Investigation 120
5.1 Introduction 121
5.2 Computational Methods and their Accuracy 124
5.3 Results and Discussion 130
5.3.1 IR spectra of aqueous $F_3C-COOH$: experiment vs. computer simulation. 130
5.3.2 IR spectroscopic signatures of covalent and proton-shared forms. 131
5.3.3 IR spectroscopic signatures of contact, solvent-shared and dissociated forms. 135
5.3.4 Structural differences between undissociated, ion-pair and dissociated forms. 141
5.4 Does it make sense to talk about ion pair

dissociation intermediates? 143
5.5 Conclusions and Perspectives 145
5.6 Appendix. 147
5.6.1 Defining pair-correlation functions g(r) between carboxyl groups and hydrogen atoms. 147
5.7 Acknowledgement 148
5.8 References 149
5.9 Supporting Information 155
6. Concerted and Sequential Proton Transfer Mechanism in Water-Separated Acid-Base Encounter Pairs 157
6.1 Introduction 158
6.2 Computational Methodology 166
6.3 Supporting Information 167
6.4 Acknowledgement 168
6.5 References 168
6.6 Supporting Information 172
6.6.1 AIMD simulation: Details and Reliability. 172
6.6.2 Changing the pKa of acid and base. The effect of the constraints. 176
6.6.3 The Continuous Complex Morlet Transform 180
6.6.4 Nuclear quantum effects 182
6.6.5 References 183
7. Conclusions 186
7.1 Conclusions 186
7.2 References 190
8. Annexe I More details on computing IR spectra from MD simulation I
9. Annexe II More details on computing time dependent vibrational spectra V

Liste des Tables

Table 1-1 **5**

Comparison of different cation motilities versus proton mobility in liquid water

Table 6-1 **177**

The values of Q and q defined in Fig. 6-2 utilized in the present calculations and the associated pKa values.

Liste des Figures

Figure 1 1. **4**

Illustration of Eigen-Weller Model.

Figure 1 2. **6**

Illustration of modern view of Grotthuss proton transport and presolvation.

Figure 1 3. **7**

Ultrafast Acid Disossiation in liquid water.

Figure 1 4. **10**

Illustration of traditional and non-traditional proton transfer view.

Figure 1 5. **12**

Structure of photoacids, HPTS and HPTA

Figure 1 6. **13**

Important normal modes in the reaction between a phenolic photoacid and a carboxylate base.

Figure 1 7. **14**

Illustration of PT inside an encounter-pair complex proposed by Nibering et.al.

Figure 1 8. **15**

Illustration of the concerted PT mechanism inside an encounter pair proposed by Bakker et.al.

Figure 2 1. **26**

Periodic Boundary counditions (PBC).

Figure 2 2. **37**

Born-Oppenheimer molecular dynamics versus Car-parinello molecular dynamics.

Figure 2 3. **43**

Path integral picture of a) single quantum particle treated as a necklace consisting of "beads" with harmonic interactions between nearest neighbors on the chain. b) Illustration of interactions between beads.

Figure 2 4. **45**

An example of a water molecule represented by 4 beads.

Figure 3 1. **63**

Lower panel: Raw reflection-absorption infrared spectra for 20 monolayers (ML) thick films of binary mixtures of hydrogen halides (HX; X=F, Cl, and Br) with H_2O at 80K on Pt(111).

Upper panel: Difference spectra calculated using the ASW absorbance spectra from the lower panel as reference: -log(Ifilm/IASW).

Figure 3 2. **66**

Experimental and Computed absolute infrared absorption spectra of equimolar amorphous mixtures of HF and H_2O at 80 K.

Figure 3 3. **71**

The mean infrared absorption frequency (filled circles) of shared-proton asymmetric stretching vibrations is correlated to the average value of δ.

Figure 3 4. **78**

The total infrared spectrum of the amorphous monohydrate computed using the centroid molecular dynamics formalism (CMD).

Figure 4 1. **93**

The influence of the plane wave basis set cutoff (upper panel) and of the fictitious electron mass (lower panel) on the calculation of IR absorption spectra using Car-Parrinello molecular dynamics and liquid water at a temperature T=345K.

Figure 4 2. **95**

A comparison between experimental and theoretical IR spectra for liquid water (lower panel), and for liquid and crystalline HF (middle and upper panels, respectively.

Figure 4 3. **96**

Experimental IR absorption spectra for room temperature (upper panel) and cryogenic (lower panel) mixtures of hydrogen fluoride and water.

Figure 4 4. **99**

The computed IR absorption spectra for the reactant (solid line) and product (dashed line) species in reaction (4-6) at 0.98 molar fraction of HF.

Figure 4 5. **100**

Comparison between theoretical and experimental absorption spectra for cryogenic mixtures of HF and H_2O. The theoretical calculations are based on a classical (i.e.: Newtonian) treatment of the nuclear dynamics and on a first-principle description of the electronic structure.

Figure 4 6. **101**

Illustrative examples of typical first solvation shell molecular environments, and of absorption spectra generated by proton-shared Fδ- ··· H ··· δ+OH2 species (blue), F-•H_3O^+ (black) contact ion pairs and H_2O•HF (red) un-ionized limiting forms.

Figure 4 7. **105**

An illustration of the magnitude of zero-point vibration and of incoherent tunneling effects on the IR spectra reported in Fig.4-5.

Figure 5 1. **122**

A pictorial view of a) proton-shared, b) contact, and c)-d) solvent-shared ion pairs.

Figure 5 2. **127**

Comparison between computed (black) and experimental (green) IR spectra of aqueous solutions of $F_3C-COOH$.

Figure 5 3. **132**

A and B: Two trajectories of the dissociation indicator (see text and Eq. 12). In panel C, the time intervals denoted (1) and (2) are used to compute the IR spectrum of the covalent form of $F_3C-COOH$ (blue) and $F_3C-COO^- \bullet H \bullet {}^+OH2$ (red), respectively, using Eq. (7). Panel D shows the autocorrelation spectra of the CO distance computed using Eq. (5.8).

Figure 5 4. **137**

A-F: The trajectories of the dissociation indicator (red; see text and Eq. 5.12) and its running median (black; see text). In G the autocorrelation spectra of the CO distance are computed using Eq. (5.8) for all labeled segments. Panels B and D correspond to panels B and A from Fig.5-3, respectively.

Figure 5 5. **140**

O···H pair correlation function g(r), and coordination numbers N(r) computed by taking into account both O atoms that form the carboxyl group and all solvent H atoms (see text and inset).

Figure 5 6. **155**

The trajectories of the running median (top) and average (bottom) computed using 2T = 0.5 ps (blue), 1ps (black) and 1.5 ps (brown) (see text).

Figure 5 7. **156**

Snapshots showing the solvation environment of covalent forms (top) and contact ion-pairs (bottom).

Figure 6 1. **159**

Panels A, B: possible H-bond patterns and acid-base reaction mechanisms inside a water separated encounter pair. Panel C: By sequentially changing the pKa values of phenol and carboxyl groups two neutralization reactions can be initiated forming a complete cycle. The pKa changes are implemented using a

dipole-field / QM approach and the actual chemical events are studied utilizing first-principles molecular dynamics (see text). The acid-base reactions and their directions are indicated at the top and bottom of panel C.

Figure 6 2. **161**

Following the advancement of the chemical reaction using the proton location indicator defined in Eq. 6-1 (panel A) or the maximum absorption frequency of normal modes of phenol, intervening water and carboxyl moieties in panels B, C, and D respectively (see text). The sigmoid function fits (black) serve as a guide to the eye.

Figure 6 3. **164**

Probability density of the O-H bond lengths defined on the right for the sequential (A) and concerted (B) transfers shown in Fig. 6-2.

Figure 6 4. **166**

The simulation box and two periodic images showing the reactive region and the interaction between the fictitious dipoles across the interface.

Figure 6 5. **172**

Mean square displacement (top panel) and oxygen-oxygen radial distribution function (bottom panel) for BLYP (370 K), BLYP-D (350 K) and real water (300 K) (see text).

Figure 6 6. **175**

Gas-phase optimization of 2,6-dicyanophenol, formate and an intervening water molecule leads to formation of Structure 2. In aqueous solution however, the intervening water rotates and forms an H-bond with the bulk (Structure 1).

Figure 6 7. **176**

Chemical structure of 2,6-dicyanophenol and the formic acid. The locations of the pseudoatoms that generate the external dipole field are also shown.

Figure 6 8. **178**

The simulation box and two periodic images showing the reactive region and the interaction between the fictitious dipoles across the interface.

Figure 6 9. **179**

Distribution of oxygen-oxygen distances relevant to the proton transfer reaction from constrained (top) and unconstrained (bottom) AIMD calculations.

Figure 6 10. **181**

A plot of the real part of the wavelet intensity as a function of time.

Dedicated to my late wife Surya

Acknowledgements

I would like to express my sincere gratitude to my advisor Prof. Radu Iftimie for welcoming me in his group for my Ph.D. and for supporting my research, for his patience, motivation, enthusiasm, and for so gracefully sharing his immense knowledge in the field. My thanks extends to his group members, past and present: Titus Sandu, Patrick Maurer, Andrei Buin, Jean-François, Delphine, Vishnu, Ugo Rivard, Marie-Hélène, Sébastien, Baldir and Francis.

I also would like to include in my thanks the other professors in theoretical chemistry, and their group members: Prof. Matthias Ernzerhof, Hilke, Hélène, François, Yangxi, Yana, Prof. Tucker Carrington, Jean Christophe and Sergei Manzhos.

I had a wonderful opportunity to spend few months at University of Tokyo, Japan. I thank Sergei Manzhos , Koichi Yamashita and Hiroshi Ushiyama for inviting me to their marvelous research group.

I had the chance to pursue some wonderful projects in collaboration with Professor Ayotte from the University of Sherbrooke and with Professor Bradley Siwick from McGill University, for which I am eternally grateful for their inspiring collaboration on the projects and for the enlightening discussions that I had with them.

The members of the administrative and technical staff of the department of Chemistry have done a masterful job, for which I am unable to ever repay them.

I am indebted to Valerie Baslon, Patrick Ayotte and Patrick Maurer for patiently going through my thesis and giving valuable comments.

My friends and family have been for me much more than a support. Saju, Sunish, Gopan, Achen, Kochamma, Rajamma, Susan, Vincy, Mommy, Pappa, Guddy, Vinny, Valérie, Kiran, Amma, Pappi, Michelle, Thierry, Marine and Boris have travelled this road with me, carried me over the obstacles, they have accompanied me all the way.

But one remained behind. The one to whom this dissertation is dedicated to. My beloved wife Surya, who has been taken away from me so very much too soon, I'll keep in my heart an image of youth and beauty, she was a constant source of love, concern, support, strength and inspiration for me throughout her life, and will remain throughout mine.

Abbreviations

AIMD	Ab initio Molecular Dynamics
CMD	Centroid Molecular Dynamics
DFT	Density Functional Theory
DF/QM	Dipole-Field/ Quantum Mechanics
FT	Fourier Transform
FFT	Fast Fourier Transform
g(r)	Pair Correlation Funcion
IR	infrared
LJ	Lennard-Jones
MD	Molecular Dynamics
MM	Molecular Mechanics
NPT	Isothermal-isobaric ensemble
NVE	Microcanonical ensemble
NVT	Canonical ensemble
PIMD	Path Integral Molecular Dynamics
PT	Proton Transfer
QM	Quantum Mechanics
RDF	Radial Distribution Function
STFT	Short-time Fourier Transform
TS	Transition state
TST	Transition state theory
UV	Ultraviolet
VdW	Van derWaals
WT	Wavelet Transform

ZPE	Zero point energy

Units

Å	Ångström
e	Elementary Charge
Hz	Hertz
K	Kelvin
Kcal	Kilocalorie
Mol	Mole
Fs	Femtosecond
ps	Picosecond
ns	Nanosecond
cm^{-1}	Wavenumber
v	Frequency

1. Introduction

1.1 Water, Hydrogen Bonding and Time Scales

Water is a fascinating, important substance which forms the matrix of life. For such a simple molecule, its condensed phase properties are surprisingly complex. Water molecules in an aqueous solution constantly rotate, vibrate and translate in an intricate and beautiful dance that underlies essential processes in electrochemical, environmental, pharmaceutical, and biological sciences. Many of the anomalous behaviour[1-3] of water like reaching maximum density ay 4°C, highest heat of vaporization per gram of any molecular liquid (2257 Jg^{-1} at boiling point), highest thermal conductivity of any liquid, and thermal expansion coefficient α_p can be attributed to the structural aspects, in particular to the nature of intermolecular forces between the water molecules, the complex Hydrogen bond. A major fashion in which this network constantly rearranges by breaking and forming H-bonds is through the reorientation of water molecules. This rearrangement also occurs when the water hydration pattern adapts to a changing solute, and water reorientation is at the heart of hydration dynamics. Thus, for chemical processes involving charge redistribution in aqueous solution, a major response of the water solvent is the reorientation of individual water molecules.

A hydrogen bond[4] is a non-bonding, simple electrostatic attraction between the positive end of the bond dipole of A-H and the negative end of the dipole associated with B (or the negative charge on B if it is an anion). Atoms A and B are usually highly electronegative atoms like F, O, and N, for which dipole moments are large. More significantly, a hydrogen atom is so small that molecules AH and B can approach closely. Since dipole-dipole attractions fall off as the fourth power of distance, this close interaction is unusually strong, so that it can be viewed as a flexible bond. The ability of water to accept and donate two hydrogen bonds gives rise to a constantly evolving

disordered tetrahedral network of molecules. At any instant, liquid water contains ~ 90% of the hydrogen bonds formed in ice. Yet, the weak nature of hydrogen bonds allows the connectivity of water's network to rapidly fluctuate and rearrange over time scales from tens of femtoseconds to picoseconds. Ultrafast spectroscopic investigations of Hydrogen-bond rearrangement[5,6] in water found three time scales over which a water molecule samples different hydrogen-bonding configuration-a 50 fs, 200 fs, and 1.5 ps time scales. The short times scale is attributed to fluctuations in the hydrogen bonds, 200 fs is for intra molecular $O\cdots H$ vibration and the long times to hydrogen-bond breaking and forming. Furthermore, the vibrational excitation energy in the O-H bond is extremely fast. It is converted rapidly into bending vibrations, hindered molecular rotations, and heating of the surroundings within less than 1 ps. Thus, the dynamics of water provide an unusually effective route for dissipating vibrational excitation, the energy relaxation process that guides the conversion of reactants to products in aqueous solutions. These structural fluctuations combined with the water molecule's large dipole moment form the heart of aqueous reactivity, allowing water to rapidly respond to changes in solute electronic structure and guide the motion of protons through solution.

1.2 Hydrogen Bonding as Incipient Proton Transfer Reaction

Rather than the conventional electrostatic view of hydrogen bond, hydrogen bonds can also be viewed as incipient proton transfer reaction and hence brings the flavour of acid-base considerations. In this view point of hydrogen-bond as an incipient proton transfer reaction, a stable hydrogen bond A-H..B is a frozen stage of reaction

$$A\text{-}H..B \rightleftarrows A^{\delta-}..H^{\delta+}..B^{\delta+} \rightleftarrows A^{-}..H\text{-}B^{+} \qquad (1.1)$$

This means that a partial bond between H and B (H…B) is already established and the A-H bond is concomitantly weakened. In the case of strong hydrogen bonds, the stage of proton transfer can be more advanced. In some hydrogen bonds the proton position

is not stable at A or B , but proton transfer actually takes place with high rates[7]. In other cases these rates are small or negligible.

1.3 Acid-Base Reactions in Water

Proton transfer and acid-base neutralization reactions are among the most widespread and important transformations in in chemistry and biology.[8-15] In aqueous solutions these reactions can be extremely complicated due to the involvement of water molecules. A qualitative picture of how protons are transferred between acids and bases in aqueous solution was painted in the 1950s and 1960s, in classic work by Eigen[16,17] and Weller[18] using temperature jump relaxation spectrometry methods which perturb the existing equilibra by means of a temperature jump method and watch it relax back to equilibrium by spectroscopic methods. The qualitative framework in which bimolecular proton-transfer reactions in solution have been understood is the following. First, diffusive motion transports the acid and base to a particular intermolecular separation (the reaction contact radius) at which point an encounter pair complex is formed. Second, the chemical event of proton transfer takes place within this reactive complex at some intrinsic rate. This can be summarised in the following reaction scheme and pictorially in Fig.1-1.

$$AH(aq) + H_2O + B^-(aq) \overset{1}{\rightleftharpoons} [AH \cdot (H_2O)_n \cdot B^-]$$

$$[AH \cdot (H_2O)_n \cdot B^-] \overset{2}{\rightleftharpoons} [AH \cdot (H_2O)_n \cdot B^-]^\dagger$$

$$[AH \cdot (H_2O)_n \cdot B^-]^\dagger \overset{3}{\rightleftharpoons} [A^- \cdot (H_2O)_n \cdot BH]^\dagger$$

$$[A^- \cdot (H_2O)_n \cdot BH]^\dagger \overset{4}{\rightleftharpoons} [A^- \cdot (H_2O)_n \cdot BH]$$

$$[A^- \cdot (H_2O)_n \cdot BH] \overset{5}{\rightleftharpoons} A^-(aq) + BH(aq) + H_2O$$

Scheme 1. Eigen-Weller Model

where, the first and the last stages of this multi-state transformations are diffusive processes. The second stage represents the formation of an activated state from which

A-H bond-breaking can occur and proton diffuses to the base, while the fourth stage corresponds to the relaxation of the dissociated acid/protonated base couple immediately after proton transfer. The actual proton translocation from the acid to the base is depicted in the third stage. If the first stage is rate limiting then the reaction is termed diffusion limited reaction is used).

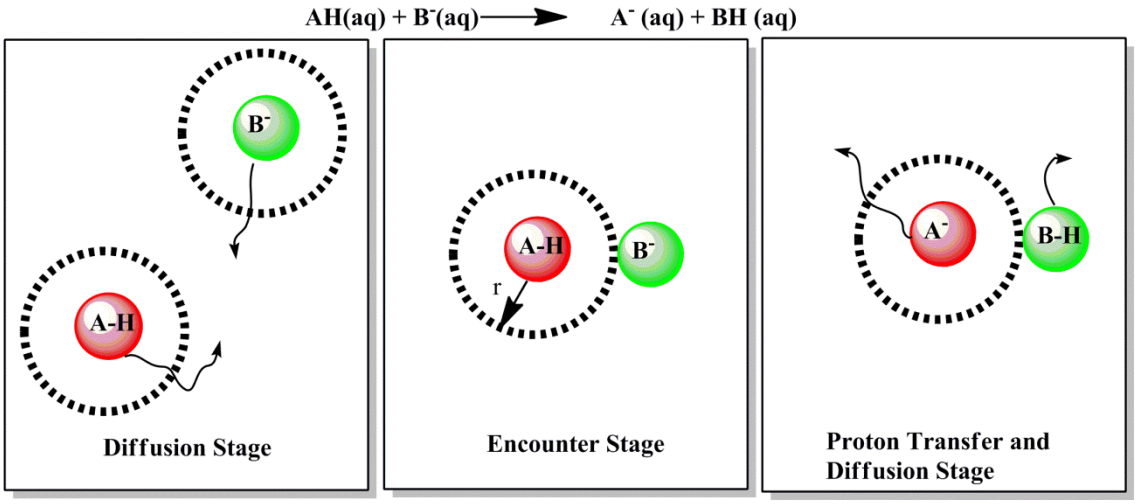

Figure 1-1. Illustration of Eigen-Weller Model. Acid (A-H) and base (B-) reactant molecules diffuse towards each other by a structural diffusion (left panel) , until an encounter complex of about 6 Å radius is formed(middle panel). Then they react and later diffuse away (right panel). Left panel corresponds to step 1 in scheme1. Middle panel corresponds to steps 2,3, and 4 in scheme1. Right panel corresponds to step 5 of scheme 1.

The idealized, spherically-symmetric encounter pair intermediate proposed by Eigen has a size ranging from r=6 to 8Å[16,19], which would correspond to a configuration in which the acid and the base are separated by approximately one or two water molecules and the proton is transferred through the water molecules.

1.4 Proton Diffusion In Water

The mobility of protons in liquid water is abnormally high[20] compared to that of other cations[21] like K^+, Na^+, Li^+, etc. Table 1-1 contrasts the different cation mobility in water

Cation	Mobility [$cm^2 V^{-1} s^{-1}$] [21]
H^+	3.62 X 10^{-3}
Na^+	0.519 X 10^{-3}
K^+	0.762 X 10^{-3}
Li+	0.663 X 10^{-3}

Table 1-1 Comparison of different cation mobility's in water versus proton

A basic picture that still guides our understanding of the anomalous diffusion process in hydrogen-bonded systems can be traced back to a paper[13,22] from 1806 by Theodor Christian Johann Dietrich von Grotthuss (1785−1822).

1.4.1 Grotthuss Mechanism of Proton Transfer

Grotthuss suggested that a structural or topological defect is transported *via* sequential proton transfer (PT) reactions along some arrangement of water molecules. However, this pure Grotthuss transport mechanism , i.e. a concerted proton hopping along chains of hydrogen-bonded polar molecules would result in an electrostatically unfavorable polarization of the chain. Consequently, protons can only be displaced over short distances before an accompanying solvent reorganization is required. Although many long-standing efforts to elucidate the details of this structural ("Grotthuss") diffusion mechanism are known[23], the details of von Grotthuss' proposal have only recently been fully revealed by state of the art theoretical and experimental techniques[24-34].The experimental method employed consists of diffraction and spectroscopic techniques like ultrafast vibrational spectroscopy and modern theoretical investigation

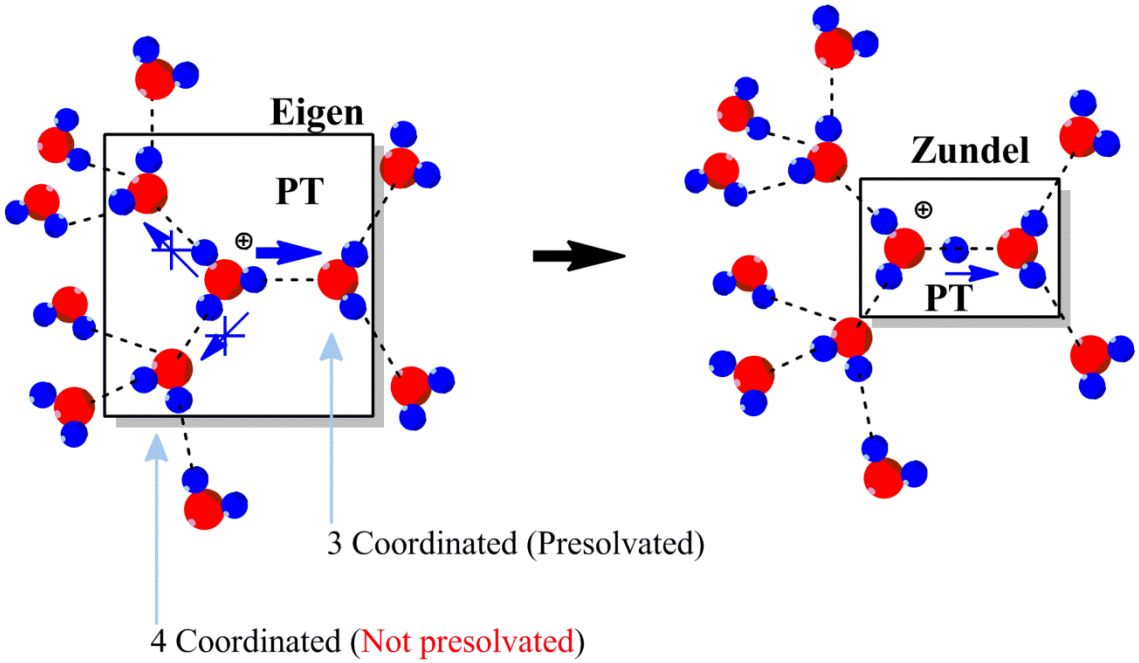

Figure 1-2. Illustration of modern view of Grotthuss proton transport and presolvation. The proton-receiving species first assume a coordination pattern like that of the species into which it will be transformed. The hydronium ion moves one molecular length at a time, continuously interconverting between zundel [$H_5O_2^{+}$] and Eigen [$H_9O_5^{+}$] species intermediates.

consists of *ab initio* molecular dynamics (AIMD) simulations[35] or parameterized empirical valence bond (EVB) simulation approaches[34,36-38]. These largely complementary methods have revealed important information about proton diffusion process. According to the modern view Grotthuss mechanism proton transfer from H_3O^+ to a neighboring water molecule takes place when the proton-receiving species t assumes a coordination pattern like that of the species into which it will be transformed. This process is called presolvation[39,40]. The accompanying proton transfer reaction occurs in relatively small charged complex such as $H_5O_2^+$, followed by solvation shell closing[41] (not shown in figure) and additional solvent reorganization in outer solvation shells. This process is also referred to as structural diffusion. The hydronium ion moves one molecular length at a time, continuously interconverting between covalent and hydrogen bonds, with the Eigen cation and Zundel species as intermediates.

This presolvation concept of proton transfer reaction is similar to the presolvation concept introduced by Marcus for electron transfer reactions[42,43] in which solvent fluctuations must occur that equalize the free energy cost before and after the electron transfer step.

A schematic representation of modern view of Grotthuss mechanism is given in Fig. 1-2.

1.4.2 Other Proton Transport Mechanism

A general notion coming out from these modern investigations is that proton transfer in aqueous solution involves only step by step sequential motion of proton involving two distinguishable molecular entities—Eigen form and Zundel form. However, recent investigations suggest that a long range ultrafast proton transfer mechanism through 4-coordinated water molecules is also possible[1]. This proton transfer mechanism depends on how the excess proton is injected in to the hydrogen bonded system. If excess protons are injected in to 4-coordinated water molecules then concerted transfers are observed which consist of proton translocation through two intervening, four-coordinated, water molecules in 0.1–1.0 ps up to a distance of 8 Angstrom (see Fig.1- 3) . This long range ultrafast transfer is only observed if the proton is injected into a four coordinated pre-existing water wire. On the other hand, if the

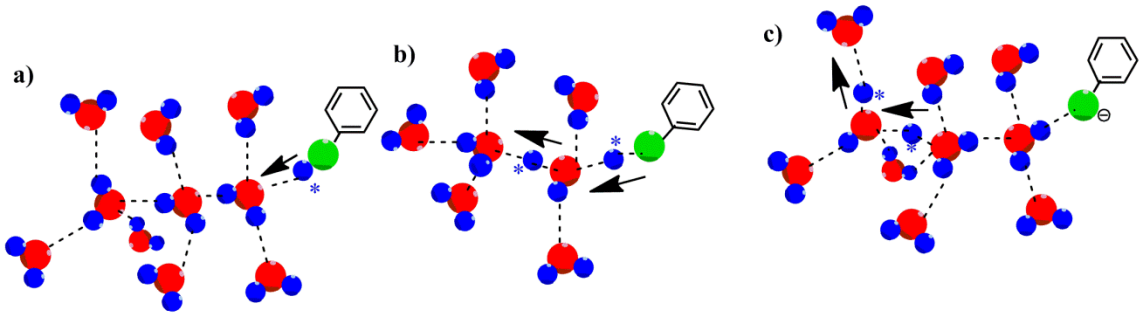

Figure 1-3. Ultrafast Acid Disossiation from a phenolic acid (shown as a phenol with a green oxygen and blue hydrogen). See Ref. [44] for details. a,b,c shows how the proton is transferred from the acid through four coordinated water molecules. Arrows represents the direction in which the transferring proton (hydrogen with *) is moving.

[1] This work is not included in this thesis

first proton-accepting water molecule in the water wire is three-fold H-bonded, the proton becomes trapped into the conducting water wire for periods equal to, or longer than the average proton hopping time in water(i.e., 1–2 ps). This proton transfer through four coordinated water molecules share the common features of proton transfer in ice, which was demonstrated[45] to be qualitatively different from proton transfer in water. A similar observation of the ultrafast proton transfer through four coordinated water was also recently reported by Parrinello *et al.* in the hydronium and hydroxide ion recombination reaction in water[24]

1.5 What drives bond-breaking and bond-forming in aqueous proton transfer

1.5.1 Bell's Picture (Traditional View)

A traditional description of proton transfer reactions was proposed by Bell[8] , Westheimer and Melander[8,46-48] based on transition state theory[49,50] . In their approach, the reaction coordinate that drive the transformation:

$$AH...B \rightarrow [A...H...B]^{\neq} \rightarrow A^{-} + HB^{+} \tag{1.2}$$

is $A...B$ distance and $A-H$ distance. According to their theory, PT reaction begins when $A-H$ starts forming hydrogen bond with the molecule B and proceeds through a transition state A…H…B, where A-H bond is partially broken and B-H is partially formed. The key assumption in this mechanism is that activation occurs in proton coordinate. This mechanism is illustrated in the Panel B of Fig.1-4. In this conventional view, kinetic isotope effect for H versus D transfer is given by

$$\frac{k_H}{k_D} = \exp\left[\frac{(-\Delta G_H^{\ddagger} - \Delta G_D^{\ddagger})}{RT}\right]; \Delta G_H^{\ddagger} - \Delta G_D^{\ddagger} = ZPE_H^{\ddagger} - ZPE_D^{\ddagger} + ZPE_H^{\ddagger}, \tag{1.3}$$

where $\Delta G^{\ddagger}$ is the activation free energy of reaction, R is the universal gas constant and T is the temperature. Kinetic isotope originates in this framework from the zero point

energy difference between reactants and the transition state. The vibrational frequency is that of proton coordinate and hence the zero point energy depends on the reduced mass of the vibrating system, which is essentially that of transferring proton.

1.5.2 Hynes Picture (Non Traditional View)

Despite the extensive use of this traditional description of proton transfer reaction, J. T Hynes[51-58] proposed a different, non-traditional description of proton transfer reactions. In this nontraditional picture of J.T Hynes, proton transfer reactions are driven by configurational changes in the surrounding solvent environment and the reaction activation free energy is largely determined by the environmental reorganization.

In this picture, the rapidly vibrating quantum proton follows the slowly rearranging environment, thereby producing a perspective in terms of the instantaneous proton potential for different environmental arrangements.

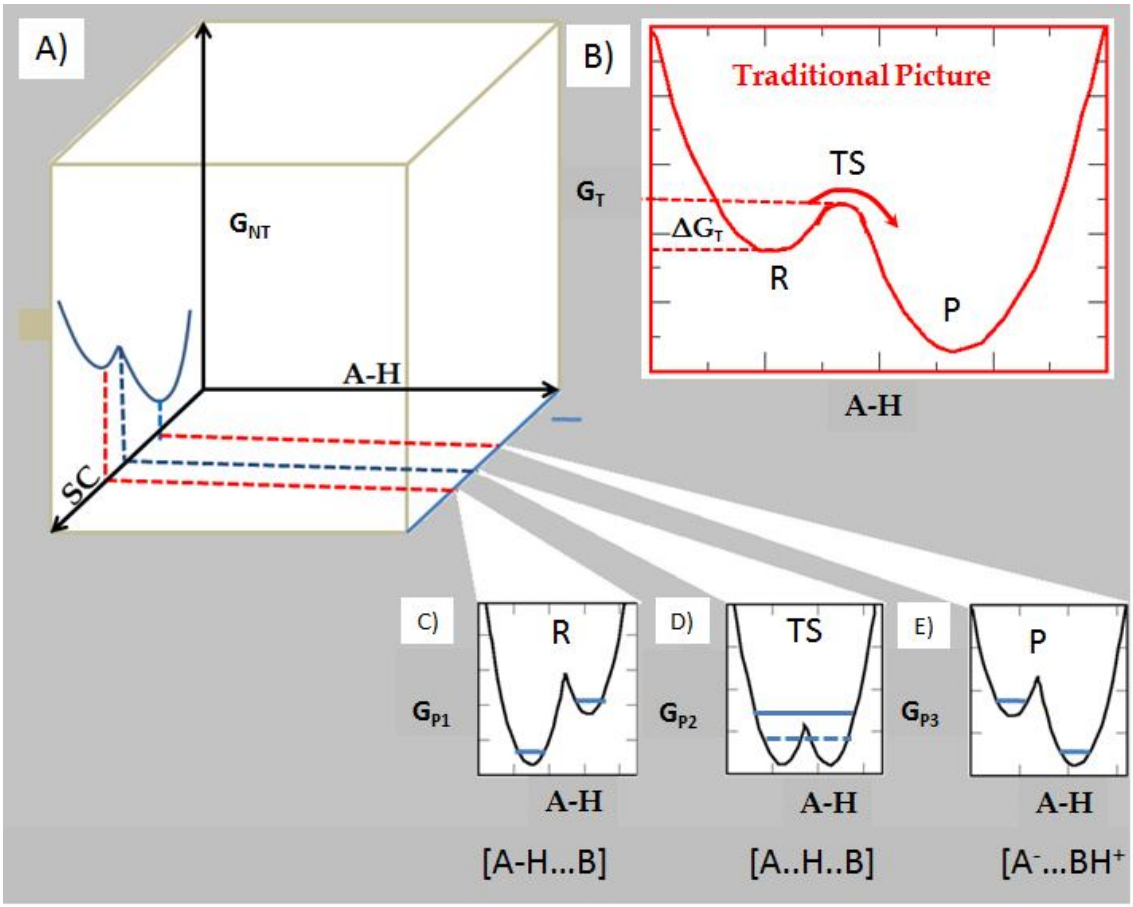

Figure 1-4. Illustration of traditional and non-traditional proton transfer view. The free energy is represented as a function of two coordinates. A proton coordinate (A-H) and a solvent coordinate (SC). See text for details. The zero point energy level is represented by the thick blue line. In the intermediate (double well) potential case (Fig. D) two possibilities for the location of zero point energy level, below the barrier (dashed blue line) and above the barrier (thick blue line) is possible.

This non-equilibrium solvent assisted proton transfer view of J.T Hynes is shown in Fig 4. Figure 1-4 A shows the free energy as a function of 2 coordinates $G_{NT}(AH, SC)$. A proton coordinate (A-H) and a solvent coordinate (SC). Evolution in the solvent coordinate (SC) leads to an evolving proton potential pattern, in which the proton is initially bound to a donor in the reactant state, to a transition state with the proton delocalized to a degree between donor and acceptor moieties, and finally to the product state with the proton bound to the acceptor. This is displayed in Fig 4. D,E,F, where the proton potential energy curves vs. proton coordinate at the reactant R, transition state

TS, and product state P solvent configurations for the reaction. The ordinate is a free energy $G_{P1}(AH, SC_R)$ for reactant state, $G_{P1}(AH, SC_{TS})$ for transition state and $G_{P1}(AH, SC_P)$ for product state, since the potential energy curves at each solvent configuration point shown have a constant free energy contribution related to the solvent interaction.

Adiabatic and Non-Adiabatic Proton Transfer

In the case of intermediate solvent configuration, there are two possibilities for the proton motion depending on the zero point vibrational level. If the zero point vibrational energy is greater than the proton barrier proton can be transferred from the acid and the base by adiabatically following the solvent fluctuations without tunneling. it is called **adiabatic proton transfer limit** while the zero point energy lesser than the proton barrier involves proton tunneling. The solvent plays a great role in this transfer because solvent fluctuations can tune the vibrations on both sides of the barrier into resonance, thereby strongly increasing the tunneling probability. This is called the **non-adiabatic proton transfer limit**.

In either cases there is no classical barrier crossing of the proton, in contrast to a conventional TS theory for the standard description.

1.6 Investigation of Ultrafast Proton Transfer Dynamics inside Encounter Pair Complex

In the second step of the Eigen-Weller model of proton transfer reactions that we discussed before, charge-transfer occurs inside the encounter complex at some intrinsic rate. Because the intrinsic rate for proton transfer is often extremely high in aqueous solution, the overall rate of such reactions tends to be 'diffusion-limited'. As a result, experimental access to the reaction kinetics inside the encounter complex has proven to be rather difficult. However, recent developments of ultrafast pump–probe spectroscopy (both visible[19,59] and infrared[60-63]) have yielded new insights into the proton transfer mechanisms involved inside solvent-separated encounter complexes and marked a new era for the proton transfer studies.

1.6.1 Ultrafast Time-Resolved Studies

In the ultrafast time-resolved studies, proton transfer is initiated by a Franck–Condon transition from a ground of a photo acid to an excited electronic state by using a pump pulse tuned in the UV/VIS region of the electromagnetic spectrum. The proto transfer reaction that happens after this pulse trigger is monitored by time resolved spectroscopic techniques. Photoacids[64] (for review see Ref[65]) are specific class of organic molecule which changes their acidity by a million folds upon photoexcitation. An examples of a commonly used photo acid is HPTS (8-hydroxypyrene-1,3,6-tri-sulphonate), which has a ground state pKa of 5.6[66] and an excited state pKa* of 8.0[67]. The structure of HPTS is shown in Fig. 1-5. This photoexcitation studies has various advantageous that the initiation of the reaction is essentially instantaneous on the reaction time scale, and can be followed by monitoring the time dependence of the spectral signature of the reactant's (product's) disappearance (appearance). The electronic excitation provides a thermodynamic driving force for the proton transfer reaction that is not present in the ground state. When a photoacid, Ar-OH, absorbs a photon, a cascade of events are initiated including intramolecular charge transfer, relaxation to the ground vibrational state of S_1, enhancement of the ROH···OH_2 hydrogen bond, and reversible PT to solvent with the proton diffusing away

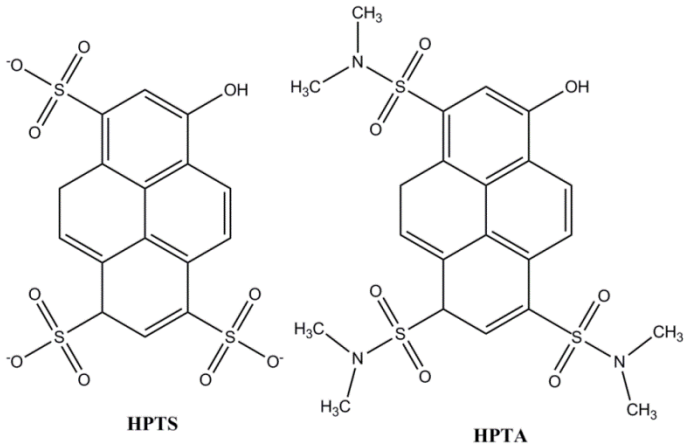

Figure 1-5. Structure of photoacits, HPTS and HPTA

from the RO^- via the Grotthuss mechanism. If there is proton acceptor present in the solution then the reaction is completed by the base taking up excess proton.

1.6.2 Ultrafast-Time Resolved Infrared Spectroscopic Studies

Time-resolved studies using time-correlated fluorescence single photon counting and UV/VIS pump-probe spectroscopy using photo acids[68] to study the proton transfer dynamics from photoacid has given direct insight into the dynamical process of proton dissociation from the photoacid by monitoring the decay of the photoacid S_1 state and the rise of the conjugated photobase S_1-species. These studies give details of the proton transfer process when the proton is instantaneously taken up by the base molecule in the solution. However, when the proton is first dissociating from the photoacid to the solvent, only to be taken up by an accepting base at later times, both the photoacid and the accepting base require monitoring. This is possible by using ultrafast time resolved mid-IR techniques[10,60,63,69-71] by following the dynamics of vibrational marker modes of the proton donating and the proton accepting species (See Fig.1-6 for an example). Ultrafast UV-pump /IR-probe spectroscopy investigations of hydroxyarenes such as 8-hydroxypyrene-1,3,6-pyrenetrisulfonic acid trisodium hydrate[60,63,69] (HPTS) or 2-naphtol-6,8-disulfonic acid dipotassium hydrate[10] (2N-6,8S) have identified several vibration marker modes that can be utilized to measure the advancement of the acid dissociation reaction.

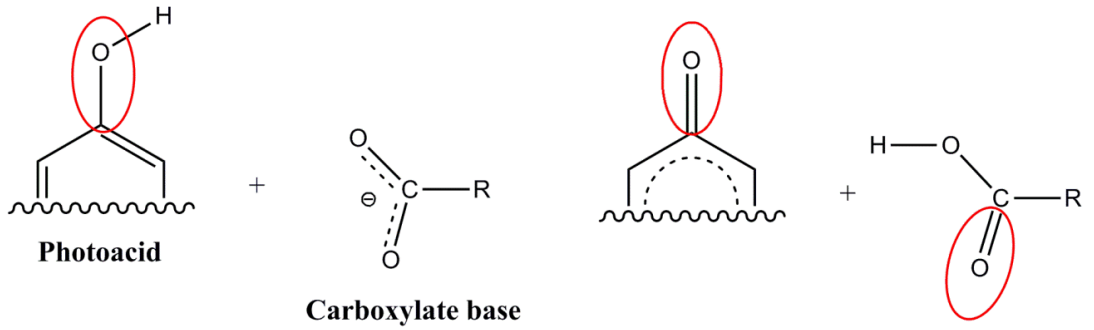

Figure 1-6. Reaction between a phenolic photoacid and a carboxylate base can in principle be monitored by the disappearence of phenolic C-O vibration, appearance of phenolic –C=O vibrational frequency and carbonyl –C=O vibrational frequency of carboxylate. The important modes are circled red in the figure.

1.6.3 Mechanism of Proton Transfer inside Encounter Pairs

In recent femtosecond mid-infrared spectroscopic studies on HPTS−acetate system[61,62,72] in aqueous solution performed by the Pines and Nibbering groups

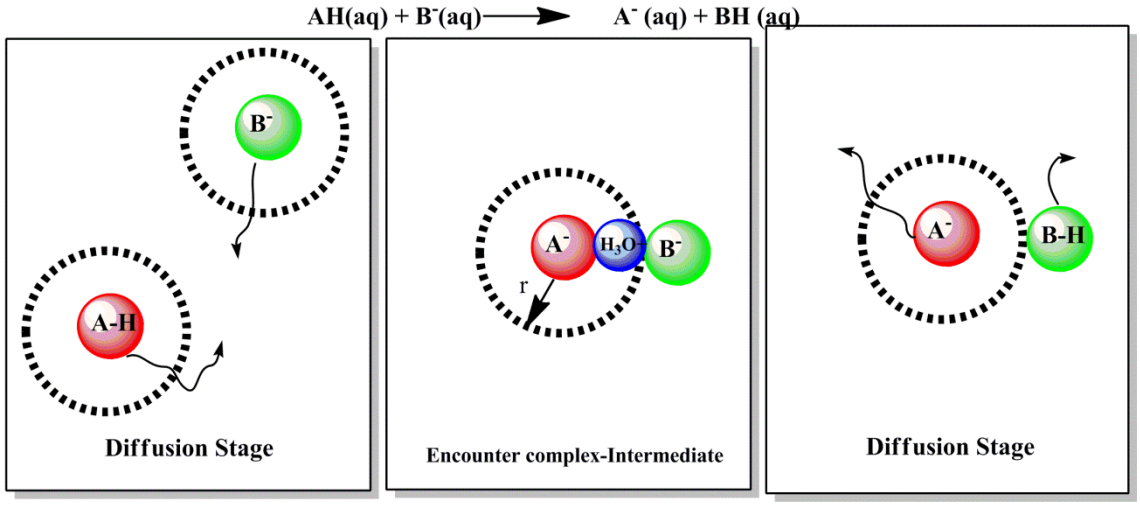

Figure 1-7. Illustration of PT inside an encounter-pair complex proposed by Nibering *et.al.*

found that three distinct components of the proton-transfer kinetics exists. The fastest component, with a time constant of ~150 fs, was assigned to PT in a population of hydrogen bound HPTS−acetate complexes already formed in the ground-state. A second slower component, with a time constant of 6 to several tens of picoseconds, was assigned to proton transfer in solvent-separated HPTS-acetate 'loose' complexes. The

third (and slowest) component with a time constant of tens of picoseconds up to few nanoseconds was assigned to the diffusive formation of tight and solvent-separated loose complexes. Based on a infrared transient absorption signature obtained for a symmetric H_3O^+, at 2750 cm^{-1}, Nibbering *et. al* concluded that elementary steps taking place inside the encounter pair is in a sequential fashion with the formation of an intermediate. This is shown in Fig. 1-7.

An alternate view on the proton transfer mechanism inside the encounter pair is given by Bakker et. al[63,73] on a similar acid-base system and with the same experimental techniques (ultraviolet (UV) pump-IR probe techniques) and proposed a concerted mechanism for the proton transfer inside an encounter complex (without the formation of intermediates). Their mechanism is shown in Fig. 1-8

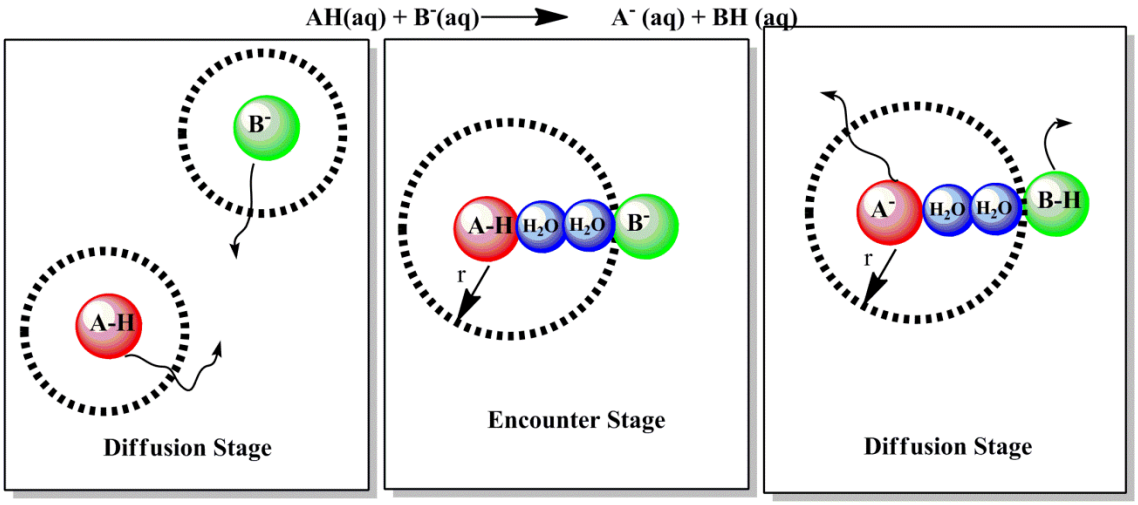

Figure 1-8. Illustration of the concerted PT mechanism inside an encounter pair proposed by Bakker *et.al.*

This controversy underscores the fact that existing condensed-phase experimental techniques which, despite recent advancements do not yet achieve subangstrom resolution in space and subpicosecond resolution in time. Consequently, the present-day mechanistic investigation of an ultrafast chemical transformation must usually be

accompanied by data interpretation, which can be subjective and can lead to opposite conclusions.

1.7 Motivation and Objective of this thesis

In addition to the above mentioned controversy, modern investigation of proton transfer reactions with photoacids has limitations. Spry and Fayer have shown evidence suggesting that the photoacid 8-hydroxypyrene-1,3,6-trisulfonic acid trisodium salt (HPTS) undergoes intramolecular charge redistribution in water on a several picoseconds timescale. This photophysical process, which may be general in the case of excited-state hydroxyarenes, can pose data interpretation more challenging, especially if photophysical and photochemical transformations happen to take place on similar timescales. Furthermore, we demonstrated that hydroxy-arene photoacids have another limitation[44], which is related to the initial nonequilibrium hydration state that is generated after electronic excitation. This forces the acid to which appears to be quite different from that of equilibrium dissociation. So it is not clear whether the general kinetic picture that can be extracted from these excited-state reactions is completely general, and, in particular, if the dissociation mechanism represents equilibrium ground-state neutralization reactions. Moreover, the model-independent details that the experimental data can provide on the nature of the proton transfer mechanism and their diversity is also limited. The experiments tend to measure the time-dependent population of reactants/products, offering little on very short-lived intermediates that may exist between these states.

Given these experimental limitations and due to the fact that many of the principal questions on proton transfer remains unanswered . These questions include:

- What are the elementary microscopic steps involved in proton transfer in aqueous solutions?
- Does acid dissociation involve proton transfer intermediates?
- How can these intermediates, if any, be characterized spectroscopically?

- How can one identify and follow the dynamics of different proton transfer intermediate species in a system?
- What is the role played by the surrounding local hydrogen bonding environment in proton transfer?
- How important is the role played by nuclear quantum effects in proton transfer process in water?

1.8 Strategy of Investigation and Outline of the Thesis

This thesis tries to answer these questions by computational investigations using ab initio molecular dynamics simulations. The details of the computational method used in this thesis are discussed in **chapter 2**.

The strategy used in this thesis involves two stages. First, we focused on the incipient stage of an acid-base reaction, namely the formation of proton transfer intermediates. Once the intermediates are characterized structurally and spectroscopically we change gears and the dynamics of acid-base reaction in solution is investigated. In this second stage, we identify the elementary reaction pathways that are responsible for proton translocation from acid to the base and their characteristic time scale.

This investigation requires prototypical systems which have considerable quantities of proton transfer intermediates. In search for such systems which has considerable amount of proton transfer intermediates, we came across the spectroscopic observation of Giguère and Turrell[74] on the strong ubiquitous "hydronium spectral signature bands" near 1200 and 1800 cm^{-1} along with strong Zundel continuum in aqueous solutions of HF. They attributed this to the $[F^- \cdot H_3O^+](aq)$ contact ion pair complexes. Unfortunately, the structure of proton transfer intermediates are usually challenging to isolate and characterize in bulk water with both experiments and theory. This is mainly due to the fast time scale of proton transfer and the complex role played by the

surrounding solvent water molecule. An alternative way is to study amorphous aqueous solids at cryogenic temperature instead of the room temperature liquids. Amorphous state[75] provide attractive alternative model systems for aqueous solutions as they can help trap metastable reaction intermediates in their liquid-like, albeit transnationally static, disordered H-bonded networks. Moreover, while slowing down tremendously the collective solvent motions responsible for the ultrafast interconversion dynamics, investigations at very low temperatures may also allow valuable insight into subtle quantum nuclear effects which are obscured by thermal agitation in liquid solutions. This quantum effects can then be theoretically studied using centroid molecular dynamics simulations. This study forms the **Chapter 3 and 4** of this thesis, which compares and contrasts experimental and computed IR spectra for cryogenic mixtures of HF and H_2O ranging from 20% to 98% mole fraction in HF. Chapter 3 is published in: *J. Am. Chem. Soc.* **130** (18): 5901-7 (2008) and Chapter 4 is published in *J. Phys. Chem. B* **113** (13): 4152-60 (2009)

Another system which is proposed to contain significant amounts of intermediate forms which are neither covalently intact, nor fully dissociated ions are moderately strong carboxylic acids. Covington et al.[76], and Gelb et al.[77] showed that infrared[78], Raman[76], ^{1}H nuclear magnetic resonance[77], and ion mobility measurements could be reconciled only by considering that ion pairs, which do not contribute to charge mobility measurements but have spectroscopic properties that resemble those of dissociated ions, are present in larger concentrations than un-ionized, covalent forms in aqueous trifluoroacetic acids system. An investigation of this trifluoroacetic acid-water system forms the **Chapter 5** of this thesis. This chapter is published in *J. Phys. Chem. B* **114** (24): 8147-55 (2010)

The strategy used in the second stage of this thesis is to study the finer details of the microscopic steps involved in proton transfer dynamics inside an encounter-pair complex. For this study we have chosen a model system involving phenolic and

carboxylic reactants closely related to the model systems investigated experimentally[19,63] using excited state proton transfer reaction. This forms the **Chapter 6** of this thesis. This chapter is published in *J. Phys. Chem. Lett.* **3** (18), 2633 (2012).

Finally, we summarize our conclusions in **Chapter 7**.

1.9 References

(1) Atkins, P.; de Paula, J. *Physical Chemistry*; 9 ed.; Oxfor University Press: New York, 2006.

(2) Franks, F. *Water, a comprehensive treatise*; Plenum Press: New York, 1972.

(3) Franks, F. *The physics and physical chemistry of water*; Plenum Press: New York,, 1972.

(4) Chen, B.; Ivanov, I.; Klein, M. L.; Parrinello, M. *Phys. Rev. Lett.* **2003**, *91*, 4.

(5) Asbury, J. B.; Steinel, T.; Kwak, K.; Corcelli, S. A.; Lawrence, C. P.; Skinner, J. L.; Fayer, M. D. *J Chem. Phys.* **2004**, *121*, 12431.

(6) Fecko, C. J.; Eaves, J. D.; Loparo, J. J.; Tokmakoff, A.; Geissler, P. L. *Science* **2003**, *301*, 1698.

(7) Zundel, G. *Hydrogen Bonds with Large Proton Polarizabilities*; Wiley: New York, 2000.

(8) Bell, R. P. *The Tunnel Effect in Chemistry*; Chapman and Hall: London, 1980.

(9) Marx, D.; Chandra, A.; Tuckerman, M. E. *Chem. Rev.* **2010**, *110*, 2174.

(10) Adamczyk, K.; Premont-Schwarz, M.; Pines, D.; Pines, E.; Nibbering, E. T. J. *Science* **2009**, *326*, 1690.

(11) Braun-Sand, S.; Strajbl, M.; Warshel, A. *Biophys. J.* **2004**, *87*, 2221.

(12) Decoursey, T. E. *Physiol. Rev.* **2003**, *83*, 475.

(13) Cukierman, S. *Biochim. Biophys. Acta-Bioen.* **2006**, *1757*, 876.

(14) Wraight, C. A. *Biochim. Biophys. Acta-Bioen.* **2006**, *1757*, 886.

(15) Swanson, J. M. J.; Maupin, C. M.; Chen, H. N.; Petersen, M. K.; Xu, J. C.; Wu, Y. J.; Voth, G. A. *J. Phys. Chem. B* **2007**, *111*, 4300.

(16) Eigen, M. *Angew. Chem. Int. Ed.* **1964**, *3*, 1.

(17) Eigen, M.; De Maeyer, L. *Proc. R. Soc. London, Ser. A* **1958**, *247*, 505.

(18) Weller, A. *Prog. React. Kinet.* **1961**, *1*, 189.

(19) Mohammed, O. F.; Pines, D.; Pines, E.; Nibbering, E. T. J. *Chem. Phys.* **2007**, *341*, 240.

(20) Agmon, N. *Chem. Phys. Lett.* **1995**, *244*, 456.

(21) Koneshan, S.; Rasaiah, J. C.; Lynden-Bell, R. M.; Lee, S. H. *J. Phys. Chem. B* **1998**, *102*, 4193.

(22) de Grotthuss, C. J. T. *Chem. Phys. Lett.* **1995**, *244*, 456.

(23) Han, J. H.; Zhou, X. Y.; Liu, H. T. *J. Power Sources* **2006**, *161*, 1420.

(24) Hassanali, A.; Prakash, M. K.; Eshet, H.; Parrinello, M. *P. Natl. Acad. Sci. USA* **2011**, *108*, 20410.

(25) Geissler, P. L.; Dellago, C.; Chandler, D.; Hutter, J.; Parrinello, M. *Science* **2001**, *291*, 2121.

(26) Izvekov, S.; Voth, G. A. *J. Chem. Phys.* **2005**, *123*, 9.

(27) Jensen, M. O.; Rothlisberger, U.; Rovira, C. *Biophys. J.* **2005**, *89*, 1744.

(28) Kobayashi, C.; Saito, S.; Ohmine, I. *J. Chem. Phys.* **2001**, *115*, 4742.

(29) Voth, G. A. *Acc Chem Res* **2006**, *39*, 143.

(30) Smiechowski, M.; Stangret, J. *J. Mol. Str.* **2008**, *878*, 104.

(31) Stoyanov, E. S.; Stoyanova, F. V.; Reed, C. A. *Chem. Eur. J.* **2008**, *14*, 3596.

(32) Vilciauskas, L.; Tuckerman, M. E.; Bester, G.; Paddison, S. J.; Kreuer, K. D. *Nat. Chem.* **2012**, *4*, 461.

(33) Woutersen, S.; Bakker, H. J. *Phys. Rev. Lett.* **2006**, *96*, 4.

(34) Wu, Y. J.; Chen, H. N.; Wang, F.; Paesani, F.; Voth, G. A. *J. Phys. Chem. B* **2008**, *112*, 467.

(35) Marx, D.; Hutter, J. *Ab Initio Molecular Dynamics*; Cambridge University Press: New York, 2009.

(36) Knight, C.; Voth, G. A. *Acc. Chem. Res.* **2012**, *45*, 101.

(37) Markovitch, O.; Chen, H.; Izvekov, S.; Paesani, F.; Voth, G. A.; Agmon, N. *J. Phys. Chem. B* **2008**, *112*, 9456.

(38) Day, T. J. F.; Schmitt, U. W.; Voth, G. A. *J. Am. Chem. Soc.* **2000**, *122*, 12027.

(39) Tuckerman, M. E.; Marx, D.; Parrinello, M. *Nature* **2002**, *417*, 925.

(40) Marx, D. *ChemPhysChem.* **2006**, *7*, 1848.

(41) Berkelbach, T. C.; Lee, H. S.; Tuckerman, M. E. *Phys. Rev. Lett.* **2009**, *103*, 238302.

(42) Marcus, R. A. *Angew. Chem. Int. Ed.* **1993**, *32*, 1111.

(43) Marcus, R. A. *Annu. Rev. Phys. Chem.* **1964**, *15*, 155.

(44) Maurer, P.; Thomas, V.; Iftimie, R. *J. Chem. Phys.* **2011**, *134*.

(45) Timmer, R. L. A.; Cox, M. J.; Bakker, H. J. *J. Phys. Chem. A* **2010**, *114*, 2091.

(46) Westheimer, F. H. *Chem. Rev.* **1961**, *61*, 265.

(47) Melander, L. C. S. *New York, Ronald Press Co.* **1960**.

(48) O'Ferrall, R. A. M. *Chapman and Hall, London* **1975**.

(49) Abdelaal, Y. A. I.; Hammock, B. D. *ACS Sym. Ser.* **1985**, *276*, 135.

(50) Laidler, K. J.; King, M. C. *J Phys. Chem.* **1983**, *87*, 2657.

(51) Borgis, D.; Hynes, J. T. *The J. Phys. Chem.* **1996**, *100*, 1118.

(52) Borgis, D.; Hynes, J. T. *Chem. Phys.* **1993**, *170*, 315.

(53) Borgis, D. C.; Lee, S. Y.; Hynes, J. T. *Chem. Phys. Lett.* **1989**, *162*, 19.

(54) Ando, K.; Hynes, J. T. *J. Mol. Liq.* **1995**, *64*, 25.

(55) Ando, K.; Hynes, J. T. *J. Phys. Chem. B* **1997**, *101*, 10464.

(56) Kiefer, P. M.; Hynes, J. T. *J. Phys. Chem. A* **2002**, *106*, 1834.

(57) Kiefer, P. M.; Hynes, J. T. *J. Phys. Chem. A* **2002**, *106*, 1850.

(58) *Wiley-VCH, Weinheim, Germany*, *303*.

(59) Cohen, B.; Huppert, D.; Agmon, N. *J Am Chem Soc* **2000**, *122*, 9838.

(60) Rini, M.; Magnes, B. Z.; Pines, E.; Nibbering, E. T. J. *Science* **2003**, *301*, 349.

(61) Mohammed, O. F.; Pines, D.; Dreyer, J.; Pines, E.; Nibbering, E. T. J. *Science* **2005**, *310*, 83.

(62) Mohammed, O. F.; Pines, D.; Nibbering, E. T. J.; Pines, E. *Angew. Chem. Int. Ed.* **2007**, *46*, 1458.

(63) Siwick, B. J.; Bakker, H. J. *J. Am. Chem. Soc.* **2007**, *129*, 13412.

(64) Tolbert, L. M.; Haubrich, J. E. *J. Am. Chem. Soc.* **1994**, *116*, 10593.

(65) Ireland, J. F.; Wyatt, P. A. H. In *Adv. Phys. Org. Chem.*; Gold, V., Bethell, D., Eds.; Academic Press: New York, 1976; Vol. 12, p 132.

(66) Barak, T. *Ph.D. Thesis, Ben-Gurion University.2005*.

(67) Pines, E.; Huppert, D. *J. Am. Chem. Soc.* **1989**, *111*, 4096.

(68) *Elsaesser T, Bakker HJ, eds. 2002. Ultrafast Hydrogen Bonding Dynamics and Proton Transfer Processes in the Condensed Phase. Dordrecht: Kluwer Acad. Page 155*.

(69) Rini, M.; Pines, D.; Magnes, B. Z.; Pines, E.; Nibbering, E. T. J. *J. Chem. Phys.* **2004**, *121*, 9593.

(70) Fang, C.; Frontiera, R. R.; Tran, R.; Mathies, R. A. *Nature* **2009**, *462*, 200.

(71) Polli, D.; Altoe, P.; Weingart, O.; Spillane, K. M.; Manzoni, C.; Brida, D.; Tomasello, G.; Orlandi, G.; Kukura, P.; Mathies, R. A.; Garavelli, M.; Cerullo, G. *Nature* **2010**, *467*, 440.

(72) Mohammed, O. F.; Dreyer, J.; Magnes, B.-Z.; Pines, E.; Nibbering, E. T. J. *ChemPhysChem.* **2005**, *6*, 625.

(73) Siwick, B. J.; Cox, M. J.; Bakker, H. J. *J. Phys. Chem. B* **2008**, *112*, 378.

(74) Giguere, P. A.; Turrell, S. *J. Am. Chem. Soc.* **1980**, *102*, 5473.

(75) Ayotte, P.; Plessis, S.; Marchand, P. *Phys Chem Chem Phys.* **2008**, *10*, 4785.

(76) Covington, A. K.; Freeman, J. G.; Lilley, T. H. *J. Phys. Chem.* **1970**, *74*, 3773.

(77) Gelb, R. I.; Schwartz, L. M.; Laufer, D. A. *J. Am. Chem. Soc.* **1981**, *103*, 5664.

(78) Leuchs, M.; Zundel, G. *J. Chem. Soc. Far. Trans. II* **1980**, *76*, 14.

2. Computational Methods

2.1 Choice of Method

Computational investigations of proton transfer processes, solvent participation and vibrational spectroscopy changes are confronted with the challenge of dynamically rearranging chemical bonding topology, that is, chemical bonds are constantly being made and broken. Standard molecular dynamics approaches based on empirical force fields do not have the capability of investigating proton transfer reactions in aqueous solution because they generally do not incorporate bond-breaking phenomena. To simulate the proton transport process in an aqueous solution computationally, one must therefore be able to treat a chemical bonding topology that is dynamically changing. This requires an explicit treatment of the electronic degrees of freedom for which first principles quantum chemical methods are often employed. We use ab initio molecular dynamics approach to describe electronic polarization and bond-breaking/bond-forming effects. Ab initio molecular dynamics simulations[1] have been successfully employed to refine our understanding of Brønsted acid-base equilibria in pure water[2,3], aqueous solutions of strong[4-10] and weak[11-19] acids and bases[20], and biochemical environments[21-23]. In the AIMD approach, the nuclear trajectory is generated using forces obtained from electronic structure calculations, employing density functional theory[24] (DFT). Electron exchange and correlation are treated at the generalized gradient approximation (GGA) level using the BLYP[25,26] functional. The BLYP scheme has been shown to give a good description of aqueous hydrogen bonding[27,28] and good results for intermolecular O−O distances. The basis set is expanded using plane waves and atomic pseudopotentials of theTroullier-Martins[29] form are used. Zero-point vibration and nuclear quantum effects are included within the framework of the centroid molecular dynamics theory[30,31] bases on Feynman Path Integral approach. The following sections will systematically introduce the details of these techniques.

2.2 Fundamentals of Molecular Dynamics Simulation

In Molecular dynamics[1,32,33] simulation technique the time evolution of a set of interacting atoms is followed by numerical, step-by-step solution of the classical Newtonian equations of motion[34] starting from a pre-specified initial state and subject to a set of boundary conditions. Thus, MD methodology is founded upon the basic principles of classical mechanics and can provide a window into the microscopic dynamical behavior of the individual atoms that make up a given system. From this information, the microscopic mechanisms of chemical processes can be observed and dynamical properties such as structural properties, absorption spectra and transport properties can be calculated[1].

Classical Newtonian equations of motion for a system of *N* particles in three dimensions is written as

$$M_I \ddot{\mathbf{R}}_I = \mathbf{F}_I(\mathbf{R}_1, \mathbf{R}_2, ..., \mathbf{R}_N, \dot{\mathbf{R}}_I), \qquad 2.1$$

where M_I and $\mathbf{R}_I$ are the mass and coordinates of particle *I*. $\mathbf{F}_i$ defines the force experienced by particle ***I*** from all the other particles in the system and from the external environment. This force, $\mathbf{F}i$ depends on the positions $\mathbf{R}_{1,...,}\mathbf{R}_N$ of all the particles in 3 dimensions and also the velocity of particle $\dot{R}_I$. In any real system, the inter particle forces are highly nonlinear functions of *N* particle positions so that the Eq. (2.1) possess high dynamical complexity and obtaining an analytical solution is impossible and a numerical solution to it will exceed the present day computational resources. Statistical mechanics can be used to calculate the physically observable properties of a real system starting from a microscopic description when the fundamental equations cannot be solved. Statistical mechanics can provide the link between the microscopic laws and macroscopic observables. One can consider a much smaller system composed of few hundred - few thousand particles subjected to controlling some variables and imposing periodic boundary conditions to eliminate the surface effects. For example we fix the number of particles *N*, total energy of the system *E* and the volume *V* and then numerically solve the equations of motion to get the time evolution of the system. These

constrain cause the trajectory to move on a "surface" of phase phase (A six dimensional space consisting of 3 position and 3 momentum coordinates)—though the dimensionality of the surface is still enormously high. The principles of statistical mechanics are then used to analyze the numerical trajectories thus generated. For example, the time average $\langle A \rangle$ can be computed for macroscopic properties from the trajectories. According to ergodic hypothesis[35] this should be same as ensemble average if time (t) is sufficiently long.

$$\langle A \rangle = \lim_{t \to \infty} \frac{1}{t} \int_{t_0}^{t_0+t} A(\tau) d\tau \qquad 2.2$$

Failure to achieve this condition leads to erroneous results.

2.2.1 Periodic Boundary Condition and Minimum Image convention

As mentioned in the previous section, a typical molecular dynamics simulation is applied to systems consisting of few hundred to few thousand atoms to predict and study the properties of a system in bulk. Such small systems are dominated by surface effects interactions of the atoms with the container walls. For example, to hold 52 water molecules at a liquid density of 1 g/cm^3, a cubic box must have an edge length of about 11.5 Angstrom. However, interaction of water molecules with the wall extends to few angstroms from each wall. A simulation of this system would provide information on the behaviour of the liquid water near a solid

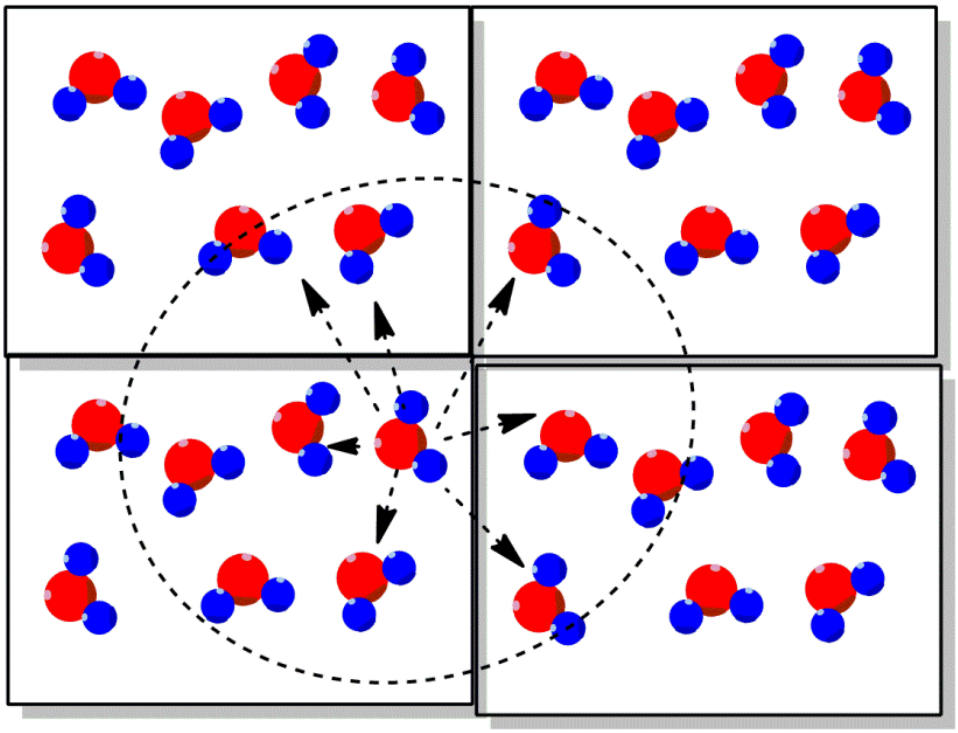

Figure 2-1. Periodic Boundary counditions (PBC).

surface, not information on the bulk liquid. In order to remove the surface artifacts molecular dynamics simulations utilize periodic boundary conditions (PBC). In order to use PBC in a simulation of *N* atoms confined to a volume *V* with edges a,b and c, we imagine that volume *V* is only a small portion of the bulk material. The volume V is called the primary cell (like unit cell in a crystal); it is representative of the bulk material to the extent that the bulk is assumed to be composed of the primary cell periodically replicated itself (called Images) in three dimensions to form the macroscopic sample of the system.

In the course of the simulation, when a molecule moves in the *central* box, its periodic image in *every one* of the other boxes moves with exactly the same orientation in exactly the same way. Thus, as a molecule leaves the central box, one of its images will enter through the opposite face. There are no walls at the boundary of the central box, and the system has no surface. The central box simply forms a convenient coordinate system for

measuring locations of the N molecules. If the atoms in the primitive cell have positions $\mathbf{r}_i$, the PBC produces mirror images of atoms at positions defined as

$$\mathbf{r}_i^{image} = \mathbf{r}_i + k\mathbf{a} + l\mathbf{b} + m\mathbf{c} \qquad 2.3$$

Where a, b, c are vectors that correspond to the edges of the box and k, l, m are integers from -∞ to ∞

2.2.2 Long Range Interactions Using PBC: Ewald's Summation

Although the concept of utilizing periodic boundary condition is simple and very effective in mimicking a bulk system by avoiding the surface effects, certain challenges arise when PBC are employed. In particular, long range forces, whose spatial range extend beyond the boundaries of the simulation box into surrounding images pose a challenge. Long range forces can only be correctly calculated by summing over all the periodic replicas of the original simulation system. However, the associated computational effort is huge. The approach used to solve this problem is called Ewald summation technique in which the potential is broken down into a short range and a long range contribution. For example, consider a system of N particles with positions $\mathbf{r}_i$ in a box of length L. The total electrostatic energy of the system in PBC is given by

$$U = \sum_{\mathbf{n}}^{!} \sum_{i,j=1}^{N} \frac{q_i q_j}{|\, \mathbf{r}_{ij} + \mathbf{n}L \,|}, \qquad 2.4$$

Where $\mathbf{r}_{ij} = \mathbf{r}_i - \mathbf{r}_j$ and $\mathbf{n} = \mathbf{n}_x L, \mathbf{n}_y L, \mathbf{n}_z L$. The symbol '!' in the summation means that the term j = i is excluded, if $\mathbf{n}$ = 0.

The short range potential can be treated with simple cut-off and the long-range potential with, which is periodic and slowly varying everywhere can be represented by the first few terms of Fourier series. This splitting is done using following identity

$$\frac{1}{r} = \frac{f(r)}{r} + \frac{1 - f(r)}{r} \qquad 2.5$$

The first term $\frac{f(r)}{r}$ in Eq. (2.5) is the short range term, which should be zero after a cutoff distance. So the summation up to this cutoff distance is a good approximation.

The second term $\frac{1-f(r)}{r}$ is a slow varying function for all **r**. So that its Fourier transform can be represented by only a few k-vectors with $|k| \leq k_{\max}$. The traditional selection for the split function is a complementary error function $erfc(r) = \frac{2}{\sqrt{\pi}} \int_0^{\infty} e^{-t^2}$.

This results in the well-known Ewald formula for the electrostatic energy of the primary box:

$$U = U^{(r)} + U^{(k)} + U^{(s)} + U^{(d)} \quad 2.6$$

where $U^{(r)}, U^{(k)}, U^{(s)}, U^{(d)}$ are the contribution from real space, reciprocal space, self energy, and dipole correction. They are given by

$$U^{(\mathbf{r})} = \frac{1}{2} \sum_{m}^{!} \sum_{i,j} q_i q_j \left(\frac{erfc(\alpha \mid \mathbf{r}_{ij} + mL \mid)}{\mid \mathbf{r}_{ij} + mL \mid} \right) \quad 2.7$$

$$U^{(\mathbf{k})} = \frac{1}{V} \sum_{\mathbf{k} \neq 0} \frac{4\pi}{\mathbf{k}^2} e^{-\frac{\mathbf{k}^2}{4\alpha^2} |\tilde{\rho}(\mathbf{k})|^2} \quad 2.8$$

$$U^{(s)} = \frac{\alpha}{\sqrt{4\pi}} \sum_i q_i^{\,2} \quad 2.9$$

$$U^{(\mathbf{d})} = \frac{2\pi}{V(1+2\varepsilon')} (\sum_i q_i \mathbf{r}_i)^2, \quad 2.10$$

Where the Fourier transform of the charge density $\tilde{\rho}(k)$ is defined as

$$\tilde{\rho} = \int_V d^3\mathbf{r} \rho(\mathbf{r}) e^{-i\mathbf{k}.\mathbf{r}_j} \quad 2.11$$

The advantage of rewriting Eq. (2.4) this way is that the exponentially converging sums over m and k in Eq. (2.7) and Eq. (2.8) allow the introduction of comparatively small cut-off's . Typically one chooses α large enough as to employ the minimum image convention in Eq. (2.7). The dipole correction Eq. (2.10) assumes that the set of periodic replications of the simulation box tends spherically towards an infinite cluster and that the medium outside this sphere is a homogeneous dielectric with dielectric constant ε′, whereas inside we set for ε=1.

More detailed account of the Ewalds summation method can be found in Ref. [36]

2.2.3 A general framework for Newton's laws: Lagrangian Formalism

Newton's equation of motion is simple to apply if the system is not required to move in some constrained manner and if the Cartesian coordinates are used. But if either of these restrictions are removed then the equations can become quite complex. So for a better way for practically handling the system in accordance with the phase space description (in terms of positions and momenta) than the Newtonian formalism is to use alternate approaches that is equivalent to Newton's equation but can deal with complicated problems in general manner. One such a method is contained in **Hamilton's principle** and the equations of motion resulting from the application of this principle are called **Lagrange's** equation of motion[34]. The Hamilton's principle is stated as follows: 'Of all the possible paths along which a dynamical system may move from one point to another within a specified time interval (consistent with nay constraints), the actual path followed is that which minimizes the time integral of difference between the kinetic *T*, and potential energies *U*.

The lagrangian L of a system is defined as the difference between the kinetic, T and potential energies, *U* expressed as a function of the position and velocities'.

$$L = \text{T- U} \tag{2.12}$$

where L depends on the particles positions $\mathbf{R}_1,..,\mathbf{R}_N$ and particles velocity $\dot{\mathbf{R}}_1,..,\dot{\mathbf{R}}_N$; that is $L(\mathbf{R}_1,..,\mathbf{R}_N,\dot{\mathbf{R}}_1,..,\dot{\mathbf{R}}_N)$

Now consider two derivatives for Eq. (2.12).

$$\frac{\partial L}{\partial \mathbf{R}_I} = -\frac{\partial U}{\partial \mathbf{R}_I} = \mathbf{F}_I \tag{2.13}$$

and

$$\frac{\partial L}{\partial \dot{\mathbf{R}}_I} = -\frac{\partial T}{\partial \dot{\mathbf{R}}_I} = M_I\dot{\mathbf{R}}_I = \mathbf{P}_I \tag{2.14}$$

Differentiating Eq.(2.14) with respect to time and recollecting Newton's equation, $\mathbf{F}_I = M\ddot{\mathbf{R}}_I = \dot{\mathbf{P}}_I$, we get

$$\frac{dL}{d\mathbf{R}_I} = \frac{d}{dt}\frac{dL}{d\dot{\mathbf{R}}_I} \qquad 2.15$$

Thus we see that the Newton's second law is exactly equivalent to Lagrange equations. So the particle's path calculated by Newton's equation will be same as the path determined by Lagrange equations. The next step is to recognize the Eq. (2.15) has the same form of Euler-Lagrange equations. Thus we can see that Lagrangian serves as the generator of equations of motion via Euler-Lagrange equations which can be better expressed as

$$\frac{d}{dt}\frac{dL}{d\dot{\mathbf{R}}_I} - \frac{dL}{d\mathbf{R}_I} = 0 \qquad 2.16$$

We have seen that the Lagrangian was serving as a generator for the equations of motion. Once we have the equations of motion and if we can compute the forces acting on each atomic center of the system then there are several algorithms to propagate the system by computing the trajectory of the particle.

2.2.4 Integrating Equations of Motion

The approach is based on a discretization of time and a repeated calculation of the forces on the particles. Many such methods exist in the literature. One method of choice is the velocity Verlet algorithm[37,38]. It has the advantage that it uses as basic variables positions **R**(t) and velocities **V**(t) at the same time instant *t*. The velocity-verlet algorithm looks like a Taylor expansion for the coordinates:

$$\mathbf{R}(t+\Delta t) = \mathbf{R}(t) + \mathbf{V}(t)\Delta t + \frac{\mathbf{F}(t)}{2M} \qquad 2.17$$

This equation is combined with the update for velocities:

$$\mathbf{V}(t+\Delta t) = \mathbf{V}(t) + \mathbf{V}(t)\Delta t + \frac{\mathbf{F}(t+\Delta t) + \mathbf{F}(t)}{2M}\Delta t^2 \qquad 2.18$$

In order to perform a molecular dynamics simulation the initial values for positions and velocities have to be chosen along with an appropriate time step Δt and the force acting on the particles, *F*(t).

2.3 Classical Molecular Dynamics Simulation

In a classical MD simulations, the instantaneous forces acting on the particles are calculated from potential energy functions *i.e.* force fields, expressed normally as simple analytical functions which can be anything from a pure guess to a fit of extensive quantum chemical calculations. A minimal model for the functional form of a general force field includes both bonded terms relating to atoms that are linked by covalent bonds, and non-bonded (also called non-covalent) terms describing the long-range electrostatic and van der Waals forces.

$$U_{total} = U_{bond} + U_{angle} + U_{dihedral} + U_{estatic} + U_{vdW}, \quad 2.19$$

where each term in Eq.13 can be expanded as:

$$U_{bond} = \sum K_b (r - r_e)^2 \quad 2.20$$

$$U_{angle} = \sum K_b (\theta - \theta_e)^2 \quad 2.21$$

$$U_{dihedral} = \sum K_\phi (1 + \cos(n\phi - \delta)) \quad 2.22$$

2.23

$$U_{elstat} = \frac{1}{4\pi\varepsilon_0} \sum \frac{q_i q_j}{r_{ij}} \quad 2.24$$

$$U_{vdW} = \sum \varepsilon_{ij} [(\frac{R_{\min,ij}}{r_{ij}})^{12} - (\frac{R_{\min,ij}}{r_{ij}})^6] \quad 2.25$$

Eq. (2.19) and Eq. (2.20) represent the bonding interactions in which, K are the force constants associated with the respective type of interactions, r_e and θ_e are equilibrium bond length and bond angle values, *n* is the periodicity of the dihedral and δ is the phase which is determines the location of maximum.

Eq. (2.21) and Eq.(2.22) represents the non-bonded interactions which includes the electrostatic and vanderwalls terms. The electrostatic terms in Eq. (2.18) are described with Columbic interactions between point charges where *qi* and *qj* are the atomic partial charges of the atoms *i* and *j* involved and ϵ_0 is the vacuum dielectric constant. For the van der Waals terms in Eq. (2.19), a Lennard-Jones potential is used with well depth $\varepsilon_{ij} = \sqrt{\varepsilon_i \varepsilon_j}$ and range $R_{\min,ij}, = \frac{\left(R_{\min,i} + R_{\min,j}\right)}{2}$ at the Lennard-Jones minimum. This interaction captures long range dispersion (r^{-6} and exchange repulsion (r^{-12})

2.3.1 Advantages and Limitation of Classical Molecular Dynamics Simulations

The relatively low computational resources associated with force-fields like CHARMM[39-42], AMBER[43], OPLS[44], GROMOS[45-47] have allowed large-scale calculations of systems ranging from simple liquids and solids to polymers and biological systems such as proteins and nucleic acids.

Despite the success and wide spread use of force fields, they have a number of limitations. First, charges appear as static parameters in the force field, and therefore electronic polarization effects are not included. This limitation has long been recognized, and attempts have been made to rectify the problem by using polarizable force field models, in which charges and induced dipoles are allowed to fluctuate in response to changing environment. This is known as fluctuating charge model (FQ)[48,49]. Several other polarizable force fields exists based on distribution of multipoles, density, bond polarization theory (BPT), reactive force fields etc. [See[50-53] for recent reviews]. Although they were somewhat successful, they also suffer from a number of serious limitations, including a lack of transferability and standardization. Second, force fields generally assume a pre-specified connectivity among the atoms and, therefore, suffer from an inability to describe chemical bond breaking and forming events. The latter problem can be treated in an approximate manner using techniques such as the

empirical valence bond method [EVB]. However, such methods are also not transferable and, therefore, need to be parmetrized for each type of reaction and may end up biasing the reaction pathways.

Since we are dealing with proton transfer reactions in this thesis which involves bond breaking and forming, we have to turn into methodology which incorporates the quantum mechanical calculations in to the MD simulation. This technique is called Ab initio molecular dynamics (AIMD).

2.4 Quantum Treatment of Electrons in Molecular Dynamics Simulations: AIMD

In molecular dynamics simulations, the interaction energies between the atoms and forces acting on the atoms have a decisive effect on the simulation results. The closer these are to reality, the more reliable and useful the simulation results are. To achieve this, the molecular dynamics simulations can be combined with high level *ab initio* calculations to calculate the potential energies and hence the forces needed in the molecular dynamics simulations. These categories of MD simulations are called ab initio molecular dynamics (AIMD) simulations. Usually the electronic structure calculations are solved using density functional theory[54]. Hence ab initio molecular dynamics simulations are also called DFT-MD simulations.

2.4.1 Density Functional Theory

DFT is based on the Hohenberg–Kohn theorem[55], which states that a one-to-one mapping exists between ground-state electronic densities and external potentials. In other words, the density (an observable in three dimensional spaces) is used to describe the complicated physics behind the interactions between electrons and, therefore, determines everything about the system. In Kohn–Sham (KS) theory, this is formulated as a simple expression for the ground state energy. This is expressed as a functional of n mutually orthonormal single-particle electron orbitals $\psi_1(\mathbf{r})$, ..., $\psi_n(\mathbf{r})$ and the N nuclear

positions, $\mathbf{R}_1$, ..., $\mathbf{R}_N$. The orbitals are related to the electronic density according to $n(\mathbf{r}) = \sum_i |\psi_i(\mathbf{r})|^2$. The total energy is given by

$$E[\{\psi\},\{\mathbf{R}\}] = -\frac{1}{2}\sum_{i=1}^{n} fi\int \psi_i^*(\mathbf{r})\nabla^2\psi_i(\mathbf{r})d\mathbf{r} + \frac{1}{2}\int\frac{n(\mathbf{r})n(\mathbf{r}')}{|\mathbf{r}-\mathbf{r}'|} + E_{XC}[n]d\mathbf{r}d\mathbf{r} + \int V_{ext}(\mathbf{r},\mathbf{R})n(\mathbf{r})d\mathbf{r} \quad 2.26$$

Where V_{ext} represents the external potential due to the N nuclei and is given by $V_{\mathbf{ext}} = -\sum_{I=1}^{N}\frac{q_I}{|\mathbf{r}-\mathbf{R}_I|}$, where q_I is the charge on each nucleus. The first two terms in Eq. (2.26) are the electronic kinetic energy and Hartree energy terms, respectively. The term $E_{\text{xc}}[n]$ called the exchange-correlation functional, is unknown and need to be approximated.

The KS sham potential can then be written from Eq.(2.26) as

$$V_{KS}(\mathbf{r},\mathbf{R}) = \frac{1}{2}\int d\mathbf{r}'\frac{n(\mathbf{r}')}{|\mathbf{r}-\mathbf{r}'|} + \frac{\delta E_{XC}}{\delta n(\mathbf{r})} + V_{ext}(\mathbf{r},\mathbf{R}) \quad 2.27$$

and the Hamiltonian for the non-interacting system is, therefore,

$$H_{KS} = -\frac{1}{2}\nabla^2 + V_{KS}(\mathbf{r},\mathbf{R}) \quad 2.28$$

The The KS orbitals will be the solutions of a set of self-consistent equations known as the Kohn–Sham equations:

$$H_{KS}\psi_i(\mathbf{r}) = \varepsilon_i\psi_i(\mathbf{r}), \quad 2.29$$

where ϵ_i are the Kohn-Sham energies. This equation need to be solved self consistently because the KS orbitals are needed to compute the density, which is needed to specify KS Hamiltonian.

Now, how is the key unknown exchange correlation term, $E_{XC}[n]$ approximated?

2.4.2 Local Density Approximation

In local density approach (LDA) this can be approximated to exchange and correlation energies of a homogeneous electron gas in which the functional is taken to be the spatial integration over the local function that depends on the density:

$$E_{XC}[n] \approx \int dr\, f_{LDA}(n(\mathbf{r})). \qquad 2.30$$

The LDA approximation is motivated by the notion that the interaction between the electrons and the nuclei creates only weak inhomogeneity's in the electron density. Therefore, the form of f_{LDA} is obtained by evaluating the exact expressions for the exchange and correlation energies of a homogeneous electron gas of uniform density n at the inhomogeneous density $n(\boldsymbol{r})$

2.4.3 Generalized gradient approximation (GGA)

An improvement for such an approach is to extend the dependence of this functional to include the density $n(\mathbf{r})$ and its gradient $\nabla n(r)$. This approximation is known as the generalized gradient approximation (GGA) and has become a popular approach due to the recent development of improved functionals.

$$E_{XC}[n] \approx \int dr\, f_{GGA}(n(\mathbf{r}), |\nabla n(\mathbf{r})|) \qquad 2.31$$

There are many different choices of GGA functionals. For instance, Perdew-Burke-Ernzerhof (PBE) functional are derived from purely physical considerations, that is, they are not fitted to any specific system, and are instead made to satisfy some general physical properties. Some make use of fitting parameters. For example, the exchange functional of Becke contains one parameter that is fitted to the exact exchange (from a Hartree-Fock calculation) of six noble gas atoms. The Lee-Yang-Parr (LYP) correlation functional contains four parameters that originate from the investigation of helium. These two functionals are often employed together, denoted as BLYP functional. This BLYP GGA functional represents a noticeable improvement upon LDA in particular for molecular systems and often works very well for hydrogen bonded systems. We have utilized BLYP functional in our investigations.

2.5 Born-Oppenheimer Molecular Dynamics

In the most straightforward type of AIMD calculation strategy the potential energy $E[\{\psi\},\{R\}]$ is minimized at every molecular dynamics step under the constrain $\langle\psi_i(r)|\psi_j(r)\rangle = \delta_{ij}$. This leads to following lagrangian:

$$L_{BO}(\{\psi_i\};\mathbf{R}_I,\dot{\mathbf{R}}_I) = \frac{1}{2}\sum_{I=1}^{N} M_I \dot{\mathbf{R}}_I^{\,2} - \min E[\{\psi_i\};\mathbf{R}_I] + \sum_{i,j}\Lambda_{ij}(<\psi_i(\mathbf{r})|\psi_j(\mathbf{r})> - \delta_{ij}) \quad 2.32$$

Where Λ_{ij} is a Hermitian Lagrangian multiplier matrix. The equation of motion is then obtained by solving the Euler-Lagrangian equation.

$$\begin{aligned}\frac{d}{dt}\frac{\partial L}{\partial \dot{\mathbf{R}}_I} &= \frac{\partial L}{\partial \mathbf{R}_I}\\ \frac{d}{dt}\frac{\partial L}{\partial <\dot{\psi}_i|} &= \frac{\partial L}{\partial <\psi_i|}\end{aligned} \quad 2.33$$

$$\begin{aligned}M_I\ddot{\mathbf{R}}_I &= -\nabla_{R_I}\left[\min E\left[\{\psi_i\};\mathbf{R}_I\right]\right]_{<\psi_i(r)|\psi_j(r)>=\delta_{ij}}\\ &= -\frac{\partial E}{\partial \mathbf{R}_I} + \Lambda_{ij}\frac{\partial}{\partial \mathbf{R}_I}<\psi_i|\psi_j>\\ &\quad -2\sum_i \frac{\partial <\psi_i|}{\partial \mathbf{R}_I}\left[\frac{\delta E}{\partial <\psi_i|} - \sum_j \Lambda_{ij}|\psi_j>\right] \quad 2.34\\ &= -H_e<\psi_i| + \sum_j \Lambda_{ij}|\psi_j>\end{aligned}$$

The first term on the right hand side of Eq. (2.34) is called Hellman-Feynman force. The second term is called pulay force or wavefunction force due to the constrain. The final term stems from the fact that, independent of the particular basis set, there is always an implicit dependence on the atomic positions through the expansion coefficient within the linear combination of atomic orbitals. The factor 2 stems from the assumption that the KS orbitals are real. However the whole term vanishes if $\psi_i(r)$ is an eigen function of the Hamiltonian. However, as the KS functional is nonlinear, eigenfunctions of its Hamiltonian are only obtained at exact self-consistency. Unfortunately, in any numerical calculations this is hard to be achieved.

The forces are then updated into velocity-verlet integration procedure together with a set of initial velocities for the nuclei yielding a new set of positions and velocities. This minimization procedure is repeated every molecular dynamics step of the simulation. Fig. 2-2 shows a pictorial representation of BOMD calculation with 6 molecular dynamics steps involving energy minimization in each step.

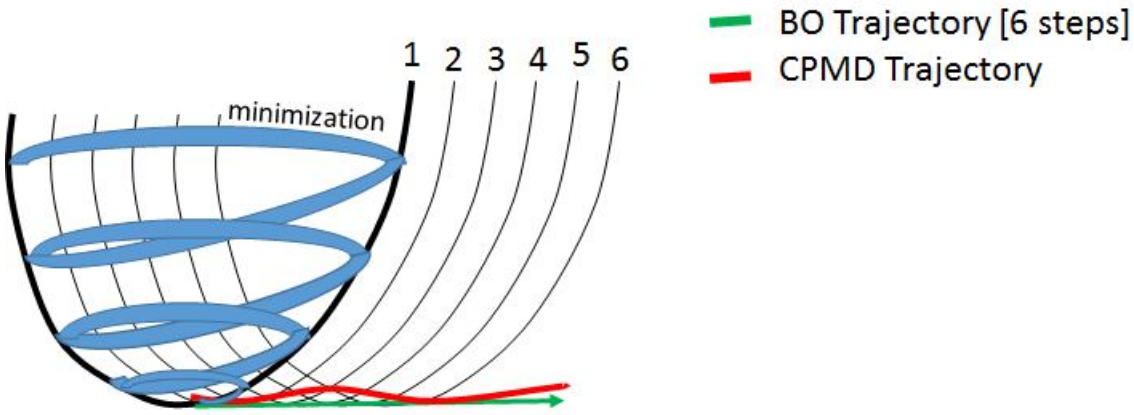

Figure 2-2. Born-Oppenheimer molecular dynamics versus Car-parrinello molecular dynamics. Each MD step in BOMD involves an electronic structure minimization while in CPMD, electronic structure minization is performed only once and then the electrons follow the nuclei. This figure shows 6 MD steps.

2.6 Car-Parrinello Molecular Dynamics

A computationally less expensive, alternative procedure for Born-Oppenheimer MD was proposed by Car and Parrinello[56], in which a fictitious dynamics for the electronic orbitals is introduced that allows them to follow the motion of the nuclei adiabatically. This dynamical procedure is constructed in such a way that if the orbitals are initially chosen corresponding to the ground state density at the initial nuclear configuration, they will remain approximately in the ground state as the nuclear configuration evolves in time reducing the need for a minimization in each nuclear step. This dynamics is controlled by introducing a set of orbital velocities and a fictitious electron mass parameter μ having units of (energy x time^2)

$$KE_{fict} = \mu \sum_i \langle \dot{\psi}_i \mid \dot{\psi}_i \rangle \qquad 2.35$$

The Lagrangian of the system is then written as

$$L_{CP}(\{\psi_i\},\{\dot{\psi}_i\};\mathbf{R}_I,\dot{\mathbf{R}}_I) = \frac{1}{2}\mu \sum_i \langle \dot{\psi}_i \mid \dot{\psi}_i \rangle + \frac{1}{2}\sum_{I=1}^{N} M_I \dot{\mathbf{R}}_I^{\,2} - E[\{\psi_i\};\mathbf{R}_I] + \sum_{i,j} \Lambda_{ij}(\langle \psi_i(\mathbf{r}) \mid \psi_j(\mathbf{r}) \rangle - \delta_{ij}) \qquad 2.36$$

Once again the equations of motion can be obtained by solving the Euler-Lagrange equation

$$\frac{d}{dt}\frac{\partial L}{\partial \dot{\mathbf{R}}_I} = \frac{\partial L}{\partial \mathbf{R}_I}$$
$$\frac{d}{dt}\frac{\partial L}{\partial \langle \dot{\psi}_i \mid}} = \frac{\partial L}{\partial \langle \psi_i \mid} \qquad 2.37$$

The resulting coupled equations of motion can then be written as

$$M_I \ddot{\mathbf{R}}_I = -\nabla_{R_I}\left[E\left[\{\psi_i\};\mathbf{R}_I\right]\right] \qquad 2.38$$

$$\mu \ddot{\psi}_i(\mathbf{r}) = -\frac{\delta}{\delta \langle \psi_i \mid} E[\{\psi_i\},\mathbf{R}_I] + \sum_j \Lambda_j \psi_j(\mathbf{r}) \qquad 2.39$$

These equations form the basis of Car-Parrinello Molecular Dynamics.

2.6.1 Car-parrinello Vs Born-Oppenheimer Molecular Dynamics

The main advantage of CPMD is the exact conservation of the Car-Parrinello Hamiltonian which leads to a stable dynamics. While thermostating is often needed in BOMD simulations to avoid heating up of the system hence micro-canonical simulations over long times can be performed efficiently with CPMD technique. This stability ensures that the system stays in the same thermodynamics state.

Another advantage of CPMD over BOMD is that there is no need of self-consistency to minimize the Kohn-Sham energy functional at each time-step, as the electronic degrees of freedom are propagated alongside the nuclei. On the other hand, the time step needed for integrating the CP motion is determined by the fastest electronic motion and is a few times shorter in BOMD than in CPMD.

The main drawback of CPMD is that the trajectory does not always remain on the Born-Oppenheimer surface. This can happen in two cases: 1) when the HOMO-LUMO gap is less than the fictitious kinetic energy. This is typically the case of metals. 2) when the fictitious kinetic energy is much smaller than the thermal energy.

2.6.2 Plane waves and Pseudopotentials

In Ab initio molecular dynamics approach a one way of reduction in computational complexity is introduced by replacing the strong electron-ion potential with a much weaker potential, called a pseudopotential[57,58]. A pseudopotential describes all the necessary features of valence electron of the molecule, including relativistic effects. Thus the original molecule is replaced by pseudo valence electrons and pseudo-ion cores. These pseudoelectrons experience exactly the same potential outside the core region as the original electrons but have a much weaker potential inside the core region. The fact that the potential is weaker is crucial, however, because it makes the evaluation of the Schrodinger equation much simpler by allowing expansion of the wave functions in a relatively small set of plane waves within the frame work of bloch theorem[59], which states that the electronic wavefunction at each k point can be expanded in terms of a discrete plane-wave basis set.

.

$$\psi_{ik}(\mathbf{r}) = \frac{1}{\sqrt{V}} e^{\mathbf{ik.r}} \sum_{G} c_G^{\,ik}\; e^{iG.\mathbf{r}}, \qquad 2.40$$

where $c_G^{\,ik}$ is a set of expansion coefficients with the reciprocal lattice vectors G are defined by $G.l=2\pi m$ for all l where l is a cell vector of the system and m is an integer and V is the volume of the system. For non-metallic systems it is sufficient to consider k=0,0,0 (Γ-point). So the plane-wave expansion becomes

$$\psi_{i}(\mathbf{r}) = \frac{1}{\sqrt{V}} \sum_{G} c_G^{\,i}\; e^{iG.\mathbf{r}}, \qquad 2.41$$

In principle, an infinite plane-wave basis set is required to expand the electronic wave function according to Bloch's theorem. However, the coefficients c_G^i with only small kinetic energy are typically important. Thus the plane-wave can be truncated at some particular cut off energy value.

2.7 Quantum Treatment of Nuclei in Ab Initio Molecular Dynamics

Although ab initio molecular dynamics simulations classical nuclei are extremely successful in simulating detailed microscopic dynamical behavior of different systems, chemical reactions at finite temperatures or dynamics of lighter particles like hydrogen with nuclear quantum effects such as zero-point motion or tunneling are crucial due to shallow potential energy surfaces are a challenge to the conventional ab initio molecular dynamics simulations. The option of solving the the time-dependent Schrödinger equation for the nuclei in a numerically exact fashion is almost impossible for larger systems. Currently, path integral[60,61] based methods such as centroid molecular dynamics[31] (CMD) simulations and ring-polymer molecular dynamics (RPMD) techniques[62] are two of the most successful and practical methods that allow for approximate quantum dynamics of complex molecular systems. In this work we include the nuclear quantum effect utilizing the quasi classical quantum dynamics of nuclei by centroid molecular dynamics approach within the frame work of ab initio molecular dynamics[63]. In the following section we will review the basic theory of Feynman Path Integrals and ab initio centroid molecular dynamics.

2.7.1 Feynman Path Integrals

One of the most suggestive pictures derived from the path integral approach[60,61] is the *quantum-classical isomorphism*. This isomorphism states that the statistical behavior of a set of quantum particles can be mapped onto a classical model of interacting ring polymers. In more precise terms, the canonical partition function, Z, of N quantum particles is equivalent to the classical partition function of N interacting ring polymers.

$$Z^{Quantum} \equiv Z^{cl}_{beads} \quad 2.42$$

Consider the quantum canonical partition function for a particle in one dimension. The quantum partition function in the canonical (NVT) ensemble for a system is given by the trace:

$$Z = tr[\exp(-\beta\hat{H}) = \int_{-\infty}^{\infty} d\mathbf{x}\langle\mathbf{x} \mid \exp(-\beta\hat{H} \mid \mathbf{x}\rangle \quad 2.43$$

where the reciprocal temperature $\beta = \frac{1}{kbT}$

$$\hat{H} = \frac{\hat{p}^2}{2m} + \hat{V} \quad 2.44$$

where m is the system mass , $\hat{V} = V(\mathbf{x})$ the potential, and $\hat{p} = \frac{i\hbar d}{dx}$ the momentum operator.

Although the kinetic-energy part can be evaluated in the momentum representation as

$$\langle\mathbf{p} \mid \exp(-\frac{\beta p^2}{2m} \mid \mathbf{p}\rangle, \quad 2.45$$

and the potential-energy part in the position representation as

$$\langle\mathbf{x} \mid \exp(-\beta V(\mathbf{x}) \mid \mathbf{x}\rangle, \quad 2.46$$

it cannot in general evaluate Eq.(2.44) which has an exponential of the total Hamiltonian because $\hat{x}$ and $\hat{p}$ do not commute. It is, however, possible to make an approximation to the Boltzmann operator using the split-operator method or Trotter splitting[64]. Using $\hat{T}$ as a shorthand representation for $\frac{\hat{p}^2}{2m}$ and U as the potential energy Trotter theorem allows $\exp(-\beta H)$ to be expressed as $\left[\exp(-\frac{\beta U}{2P})\exp(-\frac{\beta T}{P})\exp(-\frac{\beta U}{2P})\right]^P$ in the limit $P \to \infty$.

This Trotter theorem expression is then substituted in Eq. (2.44) and an identity operator $\int_{-\infty}^{\infty} dx \mid x\rangle\langle x \mid = 1$ is inserted in between each factor of Trotter expression, giving

$$Z = \lim_{P\to\infty} \int d\mathbf{x}_1 ... d\mathbf{x}_P \prod_{s=1}^{P} \langle\mathbf{x}^{(S)} \mid \exp(-\frac{\beta U}{2P})\exp(-\frac{\beta T}{P})\exp(-\frac{\beta U}{2P}) \mid \mathbf{x}^{(S+1)} \quad 2.47$$

Using

$$\langle \mathbf{x}^{(S)} \mid \exp(-\frac{\beta U}{2P})\exp(-\frac{\beta T}{P})\exp(-\frac{\beta U}{2P}) \mid \mathbf{x}^{(S+1)} \rangle = (\frac{mP}{2\pi\beta\hbar^2})^{1/2}$$
$$\exp\left[-\frac{\beta}{2P}(U(\mathbf{x}^{(s)}) + U(\mathbf{x}^{(s+1)}))\right]\exp\left[-\frac{mP}{2\beta\hbar^2}(\mathbf{x}^{(S)} - \mathbf{x}^{(S+1)})^2\right] \quad 2.48$$

we get

$$Z = \lim_{P\to\infty}\left(\frac{mP}{2\pi\beta\hbar^2}\right)^{P/2}\int d\mathbf{x}^{(1)}..d\mathbf{x}^{(P)}\, \mathrm{e}^{-\beta V_e} \quad 2.49$$

where the effective potential V_e is given by

$$V_e = \sum\nolimits_{S=1}^{P}\left[\frac{1}{2}m\omega_P^2(\mathbf{x}^{(S)} - \mathbf{x}^{(S+1)})^2 + \frac{1}{P}U(\mathbf{x}^{(s)})\right] \quad 2.50$$

where $\omega_p = \dfrac{\sqrt{P}}{\beta\hbar}$.

It is possible to introduce a set of P uncoupled Gaussian integrals in to Eq. (2.50) to express it in a quasi-phase-space form.

$$Z = \int d\mathbf{p}^{(1)}..d\mathbf{p}^{(P)}\int d\mathbf{x}^{(1)}..d\mathbf{x}^{(P)}\exp\left\{-\beta\sum_{s=1}^{P}\left[\frac{\mathbf{p}_S^2}{2m_S^{'}} + \frac{1}{2}m\omega_P^2(\mathbf{x}^{(S)} - \mathbf{x}^{(S+1)})^2 + \frac{1}{P}U(x^S)\ \right]\right\} \quad 2.51$$

which is equivalent to a classical partition function of an extended system with Hamiltonian:

$$H_N(\mathbf{p},\mathbf{x}) = \sum_{S=1}^{P}\left[\frac{\mathbf{P}_S^2}{2m_S^{'}} + \frac{1}{2}m\omega_P^2(\mathbf{x}^{(S)} - \mathbf{x}^{(S+1)})^2 + \frac{1}{P}U(\mathbf{x}_S)\right] \quad 2.52$$

This can be seen to describe the motion of a ring, related to a necklace, of P "beads", each of mass $m_S^{'}$, with momentum **p** and connected together by temperature-dependent springs in an external potential $U(\mathbf{x}_S / P$. This is known as the classical isomorphism, illustrated in Fig. 2-3.

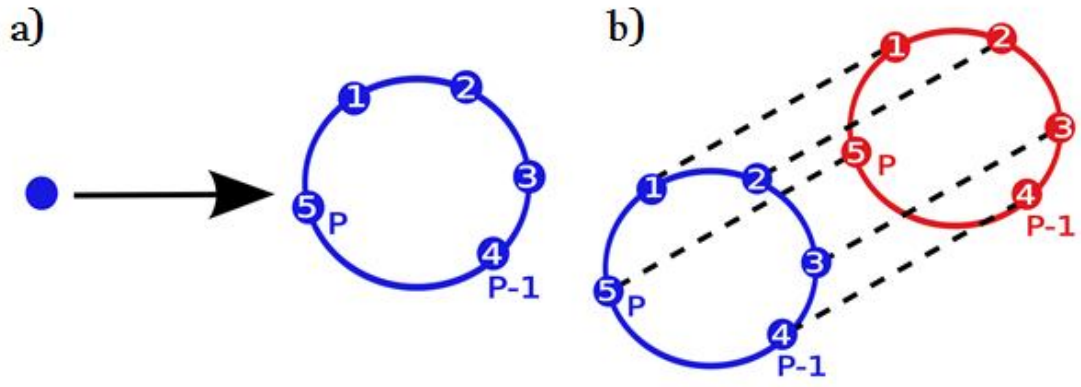

Figure 2-3. Path integral picture, a) single quantum particle is treated as a necklace consisting of P "beads" (Here $P = 5$)with harmonic interactions between nearest neighbors on the chain. This treatment is exact in the limit $P \to \infty$ b) interactions occur only between beads in the *same* time slice.

2.7.2 Ab initio Path Integral Molecular Dynamics:*Statics*

The equations of motion resulting from Eq. (2.52) can in principle be implemented as a molecular dynamics procedure to obtain the equilibrium properties of the system. For this let's first do an extension of the path integral scheme to N particles in three dimensions with nuclear degrees of freedom $\mathbf{R}_I$ and electronic degrees of freedom describing a ground-state Born–Oppenheimer surface $E_0(\mathbf{R}_I)$

$$Z = \prod_{I=1}^{N} \int d\mathbf{p}_I^{(1)} .. d\mathbf{p}_I^{(P)} \int d\mathbf{R}_I^{(1)} .. d\mathbf{R}_I^{(P)} \exp\left\{ -\beta \sum_{s=1}^{P} \left[\frac{(\mathbf{p}_I^{(S)})^2}{2m_I'} + \frac{1}{2} m_I \omega_P^2 (\mathbf{R}^{(S)} - \mathbf{R}^{(S+1)})^2 + \frac{1}{P} E_0(\mathbf{R}^{(S)}) \right] \right\} \quad 2.53$$

where $\mathbf{R}_I$ denotes the set of all nuclear positions at imaginary time slice S and ω_P is the chain frequency.

This ground state potential surface $E_0(\mathbf{R}_I)$ is obtained using density functional theory by minimizing the Kohn–Sham functional $E[\phi_i^{(S)}, \mathbf{R}_I^{(S)}]$ over the electronic degrees of

freedom $\phi_i^{(S)}$ for each time slice. In car-Parrinello method, this minimization is carried out dynamically using the extended Lagrangian:

$$L_{AIPI} = \frac{1}{P}\sum_{S=1}^{P}\left\{\sum_i \mu\langle\dot{\phi}_i^{(S)} \mid \dot{\phi}_i^{(S)}\rangle - E[\phi_i^{(S)}, \mathbf{R}_I^{(S)}] + \Lambda_{ij}^{(S)}(\langle\dot{\phi}_i^{(S)} \mid \dot{\phi}_i^{(S)}\rangle - \delta_{ij})\right\} + \sum_{S=1}^{P}\left\{+\sum_I m_I'(\dot{\mathbf{R}}_I^{(S)})^2 - \sum_{I=1} m_I\omega_P(\mathbf{R}_I^{(S)} - \mathbf{R}_I^{(S+1)})^2\right\} \quad 2.54$$

A direct implementation of Eq. (2.55) leads to non ergodic trajectories that do not properly sample the available canonical phase space[65]. This is caused by harmonic coupling of the springs which causes the MD time step to be limited by the fast vibrational modes leading to a poor sampling of low frequency modes. A solution to this problem was presented by Tuckerman[66] *et al.*, who introduced a change of variables that diagonalizes the harmonic bead coupling and then coupling the resulting equations of motion with a set of Nose Hoover chain thermostats. In this way, it was possible to ensure ergodicity of the weakly coupled modes. This is called a 'staging' transformation. We will not discuss the details of the staging method. However, a change of variable technique will be discussed in the next secion in the context of ab initio centroid molecular dynamics.

It is very important to note at this stage that the time dependence of positions ,momenta and thus the time evolution in *phase space* as generated by Eq. (2.55) has no physical meaning. The sole use of "time" is to parameterize the deterministic dynamical exploration of *configuration space*. The results will be similar to one obtained from a Monte Carlo method. The crucial difference is in computing the interactions $\boldsymbol{E_0}$ "on-the-fly" like in *Car Parrinello* molecular dynamics.

2.7.3 Ab Initio Path Centroids: Dynamics

Although the static properties can be successfully computed using the quantum-classical isomorphism, dynamic properties cannot be derived from the partition

function. However, the success of quantum-classical isomorphism has motivated Cao and Voth to propose Centroid Molecular Dynamics (CMD)[31,67-69]. CMD solves the dynamics equations of motion of classical particles in the centroid effective force. This classical effective force provides average dynamic properties of the quantum system and hence the classical dynamics produced from this effective centroid force has quantum character. It should be emphasized however that CMD is not exact; moreover, the central result, which provides the link between the exact quantum dynamics and that of the center of mass (centroid) of the ring of classical particles cannot be obtained from a series of *controlled* approximations. It is exact only for harmonic potentials appeal rests mainly on success of its utilizations in numerous condensed phase calculations in which experimental results or more sophisticated quantum calculations were available. For example, Cao and Voth suggested that classical time correlation functions of position or momentum coordinates, calculated from trajectories generated by the CMD equations, are a well-defined approximation to the Kubo transform[70] of the corresponding quantum time correlation functions.

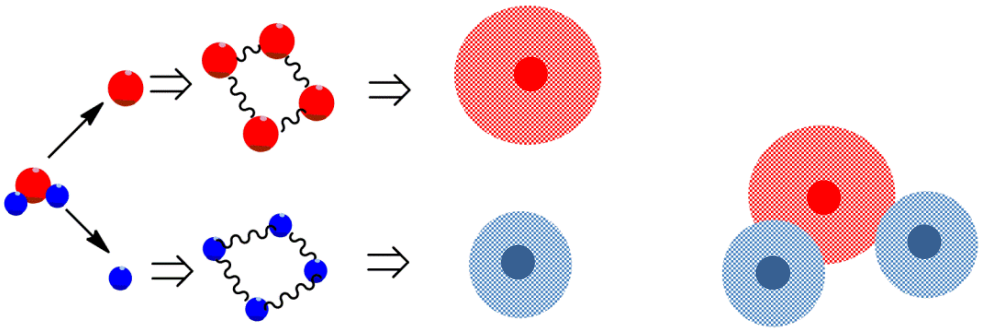

Figure 2-4. An example of a water molecule represented by 4 beads. Each atom is represented by a chain of four beads connected by harmonic springs. The central filled circle represents the centroid.

The centroid variable, which is the centre of mass of P beads of *I* th particle is given by

$$R_I^c(t) = \frac{1}{P}\sum_{s'=1}^{P}\mathbf{R}_I^{(S')} \qquad 2.55$$

Fig.2-4 illustrates a centroid To perform accurate CMD simulations, a rigorous evaluation of the forces is desirable because the CMD results critically depend on the

treatment of the forces. This is can be achieved by combining a first principle approach with the CMD method to generate the effective force "on-the-fly" as the centroids are propagated. This method is called ab initio centroid molecular dynamics[63,71]. This is implemented by converting the primitive path variable $\mathbf{R}_I^{(S)}$ to a representation based on normal modes $\mathbf{u}_I^{(S)}$ which diagonalize the harmonic nearest-neighbour harmonic coupling ad single out the centroid coordinates in terms of normal modes. The transformation follows the Fourier expansion of a cyclic path.

$$\mathbf{R}_I^{(S)} = \sum_{s'=1}^{P} \mathbf{a}_I^{(s')} \exp[\frac{2\pi i(S-1)(S'-1)}{P} \qquad 2.56$$

where the coefficients $\mathbf{a}_I^{(s')}$ are complex. The normal mode variable $\mathbf{u}_I^{(s')}$ are then given in terms of expansion coefficients according to

$$\begin{aligned} \mathbf{u}_I^{(1)} &= \mathbf{a}_I^{(1)} \\ \mathbf{u}_I^{(P)} &= \mathbf{a}_I^{\frac{(P+2)}{2}} \\ \mathbf{u}_I^{(2S-2)} &= \mathrm{Re}(\mathbf{a}_I^{(S)}) \\ \mathbf{u}_I^{(2S-1)} &= \mathrm{Im}(\mathbf{a}_I^{(S)}) \end{aligned} \qquad 2.57$$

The ab initio path integral expression in normal modes can be written as

$$\begin{aligned} L_{AIPI} = \frac{1}{P}\sum_{S=1}^{P}\Bigg\{ & \sum_i \mu\langle\dot{\phi}_i^{(S)} \mid \dot{\phi}_i^{(S)}\rangle - E[\phi_i^{(S)}, \mathbf{R}_I(\mathbf{u}_I^{(1)},\ldots,\mathbf{u}_I^{(S)}] \\ & + \Lambda_{ij}^{(S)}(\langle\dot{\phi}_i^{(S)} \mid \dot{\phi}_i^{(S)}\rangle - \delta_{ij})\Bigg\} \\ & + \sum_{S=1}^{P}\Bigg\{ + \sum_I M'_I(\dot{\mathbf{u}}_I^{(S)})^2 - \sum_{I=1} M_I^{(S)}\omega_P(\mathbf{u}_I^{(S)})^2 \Bigg\} \end{aligned} \qquad 2.58$$

where $M'^{(S)}_I$ is related tofictitious normal mode mass $M_I^{(S)}$ by

$$M'^{(S)}_I = \gamma M_I^{(S)} \qquad 2.59$$

where γ is the centroid adaibaticity parameter which can control the time-scale separation between centroid and non-centroid mode.

In Eq. (2.59) the primitive path variable $\mathbf{R}_I^{(S)}$ and normal mode variable $\mathbf{u}_I^{(s')}$ are related using the unitary matrix **U** transformation given by

$$\mathbf{u}_I^{(S)} = \frac{1}{\sqrt{P}} \sum_{S'=1}^{P} \mathbf{U}_{SS'}^{\dagger} \mathbf{R}_I^{(S')} \qquad 2.60$$

The main advantage of using the normal mode representation can be seen now. A lowest order normal mode $\mathbf{u}_I^{(1)}$ turns out to be identical to centroid $\mathbf{R}_I^c$ of the path that represents the I^{th} nucleus.

$$\mathbf{u}_I^{(1)} = \mathbf{R}_I^c = \frac{1}{P} \sum_{S'=1}^{P} \mathbf{R}_I^{(S')} \qquad 2.61$$

The equations of motion for adiabatic *ab initio* centroid molecular dynamics can be obtained using Euler–Lagrange equations from L_{AIPI}.

2.8 Computing Observables from MD Simulation

Observables are computed from the molecular dynamics simulation by performing averages of appropriate functions, $A(\mathbf{P},\mathbf{R})$ of the momenta and coordinates of the particles in the system. The procedure relies on the ergodic hypothesis which states that given an infinite amount of time, a system will visit all of its accessible phase space so that ensemble averages of $A(\mathbf{P},\mathbf{R})$ can be directly related to time averages of molecular dynamics trajectory:

$$\langle A(\mathbf{P},\mathbf{R}) \rangle = \lim_{T\to\infty} \frac{1}{T} \int_0^T dt A(\mathbf{P}(t)\mathbf{R}(t) \qquad 2.62$$

This ensemble average in Eq. (2.63) could refer to any ensemble. For example, a canonical (*NVT)* ensemble average would be given by

$$\langle A(\mathbf{P},\mathbf{R}) \rangle = \frac{1}{N! h^{3N} Q(N,V,T)} \int d_N \mathbf{P} d_N \mathbf{R}\ A(\mathbf{P},\mathbf{R})\ e^{-\beta H_N(\mathbf{P},\mathbf{R})}, \qquad 2.63$$

where $H_N(\mathbf{P},\mathbf{R})$ is the classical nuclear Hamiltonian and $Q(N,V,T)$ is the canonical partition function.

2.8.1 Radial Distribution Function

Radial distribution provides the information on the structure of the material. It gives the probability of locating pairs of atoms separated by a distance r, relative to that for a completely random distribution at the same density (i.e. the ideal liquid). For liquids and amorphous materials, g(r) exhibits its major peak close to the average atomic separation of neighboring atoms, and oscillates with less pronounced peaks at larger distances. The magnitude of the peaks decays exponentially with distance. Radial distribution function can be computed from the Molecular dynamics simulation.

Consider a system of N particles in a volume V (for an average number density $\rho = \frac{N}{V}$) and at a temperature T (so that $\beta = \frac{1}{kT}$). The particle coordinates are $\mathbf{R}_I$ with $I = 1,2,..N$. The radial distribution function (RDF) is then given as an average:

$$\begin{aligned} g(r) &= \frac{1}{4\pi r^2 \rho N Q(N,V,T)} \int d^N\mathbf{P} d^N\mathbf{R} \sum_{i\neq j} \delta\left(|\,\mathbf{R}_I - \mathbf{R}_J\,| - r\right) e^{-\beta H_N(\mathbf{P},\mathbf{R})} \\ &= \frac{1}{4\pi r^2 \rho r^2} \langle \frac{1}{N} \sum_{I\neq J} \delta\left(|\,\mathbf{R}_I - \mathbf{R}_J\,| - r\right) \end{aligned} \qquad 2.64$$

2.8.2 Diffusion Coefficient

Dynamical properties such as spectra and diffusion coefficient can be obtained from the molecular dynamics simulation using linear response theory from the time correlation functions. The time correlation function of an observable $A(\mathbf{P},\mathbf{R})$ is given by:

$$\langle A(0)A(t)\rangle = \frac{1}{Q(N,V,T)} \int d_N\mathbf{P}\, d_N\mathbf{R}\, A(\mathbf{P},\mathbf{R}) A(\mathbf{P_t(P,R)},\mathbf{R_t(P,R)}) e^{-\beta H_N(\mathbf{P},\mathbf{R})}, \qquad 2.65$$

where $(\mathbf{P}_t(\mathbf{P},\mathbf{R})$ and $(\mathbf{R}_t(\mathbf{P},\mathbf{R})$ denotes the phase space trajectory obtained from the initial condition $(\mathbf{P},\mathbf{R})$. If the observables A and B are different, then Eq. (2.66) becomes a cross correlation function.

The diffusion coefficient, D is hence computed as the autocorrelation of the velocity of the particle V.

$$D = \frac{1}{3}\int_0^\infty dt \frac{1}{N}(\sum_{I=1}^{N}\langle \mathbf{V}_I(0) \bullet \mathbf{V}_I(t)\rangle \qquad 2.66$$

2.8.3 Infrared Spectra and Vibrational Mode Analysis From Molecular Dynamics Simulation

Important insights into the dynamics and the thermodynamics of the proton translocation mechanism in hydrogen-bonded networks of various topologies can be gleaned from mid-infrared (IR) spectra. Intermolecular proton transfer is thought to be facilitated to a large degree by solvent fluctuations and rearrangements, following a mechanism that is reminiscent of Marcus' picture of electron transfer reactions. The IR absorption spectrum is particularly revealing of these underlying microscopic details since it is extremely sensitive to the local H-bonding environment of the reactive groups involved. Specifically, shifts in the O−H stretching bands and in other localized vibrational marker modes along with observations of IR absorption continua are far more revealing of solvent dynamics for proton transfer reactions than any other spectroscopy. We have already seen in section 1.6.2 that the modern investigation on proton transfer reactions using photoacids utilizes ultrafast vibrational spectroscopy in which the reaction is followed by specific vibrational marker modes of reactant and product. If specific vibrational marker modes of reactant, intermediate, and product states are identified, one can follow the proton transfer reaction by inspection of the transitions of these marker modes. Site-specific information can also be obtained in the case of vibrational marker modes that involve nuclear motions of specific molecular side groups by inspection of local modes that are affected by local interactions. For instance, it is well known that hydrogen bonding induces marked shifts in O–H bonds.

Let us now discuss how one can extract the infrared spectroscopic details from the molecular dynamics simulations.

The theoretical calculations of the linear optical constants can be performed by using linear response theory using the time-correlation formalism[72] of linear response theory[35], the value of the frequency-dependent Beer-Lambert absorptivity coefficient $\alpha(\nu)$ can be written as

$$\alpha(\nu) \overset{\text{def}}{=} -\frac{\ln(I/I_0)}{\ell} = \frac{\pi\nu\left[1-\exp\left(-\beta\hbar 2\pi\nu\right)\right]}{3\hbar c V n(\nu)\varepsilon_0} \cdot \int_{-\infty}^{\infty} \exp(2\pi i\nu\tau)\left\langle \hat{M}(0)\cdot\hat{M}(\tau)\right\rangle_{qm} d\tau \qquad 2.67$$

where qm indicates a quantum mechanical ensemble average, ℓ is the length of the optical path, α has Neperian units, $\hbar$ is Planck's constant, V is the sample's volume, ε_0 is the vacuum permittivity, and c is the speed of light. In Eq. (2.68), $\hat{M}(0)$ and $\hat{M}(\tau)$ represent the values of the quantum-mechanical dipole moment operator written in the Heisenberg representation at times $t = 0$ and $t = \tau$, respectively, and are defined using Système International (SI) units; $\beta = 1/(k_B T)$ with k_B being Boltzmann's constant and T the absolute temperature.

For condensed-phase systems such as those of interest in this, explicit eigenstate calculations[73] have a far too high computational overhead to be carried out, while direct, real-time, path-integral approaches[74] suffer from such severe phase oscillations that convergence cannot be achieved on any realistic time scale. In contrast, classical molecular dynamics can often be used to obtain the analogous correlation functions for a corresponding classical system. However, there is no general prescription for rigorously relating a quantum correlation function to a classical one. The precise relationship depends on the underlying Hamiltonian generating the dynamics.

Nevertheless, if one assumes the validity of the central approximation[75,76] of the centroid molecular dynamics theory, and considers that the electronic dipole moment operator is approximately linear, the Beer-Lambert absorptivity can be computed as

$$\alpha(\nu) \cong \frac{\beta}{6n(\nu)Vc\varepsilon_0}\int_{-\infty}^{\infty}\exp(2\pi i\nu\tau)\left\langle \dot{M}_c(0)\cdot\dot{M}_c(\tau)\right\rangle_c d\tau \qquad 2.68$$

where the autocorrelation function involves the centroid average[75] of the time-derivative of the dipole moment centroid symbol[75]. Moreover, since centroid averages are computed in practice[77] by means of a finite number of path-integral quasi-particles, one can adopt a further approximation, which consists of considering a single imaginary-time discretization of the quasi-particle chain. This amounts essentially to adopting the well-known harmonic approximation[78] which reads

$$\alpha(\nu) \cong \frac{\beta}{6n(\nu)Vc\varepsilon_0}\int_{-\infty}^{\infty}\exp(2\pi i\nu\tau)\left\langle \dot{M}_{cl}(0)\cdot\dot{M}_{cl}(\tau)\right\rangle_{cl} d\tau \qquad 2.69$$

where "cl" refers here to classical (i.e.: Newtonian) time-derivatives of the dipole moment, and to classical ensemble averages (i.e.: phase-space integration).

In order to rationalize the molecular origin of the features that appear in the computed IR spectra we have utilized three approaches. The first method is a spectrum decomposition technique that was previously proposed[15] by Iftimie and Tuckerman and is particularly useful[15,16,79] when investigating the origin of very broad and intense absorptions such as those caused by shared-proton structures, since these absorptions are not easily attributable to a localized vibration mode, and exhibit transition dipole moment intensities that vary significantly[15,79] with vibration frequency. The decomposition of the IR spectrum relies on an approximate, but chemically intuitive decomposition of the total dipole moment into molecular components, and employs maximally-localized[80,81] Wannier[82]-Boys[83] orbitals that are generated on-the-fly using a modified Car-Parrinello algorithm.[81,84] The approach proposed in Ref. [81] amounts to calculating the contribution $[\alpha(\nu)n(\nu)]_A$ of a molecule A in solution to the total absorption spectrum $\alpha(\square)n(\square)$ by computing the spectrum of the time-dependent cross-

correlation function between the molecular dipole moment μ_A of molecule A and the total dipole moment M:

$$[\alpha(\nu)n(\nu)]_A \cong \frac{\beta}{6Vc\varepsilon_0}\int_{-\infty}^{\infty}\exp(2\pi i\nu\tau)\left\langle \dot{\mu}_A(0)\cdot\dot{M}(\tau)\right\rangle_{cl} d\tau \quad 2.70$$

The second method employed here consists of calculating normal-mode vibration spectra defined as

$$I(\nu) = \int_{-\infty}^{\infty}\exp(2\pi i\nu\tau)\left\langle \dot{d}(0)\cdot\dot{d}(\tau)\right\rangle_{cl} d\tau \quad 2.71$$

where $\dot{d}$ represents the time-derivative of the normal-mode variable d.

This method of computing the normal-mode vibrational spectrum using Fourier transform can provide only frequency information and not any time-frequency information.

Third method is calculating the frequency response of different molecular species with the advancement of reaction by following a specific vibrational normal mode of the molecule. An important characteristic of these normal mode is that they form *non-stationary* time series, whose behavior in the frequency space can be investigated using appropriate time-frequency analysis techniques[85]. It should be noted that the most straight forward short-time FT approaches[85] which utilize a moving interval of fixed duration in the interior of which quasi-stationary behaviour is assumed are limited in scope because a fixed time interval that allows good resolution of high frequency oscillations will prove inadequate for sufficiently low frequency oscillations.

The wavelet transform is a multi-resolution time-frequency analysis technique that resolves high frequency and low frequency oscillations equally satisfactorily by decomposing the non-stationary time-series of interest $x(t)$ into wavelets. A wavelet is a wave-like oscillation whose amplitude starts out at zero, increases, and then decreases back to zero. The continuous wavelet transform the time-series $d(t)$ can be written as:

$$W(a,b) = \frac{1}{\sqrt{a}} \int_{-\infty}^{\infty} d(t)\psi^* \left(\frac{t-b}{a} \right) dt, \qquad 2.72$$

where ψ is a continuous function called the mother wavelet, the star represents the operation of complex conjugate, a represents the scale index and b the scale shift. The factor $1/\sqrt{a}$ is a normalization factor. The parameters a and b have the dimensions of time, but b is usually transformed into a wave number axis by the transformation $\nu = 1/(c \cdot a)$ where $c = 3 \cdot 10^{10}$ cm/s is the speed of light.

The mother wavelet can be chosen to be the so-called complex Morlet wavelet defined as[85]:

$$\psi(m) = \frac{1}{\sqrt{\pi f_b}} e^{i \cdot 2\pi f_c m} e^{-m^2/f_b} \qquad 2.73$$

where $i = \sqrt{-1}$, $m = (t-b)/a$ is a dimensionless number, f_b is called the band width and is responsible for the shape of the wavelet, and f_c is called the center frequency. The resulting scalogram $W(\nu,t)$ was subsequently utilized to compute the value $\nu_{\max}(t)$, the value of the wavenumber ν that corresponds to the maximum value of $W(\nu,t)$ at any given time t and hence obtain a time-frequency spectrum.

2.9 References

(1) Marx, D.; Hutter, J. *Ab Initio Molecular Dynamics*; Cambridge University Press: New York, 2009.

(2) Geissler, P. L.; Dellago, C.; Chandler, D.; Hutter, J.; Parrinello, M. *Science* **2001**, *291*, 2121.

(3) Strajbl, M.; Hong, G.; Warshel, A. *J. Phys. Chem. B* **2002**, *106*, 13333.

(4) Asthagiri, D.; Pratt, L. R.; Kress, J. D.; Gomez, M. A. *P. Natl. Acad. Sci. USA* **2004**, *101*, 7229.

(5) Asthagiri, D.; Pratt, L. R.; Kress, J. D. *P. Natl. Acad. Sci. USA* **2005**, *102*, 6704.

(6) Izvekov, S.; Voth, G. A. *J. Chem. Phys.* **2005**, *123*, 9.

(7) Marx, D.; Tuckerman, M. E.; Hutter, J.; Parrinello, M. *Nature* **1999**, *397*, 601.

(8) Tuckerman, M.; Marx, D.; Klein, M. L.; Parrinello, M. *Science* **1997**, *275*, 817.

(9) Tuckerman, M. E.; Marx, D.; Parrinello, M. *Nature* **2002**, *417*, 925.

(10) Tuckerman, M. E.; Chandra, A.; Marx, D. *Acc. Chem. Res.* **2006**, *39*, 151.

(11) Warshel, A. *Chem. Phys. Lett.* **1978**, *55*, 454.

(12) Warshel, A.; Weiss, R. M. *J. Am. Chem. Soc.* **1980**, *102*, 6218.

(13) Ando, K.; Hynes, J. T. *J. Phys. Chem. A* **1999**, *103*, 10398.

(14) Sillanpaa, A. J.; Simon, C.; Klein, M. L.; Laasonen, K. *J. Phys. Chem. B* **2002**, *106*, 11315.

(15) Iftimie, R.; Tuckerman, M. E. *Angew. Chem. Int. Ed.* **2006**, *45*, 1144.

(16) Iftimie, R.; Thomas, V.; Plessis, S.; Marchand, P.; Ayotte, P. *J. Am. Chem. Soc.* **2008**, *130*, 5901.

(17) Park, J. M.; Laio, A.; Iannuzzi, M.; Parrinello, M. *J. Am. Chem. Soc.* **2006**, *128*, 11318.

(18) Maupin, C.; Wong, K. F.; Soudakov, A. V.; Kim, S.; Voth, G. A. *J. Phys. Chem. B* **2006**, *110*, 631.

(19) Gu, W.; Frigato, T.; Straatsma, T. P.; Helms, V. *Angew. Chem. Int. Ed.* **2007**, *46*, 2939.

(20) Marx, D.; Chandra, A.; Tuckerman, M. E. *Chem. Rev.* **2010**, *110*, 2174.

(21) Warshel, A. *Biochemistry* **1981**, *20*, 3167.

(22) Warshel, A.; Papazyan, A. *P. Natl. Acad. Sci. USA* **1996**, *93*, 13665.

(23) Mathias, G.; Marx, D. *P. Natl. Acad. Sci. USA* **2007**, *104*, 6980.

(24) Koch, W.; Holthausen, M. C. *A Chemist's Guide to Density Functional Theory*; VCH: New York, 2000.

(25) Becke, A. *Phys. Rev. A* **1998**, *38*, 3098.

(26) Lee, C.; Yang, W.; Parr, R. G. *Phys. Rev. B* **1998**, *37*, 785.

(27) Sprik, M.; Hutter, J.; Parrinello, M. *J. Chem. Phys.* **1996**, *105*, 1142.

(28) Maurer, P.; Thomas, V.; Iftimie, R. *J. Chem. Phys.* **2011**, *134*.

(29) Troullier, N.; Martins, J. L. *Phy. Rev. B* **1991**, *43*, 1993.

(30) Marx, D.; Tuckerman, M. E.; Martyna, G. J. *Comput. Phys. Commun.* **1999**, *118*, 166.

(31) Cao, J. S.; Voth, G. A. *J. Chem. Phys.* **1993**, *99*, 10070.

(32) Frenkel, D.; Smit, B. *Understanding Molecular Simulation: From Algorithms to Applications*; 2 ed.; Academic Press: New York, 2001.

(33) Allen, M. P.; Tildesley, D. J.; Clarendon Press: Oxford, 1987, p 50.

(34) Taylor, J. R. *Classical Mechanics, University science books* **2005**.

(35) McQuarrie, D. A. *Statistical mechanics*; University Science Books: Sausalito, Calif., 2000.

(36) J. Grotendorst, D. M., A. Muramatsu (Eds.) *John von Neumann Institute for Computing, NIC Series* **2002**, *10*, 467.

(37) Verlet, L. *Part. Part. Syst. Charact.* **1967**, *159*, 98.

(38) Verlet, L. *Phys. Rev.* **1967**, *159*, 98.

(39) Anisimov, V. M.; Vorobyov, I. V.; Lamoureux, G.; Noskov, S.; Roux, B.; MacKerell, A. D. *Biophys. J.* **2004**, *86*, 415A.

(40) Knight, J. L.; Brooks, C. L. *J. Chem. Theo. Comput*.

(41) Mantz, Y. A.; Gerard, H.; Iftimie, R.; Martyna, G. J. *J. Phys. Chem. B* **2006**, *110*, 13523.

(42) Woodcock, H. L.; Hodoscek, M.; Gilbert, A. T. B.; Gill, P. M. W.; Schaefer, H. F.; Brooks, B. R. *J. Comput. Chem.* **2007**, *28*, 1485.

(43) Cornell, W. D.; Cieplak, P.; Bayly, C. I.; Gould, I. R.; Merz, K. M.; Ferguson, D. M.; Spellmeyer, D. C.; Fox, T.; Caldwell, J. W.; Kollman, P. A. *J. Am. Chem. Soc.* **1995**, *117*, 5179.

(44) Kaminski, G. A.; Friesner, R. A.; Tirado-Rives, J.; Jorgensen, W. L. *J. Phys. Chem. B* **2001**, *105*, 6474.

(45) Christen, M.; Hunenberger, P. H.; Bakowies, D.; Baron, R.; Burgi, R.; Geerke, D. P.; Heinz, T. N.; Kastenholz, M. A.; Krautler, V.; Oostenbrink, C.; Peter, C.; Trzesniak, D.; Van Gunsteren, W. F. *J. Comput. Chem.* **2005**, *26*, 1719.

(46) Eichenberger, A. P.; Allison, J. R.; Dolenc, J.; Geerke, D. P.; Horta, B. A. C.; Meier, K.; Oostenbrink, C.; Schmid, N.; Steiner, D.; Wang, D. Q.; van Gunsteren, W. F. *J Chem. Theo. Comput.* **2011**, *7*, 3379.

(47) Schmid, N.; Christ, C. D.; Christen, M.; Eichenberger, A. P.; van Gunsteren, W. F. *Comput. Phys. Commun.* **2012**, *183*, 890.

(48) Patel, S.; Brooks, C. L. *J. Comput. Chem.* **2004**, *25*, 1.

(49) Patel, S.; Mackerell, A. D.; Brooks, C. L. *J. Comput. Chem.* **2004**, *25*, 1504.

(50) Rick, S. W.; Stuart, S. J *Rev. Comp. Ch.* **2002**, *18*, 89.

(51) Lewars, E. *Computational chemistry : introduction to the theory and applications of molecular and quantum mechanics.Springer,2011* **2011**.

(52) Halgren, T. A.; Damm, W. *Curr. Opin. Struc. Biol.* **2001**, *11*, 236.

(53) Warshel, A.; Kato, M.; Pisliakov, A. V. *J Chem. Theo. Comput.* **2007**, *3*, 2034.

(54) Parr, R. G.; Yang, W. *Density-functional theory of atoms and molecules*; Oxford University Press ;
Clarendon Press: New York
Oxford England, 1989.

(55) Hohenberg, P.; Kohn, W. *Phys. Rev.* **1964**, *136*, B864.

(56) Car, R.; Parrinello, M. *Phys. Rev. Lett.* **1985**, *55*, 2471.

(57) Phillips, J. C. *Phys. Rev.* **1958**, *112*, 685.

(58) Phillips, J. C. *Phys. Rev. Lett.* **1958**, *1*, 349.

(59) Ashcroft, N. W., N. D. Mermin, *Solid State Physics (Holt Saunders, Philadelphia), page. 113* **1976**.

(60) Feynman, R. P. *Rev. Mod. Phys.* **1948**, *20*, 367.

(61) R. P. Feynman, A. R. H. *Quantum Mechanics and Path Integrals,McGraw-Hill, New York, 1965*.

(62) Craig, I. R.; Manolopoulos, D. E. *J. Chem. Phys.* **2004**, *121*, 3368.

(63) Marx, D.; Tuckerman, M. E.; Hutter, J.; Parrinello, M. *Nature* **1999**, *397*, 601.

(64) Trotter, H. F. *Proc. Amer. Math. Soc.* **1959**, *10*.

(65) Hall, R. W.; Berne, B. J. *J. Chem. Phys.* **1984**, *81*, 3641.

(66) Tuckerman, M. E.; Berne, B. J.; Martyna, G. J.; Klein, M. L. *J. Chem. Phys.* **1993**, *99*, 2796.

(67) Cao, J.; Voth, G. A. *J. Chem. Phys.* **1994**, *100*, 5093.

(68) Jang, S.; Voth, G. A. *J. Chem. Phys.* **2001**, *114*, 1944.

(69) Jang, S.; Voth, G. A. *J. Chem. Phys.* **2000**, *112*, 8747.

(70) Kubo, R. *Adv. Chem. Phys.* **1969**, *15*, 101.

(71) Tuckerman, M. E.; Yarne, D. A.; Samuelson, S. O.; Hughes, A. L.; Martyna, G. J. *Comput. Phys. Commun.* **2000**, *128*, 333.

(72) Gordon, R. G. *Adv. Magn. Reson.* **1968**, *3*, 1.

(73) Wyatt, R. E.; Zhang, J. Z. H. *Dynamics of Molecules and Chemical Reactions*; CRC Press: New York, 1996.

(74) Makri, N. *Annu. Rev. Phys. Chem.* **1999**, *50*, 167.

(75) Jang, S.; Voth, G. A. *J. Chem. Phys.* **1999**, *111*, 2357.

(76) Jang, S.; Voth, G. A. *J. Chem. Phys.* **1999**, *111*, 2371.

(77) Marx, D.; Tuckerman, M. E.; Martyna, G. J. *Comput. Phys. Commun.* **2000**, *118*, 166.

(78) Bader, J. S.; Berne, B. J. *J. Chem. Phys.* **1994**, *100*, 8359.

(79) Thomas, V.; Iftimie, R. *J. Phys. Chem. B* **2009**, *113*, 4152.

(80) Berghold, G.; Mundy, C. J.; Romero, A. H.; Hutter, J.; Parrinello, M. *Phys. Rev. B* **2000**, *61*, 10040.

(81) Iftimie, R.; Thomas, J. W.; Tuckerman, M. E. *J. Chem. Phys.* **2004**, *120*, 2169.

(82) Wannier, G. H. *Phys. Rev.* **1937**, *52*, 191.

(83) Boys, S. F. *Rev. Mod. Phys.* **1960**, *32*, 296.

(84) Thomas, J. W.; Iftimie, R.; Tuckerman, M. E. *Phys. Rev. B* **2004**, *69*, 125105.

(85) Flandrin, P. *Time-Frequency/Time-Scale Analysis*; Academic Press: London, 1999; Vol. 10.

Spectral Signatures and Molecular Origin of Acid Dissociation Intermediates

Radu Iftimie*,§,¶, Vibin Thomas*, Sylvain Plessis†, Patrick Marchand† and Patrick Ayotte†,§,¶

** Département de Chimie, Université de Montréal, CP 6128, succursale Centre-Ville, Montréal, H3C3J7, Canada; and †Département de Chimie, Université de Sherbrooke, 2500 Boulevard Université, Sherbrooke, J1K2R1, Canada §To whom correspondence may be addressed.*

Published in *J. Am. Chem. Soc.* **130** (18): 5901-7 (2008)

Abstract: The existence of a broad, mid-infrared absorption ranging from 1000 to 3000 cm^{-1} is usually interpreted as a signature for the existence of protonated water networks. Herein, we use cryogenic mixtures of water and hydrogen fluoride (HF) and show experimental and computational evidence that similarly wide absorptions can be generated by a broad distribution of proton-shared and ion pair complexes. In the present case, we demonstrate that the broadening is mainly inhomogeneous, reflecting the fact that the topology of the first solvation shell determines the local degree of ionization and the shared-proton asymmetric stretching frequency within $H_2O \cdot HF$ complexes. The extreme sensitivity of the proton transfer potential energy hypersurface to local hydrogen bonding topologies modulates its vibrational frequency from 2800 down to ~1300 cm^{-1}, the latter value being characteristic of solvation geometries that yield similar condensed-phase proton affinities for H_2O and fluoride. By linking the local degree of ionization to the solvation pattern, we are able to propose a mechanism of ionization for HF in aqueous solutions and to explain some of their unusual properties at large concentrations. However, an important conclusion of broad scientific interest is our prediction that spectral signatures that are normally attributed to protonated water networks could also reveal the presence of strong hydrogen bonds

between un-ionized acids and water molecules, with important consequences to spectroscopic investigations of biologically relevant proton channels and pumps.

3. Spectral Signatures and Molecular Origin of Acid Dissociation Intermediates

3.1 Introduction

Proton translocation constitutes a fundamental class of chemical transformations and is ubiquitous as an elementary process throughout nature. An important example is the conduction of protons along "water-chains" in the trans-membrane proton pumps of living cells[1]. Despite their fundamental role in chemistry and biology, insights into the microscopic mechanisms that facilitate proton transfer between Brønsted donors and acceptors are largely lacking. In particular, the nature of proton donor and acceptor intermediates relevant to various bioenergetics cycles is usually unknown, except for a few cases where significant progress[2,3] has been recently reported.

Important insights into the dynamics[4] and the thermodynamics[5] of the proton translocation mechanism in hydrogen-bonded networks of various topologies can be gleaned from mid-infrared (IR) spectra. Intermolecular proton transfer is thought[6] to be facilitated to a large degree by solvent fluctuations and rearrangements, following a mechanism that is reminiscent of Marcus' picture[7] of electron transfer reactions. The IR absorption spectrum is particularly revealing of these underlying microscopic details, since it is extremely sensitive[8] to the local H-bonding environment of the reactive groups involved. Specifically, shifts in the O-H stretching bands and in other localized vibrational marker modes along with observations of IR absorption continua are far more revealing of solvent dynamics for proton transfer reactions than the visible spectra. However, the interpretation of IR spectroscopic investigations can be hampered by the difficulties in unambiguously assigning IR absorption patterns to specific local structures of a fluxional H-bonded network. These difficulties are particularly severe when investigating room-temperature aqueous solutions, because of the large number

of relevant solvation topologies[9,10] and of their ultrafast dynamics.[11] Consequently, some of the most successful recent efforts that attempted to clarify how the local H-bonding environment determines the IR spectral signature of the hydrated proton focused on gas-phase clusters[12,13,14] and crystalline hydrates[15], employed ice surfaces at very low temperatures[5], or relied on computational investigations[16].

Amorphous aqueous solids at cryogenic temperature provide attractive alternative model systems for aqueous solutions as they can help trap metastable reaction intermediates in their liquid-like, albeit translationally static, disordered H-bonded networks. Moreover, while slowing down tremendously the collective solvent motions responsible for the ultrafast interconversion dynamics, investigations at very low temperatures may also allow valuable insight into subtle quantum nuclear effects which are obscured by thermal agitation in liquid solutions.

Herein, we investigate cryogenic mixtures of water and HF in order to explore the spectral signature of the transient structures that are involved in the process of ionization of HF molecules in aqueous solutions, leading to the formation of proton-shared intermediates and of contact ion pairs:

$$\left[H_2O \cdot HF\right] \leftrightarrow \left[H_2O \cdot H^+ \cdot F^-\right] \leftrightarrow \left[H_2OH^+ \cdot F^-\right] \quad (2.74)$$

Dilute cryogenic solutions of HF in H_2O were recently shown[17] to display the spectral signature of aqueous protons, similarly to the behavior observed for the strong acids HCl and HBr, suggesting a similarly extensive degree of ionization at 40K in amorphous solid water. Entropic contributions could thus play an important role in determining the weak acid behavior of dilute hydrofluoric acid liquid solutions. Reflection absorption infrared spectroscopy measurements are reported here for several concentrations, ranging from pure water to equimolar mixtures, in an attempt to provide a molecular level interpretation of the weak-to-strong acid behavior observed[18] in HF aqueous solutions near equimolar concentrations.

First-principles molecular dynamics calculations of the Beer-Lambert absorptivity provide a detailed interpretation of the structure, of the dynamics, and of the vibrational spectra of various complexes found in equimolar cryogenic hydrofluoric acid solutions. Vibrational zero-point motions as well as incoherent tunneling effects are approximately included within the framework of the centroid molecular dynamics approach[19], resulting in an improved description of proton mobility and vibrational anharmonicity effects.

Our results indicate that the local degree of advancement of reaction (1) correlates well with the microscopic solvation environment, and also with the frequency of the shared-proton asymmetric stretching vibration. Hence, the extremely broad, experimentally observed absorption ranging from 1000 to 3400 cm^{-1}, the spectroscopic hallmark of polarizable[20] hydrogen bonds in dilute solutions of strong acids, is attributed here to the large variety of microscopic solvation environments experienced by HF molecules in the amorphous binary solids. In particular, we demonstrate that the surprisingly broad and intense absorption extending from 1300 to 2000 cm^{-1}, that distinguishes the cryogenic[17] from the room-temperature[21] mixtures, signals the presence of proton-shared complexes $F^- \cdot H^+ \cdot OH_2$ in which fluoride anions and water molecules display similar condensed-phase proton affinities. These proton-shared structures are intermediates in the ionization process depicted in reaction (1), being stabilized by distinctive first solvation shell H-bonding topologies and by long-range electrostatic interactions. In contrast, the spectral region ranging from 2000 to 2800 cm^{-1} reveals the presence of the reactant and of the product species appearing in the ionization reaction (1), namely, weakly H-bonded HF molecules, and contact ion pairs, respectively.

These observations suggest the existence of a supplementary level of complexity that needs to be considered in the interpretation of all disordered phase mid-IR experimental data. In particular, when weak Brønsted acids are present, care should be exercised when assigning specific mid-IR absorptions to the presence of protonated water networks. Our work demonstrates that spectroscopic features usually attributed

to hydrated Eigen[22] $H_9O_4^+$ ions could also signal the presence of strongly hydrogen-bonded AH·OH_2 complexes between some weak Brønsted acid AH and a water molecule. In the same vein, we conclude that the appearance of broad and intense absorptions around 1800 cm^{-1}, similar to those that were recently identified in asymmetrically solvated gas-phase[14] and trans-membrane[16] protonated water clusters, could also reveal the presence of un-dissociated O-H or N-H bonds that are stretched to the brink of ionization.

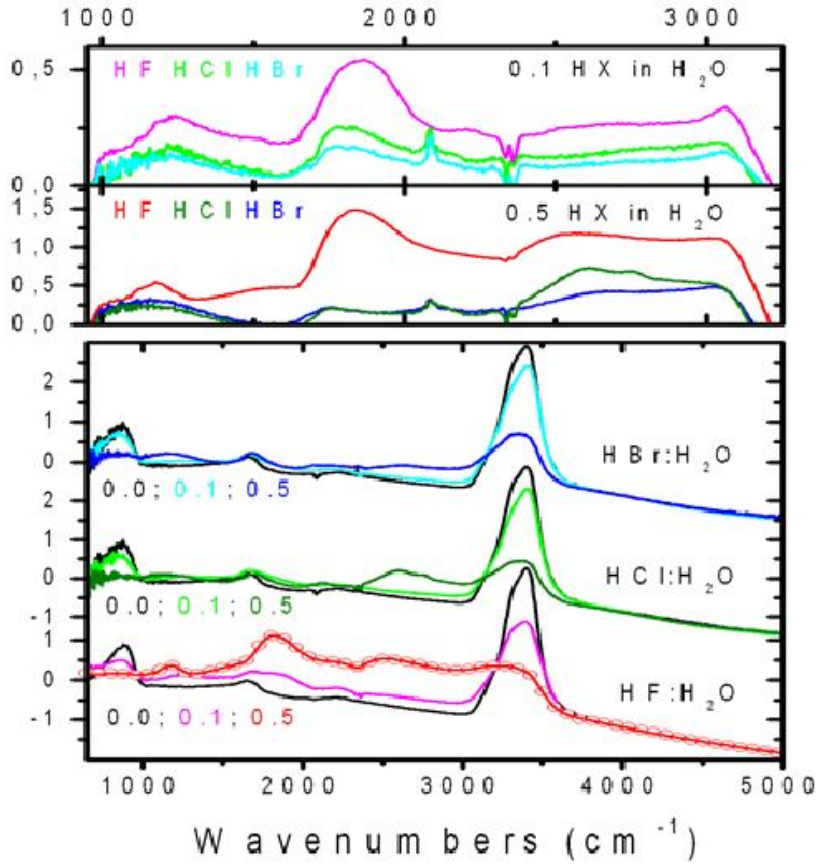

Figure 3-1. Lower panel: Raw reflection-absorption infrared spectra for 20 monolayers (ML) thick films of binary mixtures of hydrogen halides (HX; X=F, Cl, and Br) with H_2O at 80K on Pt(111). Absorbance is reported as -log(I_{film}/I_{Pt}) for 0.0 (neat amorphous solid water-ASW), 0.1 (2 ML HX and 18 ML H_2O), and 0.5 (10 ML HX and 10 ML H_2O) homogeneous mixtures of HX with H_2O. The red line through experimental spectrum (red circles) for 0.5 HF in H_2O displays model results using Fresnel relations to extract the optical constants reported in Fig.3-2. Upper panel: Difference spectra calculated using the ASW absorbance spectra from the lower panel as reference: -log(I_{film}/I_{ASW}). While the absorption continuum displayed by dilute mixtures of HF in H_2O displays similarities to those of dilute HCl and HBr mixtures, spectra for concentrated HF aqueous solutions differ significantly from those observed for concentrated cryogenic mixture of the strong acids.

3.2 Results and Discussion

3.2.1 Cryogenic mixtures of HF and H_2O show very broad absorptions that differ from those of fully dissociated acids.

To set the stage, the lower panel in Fig. 3-1 depicts the raw absorbance spectra measured at 80K for 20 monolayers (ML) thick films of pure amorphous solid water (ASW; 0.0), for dilute (0.1), and for concentrated (0.5) homogeneous binary amorphous solid mixtures of HF, HCl, and HBr in H_2O having the same optical thickness as the ASW films. For the more diluted mixtures (0.1), a broad continuum of absorption is clearly observed across the 1000-3000 cm^{-1} range in the raw spectra.

This is commonly recognized as the spectroscopic hallmark of aqueous protons. To better compare their absorption continua, difference spectra were computed for the dilute cryogenic aqueous mixtures using neat ASW spectra as reference (upper panel, top traces). Apart from differences in intensities, the absorption continua for the three dilute mixtures display striking similarities. Differences in the absorption continua are more pronounced in the more concentrated mixtures (0.5) where the cryogenic aqueous HF solutions display much larger intensities in the 1300-2500 cm^{-1} range than the HCl and HBr mixtures (upper panel-bottom traces). The very similar spectra displayed by concentrated cryogenic hydrochloric (HCl) and hydrobromic (HBr) acid solutions suggest the presence of very similar molecular entities that differ substantially from those that can be found in concentrated cryogenic hydrofluoric acid solutions.

Much smaller differences between infrared spectra of room-temperature solutions of hydrohalic acids have previously been reported[21] by Giguère and his collaborators. These researchers concluded that the similarities between the broad conspicuous bands observed in the 1000-1400cm^{-1} and the 1600-2000cm^{-1} frequency ranges in the spectra of aqueous HF solutions with those observed in the strong acid HCl, HBr, or HI aqueous

solutions, should be interpreted as evidence for the existence of $F^- \cdot H_3O^+$ contact ion pairs. This model was proposed to provide a molecular-level interpretation for the weak acid behavior of dilute hydrofluoric acid solutions as resulting from the tying up of acidic protons in strongly bound ion pairs. The data displayed in Fig.3-1 shows that lowering the temperature exacerbates the spectroscopic differences between hydrofluoric and the other hydrohalic acids.

Quantitative room-temperature investigations of the continuous absorbance generated by certain organic and inorganic acids led Zundel et al.[23] and Chapados et al.[24] to suggest that un-dissociated acid molecules in water can capture a wide distribution of local H-bonded topologies similar to those characteristic of strong, fully-dissociated acids. Progress in identifying the nature of the fluxional H-bond network in solutions of ionized, but un-dissociated acids has been reported very recently by Iftimie and Tuckerman[25]. These authors found computational evidence suggesting that broad absorptions extending between 1000 and 1400 cm^{-1} could be attributed to Zundel-like proton-shared $F^- \cdot H^+ \cdot OH_2$ complexes. Furthermore, it was concluded that broad absorptions ranging from 2000 to 3000 cm^{-1} are consistent with the presence of stretched, but un-ionized HF molecules that are strongly H-bonded to a water molecule forming a long lived $H_2O \cdot HF$ complex.

However, the computational investigations by Iftimie et al.[25] suffer from a number of limitations that could potentially limit the validity and the generality of their conclusions. First, vibrational zero-point motion was not considered in that approach, which poses a fundamental problem in view of the fact that a vibrational mode at 1700 cm^{-1} that characterizes[26] certain relevant asymmetric double-well potentials with small activation barriers, contributes a zero-point energy of $\approx 4\ k_BT$ at ambient conditions. This supplementary energy could “lift” the proton above the underlying classical transition state and dramatically increase its delocalization. In the same vein, the errors introduced by the neglect of quantum corrections to classical anharmonicity effects were only approximately and inconsistently canceled by the use of finite basis set and

fictitious electron mass, therefore limiting the reliability of the conclusions drawn from a direct comparison with the present experimental frequencies. Finally, the infrared signature of the $F^- \cdot H_3O^+$ contact ion pair limiting form was not revealed by that study of dilute solutions of HF in water, leaving open the possibility that this species might be the dominant one, as previously advocated by Giguère et al.[21]

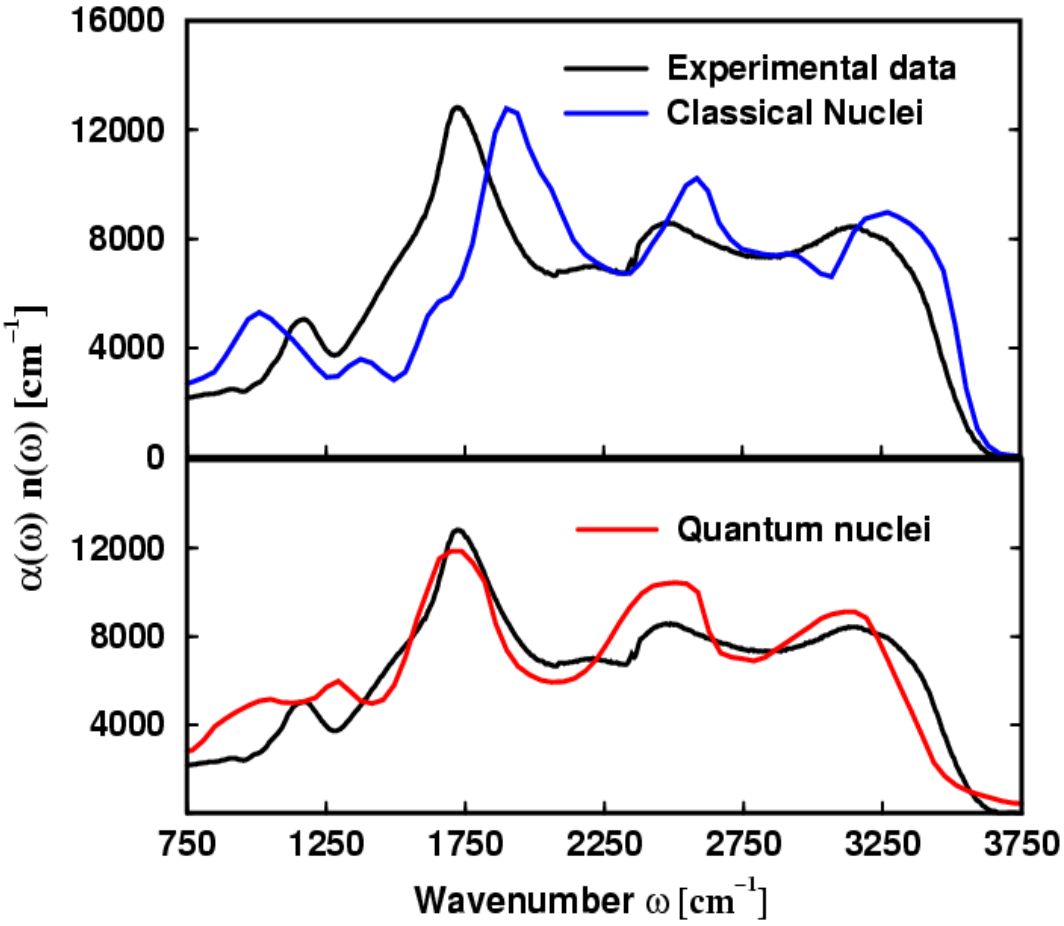

Figure 3-2. Absolute infrared absorption spectra of equimolar amorphous mixtures of HF and H_2O at 80 K. The experimental values (black trace) were obtained from raw reflection-absorption spectra by simulating the film-substrate system reflectivity using Fresnel relations and a value n_∞=1.35 for the optical index of refraction. Computational data were obtained using Car-Parrinello molecular dynamics in conjunction with either a Newtonian (blue trace) or an approximate quantum treatment (red trace) of the nuclear dynamics (see text). The excellent agreement between experiment and computation validates the simulation protocol and demonstrates that the chemical nature and concentration of the species that exist in our simulation box represent an adequate representation of the concentrated amorphous binary solid.

3.2.2 The continuum of absorption is generated by heterogeneous broadening of the shared-proton asymmetric stretching frequency.

In order to construct a detailed molecular-level model that can explain the experimental data displayed in Fig.3-1, we performed classical Car-Parrinello[27] molecular dynamics

simulations starting from five different initial atomic arrangements describing an equimolar amorphous mixture of HF and H_2O at 80K. By comparing and contrasting computed and experimental infrared absorption spectra obtained at cryogenic temperatures, we were able to identify which system, among the five that were considered, most closely matched the experimental composition for the equimolar mixture. Subsequently, we focused on this system and recomputed its IR absorption spectrum by including nuclear quantum corrections within the context of the *ab initio* molecular dynamics implementation[28] of the centroid molecular dynamics[29] theory.

With $\alpha(\omega)$ denoting the wavenumber-dependent Beer-Lambert absorptivity, $-1/\ell \cdot \ln(I/I_0)$, and $n(\omega)$ representing the index of refraction, Fig.3-2 compares the absolute values of the spectroscopic quantity $\alpha(\omega)n(\omega)$ that were computed from the raw reflection-absorption spectra of concentrated (0.5) amorphous mixtures of HF and H_2O at 80 K using our Fresnel reflectivity model, to those obtained from first principles molecular dynamics simulations. The excellent level of agreement between theory and experiment that is apparent from the results displayed in Fig.3-2 demonstrates that the microscopic composition of the system that was utilized in the first-principles simulations represents an adequate description of the amorphous binary solid prepared experimentally by simultaneous vapor condensation at 80K using molecular beams. Moreover, the moderate magnitude of the nuclear quantum effects on the infrared spectra suggests that the data gathered in the present classical simulations can meaningfully be used to understand the molecular origin of the experimental infrared spectra. It is worth mentioning that this aspect was not obvious prior to the simulation since nuclear quantum effects as large[30] as 600 cm^{-1} and anharmonicities on the

order[31,32] of 1000 cm^{-1} had previously been reported for the ionically H-bonded OH vibration in the chemically relevant gas-phase $F^- \cdot H_2O$ system.

Using the five simulations equilibrated within the classical mechanics framework, we have computed the mean frequency and the width of the infrared absorptions generated by the very intense shared-proton asymmetric stretching vibration for all structures that could be described as reactants, intermediates or products in reaction (1). We focused on these complexes as their very large transition dipole moments dominate the total infrared spectra. The vibration frequencies were computed using both the Newtonian and the approximate quantum (centroid) dynamics, and were tabulated as a function of $\delta = d(F-H) - d(O-H)$, where $d(A-B)$ is the distance between atoms A and B. The results obtained are shown in Fig.3-3 and suggest that the average value of the asymmetric proton stretch coordinate δ, which is a molecular measure of the degree of advancement of reaction (1), is strongly correlated to the shared-proton asymmetric stretching vibration frequency.

The correlation reported here is similar in spirit to the empirical relations found by Mikenda[33] and by others[34] between OH-stretching frequencies and H-bond lengths in solids and should find numerous applications. In particular, the quantitative correlation reported in Fig.3-3 could allow experimentalists to "photograph" the ionization of HF in the same way in which Mikenda's results allowed the pump-probe investigation[35] of the femtosecond dynamics of hydrogen bonds in liquid water. The broad distribution of δ's that was observed in the present simulations suggests that the chemical species appearing in reaction (1) are largely responsible for the continuous infrared absorption that ranges between 1300 and 2800 cm^{-1}. In the light of this data, the broadening appears to be largely inhomogeneous, being generated by a continuous distribution of metastable species sampling all intermediate geometries from the un-ionized $FH \cdot OH_2$ to the contact ion pair $F^- \cdot H_3O^+$ limiting structures.

3.2.3 A mechanism for acid ionization and the microscopic solvent reaction coordinate for proton transfer by a weak acid

In order to complete the present picture of hydrogen fluoride ionization in water, one must include a description of the solvation effects that are responsible for shifting the equilibria to the right in reaction (3.1). Visual investigation of the various proton transfer complexes obtained in our molecular dynamics simulations revealed an interesting correlation between the extent of proton transfer and the chemical nature of the first solvation shell, as illustrated in Fig.3-3. To understand the nature of this correlation, it is useful to divide the space of allowed values of the order parameter δ in three regions, corresponding to un-ionized, to proton-shared and to contact ion pair complexes, as indicated in colors in Fig.3-3. One should bear in mind however, that the precise definition of the boundaries separating proton-shared from un-ionized and from contact ion pair structures that was adopted in the present investigation is somewhat arbitrary. In particular, these boundaries are not dividing surfaces for slow, activated processes.

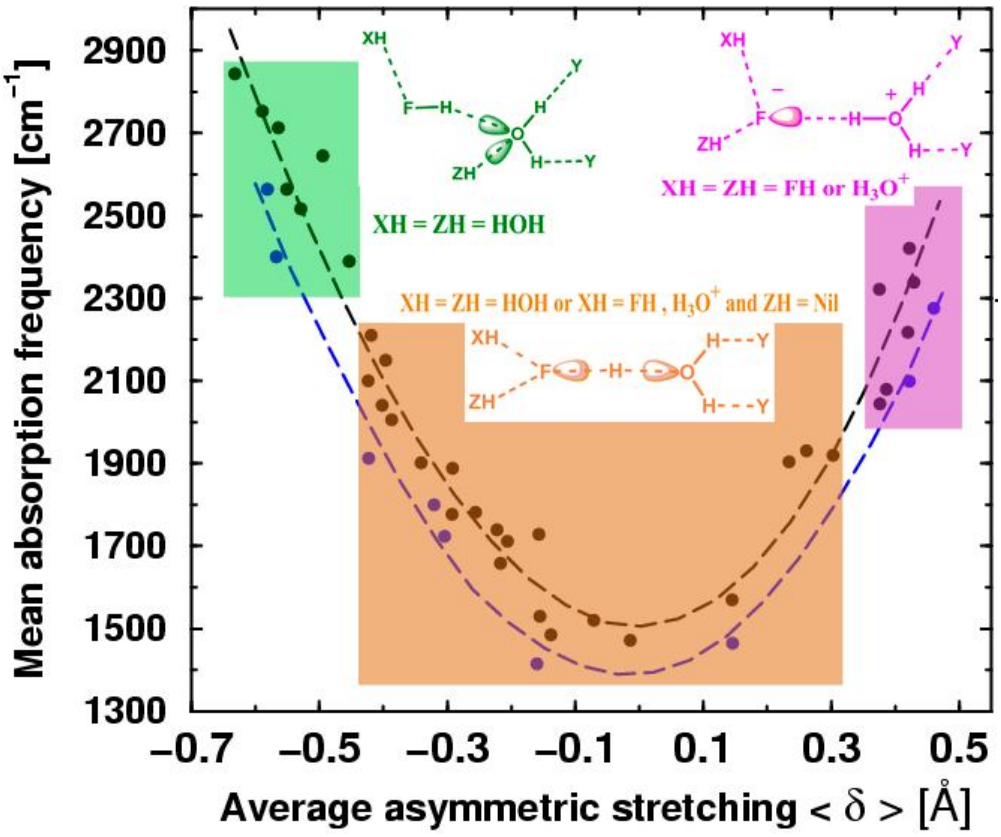

Figure 3-3. Fig.3-3 The mean infrared absorption frequency (filled circles) of shared-proton asymmetric stretching vibrations is correlated to the average value of δ (see text). The black points were obtained from classical simulations, while the blue ones correspond to centroid molecular dynamics data. The condensed-phase Brønsted basic character of the fluoride anion decreases during the ionization process. This decrease is correlated with changes in the number and the strength of the hydrogen-bond donors from the first solvation shell of the fluorine atom.

Using the *ad hoc* definition adopted in Fig. 3-3, the first important observation that can be formulated is that un-ionized $H_2O \cdot HF$ complexes appear to be unevenly solvated, with the HF molecule in a single donor-single acceptor (DA) H-bonding configuration, while the water molecule adopts a double donor-double acceptor (DDAA) binding motif. However, whenever a more symmetrical solvation pattern is reached, for example by transferring a weak H-bond donating molecule from the accepting water oxygen to the fluorine atom yielding a AAD and a ADD configuration for HF and H_2O respectively, a Zundel-like $F^- \cdot H^+ \cdot OH_2$ shared-proton dissociation intermediate is

formed. This result is consistent with the conclusions reached by Sillanpää et al.[36] who provided computational evidence suggesting that the fluorine atom increases its coordination number prior to the ionization of HF.

An interesting result that was revealed by the present low-temperature investigation is that proton-shared $F^- \cdot H^+ \cdot OH_2$ complexes can occasionally be stable in a solvation environment in which the coordination number of the oxygen atom is larger than that of the fluorine atom. However, this can only happen if the fluorine is solvated by a powerful H-bond donating molecule, such as a hydrogen fluoride HF, or a hydronium ion H_3O^+. In the same vein, it is important to mention that contact ion pairs of the form $F^- \cdot H_3O^+$, in which the proton has transferred completely to the oxygen atom, were not stable in our simulations unless the fluoride anion was solvated by at least one, and often two strong H-bond donating species. This observation is consistent with the *ab initio* molecular dynamics results previously reported by Iftimie et al.[25] and by Laasonen et al.[37] who were unable to find long-lived contact ion pairs $F^- \cdot H_3O^+$ in dilute solutions. In order to understand these findings, let us start by noting that the extent of proton transfer is a direct measure of the local condensed-phase proton affinity difference between a fluoride anion and a water molecule[14]. This proton affinity difference, which is largely in favor of the fluoride anion for the $H_2O \cdot HF$ cluster in the gas-phase as its HF stretching frequency of 3633.8 cm^{-1} testifies[38], cannot change its sign unless the condensed-phase environment acts to significantly reduce the proton affinity of fluoride. Our results suggest that such a reduction is possible provided that at least one powerful HB donor (i.e., HF or H_3O^+), and a weaker one (such as H_2O), are solvating the fluorine atom. Of course, it is highly improbable that such H-bonded topologies can be found in the first solvation shell of $H_2O \cdot HF$ complexes in binary solutions except in concentrated mixtures.

3.2.4 Assignment of the experimental spectral features

We are now in a position to propose a detailed molecular-level assignment of the broad peaks that appear between 1300 and 3400 cm^{-1} in Fig.3-2. Water molecules that are only solvated by weak H-bond donors and acceptors are exposed to an environment very similar to that of bulk water. Therefore, they are mostly responsible for the absorption that extends between 2800 and 3400 cm^{-1}. Un-ionized $H_2O \cdot HF$ complexes form stronger hydrogen bonds than those that are usually found in either pure water or pure HF and, according to the results displayed in Fig.3-3, absorb electromagnetic radiation between 2400 and 2800 cm^{-1}.

In contrast to the assignment proposed by Giguère[21] et al., our calculations suggest that $F^- \cdot H_3O^+$ contact ion pairs in an amorphous environment absorb infrared radiation with wavenumbers that fall in the 2000-2400 cm^{-1} range.

The results displayed in Fig.3-3 also indicate that $H_2O \cdot H^+ \cdot F^-$ proton-shared species are largely responsible for the surprisingly intense absorption extending between 1300 and 2000 cm^{-1}. These Zundel-like shared-proton complexes are only stable in a disordered condensed phase and owe their existence to local environments in which fluoride anions and water molecules display comparable proton affinities. Inspection of the data in Fig.3- 3 suggests that the structures that are responsible for these intense absorptions comprise FH or OH bonds on the verge of rupture, in which large amplitude proton motions and large vibrational transition dipoles are expected. It is therefore not surprising that these transitions display quantum anharmonic corrections amounting to a 200-300 cm^{-1} red-shift with respect to classical calculations, and that they are responsible for the largest features in the dipole autocorrelation spectra, while being hardly visible[33,34,39] in velocity autocorrelation spectra.

Although the focus of the present work has been on the infrared spectra of the ion pairs appearing in reaction (1), no analysis of the spectroscopic properties of HF solutions is complete without mentioning the bifluoride FHF^- ions. Such ions are indeed present in

our computational simulations of the amorphous equimolar mixtures and an analysis of the infrared absorption generated by their shared-proton asymmetric stretching vibration reveals the presence of a broad absorption ranging from 1200 to 2000 cm^{-1} whose maximum lies at 1600 cm^{-1}. These findings are consistent with the computational results[40] previously reported by Iftimie and Tuckerman for dilute solutions and with the experimental observations of KHF_2 solutions by Giguère et al.[21]

3.3 Conclusions and Outlook

In an effort to understand the infrared signature of various ion pairs, we have conducted an investigation of amorphous binary mixtures of water and HF, HCl or HBr at cryogenic temperatures. The absolute infrared spectra reported in the present investigation show the presence of extremely broad absorptions across the whole mid-IR range, which are usually considered to signal the presence of hydrated protons. We demonstrate that in the case of cryogenic hydrofluoric acid solutions, a significant part of this broad absorption is not only generated by free protons, but also by strongly hydrogen-bonded complexes between HF and H_2O, whose degree of ionization covers the entire spectrum from un-ionized species to contact ion pairs (see reaction 1). Moreover, our results suggest that the local extent of ionization can be understood in terms of how H-bonding topologies in the first solvation shell of $H_2O{\cdot}HF$ complexes affects the Brønsted acid-base properties of the fluoride anion and of the water molecule competing for the acidic proton.

As a general rule, the ionization process is promoted by a decrease in the condensed-phase proton affinity of the fluoride anion and by a concomitant increase in that of the water molecule. Our investigation reveals two mechanisms by which a fluoride ion can have its condensed-phase proton affinity decreased: either the number or the strength of the H-bond donating molecules from its first solvation shell must increase. In the same vein, we conclude that water molecules can increase their proton affinity either by decreasing their coordination number from 4 (DDAA topology) to 3 (DDA topology), or

by an increase in the H-bond acceptor propensity of those molecules to which it is coordinated. A direct consequence of this proton transfer mechanism is that the overall degree of ionization is predicted to increase with increasing concentration of HF, since these molecules can act as powerful H-bond donors. A larger degree of ionization will lead to an increase in the acidity constant as well as in the ionic mobility, therefore providing an alternative interpretation to the peculiar[18] increase in acidity displayed by HF solutions of increasing concentration at room temperature.

Last, but not least, it is important to emphasize that the use of cryogenic temperatures has been instrumental to the successful completion of the present investigation. On one hand, the experimental spectra reported here show a significantly increased degree of ionization with respect to room-temperature data allowing one to obtain reliable information about the behavior of ion pairs in dilute and concentrated solutions. On the other hand, the low thermal agitation ensures that atoms experience only moderate excursions about their quasi-equilibrium positions. Hence, the local degree of ionization and the composition of the first solvation shell do not change significantly on the computational simulation timescale, allowing one to investigate the relation between them, as well as their influence on infrared spectra.

3.4 Experimental and computational methods

3.4.1 Experimental approach.

Nanoscopic (h = 20 ML ~ 7.5 nm) films of homogeneous HF:H_2O binary amorphous solids having various concentrations were prepared using simultaneous dosing with two molecular beams on a clean Pt(111) single crystal held at 80K by a closed-cycle helium cryostat in ultra-high vacuum. The molecular beam fluxes are calibrated using thermal desorption mass spectrometry of precisely controlled quantities of both species on Pt(111) from which we define one monolayer as the substrate saturation coverage (θ_{HF} and θ_{H_2O})[17]. Film compositions are reported in monolayer fractions =

$\theta_{HF} / (\theta_{HF} + \theta_{H_2O})$. Their vibrational spectra were recorded at grazing incidence (θ_{IR}=85°) using unpolarized light from a commercial FTIR spectrometer in a specular reflection-absorption geometry. Absorbance spectra for these ultrathin films present contributions from optical interference effects, as well as absorption, both of which are modulating the reflectivity of the substrate-film system. To minimize the optical distortions due to interference effects, we recorded spectra for films having the same optical thickness (i.e., $n_\infty \cdot h \cdot \cos\theta_{IR}$), but having different relative amounts of HF and H_2O. Absorbance spectra [i.e., -log $R(\omega)/R_o(\omega)$] for our samples were numerically evaluated by calculating the reflectivity of the Pt(111) substrate [i.e., $R_o(\omega)$] and of the film-substrate systems [i.e., $R(\omega)$] using Fresnel relations. Empirical optical parameters [i.e., $k(\omega)$ and $n(\omega)$] were obtained iteratively by least-square fitting simulated Fresnel spectra to experimental absorbance data. The incompleteness of the Kramers-Kronig transform has only negligible effects in the lower portion of the spectra (<700cm^{-1}) due to poorer signal to noise. In our experiments, while the total number of layers deposited is very well known and controlled very accurately, neither the absolute film thickness, nor the density of the cryogenic solutions are known. Furthermore, the optical index of refraction is not known for aqueous solutions of HF at any temperature. A detailed sensitivity analysis of the Fresnel model was performed and the best results were obtained by calculating the relative film thicknesses for different concentrations using the density of liquid hydrofluoric acid solutions and to determine the best optical index of refraction to match the cryogenic binary amorphous films absorbance in the transparent portion of the spectra (i.e., 4000-8000 cm^{-1}).

A similar procedure was employed for mixtures of H_2O and HCl, or HBr. However, as these molecules dissociatively adsorb on Pt(111), we relied on the films optical thickness (i.e., interferometry) for molecular beam flux calibrations: 20 ML thick HCl or HBr films were defined as samples having the same interference pattern as that of a 20 ML thick amorphous solid water film in the transparent portion of the spectra (indices of refraction in the neat liquid phases are n_∞=1.3287 for HCl, n_∞=1.325 for HBr and 1.33

for H_2O). The small and sharp features that appear near 2100cm^{-1} in the experimental spectra are due to trace CO chemisorbed on the Pt(111) substrate and the doublet near 2350cm^{-1} is due to CO_2(g) in the purge gas.

3.4.2 Computational methods and their accuracy

Herein we employ the Car-Parrinello[27] approach to describe electric polarization and bond-breaking/bond forming effects. The simulations were performed using density functional theory,[41] the B-LYP generalized gradient exchange[42]-correlation[43] functional, plane wave basis sets, and norm-conserving Troullier-Martin[44] pseudopotentials. The plane wave basis set cutoff was taken to be 100 Ry, and a fictitious electron mass μ=246 a.u. in conjunction with an integration time step Δ=0.06 fs were utilized for the classical nuclei calculations. By taking room-temperature pure liquid water as a test case, we verified that the influence of the finite basis set and of the non-zero fictitious mass on the position of the maximum of absorption of room-temperature water were smaller than 40 cm^{-1}, which was the typical statistical resolution of the present classical simulations on the wavenumber axis.

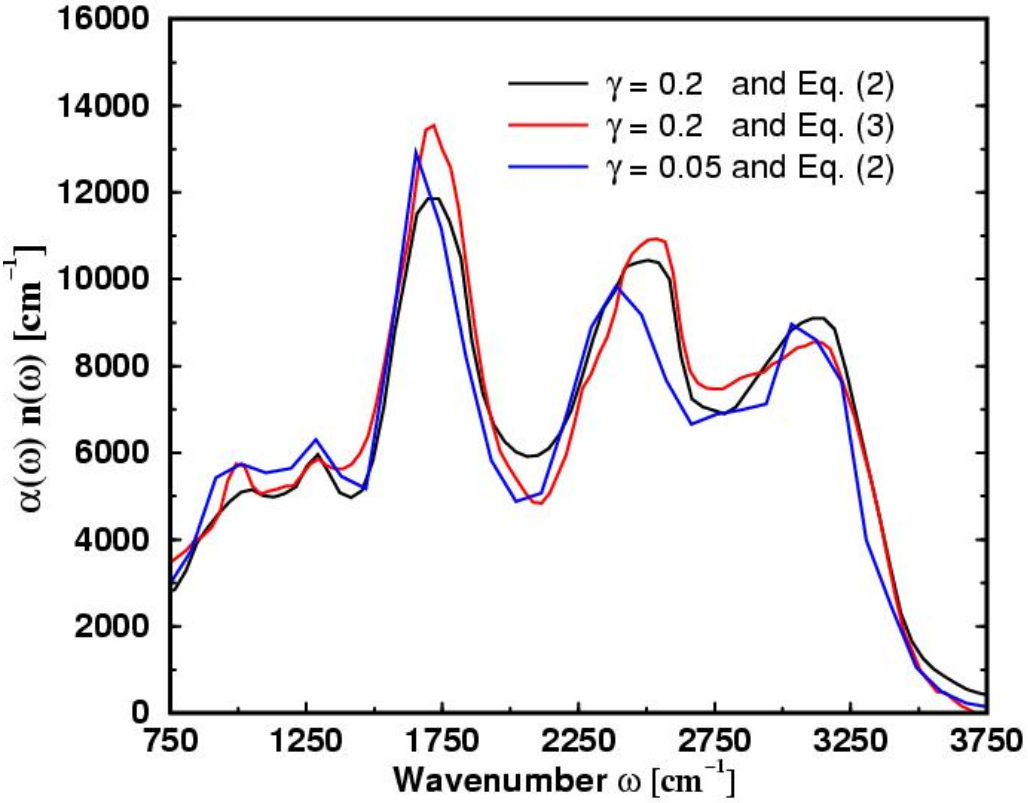

Figure 3-4. The total infrared spectrum of the amorphous monohydrate computed using the centroid molecular dynamics formalism (CMD) by assuming that the electronic dipole moment is a linear operator. Within this linear operator approximation the dipole moment centroid symbol of the CMD formalism can be calculated by employing either Eq. (3.2) or Eq. (3.3) and the resulting autocorrelation spectra should be identical. The actual differences between the spectra computed by using Eq. (3.2) and Eq.(3.3) are smaller than the statistical error bars of the simulation, suggesting that the electron dipole moment can approximately be treated as a linear operator without limiting the purpose of the present IR spectrum calculations. The figure also compares and contrasts the IR spectrum obtained with 2 values of the adiabaticity parameter γ (see text), suggesting that the magnitude of the nuclear quantum effects that can be deduced from Fig.3-2 and Fig.3-3 are likely to be underestimated by 50-100 cm^{-1}.

Absolute infrared absorption spectra were computed from the trajectory of the total dipole moment using the Berry phase approach[45], linear response theory[46], and the Kramers-Kronig relations[46] using a practical method[40] recently developed by one of us. Zero-point vibration and hydrogen tunneling effects are included within the framework of the centroid[29] molecular dynamics theory, which has been demonstrated[47] to

significantly improve IR spectrum calculations beyond the so-called "harmonic approximation". Within the limits of applicability of the centroid molecular dynamics theory, Voth et al. have demonstrated[19] that one can compute quantum time-auto-correlation functions by calculating single-time centroid symbol autocorrelation functions provided that the correlations involve operators that are linear combinations of Cartesian coordinates or momenta. Unfortunately, this is not the case for the electronic dipole moment, implying that a rigorous application of the centroid molecular dynamics theory should involve calculations of multiple-time[48] centroid symbol correlation functions, which are challenging to implement both at a theoretical and at a practical level in the present case.

The results displayed in Figs. 3-2 and 3-3 were computed from the autocorrelation of an approximate dipole moment centroid symbol $\mu_c(t)$, which was taken to be the instantaneous value of the average dipole moment, with the average being taken over all path-integral quasi-particles:

$$\mu_c(t) \cong \frac{1}{N}\sum_i \mu\ (\mathbf{R}_i;t) \tag{2.75}$$

The magnitude of the approximation introduced by the use of equation (2) can be gauged from the results displayed in Fig.3-4, where the total infrared spectrum computed within the limits of the above-mentioned approximation are contrasted with the IR results computed by approximating $\mu_c(t)$ by the value of the dipole moment computed using the coordinates of the center-of-mass normal mode:

$$\mu_c(t) \cong \mu\left(\frac{1}{N}\sum_i \mathbf{R}_i;t\right) \tag{2.76}$$

These results suggest that the reliability of the quantum spectra displayed in Figs. 3-2 and 3-3 is more likely to be limited by the fundamental approximation[19] of the centroid molecular dynamics theory, as well as by its present practical implementation, and only to a smaller extent by the nonlinear nature of the electronic dipole moment operator.

The approximate quantum nuclei calculations were performed using 16 discrete path-integral[29] replicas. The number of quasi-particles chosen in the present investigation represents a compromise between accuracy and computational cost, being consistently found close to the convergence limit in *ab initio* molecular dynamics investigations of similar systems: gas-phase $F^- \cdot H_2O$ clusters, gas-phase[49] and liquid phase[32] HF multimers, and excess proton in liquid water.[50]

A normal mode representation of path integrals was employed, with the centroid position of each atom defined as the zero-frequency mode of the corresponding quasi-particle chain. An adiabaticity parameter γ=0.2 was employed following the suggestions of Marx[28] et al. based on their studies of gas-phase quasi-harmonic (H_2) and relatively anharmonic (Li_2) diatomic potentials. Since this value of the adiabatic parameter is somewhat larger than the converged values (typically γ=0.06) reported by Voth et al. in their studies of excess proton in water, we have performed a shorter (1.5 ps), but significantly more computer-intensive simulation with γ=0.05, by starting from the same initial equilibrated configuration as the γ=0.2 investigation.

The short duration of the simulation that employs the smaller value of γ limits the statistical resolution of the calculated infrared spectra to 100 cm^{-1} for the wavenumber axis, and precludes a detailed analysis as the one shown in Fig.3-3. Nevertheless, one can see from the results displayed in Fig.3-4 that the total infrared spectrum computed by employing γ=0.05 is quite similar to the one obtained with γ=0.2, with estimated red-shifts of 50 cm^{-1} for the broad absorptions centered at 1670 cm^{-1} and at 3200 cm^{-1}. The magnitude of this red-shift is consistent with the one reported by Marx et al.[28] for similar changes in the value of γ, and is insignificant within the statistical resolution of our γ=0.05 simulation. In contrast, by reducing the value of the adiabaticity parameter γ, the absorption centered at 2450 cm^{-1} appears to be red-shifted by 100 cm^{-1}. This value of the red-shift is at the limit of resolution in our γ=0.05 simulation, and suggests that the quantum corrections to the proton stretching vibrational frequencies shown in Fig.3-

2 and in Fig.3-3 might be slightly underestimated in the case of un-ionized $H_2O \cdot HF$ complexes.

We have ensured that the forces on the electronic coefficients remained as small in the centroid molecular dynamics calculations as they were in the Newtonian calculations by employing μ=34 a.u. for the fictitious electron mass and Δ=0.02 fs for the integration time step in the γ=0.2 simulation, and by employing μ=3.06 a.u. and Δ=0.006 fs in the γ=0.05 simulation. All calculations were carried out using the PINY MD[51] simulation package. The simulations involved systems comprising 16 fluorine and 16 oxygen atoms, and employed periodic boundary conditions. The dimensions of the simulation boxes respected the values of the respective system densities at room temperature. Classical simulations involved a relatively long annealing and equilibration period of 80 ps followed by data collection for 20 ps. Quantum simulations were equilibrated for 10 ps using the staging-variable implementation[52] of the imaginary-time path-integral *ab initio* molecular dynamics formalism, followed by data collection within the adiabatic centroid molecular dynamics approach. Data collection involved a period of 10 ps in the case of the γ=0.2 and 1.5 ps in the case of γ=0.05 simulation.

The data from Fig.3-3 was obtained by computing cross-correlation spectra between the trajectory of the total dipole moment and that of the normal mode $\delta = d(F-H) - d(O-H)$ for selected pairs of fluorine and oxygen atoms, where $d(A-B)$ represents the distance between atoms A and B (classical case) or that between their centroids (quantum case).

3.5 Acknowledgments

R.I. and P.A. acknowledge financial support from the Natural Sciences and Engineering Research Council of Canada, from the Fonds Québécois de la Recherche sur la Nature et les Technologies, and from the Canadian Foundation for Innovation. The Réseau Québécois de Calcul de Haute Performance is acknowledged for allowing us to perform the calculations.

3.6 Reference

(1) Decoursey, T. E. *Physiol. Rev.* 2003, *83*, 475.

(2) (a) Garczarek, F.; Brown, L. S.; Lanyi, J. K.; Gerwert, K. *Proc. Natl. Acad. Sci. USA* 2005, *102*, 3633. (b) Garczarek, F.; Gerwert, K. *Nature* 2006, *439*, 109.

(3) (a) Mathias, G.; Marx, D. *Proc. Natl. Acad. Sci. USA* 2007, *104*, 6980. (b) Rousseau, R.; Kleinschmidt, V.; Schmitt, U.W.; Marx, D. *Angew. Chem. Int. Ed.* 2004, *43*, 4804.

(4) Mohammed, O. F.; Pines, D.; Dreyer, J.; Pines, E.; Nibbering, E. T. J. *Science* 2005, *310*, 83.

(5) (a) Buch, V.; Milet, A.; Vácha, R.; Jungwirth, P.; Devlin, J. P. *Proc. Natl. Acad. Sci. USA* 2007, *104*, 7342. (b) Buch, V.; Sadlej, J.; Aytemiz-Uras, N.; Devlin, *J.P. J. Phys. Chem. A* 2002, *106*, 9374.

(6) Ando, K.; Hynes, J. T. *J. Phys. Chem. B* 1997, 101, 10464. Ando, K.; Hynes, J. T. *J. Phys. Chem. A* 1999, *103*, 10398.

(7) Marcus, R. A. *J. Chem. Phys*. 1965, *43*, 679.

(8) Zundel, G. *The Hydrogen Bond: Recent Developments in Theory and Applications;* Elsevier, New York, 1976.

(9) Marx, D.; Tuckerman, M. E.; Hutter, J.; Parrinello, M. *Nature* 1999, *397*, 601.

(10) Schmitt, U. W.; Voth, G. A. *J. Chem. Phys*. 1999, *111*, 9361.

(11) (a) Woutersen S, Bakker, H. J. *Phys. Rev. Lett.* 2006, *96*, 138305. (b) Chandra, A.; Tuckerman, M.E.; Marx, D. *Phys. Rev. Lett.* 2007, *99*, 145901.

(12) Asmis, K. R.; Pivonka, N. L.; Santambrogio, G.; Brümmer, M.; Kaposta, C.; Neumark, D. M. *Science* 2003, *299*, 1375.

(13) Headrick, J. M.; Diken, E. G.; Walters, R. S.; Hammer, N. I.; Christie, R. A.; Cui, J.; Myshakin, E. M.; Duncan, M. A.; Johnson, M. A.; Jordan, K. D. *Science* 2005, *308*, 1765.

(14) Roscioli, J. R.; McCunn, L. R.; Johnson, M. A. *Science* 2007, *316*, 249.

(15) Delzeit, L.; Rowland, B.; Devlin, J. P. *J. Phys. Chem.* 1993, *97*, 10312.

(16) Mathias, G.; Marx, D. *Proc. Natl. Acad. Sci. USA*. 2007, *104*, 6980.

(17) Ayotte, P.; Hébert, M.; Marchand, P. *J. Chem. Phys.* 2005, *123*, 184501.

(18) Hyman, H. H.; Kilpatrick, M.; Katz, J. J. *J. Am. Chem. Soc.* 1957, *79*, 3668.

(19) Jang, S.; Voth, G. A. *J. Chem. Phys.* 1999, *111*, 2371.

(20) Zundel, G. *Adv. Chem Phys.* 2000, *111*, 1.

(21) Giguère, P. A.; Turrell, S. *J. Am. Chem. Soc.* 1980, *102*, 5473.

(22) Eigen, M. *Angew. Chem. Int. Ed. Engl*. 1964, *3*, 1.

(23) (a) Leuchs, M.; Zundel, G. *Can. J. Chem*. 1980, *58*, 311. (b) Leuchs, M.; Zundel, G. *Can. J. Chem*. 1980, *58*, 2118.

(24) (a) Max, J. J.; Chapados, C. *J. Phys. Chem. A* 2004, *108*, 3324. (b) Max, J. J.; Chapados, C. *J. Phys. Chem. A* 2002, *106*, 6452.

(25) Iftimie, R.; Tuckerman, M. E. *Angew. Chem. Int. Ed.* 2006, *45*, 1144.

(26) (a) Roscioli, J. R.; Diken, E. G.; Johnson, M. A.; Horvath, S.; McCoy, A. B. *J. Phys. Chem. A* 2006, 110, 4943. (b) Yates, B. F.; Schaefer, H. F.; Lee, T. J.; Rice, J. E. *J. Am. Chem. Soc.* 1988, *110*, 6327.

(27) Car, R.; Parrinello, M. *Phys. Rev. Lett*. 1985, *55*, 2471.

(28) Marx, D.; Tuckerman, M. E.; Martyna, G. J. *Comp. Phys. Comm.* 2000, *118*, 166.

(29) Jang, S.; Voth, G. A. *J. Chem. Phys*. 1999, *111*, 2357.

(30) Schenter, G. K.; Garrett, B. C.; Voth, G. A. *J. Chem. Phys*. 2000, *113*, 5171.

(31) Yates, B. F.; Schaeffer, H. F.; Lee, T. J.; Rice J. E. *J. Am. Chem. Soc.* 1988, *110*, 6327.

(32) Swalina, C.; Wang, Q.; Chakraborty, A.; Hammes-Schiffer, S. *J. Phys. Chem. A* 2007, *111*, 2206.

(33) Mikenda, W. *J. Mol. Struct*. 1986, *147*, 1.

(34) Novak, A. *Structure and Bonding*; Springer-Verlag: Berlin, 1974, p. 177.

(35) Gale, G. M.; Gallot, G.; Hache, F.; Lascoux, N.; Bratos, S.; Leicknam, J. C. *Phys. Rev. Lett*. 1999, *82*, 1068.

(36) Silanpää, A. J.; Simon, C.; Klein, M. L.; Laasonen, K. *J. Phys. Chem. B* 2002, *106*, 11315.

(37) Laasonen, K.; Klein, M. L. *Mol. Phys*. 1996, *88*, 135.

(38) Bulychev, V. P.; Grigoriev, I. M.; Gromova, E. I.; Tokhadze, K. G. *Phys. Chem. Chem. Phys*. 2005, *7*, 2266.

(39) Laasonen, K.; Larrucea, J.; Silanpää, A. *J. Phys. Chem. B* 2006, *110*, 12699.

(40) Iftimie, R.; Tuckerman, M. *J. Chem. Phys.* 2005, *122*, 214508.

(41) Koch, W.; Holthausen, M. C. *A Chemist's Guide to Density Functional Theory*: VCH, New York, 2000.

(42) Becke, A. *Phys. Rev. A* 1998, *38*, 3098.

(43) Lee, C.; Yang, W.; Parr, R. G. *Phys. Rev. B* 1998, *37*, 785.

(44) Trouillier, N.; Martins, J. L. *Phys. Rev. B* 1991, *43*, 1993.

(45) a) King-Smith, R. D.; Vanderbilt, D. (1993) *Phys. Rev. B* 1993, *47*, 1651. b) Vanderbilt, D.; King-Smith, R. D. *Phys. Rev. B* 1993, *48*, 4442.

(46) Kubo, R.; Toda, M.; Hashitsume, N. *Statistical Physics II* : 2nd ed., Springer, New York, 1991.

(47) Ramírez R.; López-Ciudad T.; Kumar P.; Marx D. *J Chem. Phys*. 2004, *121*, 3973.

(48) Reichman, D. R.; Roy, P. N.; Jang, S.; Voth, G. A. *J Chem. Phys.* 2000, *113*, 919.

(49) Raugei, S.; Klein, M. L. *J. Am. Chem. Soc.* 2003, *125*, 8992.

(50) (a) Straus, J. B.,; Calhoun, A.; Voth, G. A. *J. Chem. Phys.* 1995, *102*, 529. (b) Wu, Y.; Chen, H.; Wang, F.; Paesani, F.; Voth, G. A. *J. Phys. Chem. B* ASAP 10.1021/jp076658h. (c) Tuckerman, M. E.; Marx, D.; Klein, M. L.; Parrinello, M. *Science* 1997, *275*, 817.

(51) Tuckerman, M. E.; Yarne, D. A.; Samuelson, S. O.; Hughes, A. L.; Martyna, G. J. *Comput. Phys. Commun*. 2000, *128*, 333.

(52) Tuckerman, M. E.; Marx, D.; Klein, M. L.; Parrinello M. *J. Chem. Phys.* 1996, *104*, 5579.

Towards Understanding the Dissociation of Weak Acids in Water: 1. Using IR Spectroscopy to Identify proton-Shared Hydrogen Bonded Ion-Pair Intermediates

Vibin Thomas* Radu Iftimie*,§,¶

* *Département de Chimie, Université de Montréal, CP 6128, succursale Centre-Ville, Montréal, H3C3J7, Canada* §*To whom correspondence may be addressed.*

Published in *J. Phys. Chem. B* **113** (13):4152-60 (2009)

Abstract: Cryogenic conditions favor the formation of ion-pair dissociation intermediates in amorphous mixtures of HF and H_2O, making possible their characterization by means of infrared spectroscopy. The experimental infrared spectra show a structurally rich "continuous" absorption ranging from 1000 to 3400 cm^{-1}, which, in principle, contains important information regarding the microscopic structure of the aforementioned dissociation intermediates. Herein, we demonstrate that this microscopic information can be extracted by comparing and contrasting experimental spectra with those obtained by means of carefully designed first-principles molecular dynamics calculations. Very good, systematic agreement between theoretical and experimental spectra can be obtained for HF/H_2O mixtures of various compositions, revealing the presence of proton-shared, dissociation intermediates $F^{\delta-}\cdots H\cdots^{\delta+}OH_2$. The existence of similar proton-shared, hydrogen-bonded intermediates of ionization, that are stable in solution, but not in the gas phase, has been previously suggested by other groups, using, among other techniques, low temperature NMR data and aprotic, dipolar, solvents. Our investigation reveals that similar structures are also stable in aqueous solutions of HF. We discuss some of the implications of the present findings as far as the mechanism of dissociation of weak acids is concerned.

4. Towards Understanding the Dissociation of Weak Acids in Water: 1. Using IR Spectroscopy to Identify proton-Shared Hydrogen Bonded Ion-Pair Intermediates

4.1 Introduction

Proton transfer and migration are fundamental processes in chemistry[1] and biology[2]. Despite their ubiquitous nature and intense research scrutiny, insights into the microscopic mechanisms that facilitate proton transfer between Brønsted donors and acceptors are largely lacking. In particular, the exact nature of proton donor and acceptor intermediates is lacking even for relatively simple acid-base neutralization reactions that take place in bulk water, although progress has been reported recently using experimental[3,4] as well as computational approaches.[5,6,7]

Important insights into the dynamics of acid-base proton transfer reactions can be obtained by probing the underlying hydrogen-bond network with mid-infrared (IR) electromagnetic radiation. Acid-base reaction intermediates can be probed by IR spectroscopy provided that their signal can be de-convoluted from that of the background solvent, reactant and product species. In general, this is challenging to achieve by means of conventional steady-state spectroscopy methods because typical proton transfer intermediates have small equilibrium concentrations, and lack specific absorption signatures. This problem can be alleviated by using time-resolved IR spectroscopy approaches. In particular, Nibbering et al.[3], and Bakker et al.[4] have recently demonstrated that ultrafast pump-probe spectroscopy can be successfully employed to investigate details of the aqueous dissociation mechanism in solutions of photoacids. Nevertheless, it is not clear whether the general kinetic picture that can be

extracted from these excited-state reactions is completely general[8], and, in particular, if the dissociation mechanism is representative[9] for ground-state neutralization reactions.

A different avenue has recently been explored by Ayotte et al.[10] who found that very low temperature amorphous mixtures of hydrofluoric acid (HF) and water (H_2O) show spectroscopic features that are similar, but not identical, to those of fully dissociated acids. Using a combination of experimental and computational approaches, Iftimie, Ayotte, and their collaborators, have recently provided evidence[11] that cryogenic temperatures favour the formation of significant quantities of ion-pair intermediates $F^- \cdot H^+ \cdot OH_2$ of the dissociation reaction

$$FH + H_2O \rightleftharpoons [F^- \cdot H^+ \cdot OH_2] \rightleftharpoons F^- + H_3O^+ \qquad (4.1)$$

These dissociation intermediates could be stabilized in the cryogenic mixture either by kinetic trapping, or simply due to the diminishing role played by ionization/dissociation entropy effects with decreasing temperature.[12,13] The investigation by Iftimie et al.[11] was limited to the study of equimolar mixtures of HF and H_2O and one could wonder whether the conclusions reached there remain relevant in a more traditional solvent/solute scenario, which implies an excess of a chemical species over the other. The present investigation compares and contrasts experimental and computed IR spectra for cryogenic mixtures of HF and H_2O ranging from 20% to 98% mole fraction in HF. The theoretical methods combine first-principles molecular dynamics[14] calculations of the Beer-Lambert absorptivity with a spectrum decomposition approach[15] based[16] on maximally-localized Wannier orbitals. Vibrational zero-point motions as well as incoherent tunneling effects are approximately included within the framework of the centroid molecular dynamics approach[17], which has been demonstrated[11,18] to result in an improved description of proton mobility and vibrational anharmonicity effects in condensed-phase simulations. In agreement with

the results formulated by Iftimie and Tuckerman in their study[19] of very dilute HF in H_2O at room-temperature, we conclude that the formation of proton-shared ion pair intermediates $F^- \cdot H^+ \cdot OH_2$ is omnipresent, with the exception, perhaps, of very concentrated solutions, in which the solvent is constituted entirely of HF molecules.

The existence of similar proton-shared, low barrier, hydrogen-bonded intermediates of ionization, that are stable in solution, but not in the gas phase, has been previously advocated by several research groups in chemical[13] as well as biochemical[20] contexts. Limbach et al., for example, have employed[13,21] low temperature NMR data in conjunction with special aprotic, but dipolar solvents and interpreted their experimental results as suggesting that proton shared structures of the form $A^{\delta-} \cdots H \cdots B^{\delta+}$ correspond often to stable intermediates rather than to transition states. Our study demonstrates that similar intermediate structures can also be relevant in aqueous solutions. It is important to note that this conclusion does not contradict the conventional wisdom[2] that low barrier, proton-shared hydrogen bonds are unstable in polar environments. The aforementioned low-barrier hydrogen bonds usually refer to structures that are symmetric in gas-phase, but in which the proton should become localized in polar solvents due to asymmetric solvation. As will become obvious later in this paper, the proton-shared structures $F^{\delta-} \cdots H \cdots OH_2^{\delta+}$ that are relevant for the present study are not symmetric in gas-phase, and must be asymmetrically solvated in order to be stable.

The present paper starts with a detailed presentation of the theoretical methods employed. We investigate the precision of the computational approach, by testing the convergence of the theoretical spectra with respect to the values of the fictitious electron mass, and of the plane wave basis set cutoff, in the case of pure, liquid H_2O, and pure, liquid, and solid, HF. The agreement between experiment and well-converged theory in

the case of these pure, condensed-phase systems turns out to be quite good. We will use this to indicate that the present computational protocol is likely to be equally reliable in the case of the cryogenic, amorphous mixture calculations.

Since there is no information on the nature of the molecular species that are present in the cryogenic conditions of the experiments[10] that our work is referring to, the present calculations will involve multiple simulations, starting from different initial conditions. By comparing and contrasting the results from our simulations with experimental data from reference 10, we are able to assign all the important features of the broad, mid-infrared absorption that covers the 1000 to 3400 cm^{-1} interval. Our results indicate that the surprisingly broad and intense absorption extending from 1400 to 2000 cm^{-1}, that distinguishes the cryogenic[16] from the room-temperature[22] mixtures, signals the presence of proton-shared complexes $F^- \cdot H^+ \cdot OH_2$ in which fluoride anions and water molecules display similar, but not necessarily equal, condensed-phase proton affinities. These proton-shared structures are intermediates in the ionization process depicted in reaction (1), being stabilized by distinctive first solvation shell H-bonding topologies and by long-range electrostatic interactions.

4.2 Computational Methods and Their Reliability

Herein we employ the Car-Parrinello (CP) approach[14] to describe electronic polarization and bond-breaking/bond-forming effects. In the CP approach, the nuclear trajectory is generated with forces generated from electronic structure calculations performed on the fly as the simulation proceeds, employing a density functional[23] description of the electronic structure. An initially minimized set of orbitals is "propagated" from one nuclear configuration to the next via a fictitious dynamics as opposed to an explicit minimization or diagonalization. Taking n to be the number of occupied orbitals, N the

number of nuclei, $\psi_1(\mathbf{r},t),\cdots,\psi_n(\mathbf{r},t)$ the electronic orbitals, and $R_1(t),\cdots,R_n(t)$ the nuclear positions, the CP equations of motion are

$$\begin{aligned} \mu\ddot{\psi}_i(\mathbf{r},t) &= -\frac{\delta E}{\delta\psi_i^*(\mathbf{r},t)} + \sum_j \Lambda_{ij}\psi_j(\mathbf{r},t) \\ M_I\ddot{\mathbf{R}}_I &= -\frac{\partial E}{\partial \mathbf{R}_I} \end{aligned} \tag{4.2}$$

Where $E = E[\{\psi\},\{R\}]$ is the energy functional, Λ_{ij} are set of Lagrange multipliers used to maintain the orthogonality of the orbitals via a constraint, and μ is the fictitious electron mass, which determines the time scale on which the fictitious orbital dynamics occurs. The simulations are performed using the B-LYP generalized gradient exchange[24]-correlation[25] functional, plane wave basis sets, and norm-conserving Troullier-Martins[26] pseudopotentials.

4.2.1 Linear response theory and the centroid approximation.

Using the time-correlation formalism[27] of linear response theory,[28] the value of the frequency-dependent Beer-Lambert absorptivity coefficient $\alpha(\nu)$ can be written as

$$\begin{aligned} \alpha(\nu) \overset{\text{def}}{=} -\frac{\ln(I/I_0)}{\ell} &= \frac{\pi\nu\left[1-\exp\left(-\beta\hbar 2\pi\nu\right)\right]}{3\hbar c V n(\nu)\varepsilon_0} \cdot \\ &\cdot\int_{-\infty}^{\infty}\exp(2\pi i\nu\tau)\left\langle\hat{M}(0)\cdot\hat{M}(\tau)\right\rangle_{qm} d\tau \end{aligned} \tag{4.3}$$

where qm indicates a quantum mechanical ensemble average, ℓ is the length of the optical path, α has Neperian units, $\hbar$ is Planck's constant, V is the sample's volume, ε_0 is the vacuum permittivity, and c is the speed of light. In Eq. (4.3), $\hat{M}(0)$ and $\hat{M}(\tau)$ represent the values of the quantum-mechanical dipole moment operator written in the

Heisenberg representation at times $t = 0$ and $t = \tau$, respectively, and are defined using Système International (SI) charge units; $\beta = 1/(kT)$ with k being Boltzmann's constant and T the temperature of the system. For condensed-phase systems such as those of interest in this paper, explicit eigenstate calculations have a far too high computational overhead to be carried out, while direct, real-time, path-integral approaches suffer from such severe phase oscillations that convergence cannot be achieved on any realistic time scale. In contrast, classical molecular dynamics can often be used to obtain the analogous correlation functions for a corresponding classical system. However, there is no general prescription for rigorously relating a quantum correlation function to a classical one. The precise relationship depends on the underlying Hamiltonian generating the dynamics.

Nevertheless, if one assumes the validity of the central approximation[17] of the centroid molecular dynamics theory, and considers that the electronic dipole moment operator is approximately linear[29], the Beer-Lambert absorptivity can be computed as

$$\alpha(\nu) \cong \frac{\beta}{6n(\nu)Vc\varepsilon_0} \int_{-\infty}^{\infty} \exp(2\pi i\nu\tau) \left\langle \dot{M}_c(0) \cdot \dot{M}_c(\tau) \right\rangle_c d\tau \qquad (4.4)$$

where the autocorrelation function involves the centroid average[17] of the time-derivative of the dipole moment centroid symbol.[17] Moreover, since centroid averages are computed in practice[30] by means of a finite number of path-integral quasi-particles, one can adopt a further approximation, which consists of considering a single imaginary-time discretization of the quasi-particle chain. This amounts essentially to adopting the well-known harmonic approximation[31] which reads

$$\alpha(\nu) \cong \frac{\beta}{6n(\nu)Vc\varepsilon_0} \int_{-\infty}^{\infty} \exp(2\pi i\nu\tau) \left\langle \dot{M}_{cl}(0) \cdot \dot{M}_{cl}(\tau) \right\rangle_{cl} d\tau \qquad (4.5)$$

where "cl" refers here to classical (i.e.: Newtonian) time-derivatives of the dipole moment, and to classical ensemble averages (i.e.: phase-space integration).

Our approach in the present work is to adopt the computationally less expensive harmonic approximation in most of the calculations. The significantly more time-consuming centroid molecular dynamics approach will only be employed once, to estimate the effects of nuclear quantum effects on IR spectra for the cryogenic, amorphous monohydrate (i.e.: 50% HF, 50% H_2O). Anticipating the results[11] that will be presented in more detail later in this paper, we find that nuclear quantization amounts to red-shifting the entire spectrum ranging from 1300 to 3400 cm^{-1} by 200-300 cm^{-1}, without inducing significant distortions to the shape of the absorption bands. The moderate magnitude of the nuclear quantum effects will therefore be used to justify, *a posteriori*, conclusions that will be drawn based on the results of classical (i.e.: Newtonian) simulations.

4.2.2 The influence of the fictitious electron mass and of the plane wave cutoff in Car-Parrinello molecular dynamics calculations of IR spectra

Our simulation protocol involves the use of a number of approximations, whose impact on the accuracy of the computed spectra has not been adequately reported in the literature. In particular, the qualitative effect of the non-zero Car-Parrinello fictitious electron mass μ that appears in Eq. (2), and that of a finite plane-wave basis set cutoff on infrared spectra have been documented previously[15]. Nevertheless, the published literature does not contain sufficient quantitative data to allow one to make a choice of the aforementioned parameters that is consistent with a predefined desired resolution of the spectra.

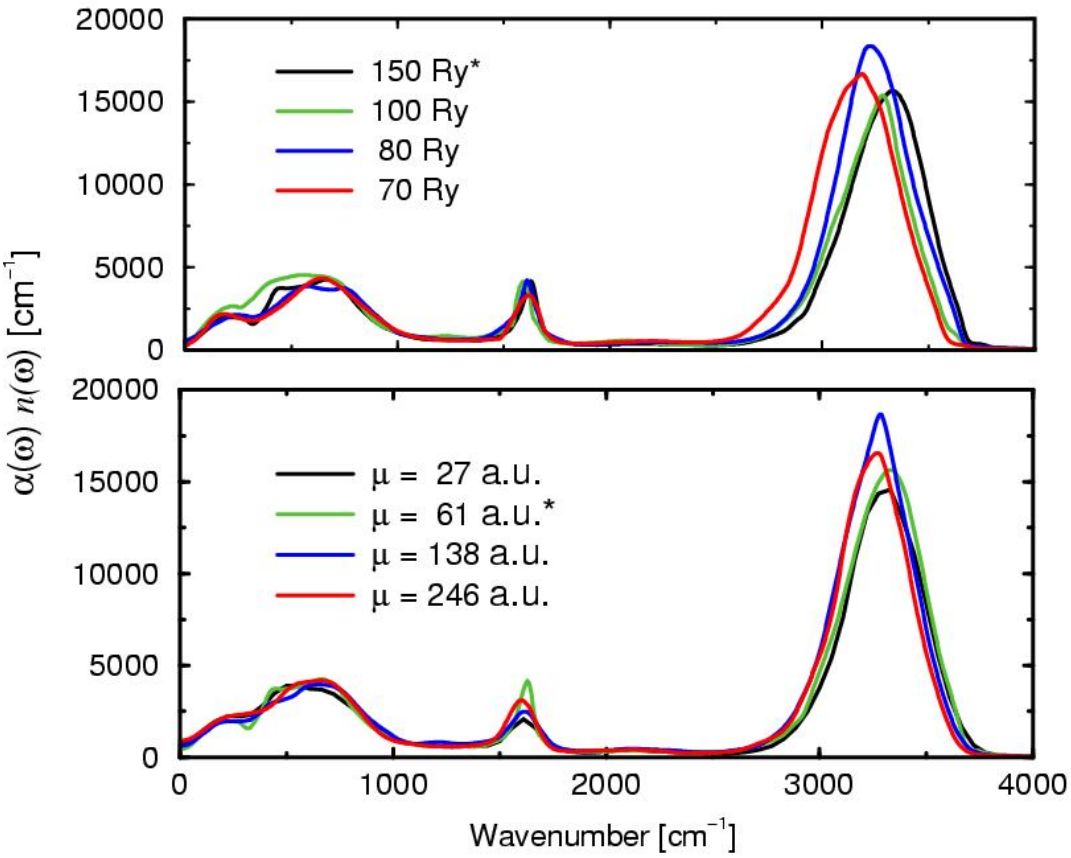

Figure 4-1. The influence of the plane wave basis set cutoff (upper panel) and of the fictitious electron mass (lower panel) on the calculation of IR absorption spectra using Car-Parrinello molecular dynamics and liquid water at a temperature T=345K. The results suggest that if one wishes to compute spectra with an accuracy of 40 cm-1for the wave number axis, the plane wave basis set cutoff should be set to at least 100 Rydberg (Ry), and the fictitious electron mass should not exceed 246 atomic units (a.u.). The results in the upper panel were obtained using a value μ= 61 a.u., while the values reported in the lower panel

Fig. 4-1 contains the results of a "control experiment" on pure, liquid water whose aim is to investigate quantitatively the effect of the fictitious electron mass and of the plane wave basis set cutoff on the accuracy of the IR spectrum calculation. The results displayed in the lower panel of Fig. 4-1 have been obtained using a basis set cutoff of

150 Rydberg (Ry), which has been demonstrated to be sufficient for converging the vibrational spectrum of gas-phase[32] as well as that of liquid water[33] when employing B-LYP exchange[24]-correlation[25] calculations in conjunction with Troullier-Martins[26] pseudopotentials. One can see from these results that if values for the fictitious mass μ smaller or equal to 246 atomic units (a.u.) are utilized, the resulting spectra become indistinguishable within the 40cm^{-1} statistical resolution of our molecular dynamics IR spectrum calculation protocol.[15] Larger values for the parameter μ lead to OH stretch absorption peaks that are red-shifted beyond the statistical resolution of our simulation, a results that is consistent with the quantitative analysis[34] of Tangney et al.

The results displayed in the upper panel of Fig.4-1 show that, in agreement with the conclusions[33] of Lee and Tuckerman, liquid water simulations performed using B-LYP exchange-correlation potentials in conjunction with Troullier-Martins pseudopotentials and cutoffs of 70 or 80 Ry are inadequate. In contrast, the present results suggest that a cutoff of 100 Ry should instead be adopted, as the resulting spectra become indistinguishable within our statistical resolution, from those computed using a cutoff of 150 Ry.

4.2.3 The reliability of the present simulation protocol in predicting IR spectra for pure H_2O and pure HF

The results of the first "control experiment" suggest that our simulations should involve the use of a basis set cutoff of 100 Ry in conjunction with a fictitious electron mass μ = 240 a.u. In order to estimate the magnitude of all other sources of error, including the inexact exchange-correlation functional and the absence of nuclear quantum effects, Fig. 4-2 compares calculated and experimental IR spectra for pure, liquid water and for pure, liquid, and crystalline hydrogen fluoride. The present

calculations were performed at constant volume, using primitive boxes comprising 32 molecules for the water simulations and 48 molecules for those involving HF. The volumes of the primitive boxes employed are consistent with experimental values for the density. In agreement with other theoretical investigations,[35] we find that room temperature structural properties (i.e.: oxygen-oxygen radial distribution functions) of B-LYP water disagree with experimental data, unless the computations are performed at a temperature that exceeds the experimental one by approximately[35c] 40K. Several factors are thought to contribute to this difference, with the limitations[35] of the current DFT approaches, and the neglect of nuclear quantum effects[18b] being among the most important ones.

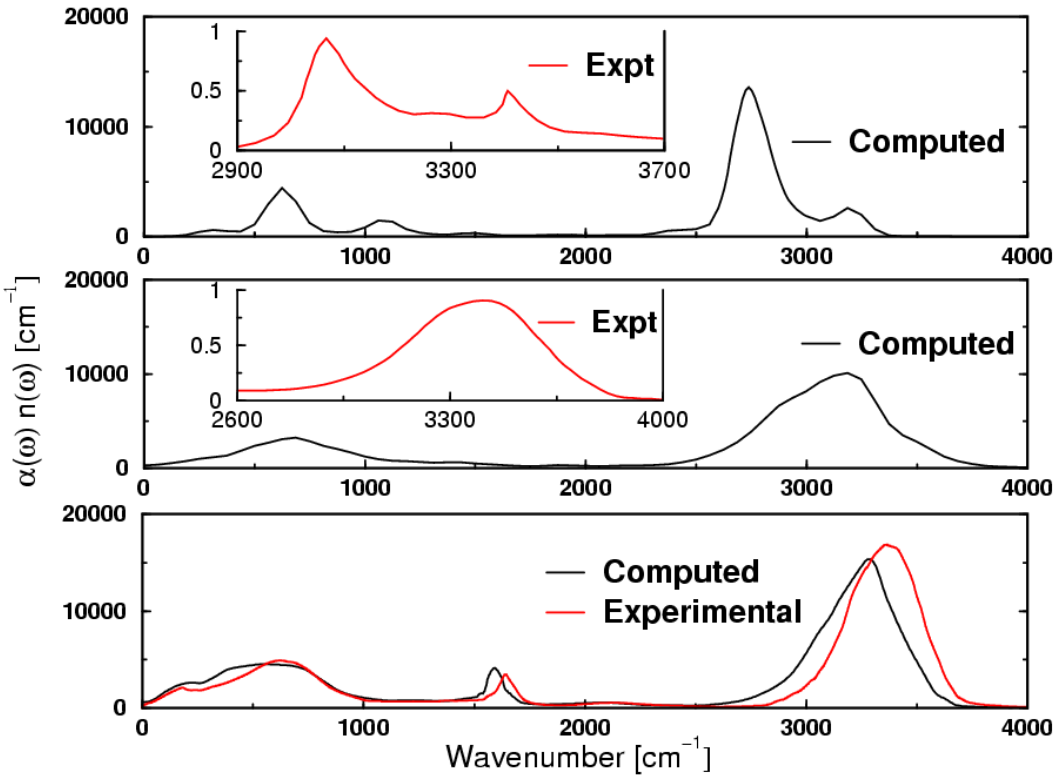

Figure 4-2. A comparison between experimental and theoretical IR spectra for liquid water (lower panel), and for liquid and crystalline HF (middle and upper panels, respectively. The experimental absorptivity data (given in the inset) is somewhat less reliable, is given in arbitrary units, and covers a more limited spectral range in the case of HF[37] than in the case of water.[36] One can see that the overall agreement between theory and experiment is quite good, although the OH and FH stretch vibration frequencies are underestimated by theory by 120 cm^{-1} for H_2O, and by 200-250 cm^{-1} for HF.

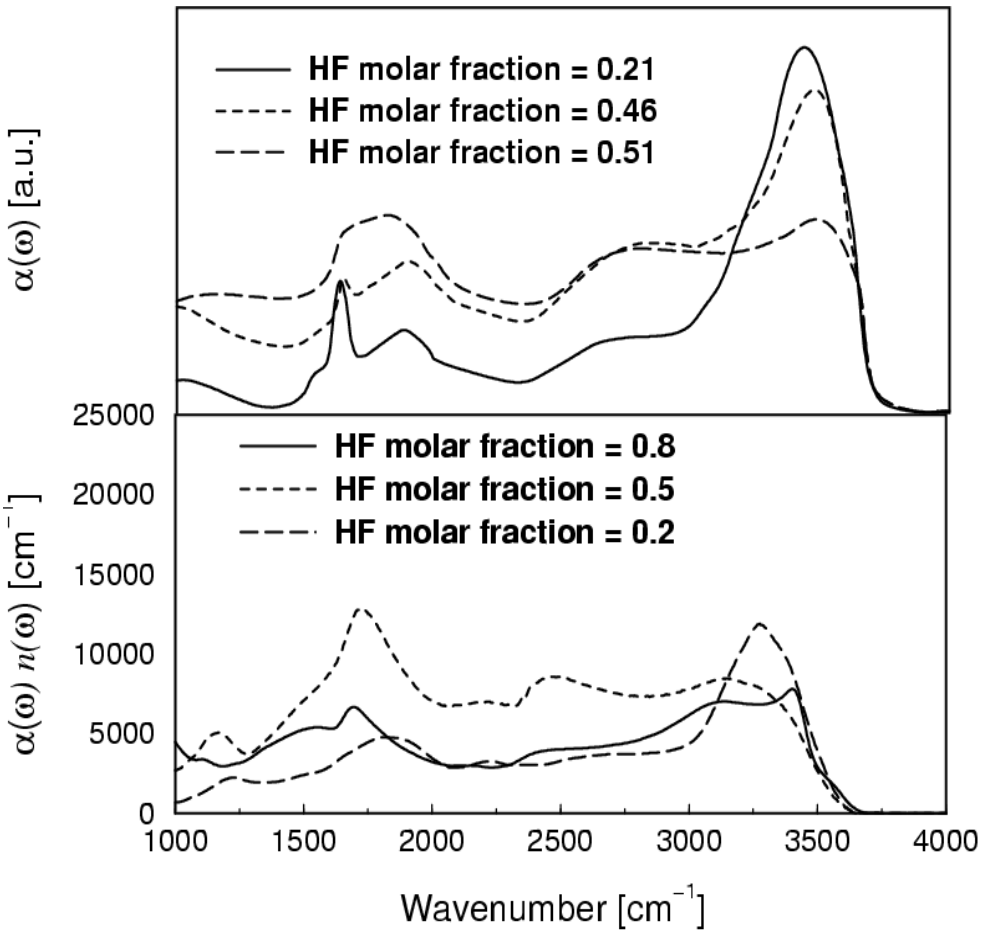

Figure 4-3. Experimental IR absorption spectra for room temperature (upper panel) and cryogenic (lower panel) mixtures of hydrogen fluoride and water. The experimental data in the upper panel is in arbitrary units and was obtained by digitizing and splining the figures that appear in reference 40. The data in the lower panel appears in reference 10 and was generously provided to us by the authors. The most important observation is that mixtures of HF and H_2O generate very broad and intense continua of absorptions despite the weak acid character of HF. Moreover, the conspicuous absorption centered around 1800 cm^{-1} is clearly visible in the room-temperature spectra and its intensity increases significantly in cryogenic conditions. The absorption spectra of HCl and HBr mixtures with water in similar conditions reveal[10,11,22] no significant absorption peak in this spectral region.

Since the absolute value of the Beer-Lambert absorptivity varies significantly with the temperature[15] in the neighborhood of the freezing point due to variations in the rigidity of the first solvation shell, we have chosen to perform our simulations at T=345 K, in order to avoid artifacts caused by poor equilibration and quasi-ergodic sampling that characterize[35] simulations in the supercooled regime. The results displayed in the lower panel of Fig.4-2 contrast experimental and theoretical IR spectra that were obtained at thermodynamic points at which structural properties of water are identical (i.e.: experimentally, T=300K, vs. T=345 K, in our simulations). The agreement between the computed and the experimental spectra[36] for liquid water represents a marked improvement over previously reported data[15], especially in the OH stretch range. The remaining difference in the case of liquid water amounts to a 120 cm^{-1} red-shift of the computed OH stretch peak and a 40 cm^{-1} red-shift of the bending absorption with respect to experimental values. In contrast, the computed FH stretching absorptions appear to be red-shifted by 200-250 cm^{-1} with respect to experimental[37] values. We have verified that the larger discrepancy between theory and experiment in the case of hydrogen fluoride does not change significantly when repeating the calculations with a basis set cutoff of 120 Ry. Most likely, these differences reflect[23] the intrinsic limitations of a generalized gradient density functional description of hydrogen-bonded systems, and are expected to affect all our subsequent calculations.

It is worth stressing at this point that the two control experiments described above are not sufficient to guarantee the relevance of the spectra that will be computed for amorphous mixtures of HF and H_2O at cryogenic temperature. Since the chemical structure of the molecular entities present in the amorphous mixtures is unknown, molecular dynamics techniques are of limited use in the absence of other experimental information. First, on a very fundamental level, it is not clear to what extent general

equilibrium thermodynamics concepts can be used to predict the molecular composition of the amorphous mixture at 80 K. Second, even if the system was ergodic within its amorphous subspace of the phase space, current first principles molecular dynamics algorithms would not be able to access the relevant, extremely slow, equilibration timescale of the cryogenic mixture. Finally, even if the two aforementioned problems could somehow be overcome, the molecular composition of the system would be dictated by the Boltzmann's factors of the relevant chemical species that appear along the dissociation pathway (see Eq. 1). Since the precision of current electronic structure calculations cannot match the thermal energy at cryogenic conditions ($k_BT \approx 0.15$ kcal/mol at T=80K), molecular dynamics approaches are of limited use as a means of achieving a realistic sampling of the potential energy surface in the present case.

4.3 Results and Discussion

4.3.1 Cryogenic spectra calculation strategy

Our strategy consists of performing multiple molecular dynamics simulations, starting from different initial configurations. The dynamics will serve only as a

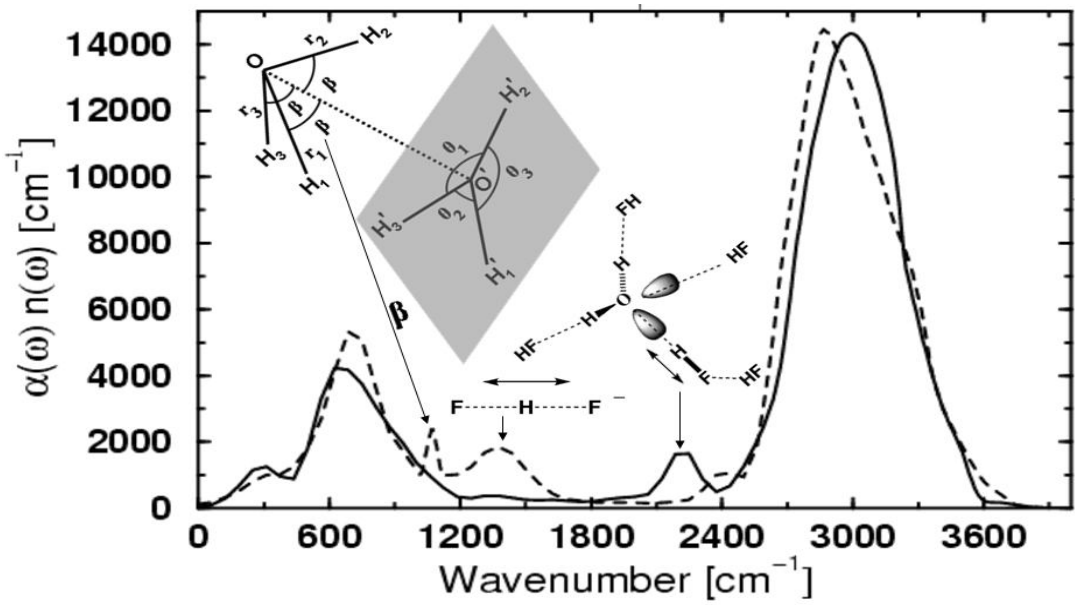

Figure 4-4. Figure 4-5. The computed IR absorption spectra for the reactant (solid line) and product (dashed line) species in reaction (6) at 0.98 molar fraction of HF. The un-ionized FH and OH_2 molecules do not absorb significantly between 1000 and 2000 cm^{-1}. However, an over-extended, but unbroken FH molecule that donates a hydrogen bond to the intact water molecule gives rise to an absorption centered at 2300 cm^{-1}. The sharp absorption at 1080 cm^{-1} is assigned to umbrella-mode vibrations of the trisector[40] angle β. The broad and relatively intense absorption centered at 1400 cm^{-1} is due to the proton stretch motion in the poly-fluoride ion.

means for computing IR spectra, including anharmonic corrections, whose relevance will be limited by the extent to which the starting configuration mimics the molecular composition of the cryogenic amorphous mixture. Comparison with experimental IR spectra will then be used to identify the chemical nature of the molecular structures that

are likely to be present in the cryogenic conditions of the molecular beam experiment, and, by extension, at room temperature conditions.

Our calculations started by generating 20 initial configurations that were consistent with a macroscopic molar ratio HF/H_2O of 0.2, 0.5, 0.8, or 0.98. These initial configurations were generated starting from equilibrated simulations of 32 molecules of pure H_2O or 48 molecules of pure HF at room temperature, by replacing several oxygen atoms by an equal number of fluorine atoms or vice versa, and by removing/adding the relevant number of hydrogen atoms. These configurations were subsequently equilibrated at ambient temperature, after which some were discarded since their equilibrated average energy was obviously too large to be relevant. The process was continued by slowly cooling down the remaining configurations, followed by equilibration and data collection at 80K, the entire process taking approximately 80 ps. The equilibrations were performed at constant temperature, using a Nose-Hoover chain thermostat[38] on each degree of freedom, but

the actual spectra were computed utilizing unbiased dynamical trajectories. All calculations were carried out using the PINY_MD[39] simulation package.

4.3.2 The relevant experimental data

To set the stage, the lower panel of Fig.4-3 compiles the relevant experimental IR spectra of Ayotte et al.[10] for amorphous, cryogenic mixtures of HF and H_2O with hydrogen fluoride molar fractions in water varying from 0.2 to 0.8. The upper panel of Fig.4-3 displays the room-temperature data of Menard et al.[40] that

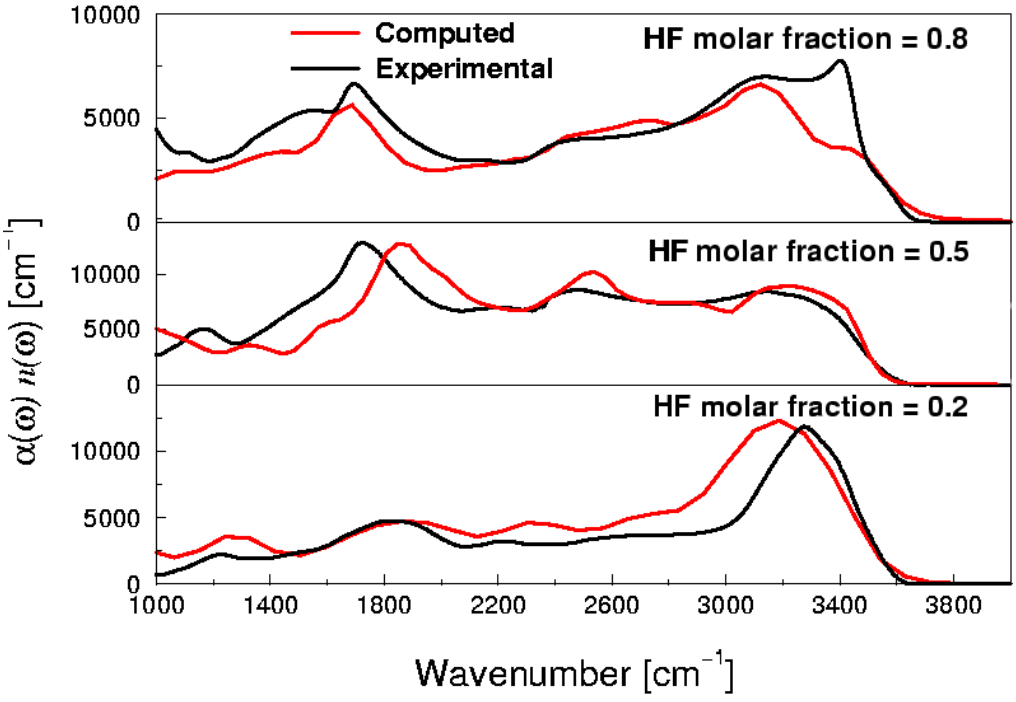

Figure 4-6. Comparison between theoretical and experimental absorption spectra for cryogenic mixtures of HF and H_2O. The theoretical calculations are based on a classical (i.e.: Newtonian) treatment of the nuclear dynamics and on a first-principle description of the electronic structure. The excellent level of agreement between experiment and computation *suggests* that the chemical nature and the concentration of the microscopic species that exist in our simulations represent an adequate representation of the amorphous binary solids obtained by simultaneous deposition of HF and H_2O at 80 K. However, *demonstrating* the relevance of these microscopic structures will not be achieved until we prove that nuclear quantum effects are unlikely to change qualitatively the shape of the computed absorption spectra (see Section 4.3.5).

corresponds to mixtures of HF and H_2O, with HF molar fractions varying from 0.21 to 0.51. As clearly pointed out by Giguère et al.[22] and by Ayotte et al.[12], the broad absorption at 1800 cm^{-1} is missing from the spectra of the other hydrohalic acids, pointing these authors to formulate two competing explanations. Giguère et al. put forward the suggestion that mixtures of HF and H_2O contain small, but detectable quantities of a chemical species that cannot be found in the aqueous solutions of other

hydrohalic acids. He identified this species with an $F^-\cdots H_3O^+$ contact ion pair and assigned the characteristic 1800 cm^{-1} absorption to the HOH "in-plane" bending of the hydronium ion engaged in the formation of the contact ion pair.

Based on the fact that the position and the shape of the 1800 cm^{-1} absorption changes little when comparing cryogenic and ambient temperature spectra, Ayotte et al.[12] pointed out that Giguere's assignment of the aforementioned peak to a bending is unlikely to be correct due to its unusually large intensity in the cryogenic environment. These authors have proposed in exchange that the peak be assigned to an OH or an FH stretching absorption in a special, unusually anharmonic environment, generated by the proximity of the fluorine atom and of the neighboring water molecule. It is important to mention that the propensity of the fluorine atom to generate significantly anharmonic proton potential environments has been demonstrated[41] in the case of monohydrated halogen ion clusters, suggesting that a similar phenomenon could be relevant in condensed phase environments.

The results of our simulations are consistent with the presence of intermediates of dissociation in mixtures of HF and H_2O as postulated by Giguère. Moreover, they also agree with Ayotte's assignment of the 1800 cm^{-1} absorption to a proton stretch rather than to a bending vibration. However, the present computational results suggest that the molecular species that are relevant in the condensed phase environment are fundamentally different from those that exist in small clusters. In particular, we conclude that the 1800 cm^{-1} absorption in condensed phase mixtures of HF and H_2O has a different origin than that observed[42] in $F^-\cdots HOH$ clusters. We attribute the broad absorption in the amorphous phase to a continuum of proton-shared species $F^{\delta-} \cdots H \cdots {}^{\delta+}OH_2$ that are stabilized by specific solvation environments. The unusually low proton stretching vibration is thus caused by strong solute-solvent hydrogen bonding

interactions rather than by large nuclear quantum effects, as is the case[18a,41,42] in small clusters.

4.3.3 Mixtures containing a large excess of HF can be used to investigate the spectral properties of FHF^- and of H_3O^+ in the amorphous phase

For reasons of simplicity, we start the main computational investigation by focusing on the mixture that contains 98% HF and 2% H_2O. Unfortunately, the experimental data is not conclusive in this concentration range, and the data presented in reference 10 indicates that a certain amount of pure, crystalline, HF might be found in mixtures that have a molar fraction of hydrofluoric acid in excess of 0.8. Nevertheless, even in the absence of feedback from experimental data, computational investigations in this concentration range can be quite informative.

The starting configurations in our system consist of a primitive box containing 1 water and 47 hydrofluoric acid molecules. Interestingly, the four simulations that were carried out indicate the presence of the following dissociation equilibrium:

$$yFH+H_2O \rightleftharpoons F^-(FH)_{y-1}+H_3O^+ \qquad (4.6)$$

No ion pair dissociation intermediates were found to be stable in these cases. Depending on the choice of the initial configuration, the water molecule either remains intact, or accepts a proton from a neighboring hydrogen fluoride molecule to form a hydronium ion. In this second case, after the equilibration period, the hydronium ion is solvated by three un-dissociated hydrogen fluoride molecules, while the fluorine "defect" migrates via Grotthus hoping and forms poly-fluoride anions.

The results displayed in Fig.4-4 contrast the IR absorption spectra generated by the reactant species with the one that is generated by the product species in reaction (6). By computing the autocorrelation spectrum of various ideal normal modes, we have assigned the absorption peaks as follows: a) The sharp and weak absorption at 1080 cm^{-1} is the signature of the umbrella-mode vibration[43] in the "ideal" Eigen form of the hydronium ion. This assignment was made based on the autocorrelation spectrum of the "trisector" angle β represented in Fig.4-4, and whose definition was adapted from reference 43; (b) The broad absorption ranging from 1200 to 1600 cm^{-1} is due to proton stretching in the poly-fluoride ions; (c) The bending vibrations of the hydronium ion, corresponding[43] to the dynamics of the projected θ angles in the plane perpendicular to the trisector, absorb at 1600 cm^{-1}, but are of weak intensity, and, therefore, obscured by the more intense poly-fluoride peak; (d) Finally, the absorption at 2300 cm^{-1} is due to over-extended, but not yet dissociated FH molecules that donate a hydrogen bond to a neighboring, intact, water molecule. It is important to remind the reader that previous computational investigations[19] by Iftimie and Tuckerman suggested that proton-shared ion pairs $F^{\delta-} \cdots H \cdots {}^{\delta+}OH_2$ were stable on a 10 ps timescale at room temperature in an environment formed exclusively from water molecules. In contrast, no computational evidence for the stability of similar species was found in the present case of a pure, hydrogen fluoride environment. Although these results are interesting in their own right, one must remember that electronic structure calculations are not sufficiently reliable to predict whether a chemical species is a transition state or a weakly stable intermediate. The important question of the stability of proton-shared ion pairs will be settled in the next section, by combining computational evidence with direct comparison with experimental data.

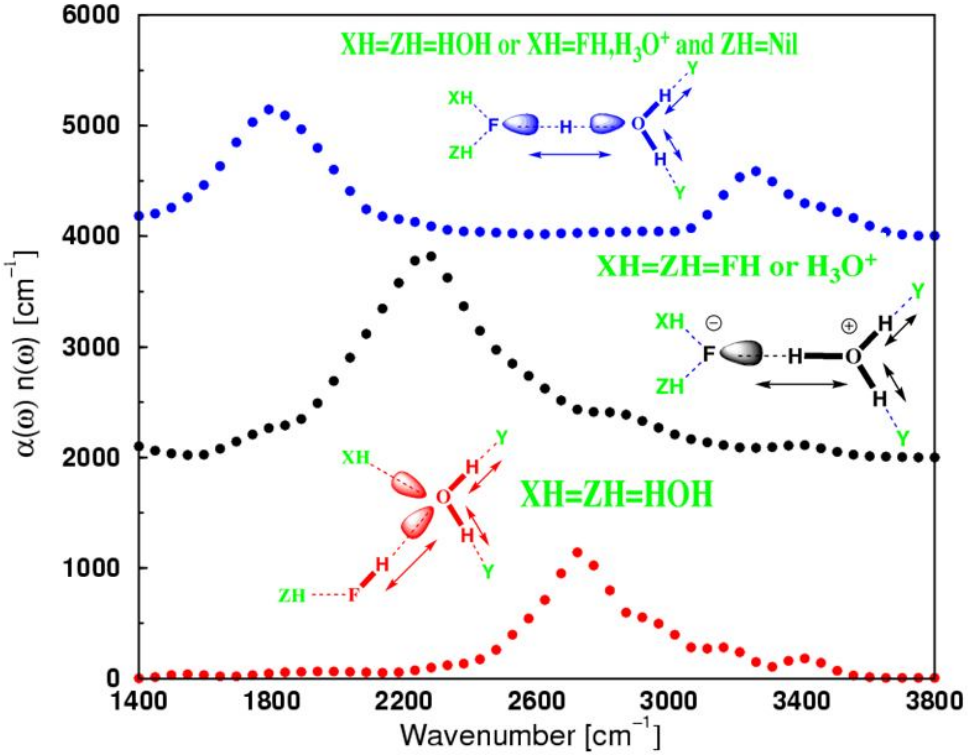

Figure 4-7. Illustrative examples of typical first solvation shell molecular environments, and of absorption spectra generated by proton-shared Fδ- ··· H ··· δ+OH2 species (blue), F-·H3O+ (black) contact ion pairs and H2O·HF (red) un-ionized limiting forms. To increase visibility, the spectra are shifted along the y-axis by 2000 cm-1. Molecular IR absorptivity decompositions are carried out using Eq. (4.7). The species depicted here are characterized by average proton positions δ = dFH –dOH of -0.28 Å, 0.37 Å and -0.53 Å for the proton-shared, the contact ion pair and the un-ionized form, respectively. The instantaneous

4.3.4 The chemical species responsible for the broad and intense absorption centered at 1800 cm^{-1} are proton-shared ion pairs.

The next step in our investigation focuses on cryogenic mixtures of HF and H_2O with water molar ratios of 0.2, 0.5, and 0.8. For each molar ratio, simulations were carried out starting from five initial configurations, as described in subsection 4.3.1. By comparing and contrasting computed and experimental infrared spectra at cryogenic temperatures,

we were able to identify which system, among the five that were considered, was the most representative of the molecular environments sampled experimentally. Figure 5 shows the IR absorption spectra that were obtained from the most relevant simulations alluded to in the previous paragraph, and compare them with the experimental data[10] of Ayotte et al. The excellent level of agreement between theory and experiment that is apparent from the results displayed in Fig.4-5 suggests that the microscopic compositions that were utilized in these selected simulations represent an adequate description of the amorphous binary solids prepared experimentally by simultaneous vapor condensation at 80 K using molecular beams.

In order to rationalize the molecular origin of the broad absorption extending from 1000 to 3400 cm^{-1} in Fig.4-5, we have utilized a spectrum decomposition technique[15] that was previously proposed by Iftimie and Tuckerman. The decomposition of the IR spectrum relies on an approximate, but chemically intuitive decomposition of the total dipole moment into molecular components, and employs maximally-localized Wannier[44]-Boys[45] orbitals that are generated on-the-fly using a modified Car-Parrinello algorithm.[16] The approach proposed in reference 15 amounts to calculating the contribution $[\alpha(\omega)n(\omega)]_A$ of a molecule A in solution to the total absorption spectrum $\alpha(\omega)n(\omega)$ by computing the spectrum of the time-dependent cross-correlation function between the molecular dipole moment μ_A of molecule A and the total dipole moment M

$$[\alpha(\nu)n(\nu)]_A \cong \frac{\beta}{6Vc\varepsilon_0}\int_{-\infty}^{\infty}\exp(2\pi i\nu\tau)\left\langle \dot{\mu}_A(0)\cdot\dot{M}(\tau)\right\rangle_{cl} d\tau \qquad (4.7)$$

Visual inspection of the chemical species that were stable in our simulations indicated the presence of un-ionized $H_2O{\cdot}HF$ complexes, of proton-shared $F^{\delta-}\cdots H\cdots {}^{\delta+}OH_2$ species, as well as that of $F^-{\cdot}H_3O^+$ contact ion pair limiting forms. Fig.4-6 illustrates the typical IR spectra generated by the three aforementioned structures in their condensed-

phase environments. The first thing that can be observed from the results displayed in Fig.4-6 is that the stretching vibrations spectral features corresponding to the dynamics of the transferring proton are very wide and intense. This suggests that the transferring proton is free to travel significant distances during a vibration period even at T=80K and, can therefore experience different local electric fields.

A second important conclusion that can be inferred from the data shown in Fig.4-6 is that the maximum of the proton stretch absorption frequency changes as the ionization process depicted in Eq. (1) unfolds. The transformation of an un-ionized $FH\cdot OH_2$ complex into a contact ion pair limiting form $F^-\cdot H_3O^+$ can only be achieved if the environment changes significantly the relative condensed-phase proton affinities of the fluoride anion, F^-, vs. that of the water, OH_2, molecule. Changes in the solvation environment induce changes in the local proton potential, which becomes more and more flat as proton-shared species are formed. This in turn causes the proton stretching vibration frequency to shift toward the red part of the absorption spectrum. Finally, as changes in the solvation environment drive the transformation in reaction (1) toward the contact ion pair limiting form $F^-\cdot H_3O^+$, the curvature of the proton potential increases[46] again. The charge separation process is also accompanied by an important increase in the transition dipole moment, as revealed by the molecular absorption spectra displayed in Fig.4-6.

In agreement with our observations[11] on equimolar mixtures of HF and H_2O, the local degree of advancement of reaction (1) correlates well with the nature of the H-bond topology of the first solvation shell. As a general rule, the ionization process is promoted by fluctuations which induce a decrease in the fluoride ion proton affinity: an increase in the number of molecules that donate H-bonds to F^-, or an increase in the strength of their H-bond donating character. Similarly, an increase in the local Brønsted

acceptor character of water molecules can also shift the equilibriums in reaction (1) to the right. Consequently, un-ionized, FH·OH_2 complexes that display an extended, but not yet broken, FH bond, prefer an environment in which the hydrogen fluoride molecule adopts a single donor, single acceptor (DA) solvation pattern, while the water molecule adopts a double donor, double acceptor (DDAA) configuration.

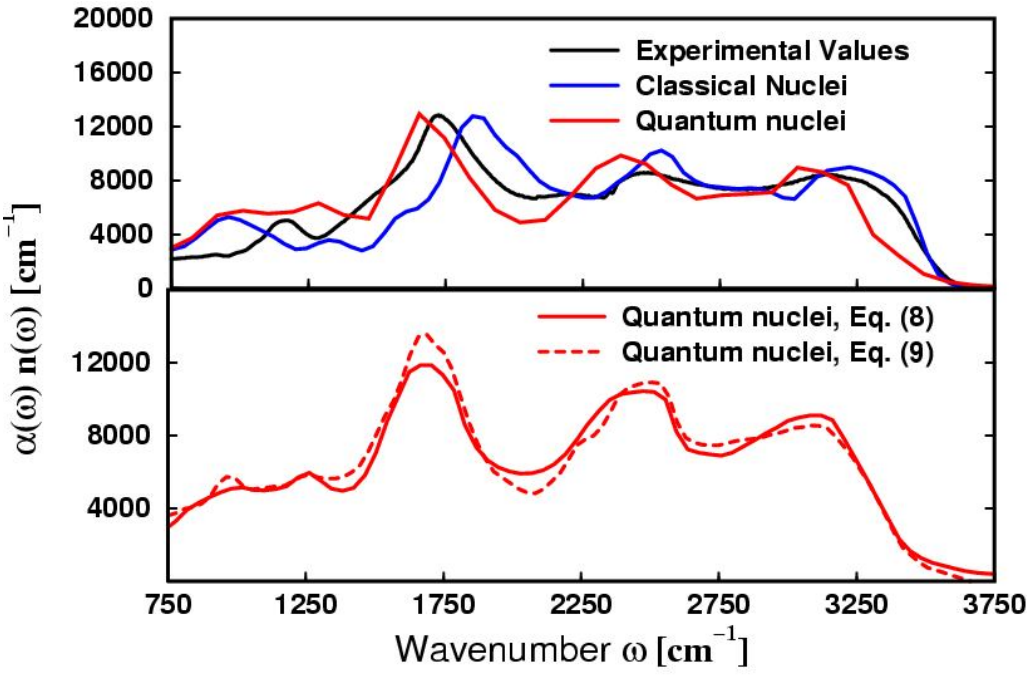

Figure 4-8. An illustration of the magnitude of zero-point vibration and of incoherent tunneling effects on the IR spectra reported in Fig.4-5. The quantum results were obtained using the centroid molecular dynamics theory[17] and Eq. (4), by assuming that the electronic dipole moment is a linear operator (see text). The results displayed in the upper panel demonstrate that including nuclear quantum effects effectively shifts the entire absorption spectrum to smaller wavenumbers by an almost constant value of 200-300 cm^{-1}, without significantly affecting its shape. The lower panel tests the validity of the linear operator approximation, by using two approximate definitions for the dipole moment centroid symbol (see Eqs. 4.8, 4. 9 and text). These definitions should in principle lead to different IR spectra unless the dipole moment was indeed a linear operator. We interpret the close similarity of the spectra reported in the lower panel as an indication that the linear operator approximation is quite appropriate in the present case.

Whenever a solvent molecule shifts from the water to the hydrogen fluoride solvation shell, yielding an AAD and an ADD configuration for HF and H_2O, respectively, a shared-proton dissociation intermediate, $F^{\delta-} \cdots H \cdots {}^{\delta+}OH_2$ is formed, in which both the FH and the OH bonds are broken, but the hydrogen atom is not necessarily equally shared. This result is consistent with the conclusions reached by Sillanpää et al.[47] who provided computational evidence suggesting that the fluorine atom increases its coordination number prior to the ionization of HF. Alternatively, proton-shared intermediates were also observed to be stable with an AADD configuration for the oxygen atom of the accepting water molecule, provided that the fluorine atom was solvated by a powerful H-bond donating molecule, such as another FH molecule, or a hydronium ion, H_3O^+. With a single exception[48], contact ion pairs were found to be unstable irrespective of the solvation topology unless the fluorine atom was solvated by at least one, and often two powerful H-bond donors. This observation is consistent with the ab initio molecular dynamics results previously reported by Iftimie et al.[19] and by Laasonen et al.[49] who were unable to find long-lived contact ion pairs $F^- \cdot H_3O^+$ in very dilute, aqueous solutions. As pointed out in reference 11, this observation is also consistent with an interpretation of the peculiar weak-to-strong acid behavior[50] observed in aqueous solutions of HF near equimolar concentrations, as originating from hydrogen fluoride self-solvation. The central result that can be extracted from the results displayed in Fig.4-5 is that $H_2O \cdot H^+ \cdot F^-$ proton-shared species are largely responsible for the surprisingly intense absorption extending between 1400 and 2000 cm^{-1}. We note, in passing, that the other species that contributes to the lower frequency range of this absorption, are bifluoride and poly-fluoride ions as can be seen in Fig.4-4, and from the experimental results of Giguere et al.[22] The shared-proton complexes are only stable in a disordered condensed phase and owe their existence to local environments in which fluoride anions and water molecules display comparable,

although not necessarily equal, proton affinities. The striking similarities between the cryogenic and the ambient temperature experimental spectra displayed in Fig.4-3 suggest that the existence of the conspicuous 1800 cm^{-1} absorption is a thermodynamic consequence of the stability of proton-shared intermediates, and not just a consequence of their being kinetically trapped in the disordered H-bond network of the amorphous ice.

Inspection of the dynamical trajectories in conjunction with spectral decomposition results suggest that the structures that are responsible for these intense absorptions comprise FH or OH bonds on the verge of rupture[51], in which large amplitude proton motions and large vibrational transition dipoles are expected.[11] It is therefore not surprising that these transitions are responsible for some of the largest features in the infrared spectra, while being hardly visible[47,49,52] in velocity autocorrelation spectra.

4.3.5 Nuclear quantum effects

Although the agreement between theory and experiment shown in Fig.4-6 appears to be compelling evidence for the correctness of the subsequent assignment of the IR spectra, and hence, for the stability of proton-shared dissociation intermediates, it is important to recall that zero-point vibration and hydrogen atom tunneling effects were neglected in all calculations up to this point. However, if one naively assumes that the gas-phase $F^-{\cdot}HOH$ cluster[41,42] can be employed as a relevant model for what the transferring proton potential in the amorphous mixture should look like, one realizes that the entire assignment of the experimental spectra, and the relevance of the computed ones, need to be reevaluated. As it turns out, nuclear quantum effects as large[18a] as 600 cm^{-1} and anharmonicities on the order[42,53] of 1000 cm^{-1} had previously been reported for the ionically H-bonded OH vibration in the gas-phase $F^-{\cdot}HOH$ cluster, raising the

possibility that the computed spectra displayed in Fig.4-6 would disagree qualitatively with experimental data once nuclear quantum effects were considered.

The results that appear in this section have already been presented in reference 11, and are included here for the sake of completeness. For the purpose of the present investigation, we have chosen to include zero-point vibration and hydrogen tunneling effects within the framework of the centroid[17] molecular dynamics theory, which has been demonstrated[54] to significantly improve IR spectrum calculations beyond the "harmonic approximation" of Eq. (4.5) that was employed to obtain the data in Fig.4-6.

Within the limits of applicability of the centroid molecular dynamics theory, Voth et al. have demonstrated[17] that one can compute quantum-time auto-correlation functions by calculating single-time centroid symbol autocorrelation functions provided that the correlations involve operators that are linear combinations of Cartesian coordinates or momenta. Unfortunately, this is not the case for the electronic dipole moment, implying that a rigorous application of the centroid molecular dynamics theory should involve calculations of multiple-time[55] centroid symbol correlation functions, which are challenging to implement both at a theoretical and at a practical level in the present case.

The results displayed in the upper panel of Fig.4-7 were computed from the autocorrelation of an approximate dipole moment centroid symbol $\mathbf{M}_c(t)$, which was taken to be the instantaneous value of an average of classical dipole moments, with the average being taken over all path-integral quasi-particles:

$$\mathbf{M}_c(t) \simeq \frac{1}{N}\sum_i \mathbf{M}(\mathbf{R}_i;t) \qquad (4.8)$$

The magnitude of the approximation introduced by the use of equation (8) can be gauged from the results displayed in the lower panel of Fig.4-7, where the total infrared spectrum computed within the limits of the above-mentioned approximation are contrasted with the IR results computed by approximating $\mathbf{M}_c(t)$ by the instantaneous value of the classical dipole moment

$$\mathbf{M}_c(t) \simeq \mathbf{M}\left(\mathbf{R}_c; t\right) \tag{4.9}$$

where the vector $\mathbf{R}_c$ stands for the center-of-mass (i.e.: centroid) coordinates of the path-integral rings of quasi-particles:

$$\mathbf{R}_c = \frac{1}{N}\sum_i \mathbf{R}_i \tag{4.10}$$

These results suggest that the reliability of the quantum spectra displayed in the upper panel of Fig.4-7 is more likely to be limited by the fundamental approximation[17] of the centroid molecular dynamics theory, as well as by its present practical implementation, and only to a smaller extent by the nonlinear nature of the electronic dipole moment operator.

The approximate quantum nuclei calculations were performed using 16 discrete path-integral[17] replicas. The number of quasi-particles chosen in the present investigation represents a compromise between accuracy and computational cost, being consistently found close to the convergence limit in ab initio molecular dynamics investigations of similar systems: gas-phase $F^- \cdot H_2O$ clusters[41,42], gas-phase[53] and liquid phase[56] HF multimers, and excess proton in liquid water.[57]

A normal mode representation of path integrals was employed, with the centroid position of each atom defined as the zero-frequency mode of the corresponding quasi-particle chain. An adiabaticity parameter γ=0.05 was utilized to obtain the data in the

upper panel of Fig.4-7, following the suggestions of Voth et al. in their studies[58] of excess proton in water.

The duration of the simulation that employs the value γ=0.05 was limited to only 2 ps due to its high computational cost. This duration limits the statistical resolution of the calculated infrared spectra to 90 cm^{-1} for the wavenumber axis. A similar simulation has also been carried out[11] with a larger (γ=0.2) value for the adiabaticity parameter γ, which enjoyed a better statistical resolution, but suffered[11] from slightly underestimating the magnitude of the nuclear quantum effects for the 2400 cm^{-1} absorption peak. Both effects were nonetheless found to affect the uncertainty of the spectrum by less than 100 cm^{-1} on the wavenumbers axis.[11]

We have ensured that the forces on the electronic coefficients remained as small in the centroid molecular dynamics calculations as they were in the Newtonian calculations by employing μ=34 a.u. for the fictitious electron mass and Δ=0.02 fs for the integration time step in the γ=0.2 simulation, and by employing μ=3.06 a.u. and Δ=0.006 fs in the γ=0.05 simulation.

4.4 Conclusions and Outlook

The long-term goal of the present investigation is to shed light on the general dissociation mechanism of weak acids in various aqueous environments. Important questions that have not yet found unique, non-controversial answers in this field include: 1) Does a weak acid dissociation process reach the Eigen loosely-bound complex state[3] in one, or in multiple steps, involving dissociation intermediates? 2) How can these intermediates, if any, be characterized spectroscopically? 3) How

important is the role played by nuclear quantum effects in the proton dissociation process?

In an effort to provide answers to some of these questions we have undertaken careful investigations of mixtures of hydrofluoric acid and water, using state-of-the-art computational tools, in the context of a close experimental/theoretical collaboration.[11] The choice of the HF/H_2O mixture was based on the observation that this system had the unusual property that it displayed a measurable infrared absorption band in a spectral region where similar hydrohalic acids did not. Given the simplicity of the system, and the paucity of molecular species which could explain the frequency as well as the intensity of the IR absorption at 1800 cm^{-1}, the system appeared to be a good candidate for investigating dissociation intermediates.

The principal conclusion that was reached in the present study does not answer the first question mentioned at the beginning of this section, but highlights the existence of another level of complexity: Even the ionization step appears to be complex in the case of the dissociation of the hydrofluoric acid, and proceeds via a proton-shared intermediate that appears to be stabilized by distinct first solvation shell environments. Since the room-temperature dynamics of molecules in the first solvation shell of liquid water is quite rapid, it is not clear whether such a structure is produced via a well-defined, slow, activated process starting from un-ionized molecules in dilute solutions of HF at ambient conditions. In that case, one might even have to deal with an almost continuous interconversion of various limiting forms of un-ionized and of proton-shared species, similar in spirit to the dynamics of the Zundel vs. Eigen limiting forms of the hydrated proton. Nevertheless, the computational results presented in the present work suggest that as the temperature decreases, or the viscosity of the

environment increases, the kinetic picture of the dissociation event will have to include the explicit presence of a proton-shared dissociation intermediate.

Although the applicability of the first conclusion mentioned above to other weak acids is far from being established, the present results also suggest an experimental means for its verification. Since proton-shared ionization intermediates are predicted to absorb electromagnetic radiation around 1800 cm^{-1}, they could be detected using time-resolved spectroscopy experiments, provided that the concentration of such intermediates becomes significant, and that no other molecules present in the system absorbs radiation in the same spectral window.

Interestingly, the results of our present investigations suggest that nuclear quantum corrections to the anharmonic dynamics of the transferring proton are much less important in amorphous mixtures of FH and OH2 than in the relevant gas-phase cluster $F^-\cdots HOH$. This result is somewhat unexpected if one considers the widely different shapes[2,46] that the proton potential should have in the three limiting species, the un-ionized complexes $FH\cdot OH_2$, the proton-shared $F^{\delta-}\cdots H\cdots {}^{\delta+}OH_2$ and the contact $F^-\cdot H_3O^+$ ion pairs.

The fact that the three absorption peaks that were more or less closely identified with proton stretching in the above-mentioned structures were equally affected by zero-point vibration and incoherent tunneling effects suggests that: 1) the shapes of the three proton potentials is more similar than previously predicted, and 2) the degree of anharmonicity is significantly smaller than what has been found[41,42] in the $F^-\cdots HOH$ clusters. Preliminary results focusing on the calculation of the transferring proton potentials in the condensed-phase amorphous environment suggest that these conclusions are warranted. In particular, we have generated proton transfer potentials

by changing the position of a hydrogen atom, while keeping all other atomic positions fixed, and have only been able to generate single-well potentials. These potentials have different locations for their equilibrium proton position, and are quite flat at the bottom, but do not show large differences in their shape.

1.1 Acknowledgements

R.I. acknowledges financial support from the Natural Sciences and Engineering Research Council of Canada, from the Fonds Québécois de la Recherche sur la Nature et les Technologies, and from the Canadian Foundation for Innovation. Both authors would like to thank Professor Ayotte from University of Sherbrooke for enlightening discussions and for critically reviewing the final stage of this manuscript. The Réseau Québécois de Calcul de Haute Performance is acknowledged for allowing us to perform the calculations.

1.2 Reference

(1) Li, G.-S.; Maigret, D.; Rinaldi, D.; Ruiz-Lo´pez, M. F. *J. Comput. Chem.* **1998**, *19*, 1675.

(2) Warshel, A.; Papazyan, A. *Science* **1995**, *269*, 102.

(3) Mohammed, O. F.; Pines, D.; Dreyer, J.; Pines, E.; Nibbering, E. T. J. *Science* **2005**, *310*, 5745.

(4) Siwick, B.; Bakker, H. *J. Phys. Chem. B* **2008**, *112*, 378.

(5) Park, J. M.; Laio, A.; Iannuzzi, M.; Parrinello, M. *J. Am. Chem. Soc.* **2006**, *128*, 11318.

(6) Gu, W.; Frigato, T.; Straatsma, T. P.; Helms, V. *Angew. Chem., Int. Ed.* **2007**, *46*, 2939.

(7) Maupin, C. M.; Wong, K. F.; Soudackov, A. V.; Kim, S.; Voth, G. A. *J. Phys. Chem. A* **2006**, *110*, 631.

(8) Tanner, C.; Manca, C.; Leutwyler, S. *Science* **2003**, *302*, 1736.

(9) Domcke, W.; Sobolewski, A. L. *Science* **2003**, *302*, 1693.

(10) Ayotte, P.; Plessis, S.; Marchand, P. *Phys. Chem. Chem. Phys.* **2008**, *10*, 4785-4792.

(11) Iftimie, R.; Thomas, V.; Plessis, S.; Marchand, P.; Ayotte, P. *J. Am. Chem. Soc.* **2008**, *130*, 5901.

(12) Ayotte, P.; Hebert, M.; Marchand, P. *J. Chem. Phys.* **2005**, *123*, 184501.

(13) Golubev, N. S.; Shenderovich, I. G.; Smirnov, S. N.; Denisov, G. S.; Limbach, H.-H. *Chem.*s*Eur. J.* **1999**, *5*, 492.

(14) Car, R.; Parrinello, M. *Phys. Re*V. *Lett.* **1985**, *55*, 2471.

(15) Iftimie, R.; Tuckerman, M. *J. Chem. Phys.* **2005**, *122*, 214508.

(16) (a) Iftimie, R.; Thomas, J. W.; Tuckerman, M. E. *J. Chem. Phys.* **2004**, *120*, 2169. (b) Thomas, J. W.; Iftimie, R.; Tuckerman, M. E. *Phys.*
Re V. *B* **2004**, *69*, 125105.

(17) Jang, S.; Voth, G. A. *J. Chem. Phys.* **1999**, *111*, 2371.

(18) (a) Schenter, G. K.; Garrett, B. C.; Voth, G. A. *J. Chem. Phys.* **2000**, *113*, 5171. (b) Fanougarkis, G. S.; Schenter, G. K.; Xantheas, S. *J. Chem. Phys.* **2006**, *125*, 141102.

(19) Iftimie, R.; Tuckerman, M. E. *Angew. Chem., Int. Ed.* **2006**, *45*, 1144.

(20) Cleland, W. W.; Frey, P. A.; Gerlt, J. A. *J. Biol. Chem.* **1998**, *273*, 25529.

(21) Shenderovich, I. G.; Tolstoy, P. M.; Golubev, N. S.; Smirnov, S. N.; Denisov, G. S.; Limbach, H.-H. *J. Am. Chem. Soc.* **2003**, *125*, 11710.

(22) Gigue`re, P. A.; Turrell, S. *J. Am. Chem. Soc.* **1980**, *102*, 5473.

(23) Koch, W.; Holthausen, M. C. *A Chemist's Guide to Density Functional Theory*; VCH: New York, 2000.

(24) Becke, A. *Phys. Re*V. *A* **1998**, *38*, 3098.

(25) Lee, C.; Yang, W.; Parr, R. G. *Phys. Re*V. *B* **1998**, *37*, 785.

(26) Troullier, N.; Martins, J. L. *Phys. Re*V. *B* **1991**, *43*, 1993.

(27) Gordon, R. G. *Ad*V. *Magn. Reson.* **1968**, *3*, 1.

(28) McQuarrie, D. A. *Statistical Mechanics*; University Science Books: Sausalito, 2000.

(29) Reichman, D.; Roy, P. N.; Jang, S.; Voth, G. A. *J. Chem. Phys.* **2000**, *113*, 919.

(30) Marx, D.; Tuckerman, M. E.; Martyna, G. J. *Comput. Phys. Commun.* **2000**, *118*, 166.

(31) Bader, J. S.; Berne, B. J. *J. Chem. Phys.* **1994**, *100*, 8359.

(32) Sprik, M.; Hutter, J.; Parrinello, M. *J. Chem. Phys.* **1996**, *105*, 1142. (33) Lee, H.-S.; Tuckerman, M. E. *J. Chem. Phys.* **2007**, *126*, 164501.

(34) Tangney, P.; Scandolo, S. *J. Chem. Phys.* **2002**, *116*, 14.

(35) (a) Kuo, I. F. W.; Mundy, C. J.; McGrath, M. J. *J. Phys. Chem. B* **2004**, *108*, 12990. (b) Serra-Fernandez, M. V.; Artacho, E. *J. Chem. Phys.* **2004**, *121*, 11136. (c) Fernandez-Serra, M. V.; Ferlat, G.; Artacho, E. *Mol. Sim.* **2005**, *31*, 361.

(36) Bertie, J. E.; Ahmed, M. K.; Eysel, H. H. *J. Phys. Chem.* **1989**, *93*, 2210.

(37) (a) Desbat, B.; Huong, P. V. *J. Chem. Phys.* **1983**, *78*, 6377. (b) Kittelberger, J. S.; Hornig, D. F. *J. Chem. Phys.* **1967**, *46*, 3099.

(38) Martyna, G. J.; Klein, M. L.; Tuckerman, M. *J. Chem. Phys.* **1992**, *97*, 2635.

(39) Tuckerman, M. E.; Yarne, D. A.; Samuelson, S. O.; Hughes, A. L.; Martyna, G. J. *Comput. Phys. Commun.* **2000**, *128*, 333.

(40) Khorami, J.; Beaudoin, R.; Menard, H. *Can. J. Chem.* **1987**, *65*, 817.

(41) Roscioli, J. R.; Diken, E. J.; Johnson, M. A.; Horvath, M. A.; McCoy, A. B. *J. Phys. Chem. A* **2006**, *110*, 4943.

(42) Yates, B. F.; Schaefer, H. F.; Lee, T. J.; Rice, J. E. *J. Am. Chem. Soc.* **1988**, *110*, 6327.

(43) Handy, N. C.; Carter, S.; Colwell, S. M. *Mol. Phys.* **1999**, *96*, 477.

(44) Wannier, G. H. *Phys. Re*V. **1937**, *52*, 191.

(45) Boys, S. F. *Re*V. *Mod. Phys.* **1960**, *32*, 296.

(46) Ando, K.; Hynes, J. T. *J. Phys. Chem. A* **1999**, *103*, 10398.

(47) Silanpa¨a¨, A. J.; Simon, C.; Klein, M. L.; Laasonen, K. *J. Phys. Chem. B* **2002**, *106*, 11315.

(48) The exception involved a simulation with the HF molar fraction of 0.2, whereby the contact ion pair was stabilized by the presence of 3 HB-donating water molecules in the first solvation shell of F^-. It is not clear, however, whether this molecular environment is statistically relevant for the dissociation of HF in very dilute aqueous solutions.

(49) Laasonen, K.; Klein, M. L. *Mol. Phys.* **1996**, *88*, 135.

(50) Hyman, H. H.; Kilpatrick, M.; Katz, J. J. *J. Am. Chem. Soc.* **1957**, *79*, 3668.

(51) For a more quantitative definition of the expression "on the verge of rupture", see Figure 3 in ref 10.

(52) Laasonen, K.; Larrucea, J.; Silanpa¨a¨, A. *J. Phys. Chem. B* **2006**, *110*, 12699.

(53) Swalina, C.; Wang, Q.; Chakraborty, A.; Hammes-Schiffer, S. *J. Phys. Chem. A* **2007**, *111*, 2206.

(54) Ramı´rez, R.; Lo´pez-Ciudad, T.; Kumar, P.; Marx, D. *J. Chem. Phys.* **2004**, *121*, 3973.

(55) Reichman, D. R.; Roy, P. N.; Jang, S.; Voth, G. A. *J. Chem. Phys.* **2000**, *113*, 919.

(56) Raugei, S.; Klein, M. L. *J. Am. Chem. Soc.* **2003**, *125*, 8992.

(57) (a) Straus, J. B.; Calhoun, A.; Voth, G. A. *J. Chem. Phys.* **1995**, *102*, 529. (b) Wu, Y.; Chen, H.; Wang, F.; Paesani, F.; Voth, G. A. *J. Phys. Chem. B* **2008**, *112*, 467. (c) Tuckerman, M. E.; Marx, D.; Klein, M. L.; Parrinello, M. *Science* **1997**, *275*, 817.

On the Formation of Proton-Shared and Contact-Ion Pair forms During the Dissociation of Moderately Strong Acids: An Ab Initio Molecular Dynamics Investigation

Vibin Thomas, Patrick Maurer * Radu Iftimie*,§,¶

* *Département de Chimie, Université de Montréal, CP 6128, succursale Centre-Ville, Montréal, H3C3J7, Canada* §*To whom correspondence may be addressed.*

Published in *J. Phys. Chem. B***113**(13):4152-60 (2010)

Abstract: Acid ionization and dissociation are phenomena that play a fundamental role in chemistry and biology, but their microscopic details are largely unknown. We use ab initio molecular dynamics to identify and characterize various structures that are formed along the pathway of dissociation of trifluoroacetic acid (pK_a = 0.5). The present results demonstrate that solutions of moderately strong ($-1 \le pK_a \le 1$) carboxylic acids contain significant quantities of at least two forms whose bonding patterns are intermediate between those of covalent and dissociated structures, $R-COOH\cdots OH_2$ and $R-COO^-(aq) + H_3O^+(aq)$, respectively. The first is a proton-shared structure of the form $R-COO^{\delta-}\cdot H^{\cdot\delta+}OH_2$ which can be distinguished from the covalent form by its characteristic "continuous" absorption below 1700 cm^{-1}. The second is a contact ion pair whose average structure can be written as $R-COO^-\cdot H_3O^+$. We demonstrate that the transformation of proton-shared into contact ion pair forms coincides with the disappearance of the carbonyl vibration mode centered around 1720 cm^{-1} and the appearance of the asymmetric and symmetric carboxylate $O{=}C{=}O$ vibration modes at 1620 and 1380 cm^{-1}, respectively. The aforementioned transformation is accompanied by significant changes in the first solvation shell of the acid molecule which we discuss.

5. On the Formation of Proton-Shared and Contact-Ion Pair forms During the Dissociation of Moderately Strong Acids: An Ab Initio Molecular Dynamics Investigation

5.1 Introduction

Proton translocation constitutes a fundamental class of chemical transformations and is ubiquitous as an Proton transfer reactions are among the most widespread and important transformations in chemistry[1,2] and biology[3-7]. Despite their ubiquitous nature and intense research scrutiny, insights into the microscopic mechanisms that facilitate proton transfer between Brønsted donors and acceptors are largely lacking. In particular, the exact nature of proton donor and acceptor intermediates is unknown even for relatively simple acid-base neutralization reactions that take place in bulk water. The relevance of these intermediates to the general dissociation mechanism of acids in water has been emphasized by Eigen[8,9] and Weller[10] half a century ago. In the Eigen-Weller model, the covalently intact acid molecule AH is in rapid equilibrium with an encounter-pair intermediate of the form $A^- \bullet H^+(H_2O)_n \bullet OH_2$ before it dissociates, according to the two-step dissociation equilibrium:

$$\begin{aligned} AH(aq) + H_2O &\overset{1}{\rightleftharpoons} [A^- \cdot H^+(H_2O)_n \cdot OH_2] \\ [A^- \cdot H^+(H_2O)_n \cdot OH_2] &\overset{2}{\rightleftharpoons} A^-(aq) + H_3O^+ \end{aligned} \tag{5.1}$$

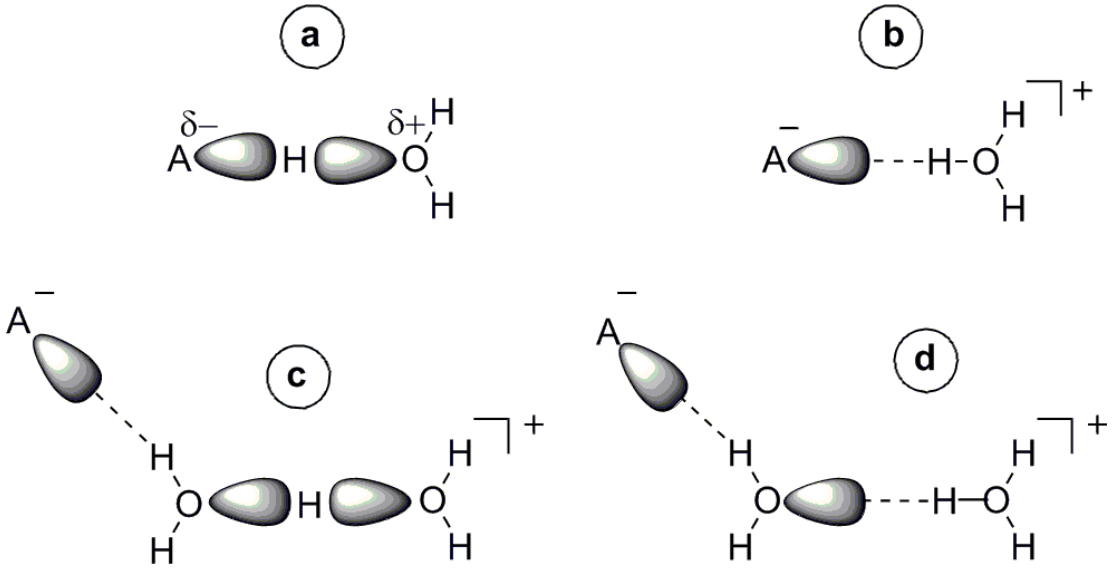

Figure 5-1. A pictorial view of a) proton-shared, b) contact, and c)-d) solvent-shared ion pairs. In the proton-shared case, the solvent creates a potential in which the proton can move in-between two electronegative atoms without having to overcome any significant barrier. These limiting forms are represented in the text as: a) $A^{\delta-} \bullet H \bullet {}^{\delta+}OH_2$; b) $A^- \bullet H_3O^+$; c)-d) $A^- \bullet OH_2 \bullet H_3O^+$

The size of the idealized, spherically-symmetric encounter pair intermediate has typical values ranging from 6 to 8 Å, corresponding to n=2 or n=3.[8,11] Equation (1) constitutes a short-hand representation which emphasizes the rupture of the covalent bond A—H, but hides the explicit[12] role played by water molecules, and the possible formation of other dissociation intermediates.[13] Nevertheless, with recent developments in time-resolved spectroscopy techniques[11,14-22] and computational approaches[23-29], these issues have started to be investigated using atomic resolution[30], leading to a deeper understanding of the complex[31] dissociation process.

Theoretical investigations based on empirical valence bond[32] models and, more recently, ab initio[23] molecular dynamics simulations, have been successfully employed to refine our understanding of Brønsted acid-base equilibria in pure water[12,29], aqueous

solutions of strong[33-39] and weak[13,40-47] acids and bases[48], and biochemical environments[24,49,50]. In this paper, we utilize ab initio molecular dynamics to investigate the structural and spectroscopic properties of intermediate structures, which are formed along the dissociation pathway of trifluoroacetic acid, $F_3C-COOH$. The choice of the solute molecule was suggested by the infrared spectroscopy results reported by Zundel et al[51], who demonstrated that aqueous solutions of this moderately strong (pKa = 0.5) acid contain significant amounts of intermediate forms which are neither covalently intact, nor fully dissociated ions. Our previous work[13,44] on hydrofluoric acid established that the earliest step along the dissociation pathway, which consists of transforming the covalent form of an acid into the proton-shared form depicted in Fig.5-1a is accompanied by the formation of an extremely wide but featureless infrared absorption ranging from 1000 to 3000 cm^{-1}. In addition to this "continuous" absorption, the dissociation of the trifluoroacetic acid must also be accompanied by changes in the vibration modes of the carboxyl moiety. An important goal of the present investigation is to establish whether these localized spectral changes that occur in the carbonyl/carboxylate vibration modes can also be related with the formation of a well defined structure along the dissociation pathway.

It is often taken for granted that the dynamics of the carbonyl and carboxylate absorption modes coincides with that of the covalent and dissociated forms, respectively. This is usually an excellent approximation because the concentration of intermediate forms can be neglected except in the case of moderately strong acids, whose pKa values belong to the interval $-1 \le pK_a \le 1$. Owing to the small value of their dissociation free energy, aqueous solutions of these acids tend to contain significant concentrations of covalent and dissociated forms, as well as ion-pairs and other intermediate forms. In this case it is necessary to explicitly consider the contribution of

dissociation intermediates to the total spectrum in order to explain discrepancies that would otherwise exist between pKa values computed from ion mobility and from spectroscopy measurements: In the particular case of the trifluoroacetic acid, Covington et al.[52], and later Zundel et al.[51] and Gelb et al.[53] showed that infrared[51], Raman[52], ^{1}H nuclear magnetic resonance[53], and ion mobility measurements could be reconciled only by considering that ion pairs, which do not contribute to charge mobility measurements but have spectroscopic properties that resemble those of dissociated ions, are present in larger concentrations than un-ionized, covalent forms.

The present investigation confirms our previous[54] conclusion that the appearance of a continuous absorption extending below 1700 wavenumbers is a signature for the formation of proton-shared forms such as those depicted in Fig.5-1a. In addition, our results indicate that the transformation of the carbonyl stretch absorption pattern into those of the carboxylate vibration modes marks the formation of contact ion pairs, whose average structure is depicted in Fig.5-1b. In addition to contributing to the understanding of the general mechanism of proton transfer reactions, these conclusions should also help the interpretation of experimental data obtained in ultrafast pump-probe experiments that employ acids or bases which become moderately strong upon electronic excitation.

5.2 Computational Methods and their Accuracy

We employ Car-Parrinello[55] (CP) molecular dynamics to describe electronic polarization effects and the bond-breaking, bond-forming dynamics. In the CP approach, the nuclear trajectory is generated using forces obtained from electronic structure calculations performed on the fly as the simulation proceeds, employing density functional theory[56] (DFT). An initially minimized set of orbitals is “propagated” from one nuclear

configuration to the next via a fictitious dynamics as opposed to an explicit minimization or diagonalization[23]. Taking n to be the number of occupied orbitals, N the number of nuclei, $\psi_1(\mathbf{r},t),\cdots,\psi_n(\mathbf{r},t)$ the electronic orbitals, and $R_1(t),\cdots,R_N(t)$ the nuclear positions, the CP equations of motion are

$$\begin{aligned} \mu\ddot{\psi}_i(\mathbf{r},t) &= -\frac{\delta E}{\delta\psi_i^*(\mathbf{r},t)} + \sum_j \Lambda_{ij}\psi_j(\mathbf{r},t) \\ M_I\ddot{\mathbf{R}}_I &= -\frac{\partial E}{\partial \mathbf{R}_I} \end{aligned} \tag{5.2}$$

where

$$E = E[\{\psi\},\{\mathbf{R}\}] \tag{5.3}$$

is the energy functional, Λ_{ij} are a set of Lagrange multipliers used to maintain the orthogonality of the orbitals via a constraint, and μ is the fictitious electron mass, which determines the time scale on which the fictitious orbital dynamics occurs. The simulations are performed using the B[57]-LYP[58] generalized gradient exchange-correlation functional, plane wave basis sets, and norm-conserving Troullier-Martins[59] pseudopotentials.

Using the time-correlation formalism[60] of linear response theory[61], the value of the frequency-dependent Beer-Lambert absorptivity coefficient $\alpha(\nu)$ can be written as

$$\begin{aligned} \alpha(\nu) \overset{\text{def}}{=} -\frac{\ln(I/I_0)}{\ell} &= \frac{\pi\nu\left[1-\exp\left(-\beta\hbar 2\pi\nu\right)\right]}{3\hbar c V n(\nu)\varepsilon_0}\cdot \\ &\cdot\int_{-\infty}^{\infty}\exp(2\pi i\nu\tau)\left\langle\hat{M}(0)\cdot\hat{M}(\tau)\right\rangle_{qm} d\tau \end{aligned} \tag{5.4}$$

where qm indicates a quantum mechanical ensemble average, ℓ is the length of the optical path, α has Neperian units, $\hbar$ is Planck's constant, V is the sample's volume, ε_0 is

the vacuum permittivity, and c is the speed of light. In Eq. (5.4), $\hat{M}(0)$ and $\hat{M}(\tau)$ represent the values of the quantum-mechanical dipole moment operator written in the Heisenberg representation at times $t = 0$ and $t = \tau$, respectively, and are defined using Système International (SI) charge units; $\beta = 1/(k_B T)$ with k_B being Boltzmann's constant and T the absolute temperature.

For condensed-phase systems such as those of interest in this paper, explicit eigenstate calculations[62] have a far too high computational overhead to be carried out, while direct, real-time, path-integral approaches[63] suffer from such severe phase oscillations that convergence cannot be achieved on any realistic time scale. In contrast, classical molecular dynamics can often be used to obtain the analogous correlation functions for a corresponding classical system. However, there is no general prescription for rigorously relating a quantum correlation function to a classical one. The precise relationship depends on the underlying Hamiltonian generating the dynamics.

Nevertheless, if one assumes the validity of the central approximation[64,65] of the centroid molecular dynamics theory, and considers that the electronic dipole moment operator is approximately linear, the Beer-Lambert absorptivity can be computed as

$$\alpha(\nu) \cong \frac{\beta}{6n(\nu)Vc\varepsilon_0} \int_{-\infty}^{\infty} \exp(2\pi i \nu \tau) \left\langle \dot{M}_c(0) \cdot \dot{M}_c(\tau) \right\rangle_c d\tau \quad (5.5)$$

where the autocorrelation function involves the centroid average[64] of the time-derivative of the dipole moment centroid symbol[64]. Moreover, since centroid averages are computed in practice[66] by means of a finite number of path-integral quasi-particles, one can adopt a further approximation, which consists of considering a single imaginary-time discretization of the quasi-particle chain. This amounts essentially to adopting the well-known harmonic approximation[67] which reads

$$\alpha(\nu) \cong \frac{\beta}{6n(\nu)Vc\varepsilon_0}\int_{-\infty}^{\infty}\exp(2\pi i\nu\tau)\left\langle \dot{M}_{cl}(0)\cdot\dot{M}_{cl}(\tau)\right\rangle_{cl} d\tau \quad (5.6)$$

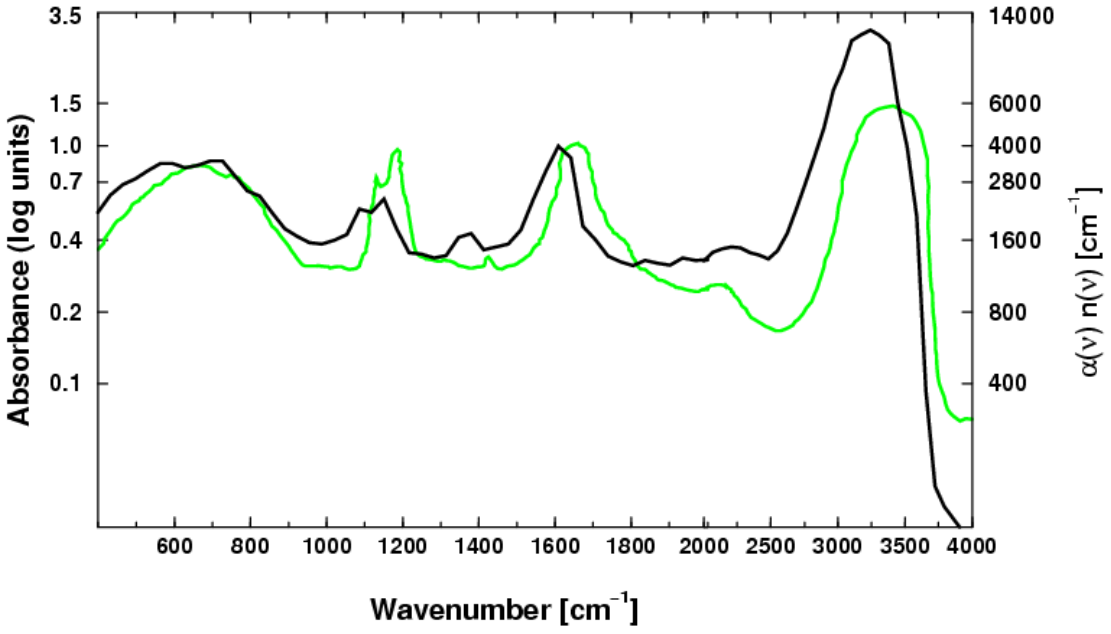

Figure 5-2. Comparison between computed (black) and experimental (green) IR spectra of aqueous solutions of $F_3C{-}COOH$. The experimental plot of the absorbance defined in Eq. (5.9) was obtained by digitizing the data given in Ref. 51. The values of the Beer-Lambert absorptivity are computed using Eq. (5.6). Note the change of scale on the wavenumber axis at 2000 cm^{-1}.

where "cl" refers here to classical (i.e.: Newtonian) time-derivatives of the dipole moment, and to classical ensemble averages (i.e.: phase-space integration). Our approach in the present work is to adopt the harmonic approximation, i.e.: Eq. (6). This is justified by our previous results[13,54] on amorphous mixtures of HF and H_2O: It was demonstrated[13] that utilizing the harmonic approximation instead of the centroid molecular dynamics formalism results in red-shifting all OH and FH vibration modes between 1000 and 3400 wavenumbers by 100-250 cm^{-1}. Moreover, neglecting nuclear quantum effects often improves agreement between experimental IR data and density

functional calculations, by reducing the latter's tendency to underestimate vibration frequencies in hydrogen-bonded systems.

In order to rationalize the molecular origin of the features that appear in the computed IR spectra we have utilized two approaches. The first method is a spectrum decomposition technique that was previously proposed[44] by Iftimie and Tuckerman and is particularly useful[13,44,54] when investigating the origin of very broad and intense absorptions such as those caused by shared-proton structures, since these absorptions are not easily attributable to a localized vibration mode, and exhibit transition dipole moment intensities that vary significantly[44,54] with vibration frequency. The decomposition of the IR spectrum relies on an approximate, but chemically intuitive decomposition of the total dipole moment into molecular components, and employs maximally-localized[68,69] Wannier[70]-Boys[71] orbitals that are generated on-the-fly using a modified Car-Parrinello algorithm.[69,72] The approach proposed in Ref. 69 amounts to calculating the contribution $[\alpha(\nu)n(\nu)]_A$ of a molecule A in solution to the total absorption spectrum $\alpha(\nu)n(\nu)$ by computing the spectrum of the time-dependent cross-correlation function between the molecular dipole moment μ_A of molecule A and the total dipole moment M :

$$[\alpha(\nu)n(\nu)]_A \cong \frac{\beta}{6Vc\varepsilon_0}\int_{-\infty}^{\infty}\exp(2\pi i\nu\tau)\left\langle \dot{\mu}_A(0)\cdot\dot{M}(\tau)\right\rangle_{cl} d\tau \quad (5.7)$$

The second method employed here consists of calculating normal-mode vibration spectra defined as

$$I(\nu) = \int_{-\infty}^{\infty}\exp(2\pi i\nu\tau)\left\langle \dot{d}(0)\cdot\dot{d}(\tau)\right\rangle_{cl} d\tau \quad (5.8)$$

where $\dot{d}$ represents the time-derivative of the normal-mode variable d. This approach was presently employed by taking d to be the distance between carbon and oxygen

atoms in the carboxyl group. Therefore, the normal-mode intensity spectrum $I(\nu)$ will be utilized to indicate the presence or absence of carbonyl C=O, and of symmetric and antisymmetric $O \cdots C \cdots O$ vibration stretching modes.

We employed regular atomic masses for all atoms except for the carbon and oxygen atoms that form the carboxyl moiety. Since previous ab initio molecular dynamics simulations suggested that the B-LYP functional understimates[73] the frequency of carbonyl stretching vibrations in gas-phase and in water by 100-150 cm^{-1}, we found it convenient to artificially decrease the mass of carbon and oxygen atoms forming the carboxyl group by 10% in order to improve agreement between experiment and calculated IR spectra.

The computational protocol involves employing a plane wave basis set cutoff of 100Ry, in conjunction with a fictitious electron mass μ=240 a.u., an integrated time step δt=0.06 fs, and a simulation temperature T=350 K. These choices were suggested by results that were previously obtained[54] in the case of pure, liquid and crystalline, HF and H_2O: It was demonstrated[54] that utilizing the present computational protocol leads to computed IR spectra that have the correct absorption intensities, and are red-shifted by only 40-100 cm^{-1} with respect to room-temperature experimental data.

At the beginning of the simulation the system consists of 43 solvent molecules and two un-dissociated solute molecules in a cubic primitive box of length L=11.5 Å. Three simulations were performed using identical protocols, but starting from different initial conditions. The equilibrations were performed in the NVT ensemble, using a Nose-Hoover chain thermostat[74] on each degree of freedom for a period of 10 ps. The actual spectra were computed from unbiased dynamical trajectories in the NVE ensemble, by

continuing the simulations for periods varying from 17 to 27 ps. All calculations were carried out using the PINY_MD[75] simulation package.

5.3 Results and Discussion

5.3.1 IR spectra of aqueous $F_3C-COOH$: experiment vs. computer simulation.

To set the stage, the graphs displayed in Fig.5-2 contrast the total IR spectrum of an aqueous solution of trifluoroacetic acid reported by Leuchs and Zundel[51] with our computational results averaged over the three simulations. The experimental plot was obtained by digitizing the data reported in Ref. 51, and consists of absorbance spectra defined as

$$A(\tilde{\nu}) = -\log\left(I(\tilde{\nu}) / I_0(\tilde{\nu})\right), \qquad (5.9)$$

with the abscissa being given in wavenumber units $\tilde{\nu} = \nu / c$. The computed spectra consist of $\alpha(\tilde{\nu})n(\tilde{\nu})$ values, which are computed using Eq. (5.6). The experimental absorbance values can be related to the computed Beer-Lambert absorptivities through the length ℓ of the optical absorption path:

$$A(\tilde{\nu}) = \frac{\alpha(\tilde{\nu}) \cdot \ell}{\ln 10}. \qquad (5.10)$$

A quantitative comparison between experiment and theory is difficult because the experimental data was obtained[51] using a wedge-shaped geometry of the absorption cell instead of the box-shaped one, for which the Beer-Lambert Eq. (5.10) applies. Nonetheless, similarities between experiment and calculation are quite striking despite the fact that experimental spectra appear[51] to be saturated in the region of the OH stretch vibration at 3400 wave numbers, and correspond to solutions that are 50% more

dilute (1.6 M) than those investigated computationally (2.4 M). In particular, all relevant experimental absorption bands can be unambiguously identified in the computed spectra at values that are red-shifted by 40-70 cm^{-1}, the only exception being the solvent OH stretch absorptions which are red-shifted by 150 cm^{-1}. These differences are consistent with our previous observations[54] concerning the agreement between experimental spectra of pure water and computed values obtained by means of the B-LYP exchange-correlation functional at temperatures that are larger by 40-75 K.

The high level of agreement between theory and experiment demonstrates that the present computational protocol is adequate and indicates that the molecular species formed in our simulations are representative of those which exist in experimental conditions. In the following, we report a detailed investigation of the structural and spectroscopic properties of the chemical species present in our simulations.

5.3.2 IR spectroscopic signatures of covalent and proton-shared forms.

Leuchs and Zundel demonstrated[51] that comparison between the spectra of aqueous solutions of $F_3C{-}COOH$ in the presence of strong acids such as HCl, or strong bases such as NaOH, can be utilized to unambiguously assign the peak (or shoulder in more dilute solutions) at 1760 cm^{-1} to C=O vibrations in the undissociated acid, and the absorption at 1430 cm^{-1} to the symmetric stretching of the negatively charged carboxyl group in the conjugate base. However, their study as well as the earlier Raman investigation of Covington et al.[52] also showed that one cannot reconcile the pKa values computed from the intensity of these two peaks with values obtained from conductivity measurements, unless the dissociation equilibrium is considered to be a two-step process involving the formation of an ion-pair intermediate of dissociation I:

$$F_3C\text{-}COOH\ (aq) + H_2O \overset{1}{\rightleftharpoons} I$$
$$I \overset{2}{\rightleftharpoons} F_3C\text{-}COO^-(aq) + H_3O^+(aq) \qquad (5.11)$$

Moreover, these researchers had to assume that the proposed intermediate I has conductivity properties identical to those of the un-ionized molecule $F_3C{-}COOH$ (aq), but that its infrared[51], Raman[52] and NMR[53] spectra are identical to those of the dissociated species $F_3C{-}COO^-$ (aq).

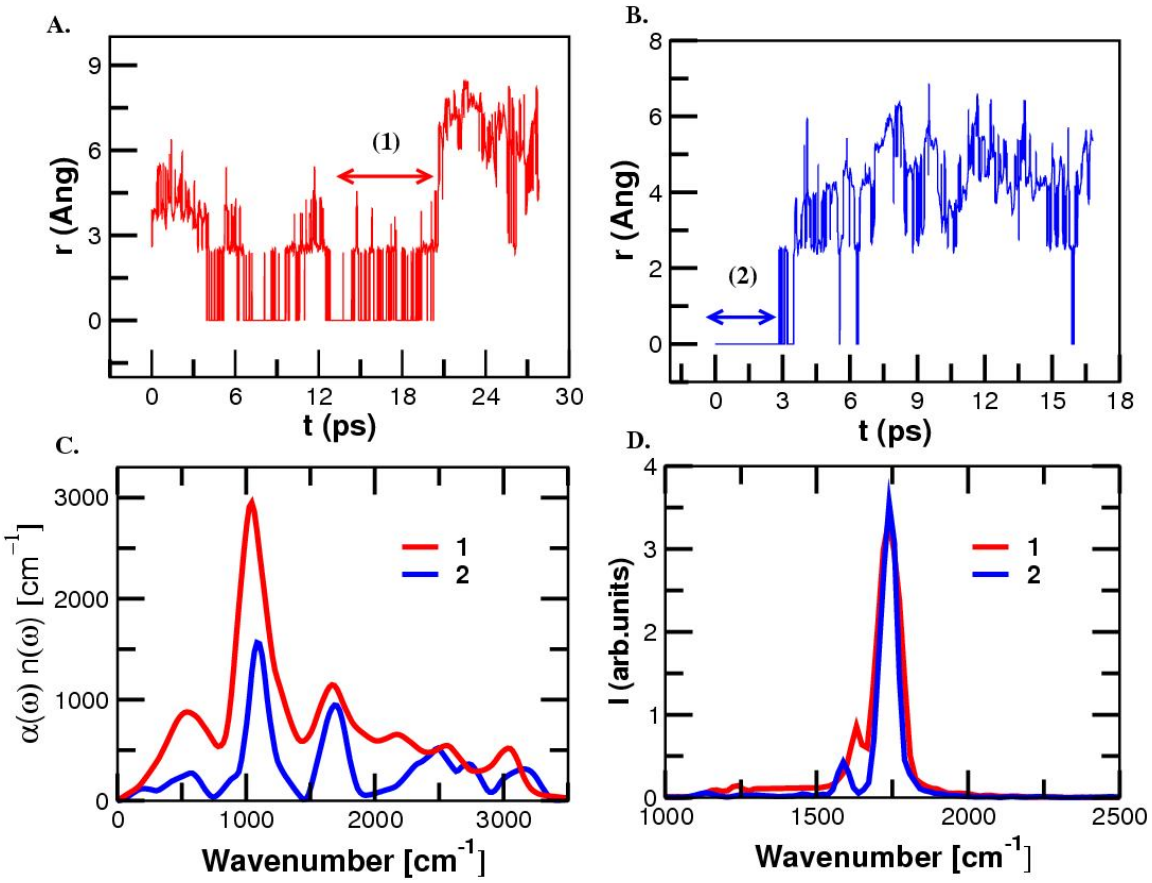

Figure 5-3. A and B: Two trajectories of the dissociation indicator r (see text and Eq. 12). In panel C, the time intervals denoted (1) and (2) are used to compute the IR spectrum of the covalent form of F3C−COOH (blue) and F3C−COO− • H • +OH2 (red), respectively, using Eq. (7). Panel D shows the autocorrelation spectra of the CO distance computed using Eq. (5.8).

Experimental investigations such as those mentioned in the previous paragraph are able to provide only indirect information concerning the actual chemical structure of the intermediate I. Covington and his collaborators were the first to point out[52] that the existing experimental data was consistent with the presence of a contact ion-pair dissociation intermediate I whose structure could resemble that drawn Fig.5-1b: First, contact ion pairs are overall neutral species, and their participation to the overall conductivity of the system is negligible. Second, a stable species whose structure can be written as $F_3C{-}COO^- \bullet H_3O^+$ is likely to display spectroscopic properties that are similar to those of the fully dissociated trifluoroacetate base $F_3C{-}COO^-$ (aq) because the IR, Raman and NMR properties of a chemical entity are primarily determined by its bonding topology, and only to a secondary extent by the nature of its first solvation shell.

In order to investigate the possible presence of contact ion-pair forms in our simulation, we first need to adopt a criterion for differentiating reactants, products, and intermediate structures. For the purpose of the present investigation we assume that the dynamics of the relevant chemical species parallels that of changes in the infrared absorption spectrum. Although this criterion may be too restrictive and hide the presence of intermediates that lack a specific spectroscopic signature, it has the advantage that it allows one to connect computation results with experimental data. In practice, this means that various segments of the molecular dynamics trajectory are considered to sample reactant, intermediate or product subspaces depending on the presence or absence of the following key spectral features: 1) An extremely wide, continuous absorption extending below 1700 cm^{-1}; 2) A localized band centered around 1720 cm^{-1} (carbonyl vibration, exp. value 1760 cm^{-1}); 3) Two localized bands centered

around 1620 and 1380 cm^{-1} (asymmetric and symmetric carboxyl stretching, exp. value for the symmetric stretch is 1430 cm^{-1}).

We start by investigating the usefulness of the following ionization indicator

$$r = \min\left\{dist(O_1, O^*), dist(O_2, O^*)\right\} \quad (5.12)$$

where O_1 and O_2 are the two oxygen atoms of the trifluoroacetate moiety, O* corresponds to the oxygen atom that carries the proton "defect" and belongs either to a water molecule or to the carboxyl residue, "dist" represents the distance between two atoms, and the mathematical "min" function returns the minimum of two numbers. The $r = 0$ subset can be viewed as an approximate representation of what is sometimes called[52,53] the un-ionized, or covalent state, since the proton "defect" is closer, in this case, to one of the carboxylic oxygen atoms than to any of the oxygen atoms of the solvent molecules. Conversely, $r > 0$ indicates that the trifluoroacetate moiety is involved in the formation of an ionic structure. The results depicted in Fig. 3-3 A and B show two trajectories of the ionization indicator r.

We start our analysis by focusing on the segment of trajectory denoted by (2) in Fig. 5-3B and which, evidently, corresponds to covalently intact forms $F_3C{-}COOH$ (aq). The data depicted in blue in Fig. 5-3C represents the contribution of the covalent form to the total IR spectrum, computed using the spectrum decomposition approach from Eq. (7). This spectrum shows clearly that the region of the absorption spectrum between 1000 and 2000 cm^{-1} can be entirely explained by considering localized vibrations modes: C-F stretching vibrations centered at 1100 cm^{-1}, C=O stretching around 1700 cm^{-1} and C-O stretching forming a shoulder between 1200 and 1340 cm^{-1}. Fig.5-3C contrasts the previously mentioned spectrum with that obtained from segment (1) displayed in Fig.5-3A, and which corresponds to the proton-shared form $F_3C{-}COO^{\delta-} \bullet H \bullet {}^{\delta+}OH_2$. The contrast between the red and the blue spectra in Fig. 5-3C is striking and shows

convincingly that the formation of the proton-shared form coincides with the apparition of an extremely wide continuous absorption which extends below 1700 wave numbers. These results are consistent with the conclusions formulated[44] by Iftimie and Tuckerman in their computational study of aqueous solutions of hydrofluoric acid. Moreover, they are also consistent with the experimental data of Leuchs and Zundel,[51] who contrasted the behavior of the moderately strong trifluoroacetic acid (pKa=0.5) with that of the weaker difluoroacetic acid (pKa=1.34): "For difluoroacetic acid, with the addition of water, a continuous absorbance arises in the region 3000-1700 cm^{-1}. This continuum is however less intense than that with trifluoroacetic acid. Furthermore, below 1700 cm^{-1} the increase in the background absorbance may be explained by the slopes of the bands, for instance at $\approx$1000 cm^{-1} by the γ_{OH} vibration …" The present results indicate that the difluoroacetic acid forms mostly covalent structures in concentrated solutions, whereas the trifluoroacetic acid forms proton-shared forms as well as ion pairs.

5.3.3 IR spectroscopic signatures of contact, solvent-shared and dissociated forms.

The results depicted in Fig.5-3D compare the carbonyl normal-mode vibration spectra of the covalent and proton-shared forms. In complete contrast with the data shown in Fig.5-3C, these spectra are almost identical, and indicate strongly that the transformation of the C=O double bond into a carboxyl $C\!=\!O$ bond whose order is 1.5 has not been accomplished upon formation of the proton-shared forms. The indicator r defined in Eq. (12) is therefore only useful to characterize the advancement of the dissociation reaction until proton-shared forms are formed. In order to characterize subsequent stages of the dissociation reaction, one needs to define additional indicators, which should be able to capture, among other things, the transition from structures that

exhibit carbonyl C=O vibrations to structures that exhibit symmetric and asymmetric $O=C=O$ vibration stretching modes.

We have tried a number of indicators, most of which were based on various definitions of coordination numbers of the oxygen atoms involved in the dissociation process. However, these indicators did not allow us to define a sharp transition between different segments of the molecular dynamics trajectory. This, in turn, rendered the definition of the time-intervals from which vibration spectra can be computed somewhat arbitrary and less useful for the present purpose.

An indicator which provides a sharp distinction between some of the intermediate forms depicted in Fig.5-1 was obtained by utilizing the concept of running or moving average of a time-series. In particular we have found that the running *median* of the ionization indicator time series $r(t)$, denoted as $\bar{r}(t)$, where its value $\bar{r}(\tau)$ at some moment τ represents the median of the trajectory of r in the time-interval $[\tau - T, \tau + T]$, represents an empirical, but useful method of separating the molecular dynamics trajectory into well-defined segments corresponding to undissociated, intermediate and dissociated forms.

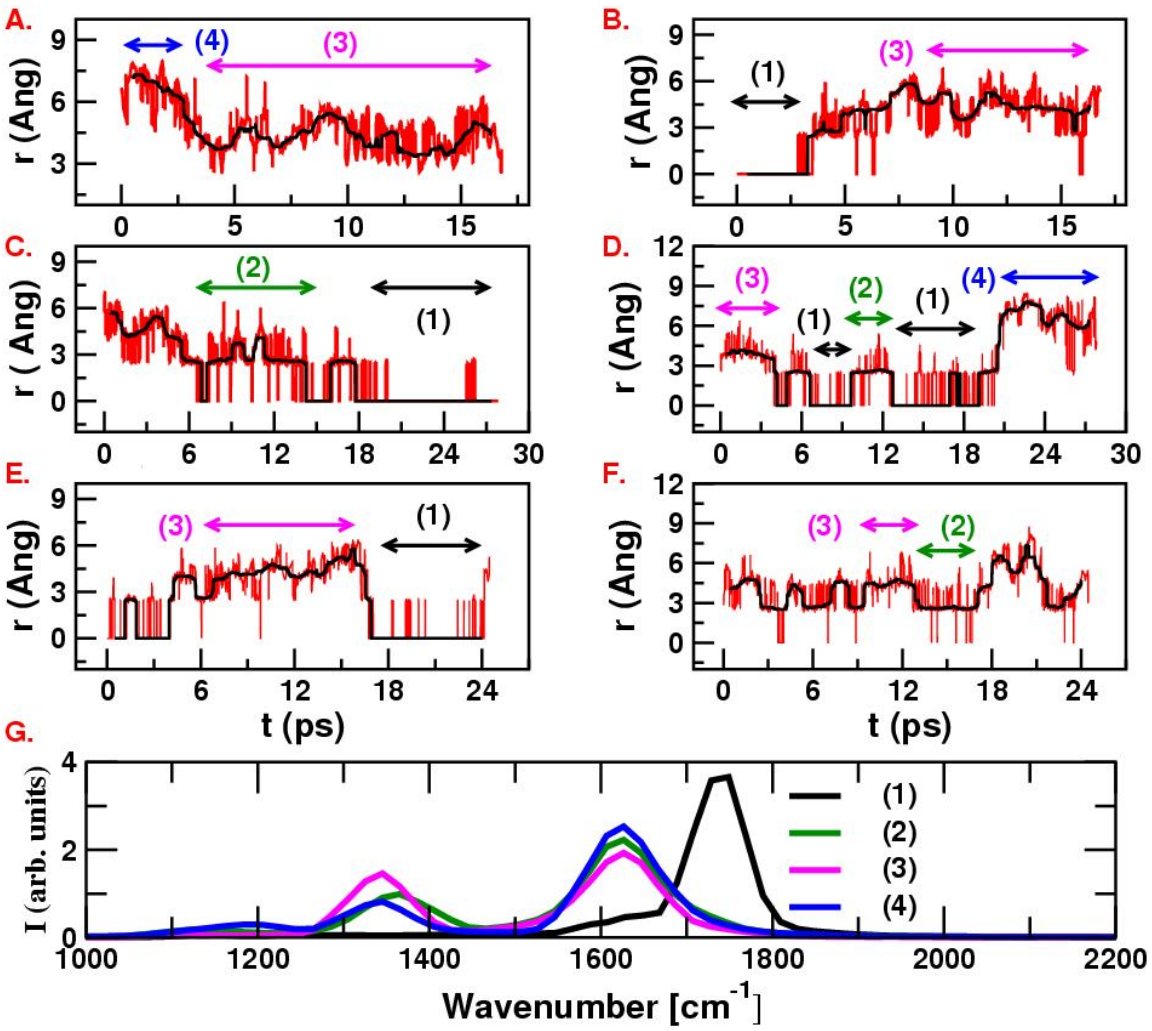

Figure 5-4. A-F: The trajectories of the dissociation indicator r (red; see text and Eq. 5.12) and its running median $\bar{r}$ (black; see text) obtained in the present investigation (2 molecules per system, 3 simulations). The segments of trajectory denoted by (1), (2), (3) and (4) correspond to undissociated molecules (black; both covalent and proton-shared forms, see text and Fig.5-3), contact (green) and solvent-shared (magenta) ion pairs, and fully dissociated ions (blue); see also text and Fig.5-2. In G the autocorrelation spectra of the CO distance are computed using Eq. (8) for all labeled segments. Panels B and D correspond to panels B and A from Fig. 5-3, respectively.

The results depicted in Fig. 5-4 A-F show that trajectories of $r(t)$ and $\overline{r}(t)$ with the median being calculated from 1 ps intervals, i.e., by using $T = 0.5\,\text{ps}$ in the above-mentioned definition of the running average. As expected, the utilization of a moving average effectively "shuts off" the details of the dynamics of $r(t)$ on a timescale smaller than $2T$ = 1ps. Moreover, using the median instead of the normal average makes the transition from $\overline{r} = 0$ to $\overline{r} \cong 2.6$ and subsequently to $\overline{r} \cong 4.6\,\text{Å}$ appear significantly sharper (data provided as supplementary information). The stepwise-like trajectory of $\overline{r}$ allows one to "color" the molecular dynamics trajectory in four different regions: Segments denoted by (1) and colored in black belong to the set of structures which remain undissociated on average. These structures can belong to a contiguous $r = 0$ segment, as in Fig.5-4B and C, in which case they qualify as covalent forms according to the definition adopted in the previous section. Alternatively, the $\overline{r} = 0$ segments also comprise proton-shared forms in which the departing proton moves almost freely between the carboxyl moiety and a solvation water molecule, but nevertheless, spends *on average* more time in the neighborhood of the oxygen atoms of the trifluoroacetate anion.

The segments denoted by (2) and colored in green comprise structures in which the identity of the oxygen atom that carries the excess proton fluctuates significantly, but, most of the time the latter belongs to a water molecule from the first solvation shell of the trifluoroacetate ion. Therefore, one can consider that these structures represent a contact ion pair $F_3C{-}COO^- \bullet H_3O^+$ such as the one depicted in Fig.5-1b. We must emphasize that the hydronium ion is not a long-lived Eigen form, the three O-H bonds being continuously formed and broken on a sub-picosecond timescale. Nevertheless, the lengths of the three OH bonds of the hydronium ion are, *on average*, almost equal, which justifies the use of the contact ion pair concept and of the representation depicted

in Fig.5-1b. The segments denoted by (3) and colored in magenta correspond to solvent-shared ion pairs, whose structures can be written as $F_3C{-}COO^- \bullet H_2O \bullet H_3O^+$ and are depicted in Fig.5-1 c)-d). Similar to the case of contact ion pairs, visual inspection of the segments labeled in magenta in Fig 4-3A-F indicate that the solvent-separated hydronium ion H_3O^+ should not be conceived as a long-lived species as was represented by Eigen, but as a highly fluctuating form. A qualitative inspection of the trajectories of the running median $\bar{r}(t)$, and, in particular, those depicted in panel F, indicate that the transitions between contact ($\bar{r} \cong 2.6$ Å) and solvent-shared ($\bar{r} \cong 4.6$ Å) forms can be located with little ambiguity. In contrast, the transitions between the solvent-shared forms and the fully dissociated ions which are colored in blue are less well-defined. Moreover, no definite conclusions can be drawn about these transitions from the present simulations due to the limited box size (L=11.5 Å).

Using the definition of undissociated, ion-pair and dissociated forms shown in panels A to F, we have computed the vibration spectrum of the CO normal mode according to Eq. (8). The results are shown in panel G and indicate that the moving median coordinate $\bar{r}(t)$ is an excellent indicator of the transition between forms that exhibit carbonyl C=O vibrations and those which exhibit symmetric and asymmetric carboxylate $O{=}C{=}O$ vibrations. Visual inspection of panels C, D and E shows that, in contrast with the ionization indicator $r(t)$, the moving median $\bar{r}(t)$ can differentiate between carbonyl and carboxyl containing forms: Although the trajectory of $r(t)$ visits the $r = 0$ subspace repeatedly inside the segments labeled in green, the spectrum of the CO distance autocorrelation function does not reveal the presence of a carbonyl moiety. In addition, the spectra displayed in panel G suggest that infrared spectroscopy cannot

distinguish between contact, solvent-shared and fully dissociated forms: The differences between the carboxyl vibration spectra of these forms are statistically irrelevant.

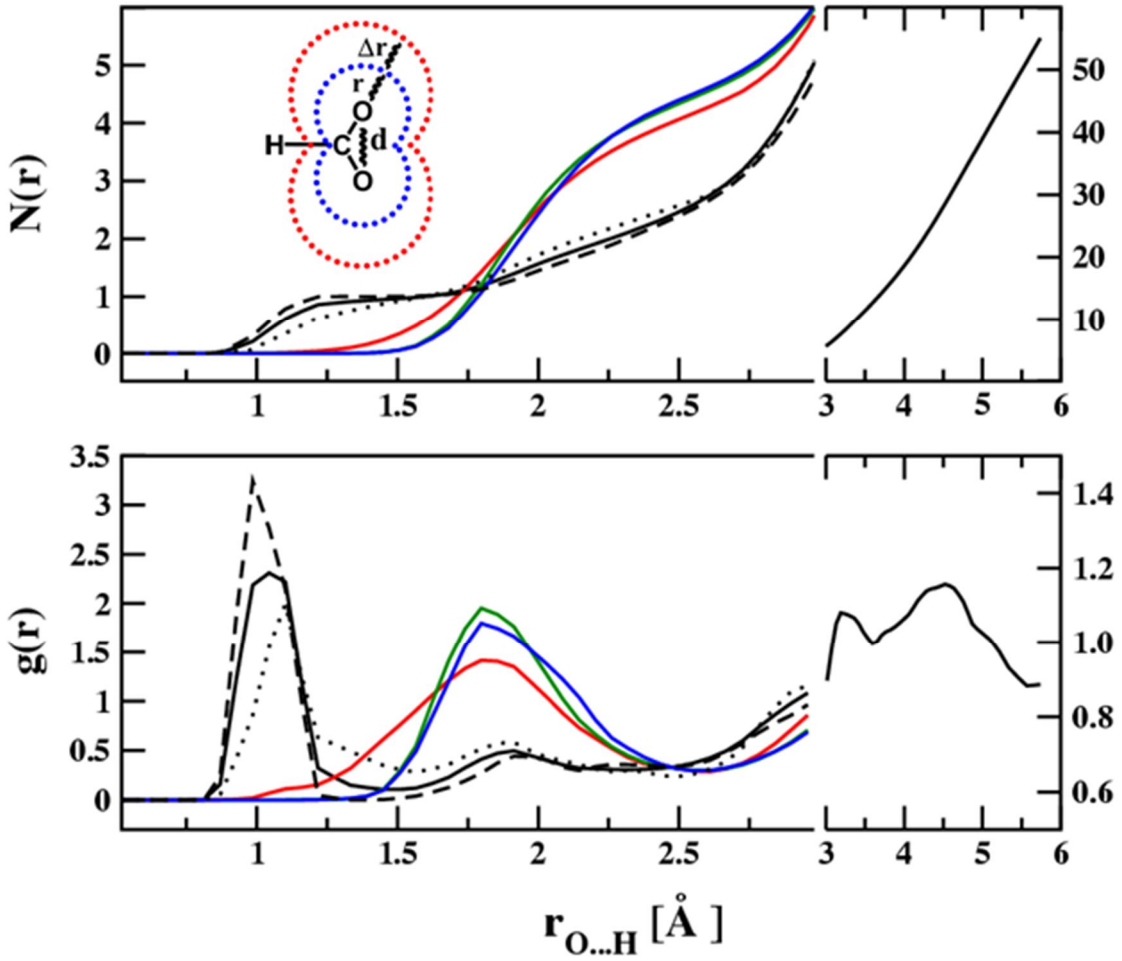

Figure 5-5. O···H pair correlation function g(r), and coordination numbers N(r) computed by taking into account both O atoms that form the carboxyl group and all solvent H atoms (see text and inset). The coloring code is consistent with the one employed in Fig.5-4: black curves correspond to undissociated forms, red is for contact ion-pairs, green is for solvent-shared pairs and blue corresponds to fully dissociated ions. The dashed line corresponds to covalent forms (Fig.5-4B from 0 to 3 ps), the dotted line to proton-shared forms (Fig.5-4D from 13 to 19 ps), and the black solid line is an average corresponding to all five trajectory segments labeled as (1) in Figure 5-4. Note the change in scale at $r_{O\cdots H}$ = 3 Å.

5.3.4 Structural differences between undissociated, ion-pair and dissociated forms.

Our analysis up to this point enabled us to separate the state space into three subspaces based on spectroscopic differences. It should be noted however that these forms may or may not be separated by sufficiently large barriers on the free energy surface, and, therefore,[76,77] do not necessarily represent reactant, intermediate, and product species whose long-term dynamics can be written in terms of elementary rate constants. In order to verify whether the distinction between covalent, proton-shared and contact ion pairs is kinetically meaningful, one should start by defining an appropriate reaction coordinate and compute the corresponding potential of mean force. The actual coordinate which drives the proton transfer event has little to do with distances between the transferring proton and the oxygen atoms involved in the bond-breaking/bond-forming processes, as emphasized by Kiefer and Hynes.[78] In contrast, researchers agree today that adiabatic proton transfer in polar solvents is driven by solvent fluctuations[79,80], an idea which is similar to the presolvation concept underlying Marcus' theory of electron transfer[81]. The experience accumulated in the study of other *ultrafast* proton transfer reactions suggests[1] that specific structural solvent fluctuations are likely to be an important contributor to the driving force.

It is therefore important to investigate the changes that take place in the solvation structure of the trifluoroacetate group and of the proton receiving water molecule during the following series of transformations: covalent → proton-shared form → contact ion-pair → solvent-shared ion-pair → dissociated ions. The most direct computational approach utilized to extract information concerning the structure of the solvation pattern consists of calculating pair correlation functions, from which first

solvation-shell coordination numbers can be obtained. Our calculations indicate that carboxyl oxygen – solvent hydrogen OH pair correlation functions have a well-defined minimum, which can be used to define the extent of the first solvation shell and compute a well-defined first-solvation shell coordination number.

The data displayed in Fig.5-5 compares and contrasts the pair-correlation functions obtained for covalent forms (dashed black line), proton-shared (dotted black line), contact (red), solvent-separated forms (green), and dissociated ions (blue). The definitions of the pair correlation functions g(r) between carboxyl groups and hydrogen atoms, and of the carboxyl group coordination numbers N(r) avoid double-counting of hydrogen atoms and are given in the Appendix. The trajectories utilized for covalent and proton-shared forms are those depicted in Fig.5-3 A and B, respectively, and the results displayed in solid black correspond to those of the undissociated state, i.e.: average values computed by taking all segments denoted by 1 in Fig.5-4. The pair-correlation functions shown in Fig.5-5 were computed by binning data in 0.1 Å intervals. This data indicates that the frontier between the first and second solvation shell is given by $r_{O\cdots H} \cong 2.3$ Å for undissociated, i.e.: covalent (black dashed line) and proton-shared (black dotted line) forms, and $r_{O\cdots H} \cong 2.5$ Å for contact (red), solvent-shared (green) ion-pairs and dissociated (blue) species. Using these definitions of the first solvation shells and the fact that undissociated forms are always hydrogen-bond donors via the hydroxyl (O-H or O⋯H) group, one can compute that undissociated forms are involved in $N = 2.0 \pm 0.2$ hydrogen-bonds, while contact, solvent-shared and dissociated ions form $N = 4.1 \pm 0.3$ such interactions. The latter result is consistent with conclusions reached by Takamuku et al.[82] in their recent large-angle X-ray scattering (LAXS) investigation of solutions of trifluoroacetic acids, who found that LAXS

intensities could be reproduced theoretically by assuming that trifluoroacetate ions are solvated by 3.85±0.36 water molecules in their first solvation shells.

The changes in the average number of hydrogen-bond interactions shown in Fig.5-5 emphasize the importance of the transition from proton-shared forms to contact ion-pairs: The differences between covalent and proton-shared forms, as well as those between contact, solvent-shared and dissociated ions amount to changes of $\Delta N \cong 0.2 \pm 0.3$ in the number of hydrogen-bond (HB) interactions. In contrast, the proton-shared → contact ion-pair transition is accompanied by an increase of $\Delta N \cong 1.8 \pm 0.3$ HB interactions (typical snapshots of the first hydration shell of covalent and contact ion-pairs are provided as supplementary information). In this respect, the changes in the number of hydrogen-bonded interactions with first-solvation shell molecules mirror those of the carbonyl → carboxylate infrared vibration modes depicted in Figs. 3 and 4.

5.4 Does it make sense to talk about ion pair dissociation intermediates?

It is important to emphasize that the running median indicator $\bar{r}(t)$ does not monitor the time evolution of a *structural*, but of a *dynamical* property, on a coarse-grained time scale. However, the close relationship between the changes in $\bar{r}(t)$ and those of the carboxyl vibration modes shown in Fig.5-4 suggest that the dynamics of $\bar{r}(t)$ is in fact driven by the dynamics of an unknown *structural* coordinate.

It is worth noting that the existence of such a structural reaction coordinate is a key concept of the theory of adiabatic proton transfer reactions in polar solvents formulated by Hynes et al.[78,79,83] According to this theory, one defines two coordinates to characterize proton transfer in polar solvents: The first is a collective solvent coordinate,

i.e.: the true reaction coordinate, which changes on a long timescale, while the second is the proton asymmetric stretch coordinate which evolves on a fast timescale. The important concept in Hynes theory is that the degree of advancement of the slow coordinate controls the asymmetry of the free energy along the proton stretch coordinate. In the present case $r(t)$ plays the role of the rapidly varying proton stretch coordinate from Hynes theory: As can be seen from the data depicted in Figs. 3 and 4 $r(t)$ changes on a 100 fs timescale. The $2T$ =1 ps timescale on which the median of $r(t)$ was computed for the data shown in Fig.5-4 is intermediate between that on which $r(t)$ changes and that on which the actual dissociation takes place. Its precise value is not important as long as there exists a clear separation between the dissociation and the asymmetric proton stretch timescales. We have verified that the trajectory of $\bar{r}(t)$ is almost identical if $2T$ = 0.5, 1, or 1.5 ps (data provided as supplementary information). Therefore, if one computes the running free energy function $F(r';t)$ defined as

$$F\left(r';t\right) = -k_B T \ln\left\langle \delta\left(r(t') - r'\right) \middle| t - T \le t' \le t + T \right\rangle \tag{5.13}$$

with the average being taken using the trajectory segment $t - T \le t' \le t + T$, one could reasonably expect that the asymmetry of $F(r';t)$ in the coordinate r' be controlled by the advancement of the slow solvent reaction coordinate. Since $F(r;t)$ is expected to be bimodal almost all the time, the running median $\bar{r}(t)$ is simply an expedient way to identify the dominant mode during the time-interval $t - T \le t' \le t + T$. For example, transitions between undissociated $\bar{r} = 0$ and contact ion-pair $\bar{r} \cong 2.6$ Å states are considered to take place when $\bar{r}(t)$ has an intermediate value, say $\bar{r}(t) \cong 1.3$ Å, which means that during the time interval $\mathrm{t} \pm 0.5$ ps the trajectory visited the undissociated and the contact ion-pair subintervals equally frequently. This picture is entirely equivalent to that proposed[78,79,83] by Hynes et al, which assumes that transitions occur when the free energy along the proton stretch coordinate becomes symmetric.

The analogy between the behavior of $\bar{r}(t)$ and that of the solvent reaction coordinate from Hynes' theory of adiabatic proton transfer reactions in polar solvents suggests that contact, and perhaps even solvent-shared ion pairs may be real kinetic intermediates. Nevertheless, until one explicitly identifies the actual collective solvent coordinate which is responsible for the dynamics of $\bar{r}(t)$, and demonstrates that contact and solvent-shared ion pairs are well-separated from the rest of the state space by significant free energy barriers, one cannot exclude the possibility that the aforementioned forms *are not kinetic* intermediates in the mechanism of acid dissociation. One alternative is that the ion-pair subsets of the state space could simply turn out to be regions where the proton diffusion is significantly affected by the proximity of the conjugate base, as pointed out by Chen et al.[84]

5.5 Conclusions and Perspectives

We draw the following main conclusions from the present investigation:

(i) Aqueous solutions of moderately strong acids, such as trifluoroacetic acid, contain important quantities of chemical forms which are neither covalent, $F_3C{-}COOH\cdots OH_2$, nor fully dissociated, $F_3C{-}COO^-(aq) + H_3O^+(aq)$. These forms can be distinguished by using infrared spectroscopy and a novel dissociation indicator $\bar{r}$.

(ii) Two intermediate forms are found to exist. The first represents a proton-shared structure $F_3C{-}COO^{\delta-} \bullet H \bullet {}^{\delta+}OH_2$ (also called Zundel, low-barrier, or strong hydrogen-bond form in other contexts), in which the equilibrium between the resonance forms depicted below is energetically unfavorable.

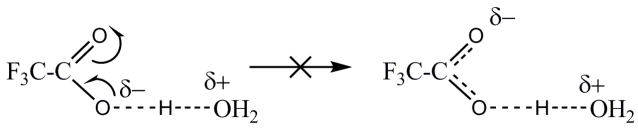

The second is a contact ion-pair $F_3C{-}COO^- \bullet H_3O^+$ in which the nascent hydronium ion is not free to diffuse in solution. The formation of the contact ion-pair coincides with the appearance of symmetric and asymmetric carboxylate vibration modes. Consequently, at this stage of the dissociation reaction, the equilibrium between the resonant forms depicted below becomes energetically favorable.

This is achieved by increasing the number of first solvation shell hydration waters by two, which effectively localizes the negative charge on the trifluoroacetate anion.

Several recent experimental studies have concluded that ion-pair intermediates play an important role in acid dissociation[31] and acid-base neutralization reactions[17,18]; these conclusions are consistent with the results obtained in the present investigation. However, an important difference exists between the results reported here and those found by Mohammed et al[17,18]: The contact ion-pairs identified in Ref. 17 involve the formation of a long-lived, symmetric hydronium ion whose structural and spectroscopic properties are similar to those of gas-phase H_3O^+. The present findings suggest that the contact ion-pair concept is more general and includes species that contain a hydronium ion whose OH bonds break and reform on a 100 fs timescale, but whose bond lengths are more or less equal when averaged on a few picosecond timescale.

5.6 Appendix.

5.6.1 Defining pair-correlation functions g(r) between carboxyl groups and hydrogen atoms.

It should be noted that the carboxyl group hydrogen-bond coordination number is somewhat smaller than the sum of the coordination numbers that are obtained individually for the two carboxyl oxygen atoms. In order to avoid this double counting of some solvent hydrogen atoms, we chose to define the carboxyl group hydrogen-bond coordination number N(r,d) as being the average number of H atoms that are situated at a distance smaller than r to either of the carboxyl oxygen atoms, i.e.:

$$\mathbf{r}_{\mathrm{O\cdots H}} = \min\left\{\mathrm{dist}(O_1, H), \mathrm{dist}(O_2, H)\right\} \le r \quad (5.14)$$

where O_1 and O_2 are the two oxygen atoms of the trifluoroacetate moiety, "dist" represents the distance between two atoms, and d is the distance between the two carboxyl oxygen atoms. The volume of intersection $V_{\cap}(r,d)$ of two spheres whose centers are separated by a distance d and whose radii are r is given by[85]:

$$V_{\cap}(r,d) = \left\{ \begin{array}{c} \frac{4\pi r^3}{3} + \frac{\pi d^3}{12} - \pi d r^2 \quad \text{if } r \ge \frac{d}{2} \\ 0 \quad \text{if } r < \frac{d}{2} \end{array} \right\} \quad (5.15)$$

Therefore, the volume $V_{\cup}(d,r)$ of the geometrical object depicted in the inset of Fig. 5-5, and which is formed by the union of two identical intersecting spheres is given by:

$$V_{\cup}(r,d) = \left\{ \begin{array}{c} \frac{4\pi r^3}{3} - \frac{\pi d^3}{12} + \pi d r^2 \quad \text{if } r \ge \frac{d}{2} \\ \frac{8\pi r^3}{3} \quad \text{if } r < \frac{d}{2} \end{array} \right\} \quad (5.16)$$

An approximate, but useful definition of the carboxyl first solvation shell can be obtained by noting that the distance between the two carboxyl oxygen atoms is almost constant, more precisely $d \cong 2.27 \pm 0.05$ Å. By neglecting the small variations of d around its average value, one can drop the dependence of N(r,d) and $V_{\cap}$ (r,d) on the distance d without introducing significant errors. Within this approximation, one can define the following carboxyl-hydrogen pair correlation function

$$g(r) = \frac{1}{\rho_H} \frac{dN(r)/dr}{dV_{\cup}(r, 2.27)/dr} =$$

$$= \begin{cases} \dfrac{1}{\rho_H} \dfrac{dN(r)/dr}{4\pi r^2 (1 + 1.135/r)} & \text{if } r \geq 1.135 \\ \dfrac{1}{\rho_H} \dfrac{dN(r)/dr}{8\pi r^2} & \text{if } r < 1.135 \end{cases} \qquad (5.17)$$

where $r = r_{O\cdots H}$ is defined in Eq. (5.12), ρ_H represents the number density of hydrogen atoms over the entire system and N(r) represents the integral of N(r,d) over all possible values of d. The definitions of g(r) and N(r) given here were utilized to compute the data displayed in Fig.5-5.

5.7 Acknowledgement

Financial support is acknowledged in the form of a Fond Québécois de la Recherche sur la Nature et les Technologies (FQRNT) Nouveaux Chercheurs Grant and a Natural Science and Engineering Research Council of Canada (NSERC) grant. The Réseau Québécois de Calcul de Haute Performance (RQCHP) is acknowledged for providing the computational hardware utilized in the calculations.

Supporting information available: Data is provided showing trajectories of the running median $\bar{r}(t)$ and running average $r_{av}(t)$ with averages being taken over intervals $2T$ = 0.5, 1, and 1.5 ps. We also show snapshots of the solvation environment of covalent forms and of contact ion pairs. This information is available free of charge via the Internet at http://pubs.acs.org.

5.8 References

(1) Marx, D.; Chandra, A.; Tuckerman, M. E. *Chem. Rev.* **2010**, *110*, 2174.

(2) Adamczyk, K.; Premont-Schwarz, M.; Pines, D.; Pines, E.; Nibbering, E. T. J. *Science* **2009**, *326*, 1690.

(3) Braun-Sand, S.; Strajbl, M.; Warshel, A. *Biophys. J.* **2004**, *87*, 2221.

(4) Decoursey, T. E. *Physio. Rev.* **2003**, *83*, 475.

(5) Cukierman, S. *Biochim. Biophys. Acta* **2006**, *1757*, 876.

(6) Wraight, C. A. *Biochim. Biophys. Acta* **2006**, *1757*, 886.

(7) Swanson, J. M. J.; Maupin, C. M.; Chen, H. N.; Petersen, M. K.; Xu, J. C.; Wu, Y. J.; Voth, G. A. *J. Phys. Chem. B* **2007**, *111*, 4300.

(8) Eigen, M. *Angew. Chem. Int. Ed.* **1964**, *3*, 1.

(9) Eigen, M.; Kruse, W.; Maass, G.; De Maeyer, L. *Prog. React. Kinet.* **1964**, *2*, 285.

(10) Weller, A. *Prog. React. Kinet.* **1961**, *1*, 189.

(11) Mohammed, O. F.; Pines, D.; Pines, E.; Nibbering, E. T. J. *Chem. Phys.* **2007**, *341*, 240.

(12) Geissler, P. L.; Dellago, C.; Chandler, D.; Hutter, J.; Parrinello, M. *Science* **2001**, *291*, 2121.

(13) Iftimie, R.; Thomas, V.; Plessis, S.; Marchand, P.; Ayotte, P. *J. Am. Chem. Soc.* **2008**, *130*, 5901.

(14) Martin, M. M.; Hynes, J. T. *Femtochemistry and Femtobiology*; Elsevier: New York, 2004.

(15) Rini, M.; Magnes, B. Z.; Pines, E.; Nibbering, E. T. J. *Science* **2003**, *301*, 349.

(16) Rini, M.; Pines, D.; Magnes, B. Z.; Pines, E.; Nibbering, E. T. J. *J. Chem. Phys.* **2004**, *121*, 9593.

(17) Mohammed, O. F.; Pines, D.; Dreyer, J.; Pines, E.; Nibbering, E. T. J. *Science* **2005**, *310*, 83.

(18) Mohammed, O. F.; Pines, D.; Nibbering, E. T. J.; Pines, E. *Angew. Chem. Int. Ed.* **2007**, *46*, 1458.

(19) Siwick, B. J.; Bakker, H. J. *J. Am. Chem. Soc.* **2007**, *129*, 13412.

(20) Siwick, B. J.; Cox, M. J.; Bakker, H. J. *J. Phys. Chem. B* **2008**, *112*, 378.

(21) Cox, M. J.; Bakker, H. J. *J. Chem. Phys.* **2008**, *128*, 10.

(22) Cox, M. J.; Timmer, R. L. A.; Bakker, H. J.; Park, S.; Agmon, N. *J. Phys. Chem. A* **2009**, *113*, 6599.

(23) Marx, D.; Hutter, J. *Ab Initio Molecular Dynamics*; Cambridge University Press: New York, 2009.

(24) Warshel, A. *Biochemistry* **1981**, *20*, 3167.

(25) Rousseau, R.; Kleinschmidt, V.; Schmitt, U. W.; Marx, D. *Angew. Chem. Int. Ed.* **2004**, *43*, 4804.

(26) Tran-Thi, T. H.; Prayer, C.; Millie, P.; Uznanski, P.; Hynes, J. T. *J. Phys. Chem. A* **2002**, *106*, 2244.

(27) Markovitch, O.; Chen, H.; Izvekov, S.; Paesani, F.; Voth, G. A.; Agmon, N. *J. Phys. Chem. B* **2008**, *112*, 9456.

(28) Tuckerman, M. E.; Marx, D.; Klein, M. L.; Parrinello, M. *Science* **1997**, *275*, 817.

(29) Strajbl, M.; Hong, G.; Warshel, A. *J. Phys. Chem. B* **2002**, *106*, 13333.

(30) Klein, M. L. *Science* **2001**, *291*, 2106.

(31) Leiderman, P.; Genosar, L.; Huppert, D. *J. Phys. Chem. A* **2005**, *109*, 5965.

(32) Warshel, A.; Florian, J. In *The Encyclopedia of Computational Chemistry*; Schleyer, P., Jorgensen, W., Schaefer H. F, I., Schreiner, P. R., Thiel, W., R., G., Eds.; John Wiley and Sons: Chichester, UK, 2004.

(33) Asthagiri, D.; Pratt, L. R.; Kress, J. D.; Gomez, M. A. *Proc. Natl. Acad. Sci. U.S.A.* **2004**, *101*, 7229.

(34) Asthagiri, D.; Pratt, L. R.; Kress, J. D. *Proc. Natl. Acad. Sci. U.S.A.* **2005**, *102*, 6704.

(35) Izvekov, S.; Voth, G. A. *J. Chem. Physics* **2005**, *123*, 9.

(36) Marx, D.; Tuckerman, M. E.; Hutter, J.; Parrinello, M. *Nature* **1999**, *397*, 601.

(37) Tuckerman, M.; Marx, D.; Klein, M. L.; Parrinello, M. *Science* **1997**, *275*, 817.

(38) Tuckerman, M. E.; Marx, D.; Parrinello, M. *Nature* **2002**, *417*, 925.

(39) Tuckerman, M. E.; Chandra, A.; Marx, D. *Acc. Chem. Res.* **2006**, *39*, 151.

(40) Warshel, A. *Chem. Phys. Lett.* **1978**, *55*, 454.

(41) Warshel, A.; Weiss, R. M. *J. Am. Chem. Soc.* **1980**, *102*, 6218.

(42) Ando, K.; Hynes, J. T. *J. Phys. Chem. A* **1999**, *103*, 10398.

(43) Sillanpaa, A. J.; Simon, C.; Klein, M. L.; Laasonen, K. *J. Phys. Chem. B* **2002**, *106*, 11315.

(44) Iftimie, R.; Tuckerman, M. E. *Angew. Chem. Int. Ed.* **2006**, *45*, 1144.

(45) Park, J. M.; Laio, A.; Iannuzzi, M.; Parrinello, M. *J. Am. Chem. Soc.* **2006**, *128*, 11318.

(46) Maupin, C.; Wong, K. F.; Soudakov, A. V.; Kim, S.; Voth, G. A. *J. Phys. Chem. B* **2006**, *110*, 631.

(47) Gu, W.; Frigato, T.; Straatsma, T. P.; Helms, V. *Angew. Chem. Int. Ed.* **2007**, *46*, 2939.

(48) Marx, D.; Chandra, A.; Tuckerman, M. E. *Chem. Rev.* **2010**, *110*, 2174.

(49) Warshel, A.; Papazyan, A. *Proc. Natl. Acad. Sci. USA* **1996**, *93*, 13665.

(50) Mathias, G.; Marx, D *Proc. Natl. Acad. Sci. USA* **2007**, *104*, 6980.

(51) Leuchs, M.; Zundel, G. *J. of Chem. Soc. Fara. Trans. II* **1980**, *76*, 14.

(52) Covington, A. K.; Freeman, J. G.; Lilley, T. H. *J. Phys. Chem.* **1970**, *74*, 3773.

(53) Gelb, R. I.; Schwartz, L. M.; Laufer, D. A. *J. Am. Chem. Soc.* **1981**, *103*, 5664.

(54) Thomas, V.; Iftimie, R. *J. Phys. Chem. B* **2009**, *113*, 4152.

(55) Car, R.; Parrinello, M. *Phys. Rev. Lett.* **1985**, *55*, 2471.

(56) Koch, W.; Holthausen, M. C. *A Chemist's Guide to Density Functional Theory*; VCH: New York, 2000.

(57) Becke, A. *Phys. Rev. A* **1998**, *38*, 3098.

(58) Lee, C.; Yang, W.; Parr, R. G. *Phys. Rev. B* **1998**, *37*, 785.

(59) Troullier, N.; Martins, J. L. *Phys. Rev. B* **1991**, *43*, 1993.

(60) Gordon, R. G. *Adv. Magn. Reson.* **1968**, *3*, 1.

(61) McQuarrie, D. A. *Statistical mechanics*; University Science Books: Sausalito, Calif., 2000.

(62) Wyatt, R. E.; Zhang, J. Z. H. *Dynamics of Molecules and Chemical Reactions*; CRC Press: New York, 1996.

(63) Makri, N. *Ann. Rev. Phys. Chem.* **1999**, *50*, 167.

(64) Jang, S.; Voth, G. A. *J. Chem. Phys.* **1999**, *111*, 2357.

(65) Jang, S.; Voth, G. A. *J. Chem. Phys.* **1999**, *111*, 2371.

(66) Marx, D.; Tuckerman, M. E.; Martyna, G. J. *Compu. Phys. Commu.* **2000**, *118*, 166.

(67) Bader, J. S.; Berne, B. J. *J. Chem. Phys.* **1994**, *100*, 8359.

(68) Berghold, G.; Mundy, C. J.; Romero, A. H.; Hutter, J.; Parrinello, M. *Phys. Rev. B* **2000**, *61*, 10040.

(69) Iftimie, R.; Thomas, J. W.; Tuckerman, M. E. *J. Chem. Phys.* **2004**, *120*, 2169.

(70) Wannier, G. H. *Phys. Rev.* **1937**, *52*, 191.

(71) Boys, S. F. *Rev. Mod. Phys.* **1960**, *32*, 296.

(72) Thomas, J. W.; Iftimie, R.; Tuckerman, M. E. *Phys. Rev. B* **2004**, *69*, 125105.

(73) Gaigeot, M. P.; Sprik, M. *J. Phys. Chem. B* **2003**, *107*, 10344.

(74) Martyna, G. J.; Klein, M. L.; Tuckerman, M. *J. Chem. Phys.* **1992**, *97*, 2635.

(75) Tuckerman, M. E.; Yarne, D. A.; Samuelson, S. O.; Hughes, A. L.; Martyna, G. J. *Compu. Phys. Commu.* **2000**, *128*, 333.

(76) Wigner, E. *Trans. Faraday Soc.* **1938**, *34*, 29.

(77) Chandler, D. *J. Chem. Phys.* **1978**, *68*, 2959.

(78) Kiefer, P. M.; Hynes, J. T. *J. Phys. Chem. A* **2004**, *108*, 11793.

(79) Borgis, D.; Hynes, J. T. *J. Phys. Chem.* **1996**, *100*, 1118.

(80) Warshel, A. *Computer Modeling of Chemical Reactions in Enzymes and Solutions*; John Wiley and Sons Canada Ltd: Toronto, 1991.

(81) Marcus, R. A. *Ann. Rev. Phys. Chem.* **1964**, *15*, 155.

(82) Takamuku, T.; Kyoshoin, Y.; Noguchi, H.; Kusano, S.; Yamaguchi, T. *J. Phys. Chem. B* **2007**, *111*, 9270.

(83) Staib, A.; Borgis, D.; Hynes, J. T. *J. Chem. Phys.* **1995**, *102*, 2487.

(84) Chen, H.; Voth, G. A.; Agmon, N. *J. Phys. Chem. B* **2010**, *114*, 333.

(85) Gibson, K. D.; Scheraga, H. A. *J. Phys. Chem.* **1987**, *91*, 4121.

5.9 Supporting Information

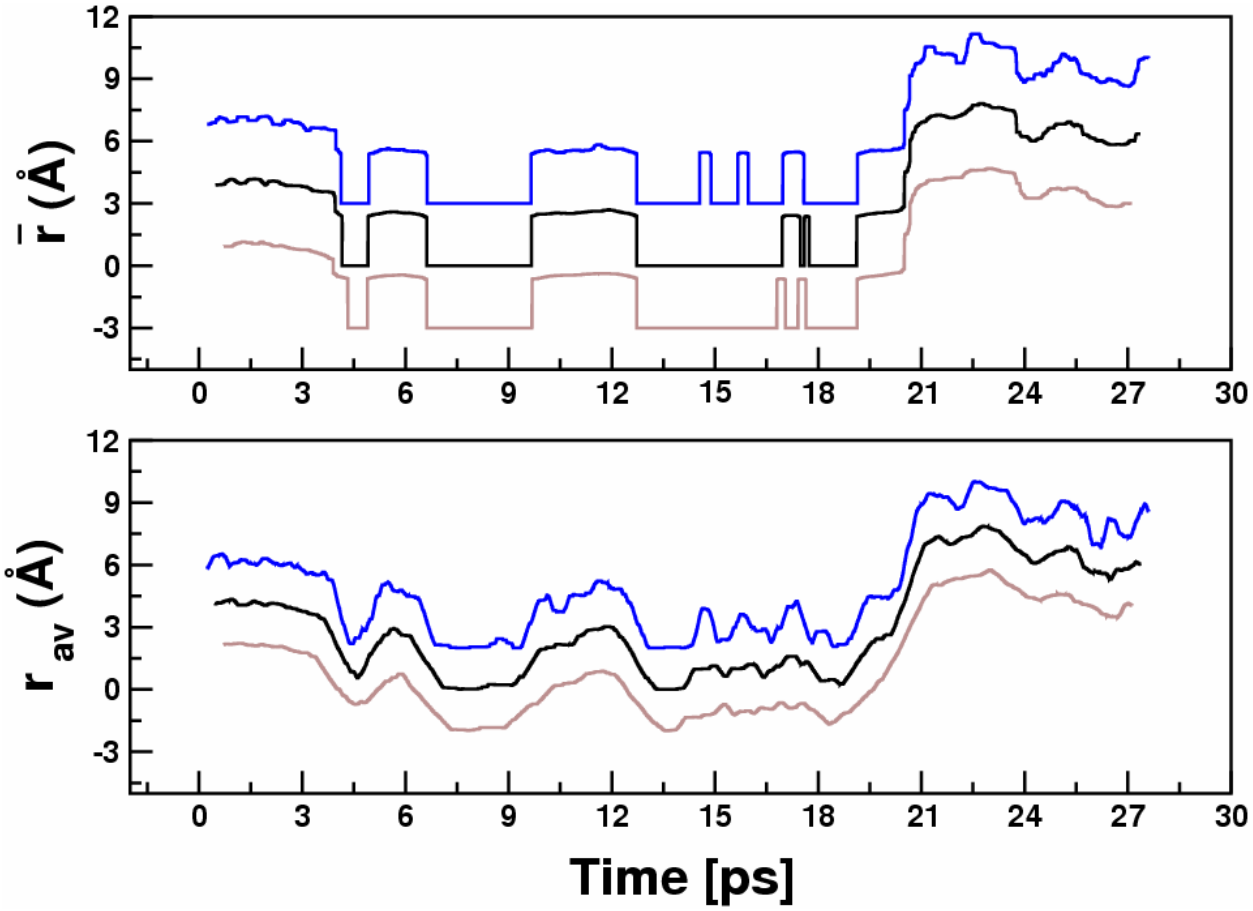

Figure 5-6. The trajectories of the running median $\overline{r}(t)$ (top) and average $r_{avg}(t)$ (bottom) computed using 2*T* = 0.5 ps (blue), 1ps (black) and 1.5 ps (brown) (see text). The results in black appearing in the top panel are also shown in Fig. 5-4 D in the main text. The different graphs are shifted by 3Å on the y-axis in order to make them easier to compare.

The running median is defined in the $\overline{r}(t)$ main text. The running average $r_{avg}(t)$ is defined as:

$$r_{avg}(t) = \frac{1}{2T}\int_{t-T}^{t+T} r(t')dt' \qquad (5.18)$$

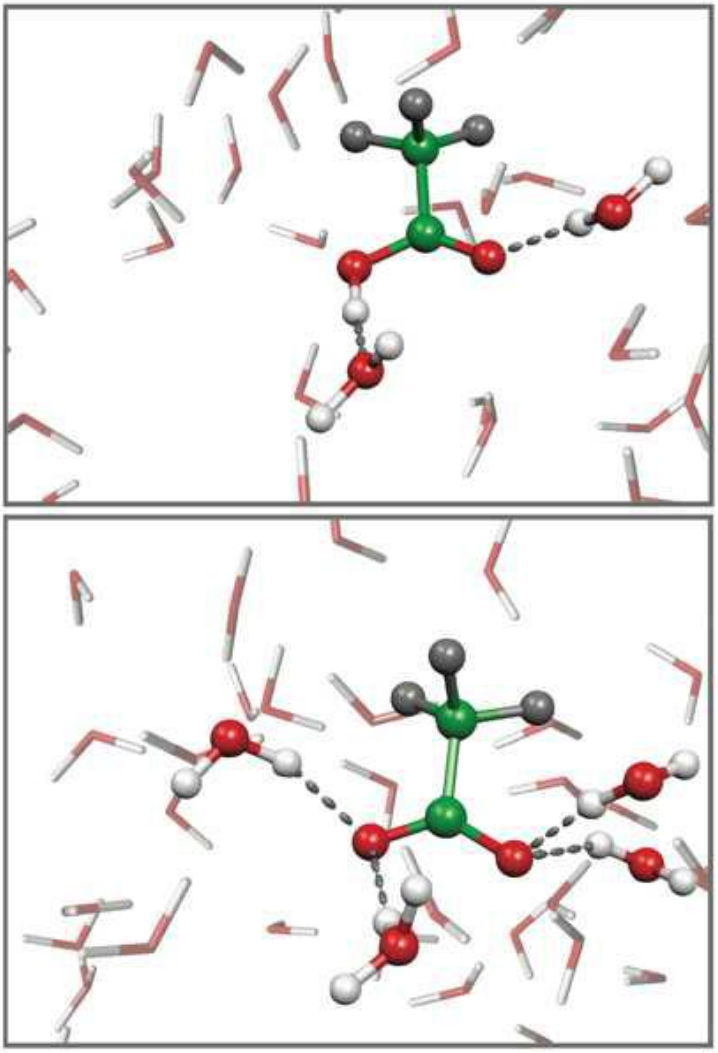

Figure 5-7. Snapshots showing the solvation environment of covalent forms (top) and contact ion-pairs (bottom). The average hydration of covalent forms involves two water molecules: One solvent molecule always accepts a H-bond from the carboxyl OH bond. The second molecule is a H-bond donor, either to the carbonyl end as shown in the figure, or to the hydroxyl end (data not shown). In contrast, the carboxylate ion always accepts two HB's at each oxygen atom.

Concerted and Sequential Proton Transfer Mechanism in Water-Separated Acid-Base Encounter Pairs

Vibin Thomas[†], Ugo Rivard[†], Patrick Maurer[†], Andrew Bruhács[‡], Bradley J. Siwick[‡] and Radu Iftimie[†]*

[†]Départément de Chimie, Université de Montréal, CP 6128, succursale Centre-Ville, Montréal, H3C3J7, Canada and [‡]Department of Chemistry and Physics, Center for the Physics of Materials McGill University 801 Sherbrooke St. West, Montréal, Canada

Published in *J. Phys. Chem. Lett.* **3** (18), 2633 (2012)

Abstract: The proton transfer mechanisms involved inside aqueous, solvent-separated encounter complexes between phenol and carboxyl moieties are studied using ab initio molecular dynamics and computational time-resolved vibrational spectroscopy. This model framework can be viewed as a ground-state analog of the excited-state proton transfer reactions that have been actively investigated using ultrafast spectroscopy. Three qualitatively distinct proton transfer pathways are observed in the simulations. These can be described as direct concerted, direct sequential, and through bulk transfers. The primary difference between the sequential and concerted mechanism is the involvement of a reaction intermediate in which the proton fluctuates for several picoseconds through the hydrogen bonds connecting donor and acceptor but resides primarily on an intervening water molecule in the encounter complex. These results contribute to our molecular level understanding of the diverse processes involved in proton transfer within water-separated encounter complexes.

6. Concerted and Sequential Proton Transfer Mechanism in Water-Separated Acid-Base Encounter Pairs

6.1 Introduction

Proton translocation constitute Bimolecular proton transfer in solution[1-3] is an extremely important class of charge transfer reaction[4] and are known to occur in two steps [3]. In the first step, diffusive motion of the reactant species leads to the formation of a sterically favorable 'encounter complex'. In the second step, charge-transfer occurs inside the encounter complex at some intrinsic rate. Since the intrinsic rate for proton transfer is often extremely high in aqueous solution, the overall rates of such reactions tend to be 'diffusion limited'[3]. As a result, experimental access to the reaction kinetics inside the encounter complex has proven to be rather difficult. However, recent investigations using ultrafast pump-probe spectroscopy (both visible[5,6] and infrared[7-12]) to study bimolecular excited-state proton transfer at high base/acceptor concentration have yielded new insights on the proton transfer mechanisms involved inside solvent-separated encounter complexes. Unfortunately, the model-independent details that the experimental data can provide on the nature of the charge transfer mechanisms and their diversity is limited. The experiments tend to measure the time-dependent population of reactants/products, offering little on very short-lived intermediates that may exist between these states.

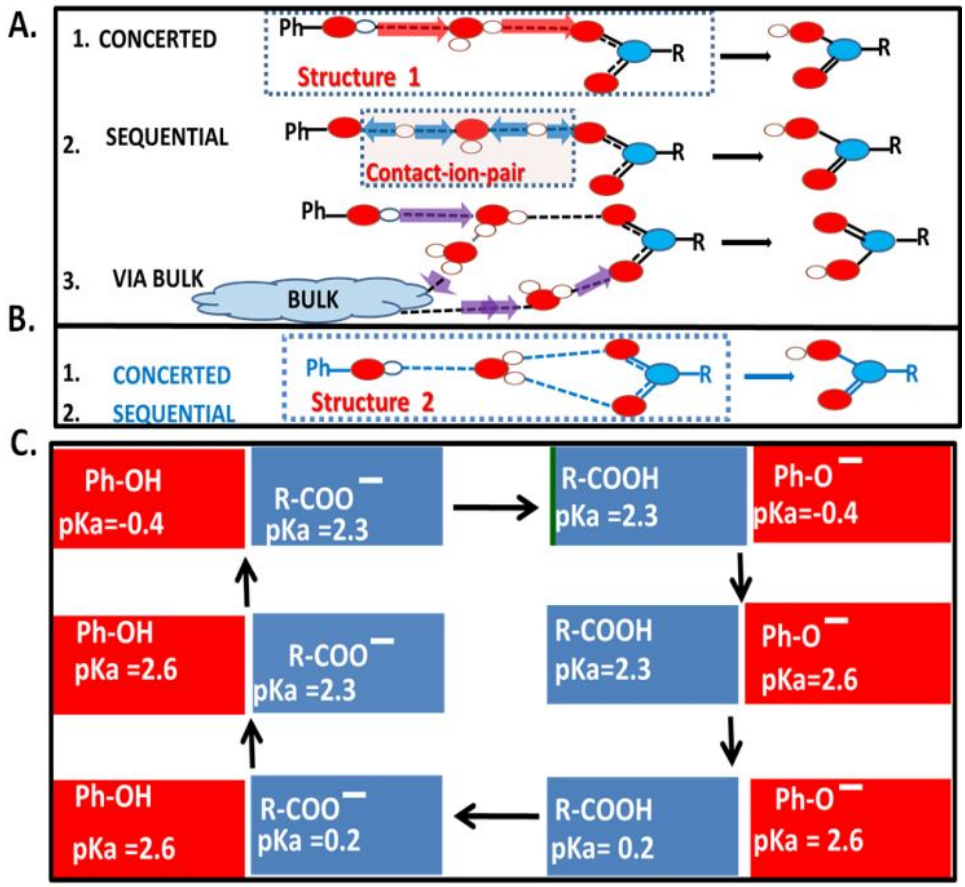

Figure 6-1. Panels A, B: possible H-bond patterns and acid-base reaction mechanisms inside a water separated encounter pair. Panel C: By sequentially changing the pKa values of phenol and carboxyl groups two neutralization reactions can be initiated forming a complete cycle. The pKa changes are implemented using a dipole-field / QM approach and the actual chemical events are studied utilizing first-principles molecular dynamics (see text). The acid-base reactions and their directions are indicated at the top and bottom of panel C. In both cases ΔpKa = pKa(acid formed) - pKa(acid consumed) ~ 2.5.

Given the current limitations of experiment, we have developed an ab initio molecular dynamics[13] (AIMD) approach to study the mechanisms involved in aqueous intermolecular proton transfer in solvent-separated encounter complexes. In particular, the goal of this work is to supplement experimental studies by providing detailed information on the proton transfer reaction dynamics when a single water molecule bridges the donor and acceptor sites of the reactants in solution;

the smallest of a family of solvent-separated complexes that have been identified in experimental studies of ESPT[9-12]

For this study we have chosen a model system involving phenolic and carboxylic reactants closely related to the model systems investigated experimentally.[7-12]

The simulations were initiated using gas-phase clusters constructed with an intervening water molecule placed between a phenol hydrogen bond donor and a carboxylate anion acceptor. The optimized gas-phase H-bond topology was found to correspond to the structure displayed in Fig. 6-1B. However, in aqueous solution one of the two H-bonds donated by the intervening water to the carboxylate anion breaks in less than 300 fs and another H-bond is immediately formed with a water molecule from the bulk, as depicted in Fig. 6-1A. The instability in solution of the H-bonding pattern shown in Fig. 6-1B on a 1 ps timescale was confirmed by repeating the calculations with a different density functional description of the molecules, by utilizing several simulation temperatures and by starting the AIMD trajectories from various initial conditions, as described in the Supporting Information.

Throughout the subsequent calculations a dipole-field/quantum mechanics (DF/QM) model, described in detail elsewhere[14-16], was employed which allows one to control the pKa value of Brønsted acids by changing the magnitude of an appropriately located external dipole moment. The DF/QM methodology has been tested in gas as well as condensed-phase conditions and was found to provide a reasonably accurate description of pKa values[14,15] and hydration structures[15] in the acetic to trifluoroacetic and phenol to 2,4,6-tricyanophenol series. By successively changing the pKa values of carboxylic R-COOH and phenolic Ar-OH acids as shown in Fig. 6-1C, seventeen acid-base reaction events were recorded in six simulations starting from different initial configurations. This approach provides a ground-state analog to the excited state proton transfer reactions studied experimentally using ultrafast spectroscopy, but

avoids the complications[17] stemming from the excited-state nature of the molecular dynamics in experimental conditions. Thus, the results should be seen as a complement to the experimental investigations rather than an attempt to simulate the experimental model system directly.

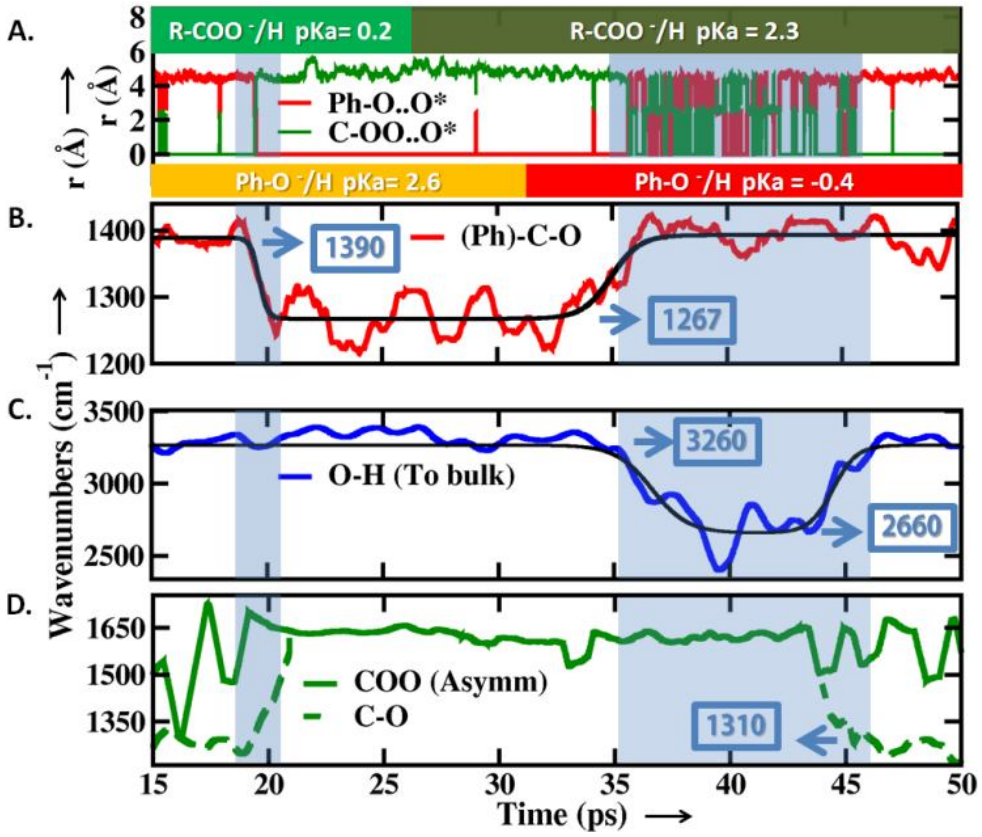

Figure 6-2. Following the advancement of the chemical reaction using the proton location indicator defined in Eq. 6-1 (panel A) or the maximum absorption frequency of normal modes of phenol, intervening water and carboxyl moieties in panels B, C, and D respectively (see text). The sigmoid function fits (black) serve as a guide to the eye. Note that the asymmetric OCO vibration and the C-O single bond stretch (panel D) are normal modes in the regions where the carboxylic acid is dissociated and undissociated, respectively. Note also that we only show the vibration spectrum of the O-H bond from the intervening water directed toward the bulk. The pKa values of the acid and base are indicated at the top and bottom of panel A.

Representative results from one of the simulation trajectories are summarized in Fig. 6-2. Data displayed in Fig. 6-2A shows the typical time evolution of the proton location indicator r defined as:

$$r = \mathrm{dist}\left(O, O^{*}\right) \tag{6.1}$$

where O is an oxygen atom from the phenol or the carboxyl moieties, O* is the oxygen atom from the system carrying the transferring proton, and "dist" represents the inter-atomic distance. Values of r=0 indicate which molecule, the carboxylic acid (green curve) or the phenol molecule (red) is protonated. In contrast, r ≈ 2.6 Å means that the transferring proton is localized on the intervening water molecule, while r ≈ 4.8 Å indicates that the molecule in not protonated. Finally, values of r > 6 Å (data not shown) are observed when acid dissociation takes place into the bulk, i.e.: to water molecules other than the one bridging the reactants. Two direct (i.e.: through the intervening water molecule) acid-base reaction events are highlighted in Fig.6-2A, the first taking place around t=19 ps from R-COOH to Ar-O^- and the second between t = 35 and t = 45 ps from Ar-OH to R-COO^-. These trajectories are representative of the two qualitatively distinct proton transfer pathways observed in this work; those characterized by a very rapid (<1 ps) long-range charge transfer between the reactants, and those that involve an interval, many picoseconds in duration, during which the proton fluctuates through the H-bonds connecting the donor and acceptor molecules, but resides primarily on the intervening water. It is important to note that these proton transfer events are time-separated by several picoseconds from the point at which the pKa of the donor and acceptor is switched (also indicated in Fig.6- 2), indicating that they are driven in a natural way by solvent fluctuations and are not an artefact of the pKa adjustment. Moreover, it is important to note that both mechanisms were observed in reactions from R-COOH to Ar-O^- (ΔpKa = 2.7; see caption of Fig. 6-1) and from Ar-OH to R-COO^- (ΔpKa = 2.4).

In addition to the proton location indicator, the acid-base reaction events were investigated using time-frequency analysis based on the complex Morlet wavelet transform (see Supporting Information). This approach allows one to follow the vibration spectrum of various modes in time, as the reaction progresses. The vibration modes followed in the present analysis are the C-O bond stretch of the Ar-O moiety, the antisymmetric O-C-O bond stretch of the carboxyl group, and the O-H bond stretch forming an H-bond with the bulk of the intervening water molecule. The data displayed in Fig. 6-2 indicates that the first neutralization event taking place at $t \approx 19$ ps consists of a single, subpicosecond elementary step: acid dissociation and base protonation occur synchronously within the time resolution $\Delta t \approx 400$ fs of the present time-frequency analysis. Equally important, the O-H bond stretch vibration frequency of the intervening water molecule shows no change during this transformation.

The second neutralization event which starts at $t \approx 35$ ps is qualitatively different. The data shown in Fig.6- 2 demonstrates that acid dissociation (the change in the phenol C-O frequency in panel B) and base protonation (the change in the O-C-O frequency in panel D) are separated by at least 6 ps. During this interval the frequency of the OH bond pointing toward the bulk decreases from 3260 to 2660 cm^{-1}, and its average bond length changed from 0.98 to 1.03 and then back to 0.98 Å (data not shown), suggesting the transient formation of a significantly stronger H-bond. It is important to emphasize that the other two O-H bonds (those shared with the donor and acceptor) display very wide and almost featureless absorption spectra between 35 and 45 ps, ranging from 1000 to 3000 cm^{-1} (data not shown).

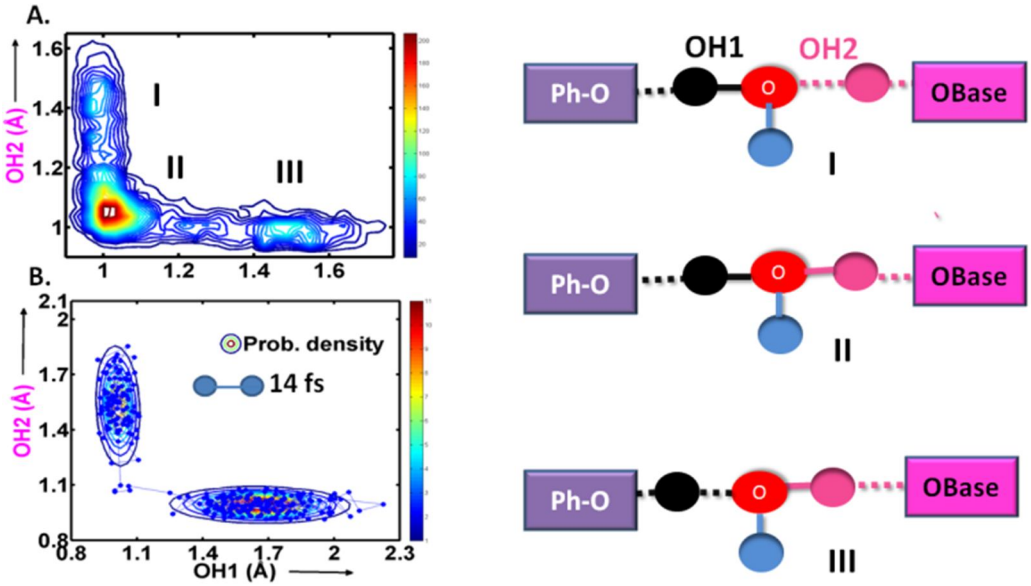

Figure 6-3. Probability density of the O-H bond lengths defined on the right for the sequential (A) and concerted (B) transfers shown in Fig. 6-2. Note that the Eigen contact ion pair form (structure II) is a long-lived intermediate along the sequential neutralization pathway, but a transition structure during the concerted one.

The qualitative difference between these two mechanisms, which we call concerted and sequential, respectively, is also captured in Fig. 6-3 which shows the structure of the reaction intermediates. Panel A displays the probability density of the O-H distances formed between the intervening oxygen and the two transferring protons during the time interval $37 \leq t \leq 43$ ps. Three free energy minima corresponding to two low-barrier H-bond forms and one Eigen-like hydronium ion in intimate contact with phenolate and carboxylate anions can be easily identified, although the proton location indicator data in Fig. 6-2A indicates a rapid interconversion between these structures.

The data displayed in Fig. 6-3B shows the evolution of the same O-H bond lengths in the case of the concerted trajectory. In contrast with the sequential case, the region in which both the $O\text{-}H_1$ and $O\text{-}H_2$ bond lengths are smaller than 1.2 Å is visited for approximately 50 fs. Acid dissociation and base protonation can therefore be considered to occur simultaneously without formation of a reaction intermediate.

In addition to the direct neutralization mechanisms shown in Figs.6- 2 and 3, indirect neutralization pathways via dissociation to the bulk, as depicted in Fig. 6-1A, were also observed in the present simulations (data not shown). In total, seventeen proton transfers were observed: eight were concerted, four sequential, and five corresponded to dissociation to the bulk.

The present calculations are broadly in support of the notion that a number of qualitatively distinct proton transfer pathways contribute to acid-base reactions inside solvent-separated encounter complexes[18,19]. The nature of the various pathways observed here has been discussed in context of previous experimental work[7-12]. The direct, long-range concerted mechanism has been emphasized previously in the work of Siwick et al. and Cox et al. who have discussed the concerted mechanism in terms of an adiabatic proton transfer picture where solvent fluctuations control the charge-transfer[10-12]. In the context of the model system investigated here this mechanism appears to be the dominant charge transfer channel, but the adiabatic picture suggests that these weights will depend sensitively on the ΔpKa of the reaction[11]. The sequential mechanism identified in this work involves the participation of a protonated intervening water molecule that contains two O-H bonds that form and break on a sub-picosecond timescale, and a third, slightly elongated O-H bond that fluctuates around its equilibrium position for the entire lifetime of the ion-pair intermediate. While this intermediate has a different structure than the one proposed by Mohammed et al. in their studies[8,18] of excited-state proton transfer between HPTS and carboxylate bases, it holds other features in common. For example the observation of the vibrational signature of a deprotonated acid many picoseconds ahead of the vibrational signature for the protonated base and the transient formation of stronger H-bonds by the intervening water molecule along the sequential pathway. In other respects, this fluctuating hydronium is in keeping with the solvent controlled adiabatic perspective[20,21] which forms the basis of the model outlined in the work of Siwick and

Bakker[10]. The PT to the bulk channel and diffusion through the solvent has been discussed in numerous previous experimental[22] and computational[16,23-25] investigations.

These results contribute to a detailed molecular level understanding of the diverse processes involved in proton transfer within water separated encounter complexes, and demonstrates the important ways in which such simulations can complement experimental work in this area.

6.2 Computational Methodology

Born-Oppenheimer molecular dynamics (BOMD) simulations were carried out using density functional theory by utilizing the CPMD simulation package[26]. The nuclear trajectories are generated using forces obtained from electronic structure calculations based on the density functional theory (DFT) formalism. The simulations are performed using the BLYP[27,28] exchange-correlation functional, plane wave basis sets and norm-conserving Troullier-Martins[29] pseudopotentials. The basis set was expanded up to a kinetic energy cut-off of 70 Ry. The justification for the use of the BLYP generalized gradient exchange-correlation functional is provided in the Supporting Information.

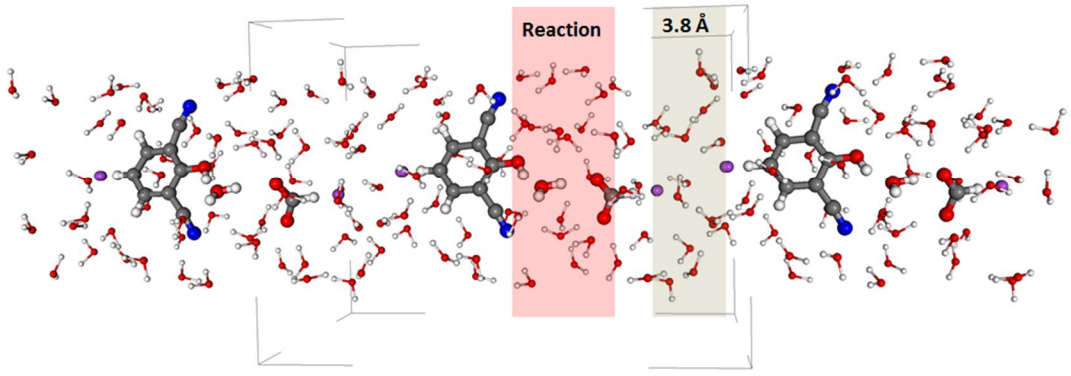

Figure 6-4. The simulation box and two periodic images showing the reactive region and the interaction between the fictitious dipoles across the interface. Color code: Oxygen, nitrogen, carbon and hydrogen atoms are depicted in red, blue, black and grey. The pseudo-atoms forming the pseudo-dipole moments are shown in violet.

The pKa values shown in Fig. 6-1C were implemented using appropriately located external dipole moments to model inductive field effects. The simulated system contains one molecule of 2,6-dicyanophenol with a dipole in the para position, one molecule of formic acid with a dipole along the H-C axis, solvated with 56 water molecules in a rectangular box of size 17x11x11 $Å^3$, corresponding to a macromolecular concentration of 0.80 mol L^{-1}. A snapshot of the simulation system (with two periodic images) is depicted in Fig. 6-4 showing that the system is homogeneously solvated. All atoms, including the pseudo-atoms that form the pseudo-dipole moments (shown in violet in Fig. 6-4) are periodically replicated.

The BOMD calculations were carried out by fixing the distance between the acid and the base by fixing H7, C4, H8 and C9 atoms (see Fig.6-7 of Supporting Information) in order to focus on the actual reactive event inside a water-separated Eigen encounter pair. This restriction is necessary because the AIMD would otherwise sample the entire state space, thus significantly reducing the number of water-separated acid-base reactions that could have been observed given the same computational effort; for example, Mohammed et al.[8] estimated that the population of water-separated encounter pairs between HPTS and trifluoroacetate ions represents about 7% of the total population. However this translational constrain between the molecule will not restrict the freedom of the reactive groups in the molecules (-COOH and –OH) to explore all relevant oxygen-oxygen separation distances as shown in the Supporting Information.

6.3 Supporting Information

Details of the methods utilized in this study. This material is available free of charge via the Internet at http://pubs.acs.org.

6.4 Acknowledgement

R.I. and B.J.S. acknowledge financial support from Natural Sciences and Engineering Research Council (NSERC) and Fonds Québécois pour la Recherche de la Nature et les Technologies (FQRNT) grants. B.J.S. also acknowledges support from the Canada Research Chairs (CRC) program and the Canada Foundation for Innovation (CFI).

6.5 References

(1) E. T. Nibbering; E. Pines. in Hydrogen-Transfer Reactions, Vol. 1 (Eds.: J. T. Hynes; J. P. Klinman; H. H. Limbach; R. L. Schowen), *WILEY-VCH, New York*, **2007**, *443-458*;

(2) P. M. Kiefer; J. T. Hynes. idem, 303-348;

(3) Eigen, M.; Proton Transfer, Acid-Base Catalysis, and Enzymatic Hydrolysis. Part I: ELEMENTARY PROCESSES. *Angew. Chem. Int. Ed* **1964**, *3 (1), 1-19*

(4) Marcus, R. A.; Electron Transfer Reactions in Chemistry: Theory and Experiment (Nobel Lecture). *Angew. Chem. Int. Ed*. **1993**, *32 (8), 1111-1121.*

(5) Genosar, L.; Cohen, B.; Huppert, D. Ultrafast Direct Photoacid−Base Reaction. *J. Phys. Chem. A*, **2000**, *104 (29), 6689–6698*;

(6) Cohen, B.; Huppert, D. Non-Exponential Smoluchowski Dynamics in Fast Acid−Base *Reaction J. Am. Chem. Soc.*, **2000**, *122 (40), 9838–9839*

(7) Rini, M.; Magnes, B. Z.; Pines, E.; Nibbering, E. T. J. Real-time observation of bimodal proton transfer in acid-base pairs in water. *Science* **2003**, *301, 349-352*;

(8) Mohammed, O. F.; Pines, D.; Dreyer, J.; Pines, E.; Nibbering, E. T. J. Sequential Proton Transfer Through Water Bridges in Acid-Base Reactions *Science* **2005**, *310, 83-86*;

(9) Mohammed, O. F.; Pines, D.; Nibbering, E. T. J.; Pines, E., *Angew. Chem., Int. Ed.* **2007**, *46, 1458-1461*;

(10) Siwick, B. J.; Bakker, H. J. On the Role of Water in Intermolecular Proton-Transfer Reactions *J. Am. Chem. Soc.* **2007**, *129, 13412-13420*;

(11) Siwick, B. J.; Cox, M. J.; Bakker, H. J. Long-range proton transfer in aqueous acid-base reactions *J. Phys. Chem. B* **2008**, *112, 378-389*;

(12) Cox, M. J.; Timmer, R. L. A.; Bakker, H. J.; Park, S.; Agmon, N. Distance-dependent proton transfer along water wires connecting acid-base pairs *J. Phys. Chem. A* **2009**, *113, 6599-6606.*

(13) Marx, D.; Hutter, J. Ab Initio Molecular Dynamics, *Cambridge University Press, New York*, **2009**.

(14) Maurer, P.; Iftimie, R. Combining ab initio quantum mechanics with a dipole-field model to describe acid dissociation reactions in water: first-principles free energy and entropy *calculations J. Chem. Phys.* **2010**, *132, 074112-074116*;

(15) Maurer, P.; Thomas, V.; Rivard, U.; Iftimie, R. A computational study of ultrafast acid dissociation and acid-base neutralization reactions. I. The model *J. Chem. Phys.* **2010**, *133, 044108*;

(16) Maurer, P.; Thomas, V.; Iftimie, R. A computational study of ultrafast acid dissociation and acid–base neutralization reactions. II. The relationship between the coordination state of solvent molecules and concerted versus sequential acid dissociation *J. Chem. Phys.* **2011**, *134, 094505-094513*.

(17) Spry, D. B.; Fayer, M. D. Charge redistribution and photoacidity: Neutral versus cationic photoacids *J. Chem. Phys.* **2008**, *128, 084508*

(18) Mohammed, O. F.; Pines, D.; Pines, E.; Nibbering, E. T. J. Aqueous bimolecular proton transfer in acid–base neutralization. *Chem. Phys.* **2007**, *341, 240-257*;

(19) Hynes, J. T. The Peripatetic proton. *Nature* ***2007**, 446, 270-273.*

(20) Staib, A.; Borgis, D.; Hynes, J. T. Proton transfer in hydrogen-bonded acid–base complexes in polar solvents. *J.Chem. Phys.* **1995**, *102, 2487*;

(21) Ando, K.; Hynes, J. T. Molecular Mechanism of HF Acid Ionization in Water: An Electronic Structure−Monte Carlo Study. *J.Phys. Chem. A* **1999**, *103, 10398-10408*.

(22) Leiderman, P.; Genosar, L.; Huppert, D. Excited-State Proton Transfer: Indication of Three Steps in the Dissociation and Recombination Process. *J. Phys. Chem. A* **2005**, *109, 5965*.

(23) Marx, D.; Tuckerman, M. E.; Hutter, J.; Parrinello, M. The nature of the hydrated excess proton in water. *Nature* **1999**, *397, 601-604*;

(24) Marx, D. Proton Transfer 200 Years after von Grotthuss: Insights from Ab Initio Simulations. *Chemphyschem* **2006**, *7, 1848-1870*;

(25) Markovitch, O.; Chen, H.; Izvekov, S.; Paesani, F.; Voth, G. A.; Agmon, N. Special Pair Dance and Partner Selection: Elementary Steps in Proton Transport in Liquid Water. *J. Phys. Chem. B* **2008**, *112, 9456-9466.397, 601-604*;

(26) CPMD V3, *Copyright IBM Corp 1990-2006, Copyright MPI für Festkörperforschung Stuttgart* **1997-2001**. For more details see *www.cpmd.org*

(27) Becke, A. D. Density-functional exchange-energy approximation with correct asymptotic behavior. *Phys. Rev. A* **1988**, *38, 3098-3100.*

(28) Lee, C. T.; Yang, W. T.; Parr, R. G. Development of the Colle-Salvetti conelation energy formula into a functional of the electron density. *Phys. Rev. B* **1988**,*37, 785-789.*

(29) roullier, N.; Martins, J. L. Efficient pseudopotentials for plane-wave calculations. *Phys. Rev. B* **1991**, *43, 1993-2006.*

6.6 Supporting Information

6.6.1 AIMD simulation: Details and Reliability.

In the present work we employ the Born-Oppenheimer molecular dynamics[1] (BOMD) approach whereby the nuclear trajectory is generated using forces obtained from electronic structure calculations based on the density functional theory[2] (DFT) formalism. The simulations are performed using the BLYP[3,4] exchange-correlation functional, plane wave basis sets and norm-conserving Troullier-Martins[5] pseudopotentials. The basis set was expanded up to a kinetic energy cut-off of 70 Ry.

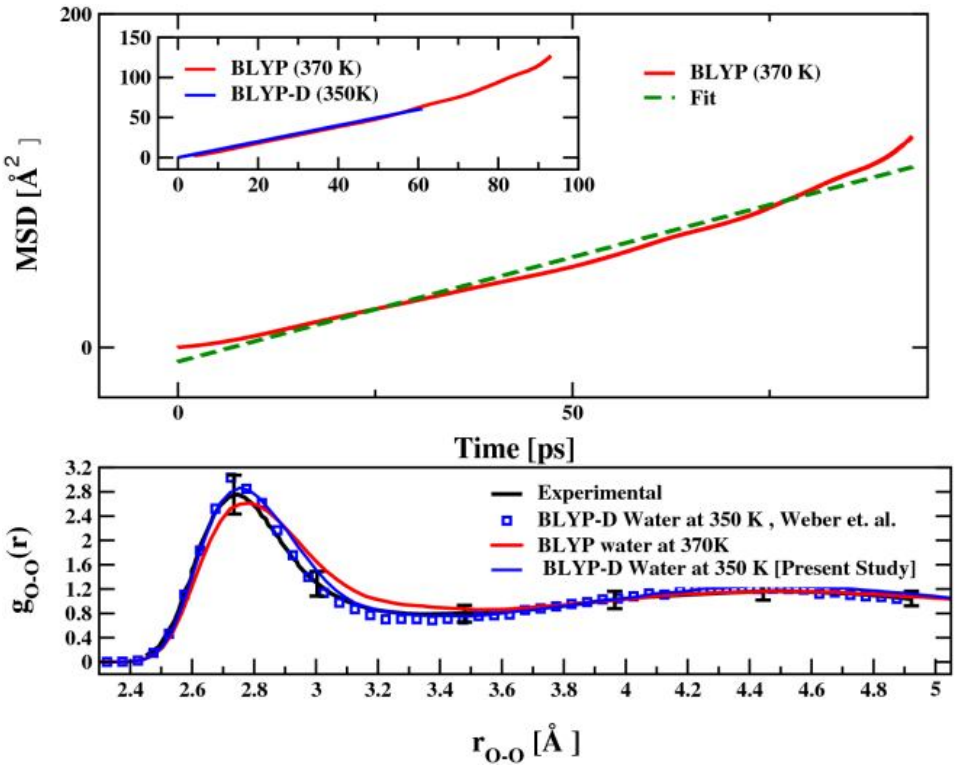

Figure 6-5. Mean square displacement (top panel) and oxygen-oxygen radial distribution function (bottom panel) for BLYP (370 K), BLYP-D (350 K) and real water (300 K) (see text).

There are numerous examples of the successful application of the DFT/BLYP approach to the investigation of aqueous systems and, in particular, acid-base reactions. Some

recent examples are provided in Ref. [6-19]. An interested reader can find more information in recent reviews[20,21] and books[1].

All calculations were carried out using the simulation package CPMD.[22] With the exception of the pseudoatoms forming the external dipoles (vide infra), all atoms, including those forming the solvent molecules, were described via full-QM electronic structure calculations. Periodic boundary conditions were employed throughout the simulations. The BOMD calculations were carried out in the canonical (i.e., NVT) ensemble at T=370 K, with an integration time-step of 15 a.u. (≈ 0.36 fs). This temperature is identical to that used in previous, related investigations[23,24] and was chosen[25] because BLYP water at ρ = 1g / cm^3 and T = 370 K correctly describes the structural and dynamical properties of real room-temperature water during the ~100 ps timescale of the present AIMD trajectories as can be seen from the data shown in Fig. 6-5. This data was partly shown in Ref. 6c from the main article, the difference shown here being the data for the functional BLYP-D.[26] The reader is referred to Ref. 6c from the main article for supplementary details. The data shown in the top panel of Fig. 6-5 can be utilized to compute diffusion coefficients D=0.21 Å^2/ps for both BLYP at 370 K and BLYP-D at 350 K. Both values compare very well with the experimental value[27] D=0.23 Å^2/ps for pure liquid water at room temperature. Water structure is also very well described by both BLYP and BLYP-D functionals at their respective temperatures as can be seen from the data shown in the bottom panel of Fig. 6-5. The BLYP-D pair correlation function was reported by Weber et al.[28] (blue squares in Fig. 6-5) and confirmed by our calculations (blue solid line). The experimental data including error bars for pure water at T=298 K was digitized from Refs. [29] and [30].

The exchange-correlation functional BLYP-D[26] differs from BLYP by the addition of an empirical potential energy term which describes dispersion interactions between all atoms present in the system. This energy term correctly describes intermolecular London interactions which are absent from the BLYP density functional treatment of the system, enabling one to correctly model the structure and diffusion of real room

temperature (i.e.: T=300 K) water by performing simulations at a temperature T=350 instead of T = 370 K, as can be seen from the data shown in Fig. 6-5 of the Supporting Information. However, even though this empirical term improves the description of the interaction between atoms separated by intermolecular distances, more investigations need to be performed in order to understand its effects at separations smaller than the van der Waals radii. At these separations the magnitude of the dispersion interactions must diminish in order to become zero at covalent separations, and this is usually implemented via empirical cut-off functions[26].

The effect of these empirical cut-off functions on the energy of various intermediate and transition state structures that can be formed in proton transfer reactions has not yet been reported. For example, the transferring proton in BLYP-D $H_5O_2^+$ interacts with both water molecules via an empirical damped dispersion interaction, but it is not clear whether this interaction is physically meaningful. For example, Arey et al.[31] reported that "dispersion-corrected BLYP exhibited a systematic bias towards over-binding in the case of charged H-bonded clusters" (such as $H_2O \bullet H^+ \bullet OH_2$ or $NH_4^+ \bullet\bullet OH_2$) "while pure BLYP handled these systems better" and concluded that "dispersion-corrected BLYP overcorrects the strength of charge-assisted H-bonds". We have verified that the results reported by Arey et al. also apply to the BLYP-D case. Since the present system involves charged H-bonds all along the acid-base neutralization pathway we preferred to adopt a conservative approach and employ the well-tested BLYP functional at 370 K. Since the current study investigates PT inside a solvent separated encounter complex we do not want these local interactions to be impacted by an empirical cut-off artifact and therefore make use of the BLYP functional.

The simulation cell contains one molecule of 2,6-dicyanophenol, one formate anion, and 56 water molecules in a rectangular box of size 17x11x11 $Å^3$, corresponding to a macromolecular solvent concentration of 0.80 mol/L. The starting structure was obtained by first optimizing the gas-phase geometry of an H-bonded cluster formed by

2,6-dicyanophenol, water and the formate ion. The optimized H-bond topology was found to correspond to the one depicted in Fig. 6-1B in the main article (see also Structure 2, from Fig. 6-6, to the right). The H-bonded cluster was subsequently placed in a box of SPC[32] water molecules that had been equilibrated using classical molecular

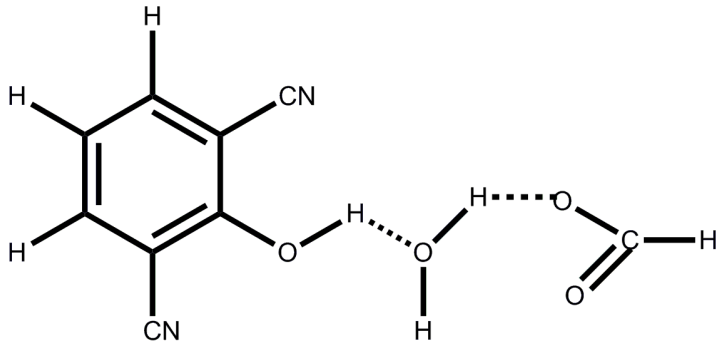

Structure 1

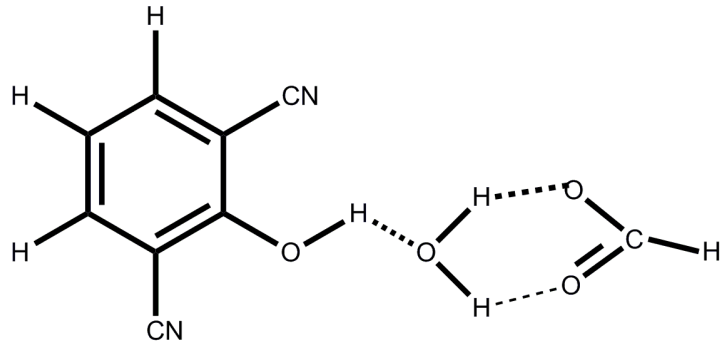

Structure 2

Figure 6-6. Gas-phase optimization of 2,6-dicyanophenol, formate and an intervening water molecule leads to formation of Structure 2. In aqueous solution however, the intervening water rotates and forms an H-bond with the bulk (Structure 1).

dynamics. The geometry of the solute, i.e.: phenol, formate and intervening water molecule was then fixed for a period of 13 ps, while allowing full equilibration of the solvent molecules. Finally, all geometry constraints were relaxed. It was observed that the initial H-bond topology (see Structure 2 from Fig. 6-6) was stable for less than 300 fs. The H-bond topology that formed subsequently and which remained stable for the rest of the simulations is shown in the top panel of Fig. 6-6. This result was confirmed by repeating the equilibration at T= 300, 350 and 370 K using the generalized-gradient

exchange-correlation functional BLYP as well as its dispersion-corrected version BLYP-D[26]. In all cases the H-bond rearrangement took place in less than 300 fs suggesting that the stable conformer in solution is the mono-dentate structure depicted as structure 1 in Fig.6-6.

6.6.2 Changing the pKa of acid and base. The effect of the constraints.

The pKa changes shown in Fig. 6-1C in the main article were implemented by employing a dipole-field / quantum mechanics DF/QM model, which is schematically depicted in Fig. 6-7. Within this model, the pKa changes are carried out by means of an

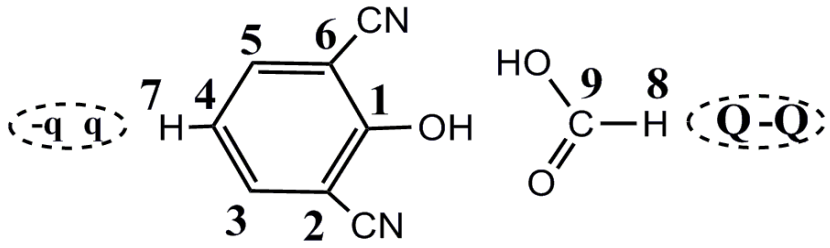

Figure 6-7. Chemical structure of 2,6-dicyanophenol and the formic acid. The locations of the pseudoatoms that generate the external dipole field are also shown. More details can be found in Ref. 9.

external potential. The potential in question is created by two appropriately placed external charges, as indicated in Fig. 6-7, and mimics the effects that would be exerted by a point dipole field which screened at short distance.[23,24] The values of the external pseudocharges used in the transformation shown in Fig. 6-1C from the main text are given in Table 6-1 bellow.

Previous investigations demonstrated that the DF/QM model is capable of predicting key properties of ortho and para cyano-substituted phenols[24] and of various aliphatic carboxylic acids[23] in gas phase as well as in aqueous solution. The pseudo-dipoles utilized in the DF/QM approach affect the solvation structure around the

Pseudo-charge	pKa (calc.)
Q = 7.38	0.2 ± 0.6
Q = 0	2.3 ± 0.6
q = 5.4	-0.4 ± 0.7
q = 0	1.6 ± 0.8
q = - 2.7	2.6 ± 0.9

Table 6-1. The values of Q and q defined in Fig. 6-2 utilized in the present calculations and the associated pKa values. The pKa values and the location of the charges were reported in Ref. 9.

carboxyl and phenol moieties in the same way as the full-QM substituents they are meant to model, as demonstrated in Figs. 9 and 10 from Ref. [24].

The simulation system, including two periodic images, is depicted in Fig. 6-4 bellow, showing that the system is homogeneously solvated. All atoms, including the pseudo-atoms that form the pseudo-dipole moments (shown in violet in Fig. 6-4) are periodically replicated. The distance separating the pseudo-dipoles across the interface is d=3.8 Å, which means that their interaction is screened by the presence of bridging water molecules. It should be noted that even though the formate ion present in our calculation has no explicit counter-ion, electrostatic interactions are computed via Ewald summation which adds a uniform positive neutralizing background charge (see Ref. 5 from the main article). What this means is that the system has an effective ionic strength I ~ 1M, and, therefore, the Debye length is approximately κ^{-1} ~ 3.04 Å, which is smaller than the separation between the two pseudo-dipoles. Hence, the interaction

between the pseudo-dipole moments across the periodic boundary can safely be assumed to play a negligible role.

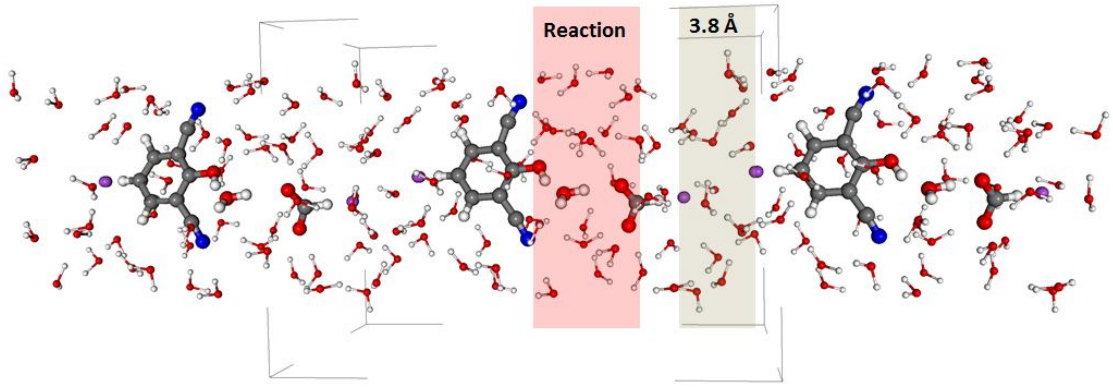

Figure 6-8. The simulation box and two periodic images showing the reactive region and the interaction between the fictitious dipoles across the interface. Color code: Oxygen, nitrogen, carbon and hydrogen atoms are depicted in red, blue, black and grey. The pseudoatoms forming the pseudo dipole moments are shown in violet.

The positions of the atoms H7, C4, H8 and C9 defined in Fig. 6-7 are fixed within the DF/QM approach for reasons which are explained in detail in Ref. [23]. Their coordinates correspond to those obtained during the gas-phase geometry optimization of the H-bond cluster mentioned above. One consequence is that the distance between the carbon atoms C4 and C9 becomes fixed at 9.13 Å during the present AIMD calculations. Another consequence is that the acid and base molecules are properly oriented for proton transfer: analysis of all AIMD trajectories indicates that the acid and base molecules were connected by a one water molecule H-bond bridge approximately 95% of the time. The remaining 5% of the AIMD configurations corresponded to acid and base being separated by two intervening water molecules

Since proton transfer critically depends on the distance between acid and base we have computed the distribution of the relevant oxygen-oxygen distances recorded in the present constrained AIMD calculations. These results are shown in Fig. 6-9 A, B and show that the rigid constraints on the atoms H7, C4, H8 and C9 translate into weak

constraints on the distances between the phenolic and the two carboxylic oxygen atoms since these distances are allowed in the present model to vary anywhere between 4.0 and 6.0 Å. Moreover, and equally important, the length of the shortest H-bond wire connecting the donor to the acceptor via the intervening water molecule can vary between 5Å (O(phenol)-O(water) ≈ O(water)-O(carboxyl) ≈ 2.5 Å) and 6.5 Å (O(phenol)-O(water) ≈ O(water)-O(carboxyl) ≈ 3.25 Å). Therefore, the oxygen atoms have sufficient freedom to explore all relevant oxygen-oxygen separation distances. This is expected because the constraints involve only atoms that are relatively far from the reaction core. In addition the acid and base molecules are free to vibrate, bend and rotate, while the solvent molecules are entirely free to move.

In order to estimate quantitatively the effects of the constraints we have also run a 64 ps AIMD dynamics with no constraints, using the 2,6 dicyanophenol acid and the trifluoroacetate base. The acid-base reaction did not take place with the weaker trifluoroacetate base, which allowed us to compute the same oxygen-oxygen distance

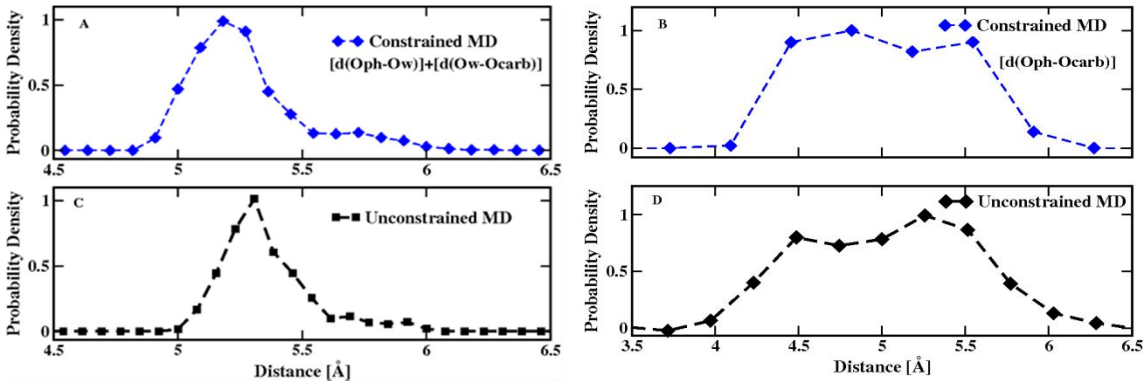

Figure 6-9. Distribution of oxygen-oxygen distances relevant to the proton transfer reaction from constrained (top) and unconstrained (bottom) AIMD calculations (see text). Panels B and D display the distribution of distances between donor and acceptor oxygen atoms. Panels A and C depict the distribution of the distances connecting the acid to the intervening water molecule plus the intervening water to the base (see text).

distributions as in the constrained case. The results are shown in Fig. 6-9 C, D and were obtained by utilizing only the AIMD frames in which the acid and base molecules could be connected by a one water molecule H-bond bridge. In particular we considered that

acid and base were separated by an intervening water molecule when both the distance O(phenol)-O(water) and O(water)-O(carboxyl) were smaller than 3.25 Å.

The data shown in Fig. 6-9 suggests that by constraining the atoms H7, C4, H8 and C9 to their gas-phase coordinates effectively restricts the exploration of the entire state space to the subspace of water-bridged acid-base encounter pairs. This restriction was necessary because the AIMD would otherwise sample the entire state space, thus significantly reducing the number of water-separated acid-base reactions that could have been observed given the same computational effort; for example, Mohammed et al.[33] estimated that the population of water-separated encounter pairs between HPTS and trifluoroacetate ions represents about 7% of the total population.

6.6.3 The Continuous Complex Morlet Transform

The input signals utilized to produce the data depicted in Fig. 6-2b-d in the main article are the trajectories of the carbon-oxygen and oxygen-hydrogen bond lengths computed for the phenol, carboxylate, and intervening water molecules, as explained in the main article. An important characteristic of these signals is that they form *non-stationary* time series, whose behavior in the frequency space must be investigated using appropriate time-frequency analysis techniques[34]. As a parenthesis, it should be noted that the traditional signal analysis based on the Fourier transform (FT) is inadequate because FT is a global transform, thus being unable to express time-frequency local properties that characterize non-stationary signals. Moreover, short-time FT approaches[34] which utilize a moving interval of fixed duration in the interior of which quasi-stationary behaviour is assumed are also limited in scope because a fixed time interval that allows good resolution of high frequency oscillations will prove inadequate for sufficiently low frequency oscillations.

The wavelet transform is a multi-resolution time-frequency analysis technique that resolves high frequency and low frequency oscillations equally satisfactorily by decomposing the non-stationary time-series of interest $x(t)$ into wavelets. A wavelet is

a wave-like oscillation whose amplitude starts out at zero, increases, and then decreases back to zero.

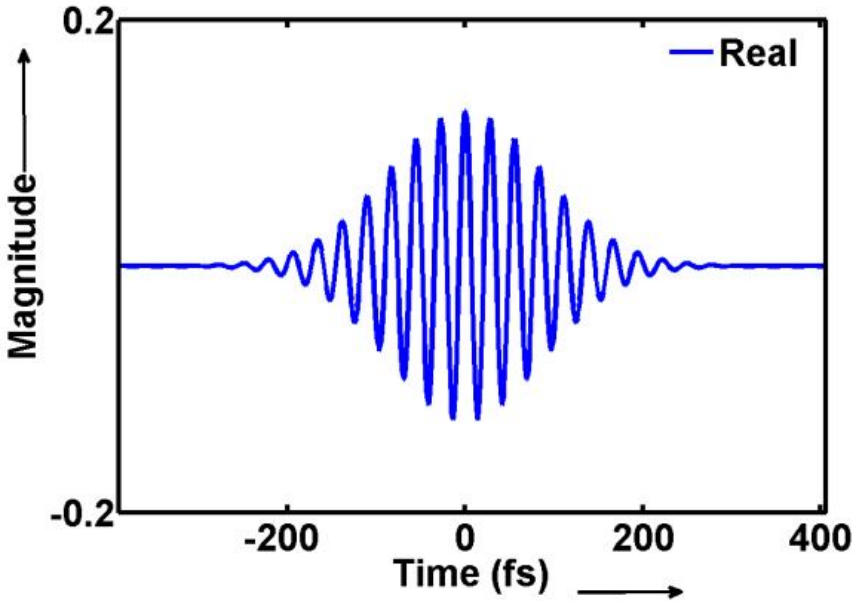

Figure 6-9. A plot of the real part of the wavelet intensity Ψ(t) defined in Eq. (6.2) and the text accompanying it as a function of time. The wavelet depicted here corresponds to a wavenumber $\nu = 1200$ cm^{-1} (see text). Note that the amplitude of the oscillatory signal is significant for approximately 400 fs, which can be taken as a rough estimate for the time resolution of the present wavelet decomposition approach.

The continuous wavelet transform the time-series $x(t)$ can be written as:

$$W(a,b) = \frac{1}{\sqrt{a}} \int_{-\infty}^{\infty} x(t)\psi^* \left(\frac{t-b}{a} \right) dt, \qquad (6.1)$$

where ψ is a continuous function called the mother wavelet, the star represents the operation of complex conjugate, a represents the scale index and b the scale shift. The factor $1/\sqrt{a}$ is a normalization factor. The parameters a and b have the dimensions of time, but b is usually transformed into a wave number axis by the transformation $\nu = 1/(c \cdot a)$ where $c = 3 \cdot 10^{10}$ cm/s is the speed of light.

In the present study the mother wavelet was chosen to be the so-called complex Morlet wavelet defined as[34]:

$$\psi(m) = \frac{1}{\sqrt{\pi f_b}} e^{i \cdot 2\pi f_c m} e^{-m^2/f_b} \qquad (6.2)$$

where $i = \sqrt{-1}$, $m = (t-b)/a$ is a dimensionless number, f_b is called the band width and is responsible for the shape of the wavelet, and f_c is called the center frequency. The form of a wavelet function $\psi(t)$ as a function of time is displayed in Fig. 6-10 in the particular case $f_b = 20$, $f_c = 1$, $b = 0$ fs, $a = 27.77$ fs. The value of b chosen here corresponds to a wavelet centered at 0 fs and the value chosen for the scale index a corresponds to a wave number $\nu = 1200$ cm^{-1}, characteristic to C-O bond stretch vibrations in the phenol molecule. The aforementioned values for the parameters f_b and f_c were empirically found to provide acceptable resolutions for the time and wavenumber axes. The resulting scalogram $W(\nu,t)$ was subsequently utilized to compute the value $\nu_{\max}(t)$ reported in Fig. 6-2b-d in the main article, which represents the value of the wavenumber ν that corresponds to the maximum value of $W(\nu,t)$ at any given time t.

6.6.4 Nuclear quantum effects

Although, it is desirable to include nuclear quantum effects explicitly in simulations of proton transfer reactions, existing experimental data suggests that such a treatment is not mandatory in the present case. Kinetic isotope effects (KIE) values of 1.4 have been reported[35,36] for excited-sate acid-base neutralization reactions between HPTS and carboxylate bases, indicating that tunneling effects play only a minor role. Hence, it was decided to describe nuclear dynamics within the framework of Newton's mechanics, which rendered the computational effort an order of magnitude less computer intensive.

6.6.5 References

(1) Marx, D.; Hutter, J. *Ab Initio Molecular Dynamics*; Cambridge University Press: New York, 2009.

(2) Koch, W.; Holthausen, M. C. *A Chemist's Guide to Density Functional Theory*; VCH: New York, 2000.

(3) Becke, A. *Phys. Rev A* **1998**, *38*, 3098.

(4) Lee, C.; Yang, W.; Parr, R. G. *Phys. Rev. B* **1998**, *37*, 785.

(5) Troullier, N.; Martins, J. L. *Phys. Rev. B* **1991**, *43*, 1993.

(6) Vilciauskas, L.; Tuckerman, M. E.; Bester, G.; Paddison, S. J.; Kreuer, K. D. *Nat. Chem* **2012**, *4*, 461.

(7) Hassanali, A.; Prakash, M. K.; Eshet, H.; Parrinello, M. *Proc. Natl. Acad. Sci. USA* **2011**, *108*, 20410.

(8) Hassanali, A. A.; Cuny, J.; Ceriotti, M.; Pickard, C. J.; Parrinello, M. *J. Am. Chem. Soc.* **2012**, *134*, 8557.

(9) Berkelbach, T. C.; Lee, H. S.; Tuckerman, M. E. *Phys. Rev. Lett* **2009**, *103*, 238302.

(10) Rousseau, R.; Kleinschmidt, V.; Schmitt, U. W.; Marx, D. *Angew. Chem. Int. Ed.* **2004**, *43*, 4804.

(11) Mathias, G.; Marx, D. *Proc. Natl. Acad. Sci. USA* **2007**, *104*, 6980.

(12) Iftimie, R.; Tuckerman, M. E. *Angew. Chem. Internat. Ed.* **2006**, *45*, 1144.

(13) Chandra, A.; Tuckerman, M. E.; Marx, D. *Phys. Rev. Lett* **2007**, *99*, 4.

(14) Heyden, M.; Sun, J.; Funkner, S.; Mathias, G.; Forbert, H.; Havenith, M.; Marx, D. *Proc. Natl. Acad. Sci. USA* **2010**, *107*, 12068.

(15) Ludwig, R. *Angew. Chem. Int. Ed.* **2003**, *42*, 258.

(16) Kirchner, B.; Stubbs, J.; Marx, D. *Phys. Rev. Lett.* **2002**, *89*.

(17) Tuckerman, M. E.; Marx, D.; Parrinello, M. *Nature* **2002**, *417*, 925.

(18) Geissler, P. L.; Dellago, C.; Chandler, D.; Hutter, J.; Parrinello, M. *Science* **2001**, *291*, 2121.

(19) Iftimie, R.; Thomas, V.; Plessis, S.; Marchand, P.; Ayotte, P. *J. Am. Chem. Soc.* **2008**, *130*, 5901.

(20) Marx, D. *ChemPhysChem* **2006**, *7*, 1848.

(21) Marx, D.; Chandra, A.; Tuckerman, M. E. *Chem.Rev.* **2010**, *110*, 2174.

(22) CPMD V3.11, Copyright IBM Corp 1990-2006, Copyright MPI für Festkörperforschung Stuttgart 1997-2001. For more details see www.cpmd.org

(23) Maurer, P.; Iftimie, R. *J. Chem. Phys.* **2010**, *132*, 074112.

(24) Maurer, P.; Thomas, V.; Rivard, U.; Iftimie, R. *J. Chem. Phys.* **2010**, *133*, 044108.

(25) Maurer, P.; Thomas, V.; Iftimie, R. *J. Chem. Phys.* **2011**, *134*, 094505.

(26) Grimme, S. *Journal of Computational Chemistry* **2006**, *27*, 1787.

(27) Price, W. S.; Ide, H.; Arata, Y. *J. Phys. Chem. A* **1999**, *103*, 448.

(28) Weber, V.; Asthagiri, D. *J. Chem. Phys.* **2010**, *133*, 141101.

(29) Soper, A. K. *Chem. Phys.* **2000**, *258*, 121.

(30) Habershon, S.; Markland, T. E.; Manolopoulos, D. E. *J. Chem. Phys.* **2009**, *131*, 024501.

(31) Arey, J. S.; Aeberhard, P. C.; Lin, I. C.; Rothlisberger, U. *J. Phys. Chem. B* **2009**, *113*, 4726.

(32) Berendsen, H. J. C.; Postma, J. P. M.; van Gunsteren, W. F.; Hermans, J. In *Intermolecular Forces*; Pullman, B., Ed.; Reidel: Dordrecht, 1981, p 331.

(33) Mohammed, O. F.; Pines, D.; Nibbering, E. T. J.; Pines, E. *Angew. Chem. Int. Ed.* **2007**, *46*, 1458.

(34) Flandrin, P. *Time-Frequency/Time-Scale Analysis*; Academic Press: London, 1999; Vol. 10.

(35) Siwick, B. J.; Bakker, H. J. *J. Am. Chem. Soc.* **2007**, *129*, 13412.

(36) Mohammed, O. F.; Pines, D.; Dreyer, J.; Pines, E.; Nibbering, E. T. J. *Science* **2005**, *310*, 83.

7. Conclusions

7.1 Conclusions

Aqueous proton transfer reaction is fundamental to many aspects of chemical[1,2] and biochemical[3-7] processes, including enzymatic catalysis, biochemical energy storage and transport through biological membranes[3,4,8,9] and photosystems[10]. Yet, despite its extreme importance and extensive research for over three centuries, a completely conclusive and comprehensive picture of the mechanism of the elementary steps involved in the aqueous proton transfer reactions and the role played by the solvent water molecules are not very well understood. Several important questions remains open, which includes

- Does acid dissociations in aqueous solutions involves proton transfer intermediates?
- How can these intermediates, if any, be trapped?
- How can these intermediates, if any, be characterized spectroscopically?
- What is the exact nature of proton donor and acceptor intermediates?
- What is the exact role played by the surrounding local hydrogen bonding environment in proton transfer?
- How important is the role played by vibrational zero-point energy and nuclear quantum effects in the proton transfer process in aqueous environment?
- How can we identify and follow the dynamics of different proton transfer intermediate species in a system?
- What are the quantitative elementary microscopic steps involved in the proton transfer reactions in an encounter complex?

In this thesis the above mentioned questions were addressed by carefully designed first principle molecular dynamics simulations and state-of-the-art analysis techniques.

An ab initio molecular dynamics simulations calibrated against experimental infrared spectroscopic study on very low temperature amorphous mixtures of hydrofluoric acid (HF)−water (H_2O) system provided the evidence that cryogenic temperatures favor the formation of significant quantities of proton shared ion-pair intermediates $[F^- \bullet H^+ \bullet OH_2]$ to conclude that dissociation of the hydrofluoric acid proceeds mainly through a proton-shared intermediate that are found to be stabilized by distinct first solvation hydrogen bond topologies (local solvation). These proton shared intermediates, which are the species involved in the first stage in acid ionization were found to have distinct infrared spectral signature. This would enable them to be detected using time-resolved infrared spectroscopy experiments, provided that the concentration of such intermediates becomes significant, and that no other molecules present in the system absorbs radiation in the same spectral window.

Nuclear quantum effects should in principle play an important role when anharmonic proton potentials are involved, and this is expected to be the case for the species such as strongly bonded $[F\text{-}H \bullet OH_2]$ or contact-ion pairs $[F^- OH_3^+]$. To this end, vibrational zero-point vibration as well as incoherent tunneling effects were approximately incorporated in our calculations within the framework of centroid molecular dynamics[11-13]. It was found that the anharmonic dynamics of the transferring proton favors the formation of proton shared species $[F^- \bullet H^+ \bullet OH_2]$ in which the proton vibrates in an almost barrier less potential. This gives rise to an extremely wide and intense infrared absorption centered at 1700 cm^{-1}.

Although, this study on the textbook model system (aqueous hydrofluoric acid) established that the earliest step along the dissociation pathway consists of

transforming the covalent form of acid into the proton-shared form, accompanied by the formation of an extremely wide but featureless infrared absorption, it was unclear whether the conclusions reached in this study were general. To verify this we focused on aqueous carboxylic acid, trifluoroacetc acid. This second investigation confirmed our previous findings on the presence of proton transfer intermediates in acid dissociation. Aqueous solution of trifluoroacetic acid contains proton shared structures of form $[\text{R-COO}^{\delta-} \cdot \text{H} \cdot^{\delta+} \text{OH}_2]$ and contact-ion pair structures of form $[\text{R-COO}^- \cdot \text{H}_3\text{O}^+]$. It was also demonstrated that the formation of proton-shared form is characterized by "continuous" absorption below 1700 cm^{-1}. Transformation from proton-shared into contact-ion pair was found to be accompanied by significant change in local H-bond topology and characterized by the disappearance of carbonyl vibration mode (1700 cm-1) and the appearance of carboxylate stretching modes.

In the final project, attention was focused on the proton transfer involving a proton donor and a proton acceptor in aqueous solutions. A model system involving phenolic and carboxylic reactants closely related to the model systems investigated experimentally were investigated. We identified three distinct proton transfer pathways that contribute to acid-base reactions inside solvent-seperated encounter complexes:

1. direct concerted transfer from acid to base through the bridging water molecule with no formation of intermediates
2. A sequential transfer with the participation of a protonated intervening water molecule that contains two O-H bonds that form and break on a sub-picosecond timescale, and a third, slightly elongated O-H bond that fluctuates around its equilibrium position for the entire lifetime of the ion-pair intermediate
3. An indirect neutralization pathway via dissociation to the bulk.

A direct comparison of this study was made possible using time-frequency analysis based on the complex Morlet wavelet transform which allowed to follow the vibration spectrum of various vibrational modes in time with the progress of the reaction.

The results discuscussed in this thesis contribute significantly to the molecular level understanding of the diverse proton transfer processes involved in acid dissociation in liquid water and acid-base neutralization reactions. Our work demonstrates also the important ways in which molecular dynamics simulations can complement experimental work. Nevertheless, there are still some fundamental questions that require further attention, which includes:

1) What is the solvent reaction coordinate which drives proton transfer? Although we were able to correlate the discrete stages of proton transfer to the local H-bond topology of the proton donor, intermediate species and proton acceptor, it is unclear whether this is the only solvent coordinate that plays an important role. Investigations are underway to quantify the role of rare electric field fluctuation originating from solvent rearrangement.
2) How different is the microscopic mechanism of proton abstraction by a base in liquid water (reverse proton transfer) from acid dissociation?.
3) In this thesis we have considered only the proton transfer from neutral acids leading to formation of ion-pairs. What about cationic acids that undergoes the reaction $A\text{-}H^+ \rightarrow A + H^+$ in which the proton transfer does not lead to the formation of ion-pairs ?. What is the role of solvation in such a proton transfer?.
4) Are proton transfer reactions functional group dependent ?. Experimental studies on anilinium acids indicated a very large kinetic isotope effect of magnitude 5.0^{14}, independent of the pKa value , which is different from proton transfer from oxygen or fluorine, suggesting a different proton transfer mechanism.

5) The acid-base reaction studied in this thesis consisted of an acid and a base molecule bridged by a single water molecule $A\text{-}H\cdots H_2O\cdots^- B$. The results of this investigation showed strong weightage for the concerted proton transfer

pathway. Is this mechanism depends on the relative orientation and distance between acids-base pairs?

It seems like the present study has lead to more questions than answers. Nevertheless, this study has made a significant progress in the molecular level understanding of proton transfer process in aqueous solutions.

7.2 References

(1) Marx, D.; Chandra, A.; Tuckerman, M. E. *Chem Rev* 2010, *110*, 2174.

(2) Adamczyk, K.; Premont-Schwarz, M.; Pines, D.; Pines, E.; Nibbering, E. T. J. *Science* 2009, *326*, 1690.

(3) Braun-Sand, S.; Strajbl, M.; Warshel, A. *Biophysical Journal* 2004, *87*, 2221.

(4) Decoursey, T. E. *Physiological Reviews* 2003, *83*, 475.

(5) Cukierman, S. *Biochimica Et Biophysica Acta-Bioenergetics* 2006, *1757*, 876.

(6) Wraight, C. A. *Biochimica Et Biophysica Acta-Bioenergetics* 2006, *1757*, 886.

(7) Swanson, J. M. J.; Maupin, C. M.; Chen, H. N.; Petersen, M. K.; Xu, J. C.; Wu, Y. J.; Voth, G. A. *J Phys Chem B* 2007, *111*, 4300.

(8) Garczarek, F.; Brown, L. S.; Lanyi, J. K.; Gerwert, K. *P Natl Acad Sci USA* 2005, *102*, 3633.

(9) Garczarek, F.; Gerwert, K. *Nature* 2006, *439*, 109.

(10) Maeda, A.; Morgan, J. E.; Gennis, R. B.; Ebrey, T. G. *Photochemistry and Photobiology* 2006, *82*, 1398.

(11) Cao, J.; Voth, G. A. *J Chem Phys* 1994, *100*, 5093.

(12) Cao, J. S.; Voth, G. A. *J Chem Phys* 1993, *99*, 10070.

(13) Marx, D.; Tuckerman, M. E.; Martyna, G. J. *Comput Phys Commun* 1999, *118*, 166.

(14) Shiobara, S.; Tajima, S.; Tobita, S. *Chem Phys Lett* 2003, *380*, 673.

1. Annex I

More Details on Computing IR spectra from MD Simulation

I.1 General

In this annex we will see more details on the theoretical foundation for the calculation of infrared spectra from ab initio molecular dynamics simulations discussed in section 2.8.3.

Imagine a molecule in a time-dependent electric field $E(t) = \epsilon E_0 \cos(\omega t)$, where E_0 is the amplitude and ϵ is the unit vector along the electric field. The interaction of the molecule with the external field can be described by a small perturbation to molecular Hamiltonian, $\hat{H}^{(0)}$ as $\hat{H}^{(1)}(t) = -\hat{M}E(t)$, with $\hat{M}$ being the total electric dipole moment operator of the system. In quantum mechanical picture the probability $P_{i\to f}(\omega)$ for a transition between an initial quantum state $|i\rangle$ and a final quantum state $|f\rangle$ is calculated using *Fermi golden rule* of time-dependent perturbation theory[1]. The rule states that, in first-order perturbation theory, the transition rate depends only on the square of the matrix element of the operator $\hat{M}$ between initial and final states and explicitly requires energy conservation via the δ-function. Fermi's Golden Rule predicts the probability of transitions from a specific initial state $|i\rangle$ to a final state $|f\rangle$, both of which are eigenstates of $\hat{H}^{(0)}$ and which are connected via the energy conservation condition $E_f = E_i + \hbar\omega$. The rule is written as:

$$P_{i\to f}(\omega) = \frac{\pi E_0^2}{2\hbar^2} |< f | \varepsilon \hat{M} | i >|^2 \left[\delta(\omega_{fi} - \omega) + \delta(\omega_{fi} + \omega)\right], \qquad \text{(I.1)}$$

where $\hat{M}$ is the dipole moment operator, ω is the frequency of the incoming radiation and the additional frequencies in the arguments of the δ-functions , $\omega_{f,i}$ is defined as the energy difference between the final and initial state ($\omega_{f,i} = \frac{E_f - E_i}{\hbar}$).

The second δ-function in Eq. (I.1) is responsible for what is called *stimulated absorption* of the radiation by the molecular system from the radiation field, since when multiplied by the frequency distribution of the incoming radiation and then integrated over ω it imposes the condition $E_f = E_i + \hbar\omega$. Similarly the first δ-function in Eq.(I.1) then is responsible for the *stimulated emission* of energy from the molecular system as it imposes the condition $E_f = E_i - \hbar\omega$.

Transforming Eq. (I.1) to a macroscopic (ensemble) level is accomplished by defining a transition rate in to final state

$$-\dot{E}_{rad} = \sum_{i,f} \rho_i \hbar\omega_{fi} P_{i\to f} \tag{I.2}$$

$$\begin{aligned} &= \frac{\pi E_0^2}{2\hbar} \sum_{f,i} \omega_{fi}\rho_i \mid \langle f \mid \varepsilon.M \mid i\rangle \mid^2 [\delta(\omega_{fi} - \omega) + \delta(\omega_{fi} + \omega)] \\ &= \frac{\pi E_0^2}{2\hbar} \omega_{fi}(\rho_i - \rho_f) \mid \langle f \mid \varepsilon.M \mid i\rangle \mid^2 \delta(\omega_{fi} - \omega) \\ &= \frac{\pi E_0^2}{2\hbar} \omega_{fi} \sum_{fi} \omega(1 - e^{-\beta\hbar\omega}\rho_i \mid \langle f \mid \varepsilon.M \mid i\rangle \mid^2 \delta(\omega_{fi} - \omega) \end{aligned} \tag{I.3}$$

where the final step is obtained by assuming that initial and final states are populated by a Boltzman-weighted factor $\rho_f = \rho_i e^{-\beta\hbar\omega}$. Note that not all initial states can end up in final state due to the energy conservation.

Then by defining absorption coefficient $\alpha(\omega)$ as

$$\alpha(\omega) = \frac{\dot{E}_{rad}}{E_{rad}} = \frac{4\pi^2}{\hbar cn} \omega(1 - e^{-\beta\hbar\omega} \sum_{f,i} \rho_i \mid \langle f \mid \vec{\varepsilon}.\vec{M} \mid i\rangle \mid^2 \delta(\omega_{fi} - \omega) \tag{I.4}$$

At this point, introducing the lineshape quantity as

$$I(\omega) = \frac{3\hbar cn\alpha(\omega)}{4\pi^2\omega(1-e^{-\beta\hbar\omega})} = 3\sum_{f,i}\rho_i \mid \langle f \mid \varepsilon.M \mid i\rangle \mid^2 \delta(\omega_{fi}-\omega) \tag{I.5}$$

Rewriting the delta function in Eq. (I.5) by its Fourier integral, and rearranging we get

$$\begin{aligned} I(\omega) &= \frac{3}{2\pi}\sum_{i,f}\rho_i\langle i \mid \varepsilon M \mid f\rangle\langle f \mid M \mid i\rangle \frac{1}{2\pi}\int_{-\infty}^{\infty} e^{i(\frac{E_f-E_i}{\hbar})tdt} \\ &= \frac{3}{2\pi}\int_{-\infty}^{\infty} dt\left[e^{i\omega t}\sum_{f,i}\rho_i\langle i \mid \varepsilon\cdot M \mid f\rangle\langle f \mid e^{iE_f t/\hbar} \mid \varepsilon\cdot M \mid e^{-iE_f t/\hbar}\rangle\right] \\ &= \frac{3}{2\pi}\int_{-\infty}^{\infty} dt\left[e^{i\omega t}\sum_{f,i}\rho_i\langle i \mid \varepsilon\cdot M \mid f\rangle\langle f \mid e^{iH^{(0)}\ t/\hbar} \mid \varepsilon\cdot M \mid e^{-iH^{(0)}t/\hbar}\rangle\right] \end{aligned} \tag{I.6}$$

Converting the last equation of Eq. (I.6) in to Heisenberg representation and using the identity

$$\sum_f \ \langle f \mid f\rangle = 1 \tag{I.7}$$

$$\begin{aligned} I(\omega) &= \frac{3}{2\pi}\int_{-\infty}^{\infty}\ \sum_i \rho_i\langle i \mid \varepsilon\cdot\hat{M}(0)\ \varepsilon\cdot\hat{M}(t)\mid i\rangle e^{i\omega t}dt \\ &= \frac{1}{2\pi}\int_{-\infty}^{\infty} e^{-i\omega t}dt\langle\hat{M}(0).\hat{M}(t)\rangle_{qm} \end{aligned} \tag{I.8}$$

Substituting Eq. (I.8) in Eq. (I.4), absorption coefficient $\alpha(\omega)$ becomes

$$\alpha(\omega) = \frac{2\pi}{3\hbar cn}\omega(1-e^{-\beta\hbar\omega})\int_{-\Delta}^{\infty}\langle\hat{M}(0)\hat{M}(t)\rangle_{qm} \tag{I.9}$$

where the $\langle..\rangle_{qm}$ represents the quantum mechanical ensemble average , $\hat{M}(0)$ and $\hat{M}(t)$ are the quantum mechanical dipole moment operators written in Heisenberg representation at time t=0 and t=t.

A rigorous calculation of quantum correlation function is hard to compute for condensed phase systems. However, if we assumes the validity of the central approximation of the centroid molecular dynamics[2,3] theory. The term, $\langle\hat{M}(0)\hat{M}(t)\rangle_{qm}$ can be approximately[4] written as

$$\langle M(0)M(t)\rangle = \left[(1 + c\tanh(\frac{\beta\hbar\omega}{2})\right]\frac{\hbar\beta\omega}{2}\int_{-\infty}^{\infty} e^{i\omega t}\langle M(0)M(t)\rangle_{centroid}$$
$$= \frac{2}{1-e^{-\beta\hbar\omega}}\frac{\beta\hbar\omega}{2}\int_{-\infty}^{\infty} e^{i\omega t}\langle M(0)M(t)\rangle_{centroid} \quad \text{(I.10)}$$

and

$$\alpha(\omega)n(\omega) = \frac{2\pi\beta}{3c}\int e^{i\omega t}dt\langle \dot{M}0)\dot{M}(t)\rangle_{centroid} \quad \text{(I.11)}$$

where the autocorrelation function involves the centroid average of the time-derivative of the dipole moment centroid symbol. Since centroid averages are computed in practice by means of finite number of path-integral quasi-particles, a further approximation consists of considering a single imaginary-time discretization of the quasi-particle chain can be adopted. This amounts essentially to adopting the well-known harmonic approximation[5]. Our approach in the present work is to adopt the computationally less expensive harmonic approximation in most of the calculations.

Converting Eq. (I.11) in to SI units gives,

$$\alpha(\omega)n(\omega) = \frac{1}{6kT\varepsilon_0 cV}\int_{-\infty}^{\infty} e^{-i\omega t}\langle \dot{M}(0)\dot{M}(t)\rangle_{classical} \quad \text{(I.12)}$$

I.2 References

(1) McQuarrie, D. A. *Statistical Mechanics, Univeristy Science books page 554* **2000**.

(2) Cao, J.; Voth, G. A. *J Chem Phys* **1994**, *100*, 5093.

(3) Cao, J. S.; Voth, G. A. *J Chem Phys* **1993**, *99*, 10070.

(4) Iftimie, R.; Tuckerman, M. E. *J Chem Phys* **2005**, *122*, 11.

(5) Bader, J. S.; Berne, B. J. *J Chem Phys* **1994**, *100*, 8359.

2. Annex II

More Details on Computing Time-dependent Vibrational Spectra from MD Simulation

2.1 I.1 General

In this annex we will see more details on obtaining time dependent vibrational spectra calculations used in Chapter 6 of this thesis. The most basic technique for determining the frequency distribution of a signal is the Fourier transform. The Fourier transform[1] decomposes a signal in complex exponential functions at different frequencies. Using the notation of inner product, the Fourier transform of a signal $x(t)$ is written as

$$X(\omega) = \langle x, e^{i\omega t} \rangle = \int_{-\infty}^{\infty} x(t) e^{-i\omega t} dt \qquad \text{(II.1)}$$

where t stands for time and $\omega = 2\pi\nu$ for frequency.

Accordingly, the inverse Fourier transform is written as

$$x(t) = \int_{-\infty}^{\infty} X(\omega) e^{i\omega t} d\omega \qquad \text{(II.2)}$$

As seen from the Eq. (II.1), Fourier transform provides what spectral components exist and not where in time they are located. One of the simplest methods to locate the change in frequency component over time is to segment the signal in to narrow time intervals, narrow enough to be considered stationary and then take the Fourier transform of each segment. This analysis window of certain length slides through the entire signal along the time axis to perform Fourier transform at each segment. As a result, the time domain signal is transformed in to a two-dimensional time-frequency representation. This method of short time Fourier transform[2] is introduced by Dennis Gabour (also called Gabour transform). This procedure is illustrated in Fig II-1.

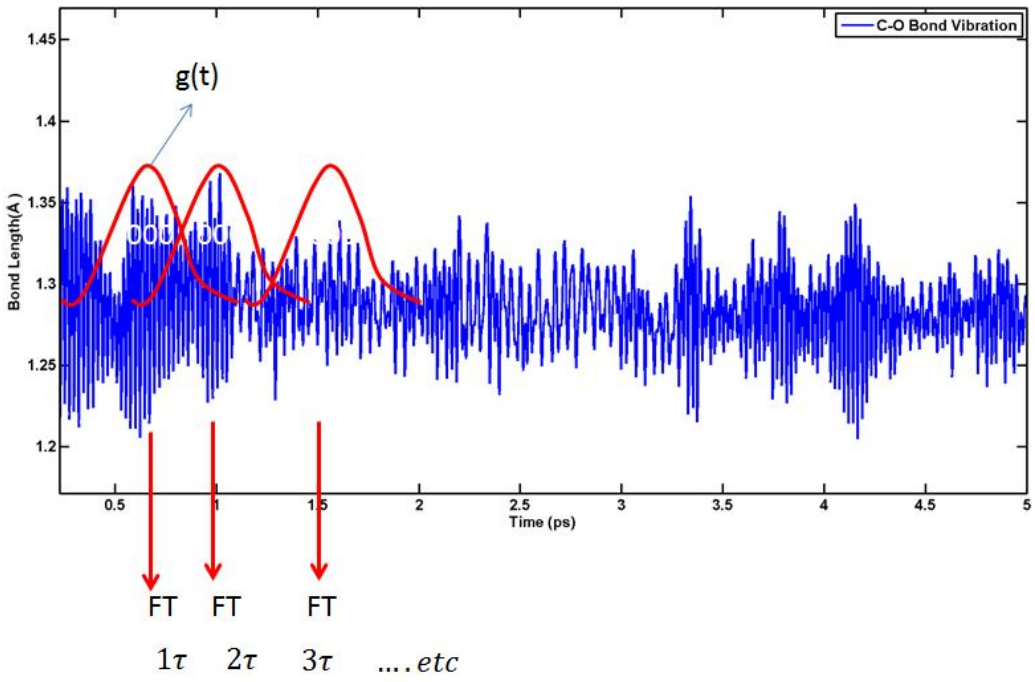

Figure II-1. Illustration of short time fourier transform on a a signal (CO bond vibration).

Short time Fourier transform can be mathematically written as

$$Tx(\tau,\omega) = \langle x, g_{\tau,\omega} \rangle \int_{-\infty}^{\infty} g(t-\tau)x(t)e^{-i\omega t}dt, \qquad \text{(II.3)}$$

where $g(t)$ is the window function and τ is the location. An example of a window function is a Gaussian window function $g(t) = e^{-\alpha t^2 \tau^2}$,where α being a constant and τ controls the length of window.

A subtle limitation of this method is associated with a constant window size. A narrow window will nicely localize higher frequencies both in time and frequency, but lower frequencies will be "blurry" in frequency. A winder window will make the lower frequencies better, but the higher frequencies will be "blurry" in time. This effect of window size on time and frequency is illustrated in figure II-2.

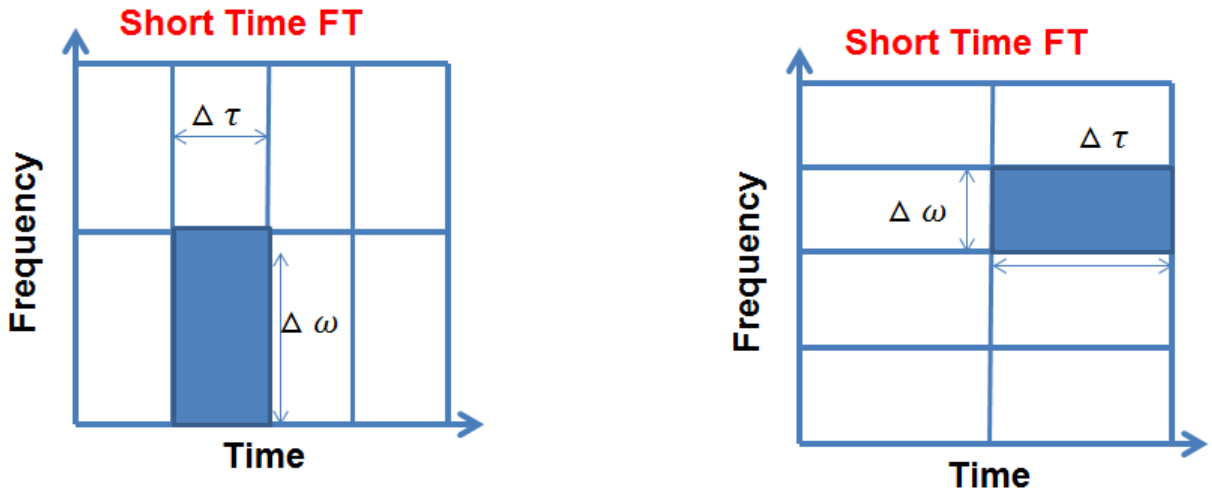

Figure II-2. Ilustration of the frequency and time resolution with respect to window size in short-time Fourier transform. A winder time window gives good time resolution and poor time resolution. A narrow time window gives better time localization but poor frequency resolution.

This limitation can be overcome by using a more flexible window approach by varying the window size. This approach is called wavelet transform[3]. The Wavelet Transform (WT) in its continuous form provides a flexible time-frequency window, which narrows when observing high frequency phenomena and widens when analyzing low frequency behaviour. Thus time resolution becomes arbitrarily good at high frequencies, while the frequency resolution becomes arbitrarily good at low frequencies. This is realized by comparing the signal with a set of template functions obtained from the scaling (dilation and contraction) and shift (translation along the time axis) of a base wavelet $\psi(t)$ and looking for their similarities.

A wavelet is a wave-like oscillation whose amplitude starts out at zero, increases, and then decreases back to zero. The continuous wavelet transform the time-series $x(t)$ can be written as:

$$W(a,b) = \frac{1}{\sqrt{a}} \int_{-\infty}^{\infty} x(t)\psi^* \left(\frac{t-b}{a} \right) dt, \qquad \text{(II.4)}$$

where the symbol a represents the scaling parameter, which determines the time and frequency resolution of the scaled base wavelet $\psi(\frac{t-b}{a})$. The specific values of scale a are inversely proportional to the frequency. The scaled wavelet is translated along the time axis by shifting parameter b.

The base wavelet can be chosen to be a complex Morlet (shown in Fig. II-3), defined as

$$\psi(m) = \frac{1}{\sqrt{\pi f_b}} e^{i \cdot 2\pi f_c m} e^{-m^2/f_b} \tag{II.5}$$

where $i = \sqrt{-1}$, $m = (t-b)/a$ is a dimensionless number, f_b is called the band width and is responsible for the shape of the wavelet, and f_c is called the center frequency. The resulting scalogram $W(\nu, t)$ for a C-O bond vibration trajectory is shown in Fig. II-4. The value, $\nu_{\max}(t)$ the value of the wavenumber ν that corresponds to the maximum value of $W(\nu, t)$ at any given time t can be used to obtain a time-frequency 1-D spectrum.

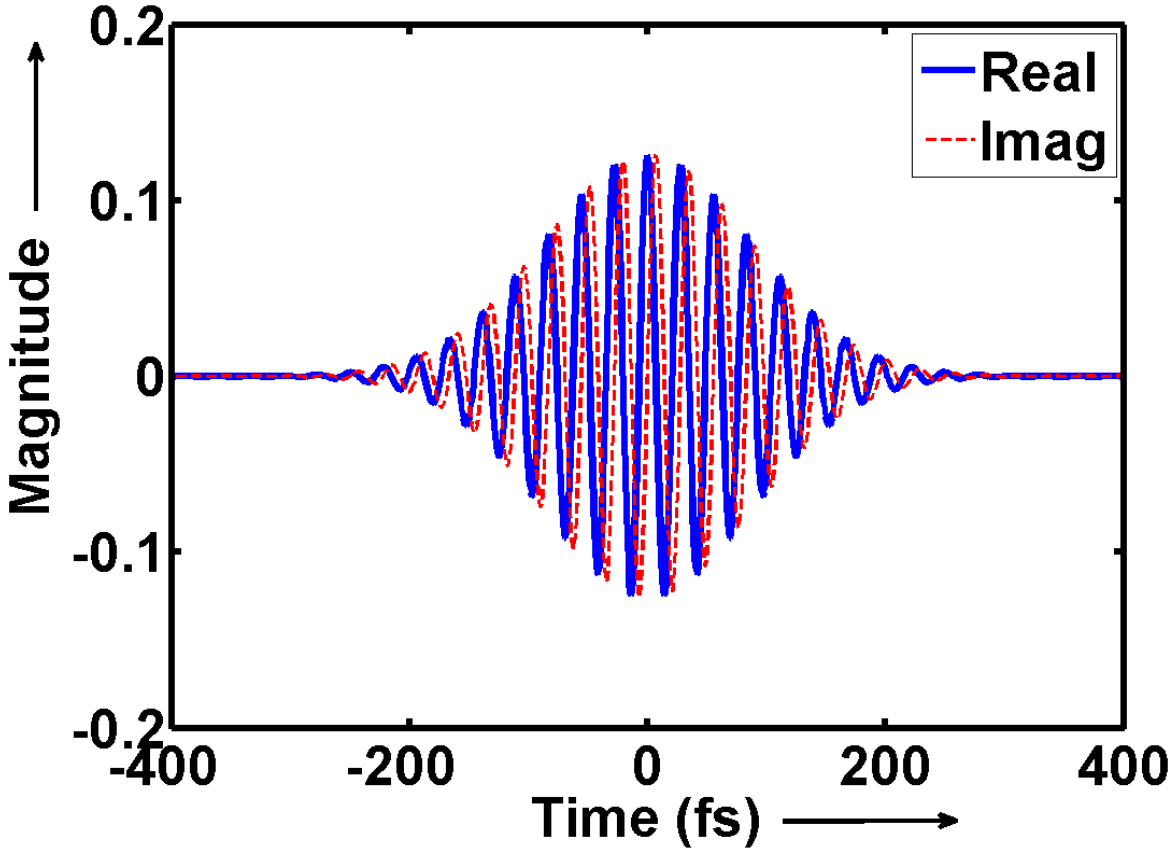

Figure II-3. Complex Morlet wavelet

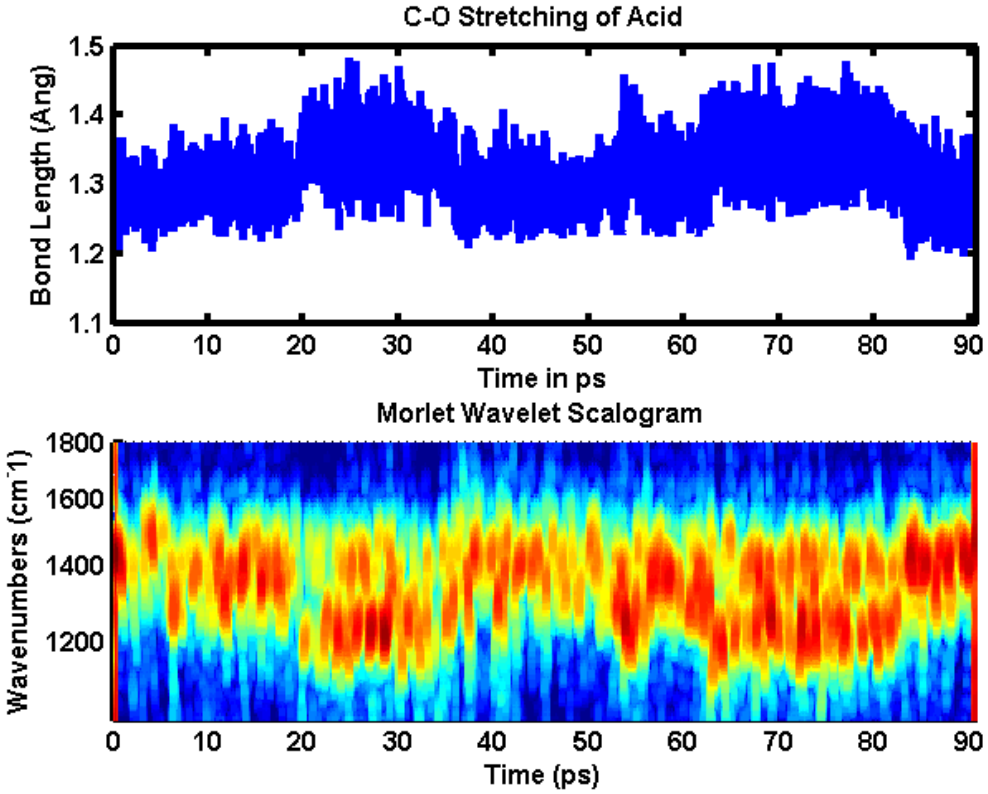

Figure II-4. Scalogram of C-O bond vibration. Top panel shows the analyzed C-O bond trajectory.

I.2 References

(1) Bracewell, Ronald. *Fourier Transform and its applications, McGraw Hill* **2000**.

(2) Jacobsen, E.;Lyons R. *Signal Processing Magazine, IEEE 20,74* **2003**

(3) Daubechies, Ingrid. *Ten Lectures on Wavelets*, Society for Industrial and Applied Mathematics, Philadelphia **1992**